# ABSTRACT

TALLEY, MATTHEW LOWELL. High Voltage RFEA Design, Optimization, and Operation in the Cathode of a Dual Frequency Capacitively Coupled Plasma. (Under the direction of Dr. Steven Shannon).

In plasma processing of the semiconductor industry, the ion energy has a significant effect during the manufacturing process whether it be material deposition, material etch, or ion implantation. When measuring the ion energy, the results are presented as an ion flux energy distribution function (IEDf). Since the IEDf has such a strong impact on the manufacturing process, it becomes necessary to have a detailed and comprehensive understanding of these effects to properly design the industrial plasma systems suited to the manufacturing process. Traditionally, IEDfs have been obtained using retarding field energy analyzers (RFEAs) in two different configurations. The first is where RFEAs are imbedded in a diagnostic wafer that replaces the process wafer on top of the radio frequency (RF) biased electrode. The second is where the RFEAs are imbedded in a unique RF biased electrode that is installed in the plasma system. However, as the semiconductor industry desires to design, characterize, and monitor next generation plasma systems, a more complete, more accurate, and less invasive measurement diagnostic is required. The focus of this research was to extend the capabilities of the REFA so that it could operate in an industrial plasma system under typical manufacturing conditions. This requires the sensor to be able to measure higher ion energies (i.e. operate at higher potentials) and handle process gases. To test the concept and feasibility of this type of diagnostic, a typical RFEA was redesigned for high voltage operation and installed in the RF biased electrode of an industrial plasma system. The redesign for high voltage operation involved using electrostatic simulations to optimize the electric field between the grids and increase energy resolution. It was found that the highest energy resolution is obtained when the grid gap distance is large, and the grid hole diameter is small. The analysis of the redesign also included using particle-in-cell (PIC) simulations to analyze the effects of space charge distortion on the current-voltage (*IV*) curves and IEDfs obtained by the RFEA. The IEDfs were obtained from the IV curves using a regularized least-squares (RLS) solution. The space charge distortion was found to be linked to the grid gap distance and incoming ion flux. A first order model of the space charge potential was developed to truncate the system matrix of the RLS method to compensate for space charge distortion. It was found that if the space charge potential can be accurately modelled, the truncation of the system matrix will provide an undistorted IEDf. To install the RFEAs in the electrode of an industrial system, a new electrode with a cavity was created to the same outer dimensions of the industrial electrode it replaced. Multiple probes were installed in the electrode cavity and IEDf measurements were taken when the electrode was grounded and RF biased. The IEDfs obtained from the electrode RFEAs for an argon plasma were compared with IEDfs from a commercial probe under the same plasma conditions. The IEDfs were found to be very similar to one another showing the redesigned RFEAs were operating correctly. The IEDfs obtained when the electrode was RF biased displayed the expected bimodal peaks (i.e. saddle shape) at reasonable energies. IEDfs measurements were also obtained from plasmas with gas mixtures similar to industrial process mixtures. For these measurements an argon-carbon tetrafluoride or argon-carbon tetrafluoride-oxygen gas mixture was used. The IEDfs obtained from these plasmas for an RF biased electrode also showed the expected saddle shape but with additional peaks caused by ions with different masses. The measurements obtained show it is possible to use this diagnostic to measure the IEDf of industrial systems.

# High Voltage RFEA Design, Optimization, and Operation in the Cathode of a Dual Frequency Capacitively Coupled Plasma

by
Matthew Lowell Talley

A dissertation submitted to the Graduate Faculty of
North Carolina State University
in partial fulfillment of the
requirements for the degree of
Doctor of Philosophy

Nuclear Engineering

Raleigh, North Carolina
2018

APPROVED BY:

Dr. Steven Shannon
Committee Chair

Dr. John Muth

Dr. Alok Ranjan
External Member

Dr. Katharina Stapelmann

Dr. Mohamed Bourham

# BIOGRAPHY

The author graduated from Brigham Young University (BYU) with a Bachelor of Science degree in Mechanical Engineering in 2012. As an undergraduate student at BYU, he started work on a research project with a professor in developing an algorithm to study the evolution of nuclear fuel composition during burn up. While attending BYU, he also took part in a Student Undergraduate Laboratory Internship at the Princeton Plasma Physics Laboratory (PPPL) in Princeton, New Jersey. He also deferred his studies for two years to serve as a missionary in Kyiv, Ukraine for the Church of Jesus Christ of Latter-Day Saints. While there, he was able to develop fluency in the Ukrainian language. His research experience at BYU and PPPL led him to pursue a Master of Science degree enroute to a Doctor of Philosophy degree both in Nuclear Engineering. He finished his Master of Science degree in Nuclear Engineering at North Carolina State University (NCSU) in May of 2015. His work for this degree focused on creating an algorithm to model and control bubble coalescence in a dual phase simulation code called PHASTA. After finishing his Master of Science Degree, he continued on at NCSU working on a Doctor of Philosophy degree in Nuclear Engineering focused on plasma physics research. As hobbies, he enjoys rock climbing, watching movies, and spending time with his family.

# ACKNOWLEDGMENTS

I would first like to give my appreciation to Heavenly Father and His Son who have blessed me greatly and given me the faith and strength to become the person I am today. I also cannot express the thanks my wife McKenna deserves for all her support, love, and patience. She has endured even more days waiting patiently for me to finish the last leg of my studies. She has been constant source of encouragement and a listening ear when I need to discuss issues with my research. Her perspective continues to help provide me with insight and has always helped me improve my understanding and clarity when describing my work. I want to thank my parents for all their love and support. I appreciate my father for the example he has set for me as a husband, provider, and man of God as well as his support in all my endeavors. I also have deep gratitude for my mother and the love, help, and nurturing she has provided throughout my life. She has always been there for me no matter the situation. I would not have been able to make it to this point in my education without them.

I could also not have come to this point without the guidance from Steve Shannon. I am especially appreciative of his willingness to take this wide-eyed student under his wing although I come from a place (Ohio) he refuses to set foot in. I will always be indebted for all the, time, knowledge, and experience he has provided to me who started with a bare minimum understanding of what a plasma is and what can be done with it. I am most grateful for his ability to make me feel like a peer while discussing the research while also guiding me though my own thoughts and ideas to come to the most logical conclusion. I am sure that this process he has taught me will be invaluable in my future work as a researcher and engineer. I also couldn’t have made it this far without the help from my fellow students, especially Casey Icenhour, Abdullah Zafar, and Dave Peterson. They have been excellent teachers, study partners, and sounding boards throughout this whole process.

Lastly, I would like to thank all those at the Austin Plasma Lab (now the Concept and Feasibility Lab) at TEL. I could not have completed this work without them. Lee Chen, Barton Lane, Merrit Funk, Peter Ventzek, and Alok Ranjan were all excellent mentors guiding me through my work there. Mike Hummel was an amazing resource for one who has never had much experience in designing and manufacturing parts in industry. Joel Blakenly and Zhying Chen where essential in helping me understand the RFEA diagnostic and previous work that led up to my own work. Without any of them at this lab, I would not have been able to finish the work presented here and I thank them from the bottom of my heart.

# TABLE OF CONTENTS

# LIST OF TABLES

# LIST OF FIGURES

# CHAPTER 1: INTRODUCTION

Plasma processing is a major component in the semiconductor industry. As such, the semiconductor industry is consistently trying to understand and measure the basic properties of the plasmas used in the manufacturing process. The one-dimensional ion velocity impinging on the substrate is one such property. In order to picture the one-dimensional ion velocity impinging on the substrate from the plasma, an ion velocity distribution function is obtained through diagnostic measurement and modelling. This is typically presented in the form of an ion flux energy distribution function. The ion flux energy distribution function allows for a more direct comparison to other characteristic plasma parameters and variables being considered (e.g. plasma potential, measurement diagnostic operating potential, cathode peak-to-peak voltage and direct current (DC) bias, electron temperature, material interactions, etc.) [ 1 - 7 ]. This distribution function is often referred to, although incorrect, as the ion energy distribution function (IEDf) [ 8 ]. For consistency with the nomenclature used in the majority of the referenced material in this thesis, the ion flux energy distribution function will be referred to as the IEDf throughout.

Plasmas used in materials processing rely primarily on the reactive chemistries formed in the bulk volume of the plasma region through electron impact, and the energetic, directional ions that bombard the plasma facing surfaces after being accelerated through the plasma’s boundary layers.  This thesis focuses on the measurement of the latter. During plasma formation of a DC or radio frequency (RF) electropositive discharge, the majority of the energy is being supplied to the electrons and with a small fraction going to the ions from the DC or RF electric field. This is due to the much smaller electron mass and their higher mobility. Therefore, they leave the plasma much more quickly for the grounded chamber walls or powered electrodes. This results in the plasma charging positively with respect to ground. The plasma's boundary layers, called sheaths, form between the positive quasineutral state of the plasma and the chamber surfaces that reside at a different potential (See Fig. 1). The sheath is where the largest electric fields reside, and the source of anisotropic trajectory and energy gain of the ions used in industrial processes.

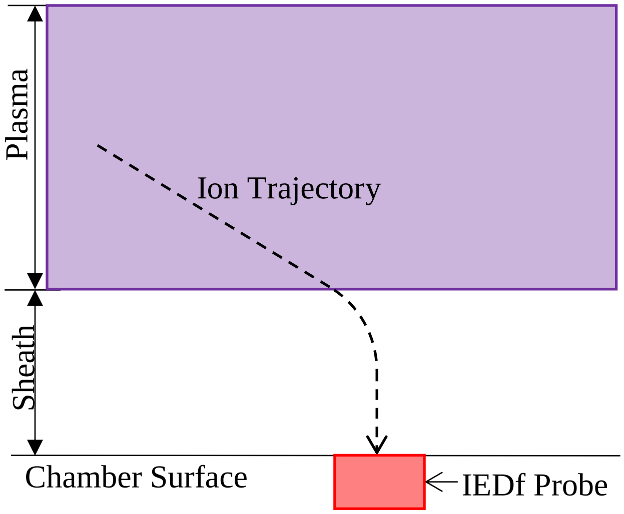

*Fig. 1*: Depiction of the plasma and the boundary layer (sheath) between it and the chamber surface. How the ion trajectory responds to the sheath can also be seen.

For an RF sheath, which is typically found in industrial systems, the dynamics and effects on the IEDf are a bit more complicated than a DC sheath where all the ions gain the same amount of energy. In an RF sheath, the sheath oscillates in size between sheath expansion and sheath collapse as a response to the oscillation of the RF waveform on the powered electrode. Depending on the frequency of the powered electrode and the mass of the ions, the ion trajectory and ion energy will change [ 9 - 12]. To illustrate the effect of the electrode frequency $(\omega)$ on the ion trajectory and energy, a simple figure was created (See Fig. 2). In Fig. 2 the ion mass is assumed to be the same between both *(a)* and *(b)* and only $\omega$ is changed. The plasma ion frequency $(\omega_{pi})$ is used for comparison to $\omega$ where:

$$\omega_{pi} = \sqrt{\frac{e^2 n_i}{\varepsilon_0 m_i}} \tag{1}$$

In Eq. 1, $n_i$ is the ion density and $m_i$ is the ion mass. The comparison of $\omega$ to $\omega_{pi}$ represents whether the ions are responding to an instantaneous electric field or a time-averaged electric field. This is due to the fact that the ion transit time ($\tau_i$) is approximately equal to $\omega_{pi}^{-1}$ and depending on how long the ions remain in the sheath determines if they see a changing electric field [ 9, 10]. Therefore, in Fig. 2 *(a)*, the ions respond to instantaneous changes in the electric field in the sheath. This means that the time and trajectory of the ion as it enters the sheath has a significant impact on the energy the ion gains. In this case, it is possible for an ion to enter the sheath while the sheath is close to its maximum height only to be over taken by the boundary as the sheath collapses. This ion will have a significantly different energy than one that enters the sheath and is never overtaken. Looking at Fig. 2 *(b)* now, $\omega$ in this case is much larger than $\omega_{pi}$. Under these conditions, the ions do not respond to the instantaneous changes, but they respond to the time-averaged electric field changes. This means that the ion energy is much less sensitive to the time and trajectory at which the ions enter the sheath. As such, the sheath dynamics have a significant impact on the ion energy and therefore the IEDf and its shape.

Just as changing from a DC to an RF sheath can change the IEDf and its shape, other methods have been devised to further control the IEDf and adjust its skew. As the frequency of the RF waveform has a significant impact on the IEDf, the shape of the waveform can also have a significant effect [ 11, 13]. The data presented by Rauf showed that a sinusoidal waveform gives a high energy peak with a gentle decreasing slope with decreasing energy. The data for a triangular waveform creates a constant IEDf and the data for a square waveform creates a step

IEDf. Another very common method to control the IEDf is to use multiple frequencies for the discharge. The most widely used version in industry is to use two frequencies, one as the

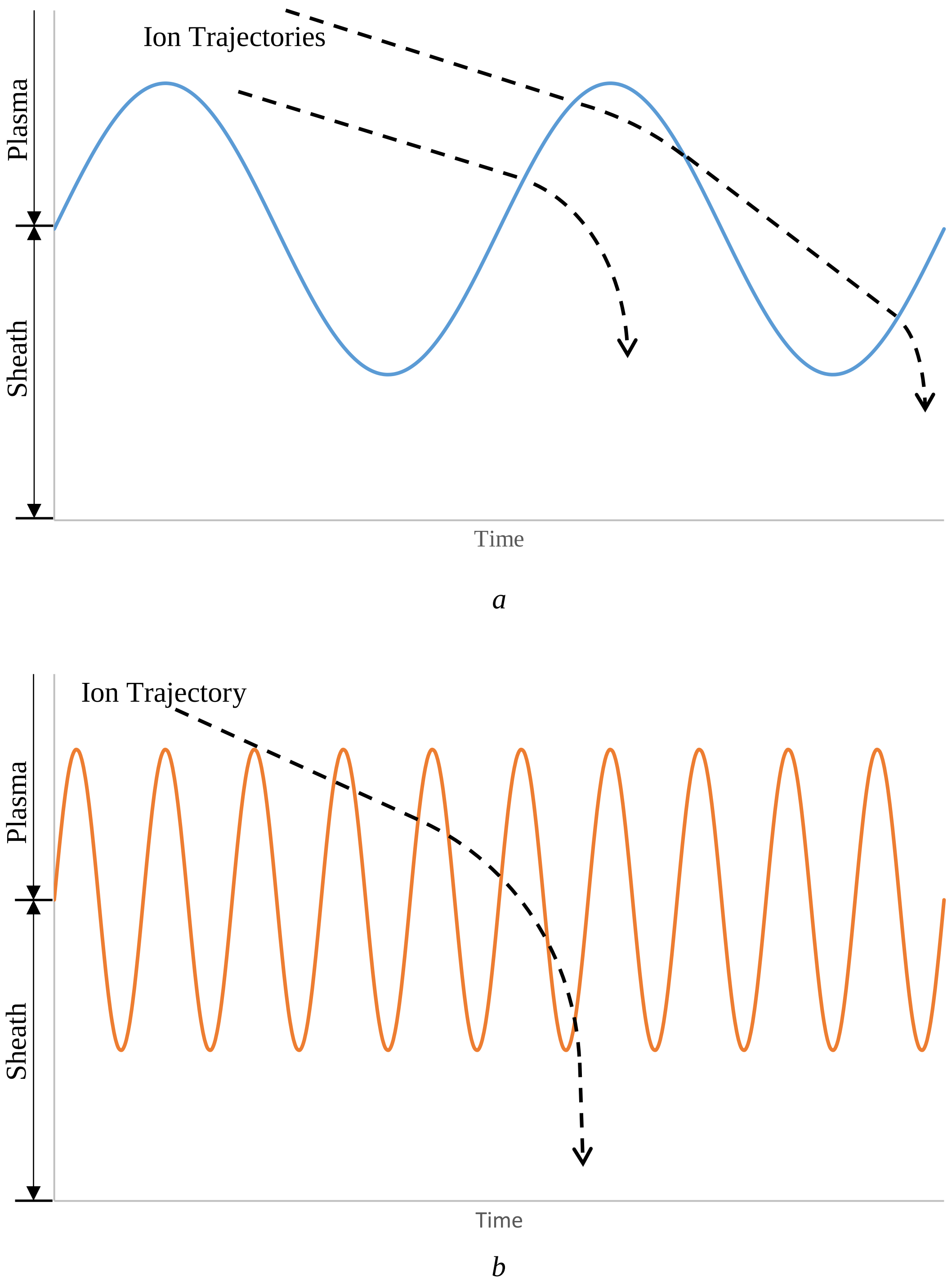

*Fig. 2*: Plots depicting the sheath position over time for two different bias frequencies. (*a*) $\omega \sim \omega_{pi}$ (*b*) $\omega \gg \omega_{pi}$.

source power and a separate applied as a bias to the substrate. The two frequencies essentially decouple the density and IEDf making it possible to control the IEDf with the bias frequency [ 2, 3, 5, 10, 11, 13 - 23]. For a constant plasma density, adjusting the RF bias power applied to the substrate will shrink or expand the overall length of the sheath. If the sheath gets smaller, the ion travel time across the sheath decreases so they respond to the instantaneous electric field of the sheath. On the other hand, if the sheath expands, the ion travel time increases which means they trend more towards the time-averaged electric field of the sheath. Lastly, another method to control the IEDf and its skew is done by adding a second frequency component to the bias frequency applied to the substrate. This second frequency is a harmonic to initial RF waveform and is phase locked so that the two waveforms stay at a consistent phase difference [ 2, 24 ]. By changing the phase difference between the bias waveform and its harmonic between 0° and 180°, it is possible to adjust the skew of the IEDf (See Fig. 4). By using these methods, it is possible to alter the IEDf and its skew which plays a key role in material processing.

The IEDf plays a significant role in the manufacturing process being performed whether it be material deposition, material etch, or ion implantation [ 2, 3, 5, 8, 10 - 16, 23, 25 - 41]. Within each of these processes, the IEDf has a significant impact on the critical details of the manufacturing processes such as the amount of heat transferred to the surface during material deposition, the depth and shapes of the channels during the etch process (See Fig. 3), the selectivity of material during etching (See Fig. 4), and the depth at which ion implantation stops just to name a few.

Since the IEDf has such an effect on the manufacturing processes, it becomes necessary to have a detailed and comprehensive understanding of these effects to properly design plasma systems suited to the manufacturing process.  As the semiconductor fabrication industry moves

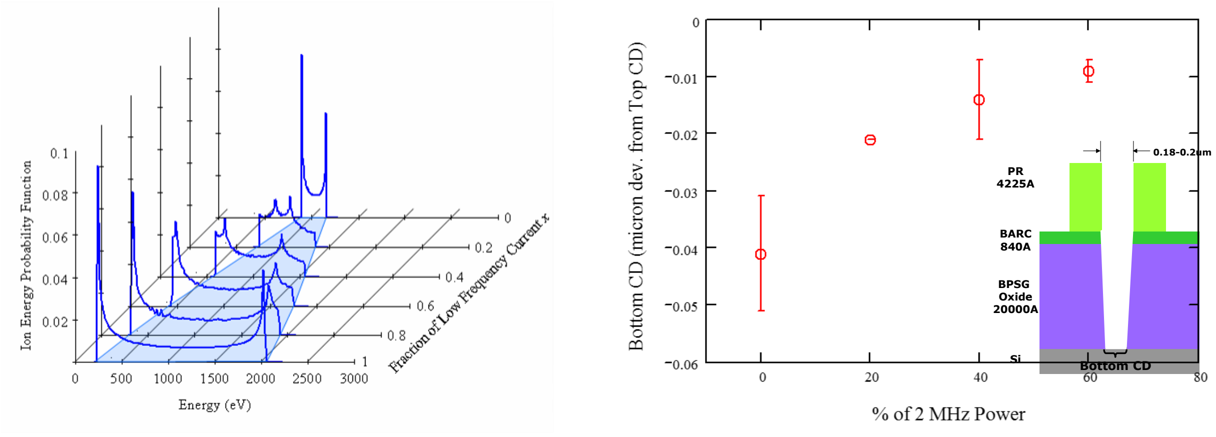

*a* *b*

*Fig. 3*: Plots presented by Shannon et al. [ 42 ]. (a) shows how the IEDf changes based on the amount of low frequency current added to a plasma. (b) shows how the bottom width of the etch profile changes in comparison to the top width based on the percentage of 2MHz power added.

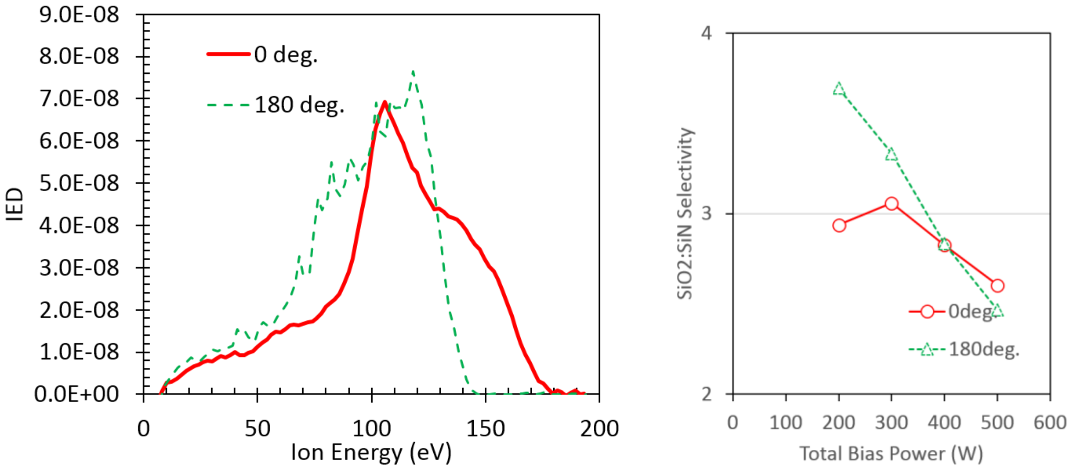

*a* *b*

*Fig. 4*: Plots presented by Yoshida et al. [ 43 ]. (a) shows how the shape of the IEDf changes when controlling higher order moments by changing the phase between the low frequency power and one of its harmonics. (b) shows how the etch selectivity changes as the skew of the IEDf changes.

forward with research on microcircuit designs made on silicon wafers using plasmas, it is all the more important to utilize the knowledge of IEDf process effects in the development of the new generation of plasma systems that will be used to make these future microcircuits. One particular example of this is found in the high aspect ratio etch process and the plasma immersion ion implantation process [ 12, 35 - 38 ]. Manufacturers that use either of these processes have been requiring plasma systems that provide higher ion energies that reach the substrate. They are also looking for ways to obtain better estimations or measurements of the IEDf during process conditions. Just as the plasmas systems are evolving, there is a growing need to broaden the capabilities and application of diagnostics that provide the IEDf.

The objective of this research is to extend the capabilities of an established ion energy measurement diagnostic to provide a more complete, more accurate, and less invasive measurement technique desired by the semiconductor fabrication industry to design, characterize, and monitor next generation plasma systems. The sensor's design must allow for operation in the regimes required by manufacturers. This sensor should also be able to measure the IEDf of a plasma during process conditions or in a scenario that is very similar to process conditions and not rely on surrogate gases that may not accurately represent actual process conditions. This includes the ability of the diagnostic to handle process gases. There are a few diagnostics to be discussed later that meet these requirements but in order to meet this goal, it was decided that whichever diagnostic is used, will be placed inside a cavity below the surface of the biased RF electrode of an industrial system on which the substrate sits. This will make it possible to run with conditions similar to manufacturing process conditions while a silicon wafer can sit on top of the electrode during the time of the measurements. It also makes it possible to leave the rest of the industrial chamber minimally modified, with diagnostic and manufacturing capabilities provided simultaneously by one of these sensors for the first time. By fulfilling these objectives, the newly modified diagnostic will be able to provide the IEDf for a broader set of plasmas and operating conditions.

A diagnostic must be chosen that can provided the IEDf of a plasma. Multiple diagnostics and methods have been created to measure and calculate the IEDf. The most common diagnostics and methods to obtain the IEDf from a plasma are to use an energy analyzer-mass spectrometer, a sheath or circuit model in a simulation which is compared to direct IEDf measurements or these models are used in connection with other diagnostics that do not measure ion velocity directly to calculate the IEDf, and a retarding field energy analyzer (RFEA). Each diagnostic or method has its advantages and disadvantages, but all provide an IEDf. The following is a brief overview of the design and operation of each along with a summary of some results obtained using each diagnostic.

Energy analyzer-mass spectrometers (See Fig. 5) have been used extensively to obtain particle energy or particularly, the IEDf of a plasma [ 8, 15, 17, 18, 40, 44 - 56]. However, as the second half of the name suggests, mass spectrometers were originally designed to determine the mass of different unknown species in a gas mixture. The most common energy analyzer-mass spectrometer design comes with three distinct regions or parts: an ionizer, an energy analyzer, and a quadrupole residual gas analyzer (See Fig. 5). To distinguish the energy and mass of the different species in a neutral gas, particles in the neutral gas mixture are ionized by an electron gun. However, when used with a plasma, the ionization of the gas species has already taken place, so this portion of the system is typically turned off or removed from the system.

To distinguish the ion energy of the newly ionized particles, the energy analyzer-mass spectrometer deflects the trajectory of the incoming ions around a single (e.g. a 45° - 90° electrostatic energy selector [ 47 - 49, 51, 52 ], See Fig. 5) or multiple bends (e.g. a cylindrical mirror analyzer [ 46, 50 ], See Fig. 6). Since the ability of an ion to change its trajectory is dependent on its momentum and charge, it is possible to tune the deflection of the ions so that

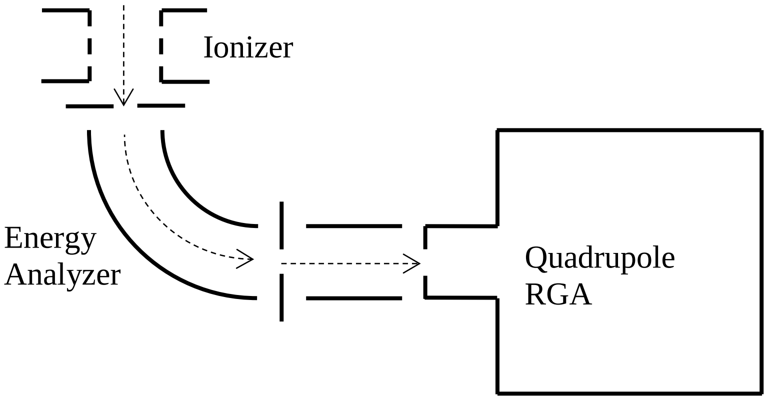

*Fig. 5*: Simple schematic of an energy analyzer-mass spectrometer. The dashed arrows represent the flow of particles through the device. In this figure the Energy Analyzer is a 90° electrostatic energy selector.

only ions with a specific momentum and charge pass through the bend or bends without hitting any other surface. This discrimination process may not be unique to a single momentum and charge combination though, so a quadrupole residual gas analyzer is also used to discriminate further in a similar process of the energy analyzer. In order to remove velocity from this discrimination process, all of the incoming ions are accelerated to the same velocity.

The quadrupole analyzer is made of four parallel metal rods where rods opposite from one another are electrically connected. An RF signal with a DC offset is applied between the different pairs of rods. As the ions pass through the quadrupole analyzer only those with a specific mass-to-charge ratio pass through the analyzer without colliding with the rods or wall. This makes it possible to collect only ions with a specific mass-to-charge ratio. By knowing the mass, the charge, and the strength of the deflecting field of the energy analyzer, it is possible to calculate the incident ion velocity. By taking measurements when sweeping the strength of the deflecting field, it is then possible to generate and IEDf for the plasma.

Using an energy analyzer-mass spectrometer Janes and Huth [ 45 ] were able to obtain the IEDf and ion angular distribution function (IADf) at the surface of a RF powered electrode in

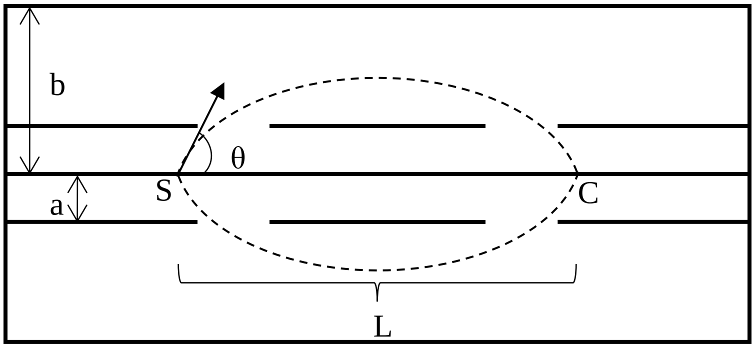

*Fig. 6*: Simple schematic of a cylindrical mirror analyzer. S represents the particle source, C is the particle collector, L is the distance between them, a and b are the radii of the cylinders, and θ is the angle at which the particles leave from the source. The dashed lines represent the trajectory of the particles.

a capacitively coupled plasma (CCP) allowing them to investigate the effects of argon ion collisions within the sheath. Their results showed distinct peak structures in the IEDf resulting from ions created through charge exchange collisions responding to the RF modulated electric field of the sheath. The results also show that for pressures greater than 30mTorr, multiple scattering events become more significant in the development of the IEDf. Their results for the IADf show that a maximum in peak intensity is obtained at 0° in reference to the surface normal and intensities found at angles between ±3° are the result of elastic scattered ions.

Mizutani *et al.* also used an energy analyzer-mass spectrometer to look at how the operational mode of the energy analyzer changes the shape of the IEDf when taking a measurement at the surface of a RF powered electrode [ 50 ]. When taking a measurement, there are two modes in which the energy analyzer can be run: a DC mode and an RF mode. For the DC mode, the electric potential of the analyzer remains constant while in the RF mode, the electric potential of the analyzer oscillates with the same frequency, amplitude, and phase present on the RF electrode. Their results show that an energy analyzer running in RF mode produces the expected saddle shape (dual) peak formation. A saddle shape peak was also produced when running in DC mode, but multiple other peaks of a distinguishable intensity were also observed in the continuum region. For the DC mode, there was also a significant shift in the peak location of the high energy peak compared to the RF mode results. Their results show the necessity to run an energy analyzer in RF mode when used to measure the IEDf incident on a RF powered electrode.

Another common method to obtain the IEDf of a plasma is to develop a sheath or circuit model (See Fig. 7) for the plasma. These models predict the spatiotemporal sheath dynamics during process conditions to determine the IEDf in the bulk plasma or IEDf incident on the silicon wafer surface [ 1, 2, 5, 7, 10, 12 - 15, 23, 25, 30, 32, 39, 57 - 63]. These models typically use a combination of Poisson's equation, energy conservation, flux continuity, Boltzmann's relation, and ion transit time (See Eqs. 2 - 6) [ 10, 12, 63] in describing ion transport and energy through the sheath. The combination of these equations gives the first necessary component in creating a model to obtain an IEDf.

$$\nabla^2\Phi = \frac{-\rho}{\varepsilon_0} \tag{2}$$

$$\frac{1}{2}m_i u^2(x) = \frac{1}{2}m_i u_s^2 - e\Phi(x) \tag{3}$$

$$n_i(x)u(x) = n_{is}u_s \tag{4}$$

$$n = n_0 \exp(-\Phi/T) \tag{5}$$

$$\tau_i = 3s\sqrt{m_i/(2eV_{sh})} \approx \omega_{pi}^{-1} \tag{6}$$

The second necessary component of the model is to properly represent the dependence of the IEDf on the RF power and frequency. As mentioned earlier, the frequency and magnitude at which the bias power is provided to the substrate are the major controlling factors of the sheath dynamics. This means that the frequency and magnitude applied has a direct impact on the energy ions gain as they travel through the sheath. The RF power and frequency are typically applied through the resistive $(R)$ and reactive $(C, L)$ components of the plasma circuit model (See Fig. 7). By developing this equivalent circuit model of the sheath and coupling it with particle transport equations through the sheath it is possible to estimate the IEDf that reaches the substrate. To get the necessary input parameters for the circuit model and particle transport equations, other diagnostics such as voltage-current (VI) probes, capacitive probes, and Faraday cups are used to measure the input quantities. From there, it is possible to obtain the IEDf for a plasma at specific operating conditions.

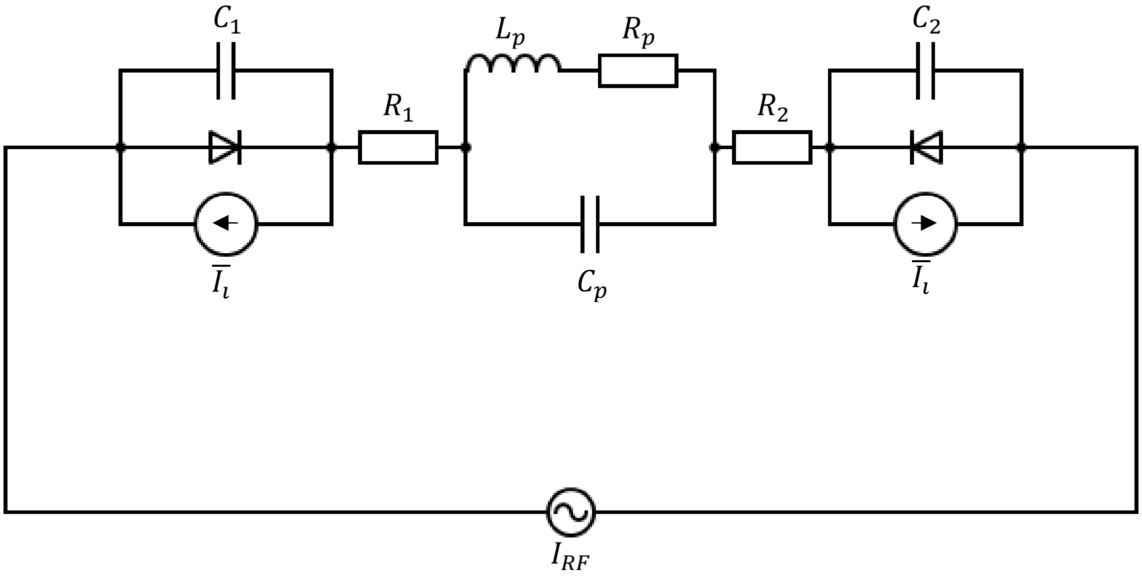

*Fig. 7*: Nonlinear plasma circuit model for a homogeneous RF plasma based off of a figure by Lieberman and Lichtenberg [ 12 ]. The components $C_1$ and $C_2$ represent the sheath capacitance. $R_1$ and $R_2$ represent the sheath resistance. $\overline{I_\iota}$ is the DC current source that represents ion heating.

Panagopoulos and Economou were able to make affective use of a plasma sheath model to simulate the IEDf dependence on the ion modulation $(\omega\tau_i)$ in the sheath [ 10 ]. Using Eqs. 2 - 6 coupled to the waveform function at the wall $(V_w)$ coming from the RF generator, an equation for the damped wall potential $(\overline{V_w})$ was obtained (See Eq. 7). Based on the value of $\omega\tau_i$, the $\overline{V_w}$

mimics $V_w$ very closely or deviates quite a bit from $V_w$. By using $\overline{V_w}$, they were able to simulate the IEDf that would be generated for different values of $\omega\tau_i$. The simulation showed that for small values of $\omega\tau_i$, a bimodal IEDf is generated with a wide dispersion between the peak energies. When the value of $\omega\tau_i$ got larger, the dispersion between the energy peaks became smaller. Eventually, the IEDf switched from a bimodal peak distribution to a single peak distribution at sufficiently high values of $\omega\tau_i$.

$$\overline{V_w}(t) = V_{DC} + \sum_j \frac{V_{ACj}}{1 + (j\omega\tau_i)^2}\left[\cos\left(j\omega t + \theta_j\right) + (j\omega\tau_i)\sin\left(j\omega t + \theta_j\right)\right] \qquad 7$$

Sobolewski, Wang, and Goyette also used a plasma sheath model when looking at the IEDf of an RF inductively coupled plasma (ICP) composed of only $CF_4$ [ 15 ]. In contrast to Panagopoulos and Economou, they used a less complex sheath model in conjunction with experimental data from a Faraday cup and capacitive probe to obtain an IEDf at an RF biased surface. They assumed their sheaths were consistent with a matrix sheath model where the electron density profile is step function at the plasma sheath interface. This simplifies Poisson’s equation allowing them to avoid an iterative solution for electron density. The IEDf from the sheath model was also compared to the IEDf obtained from an energy analyzer-mass spectrometer that was attached at the chamber wall. Even though the spectrometer was grounded, it was positioned close to the RF biased electrode so that the sheath in front of the spectrometer developed an RF voltage when RF power was applied to the electrode. This made it possible to study RF bias effects with the spectrometer and compare the results with the sheath model.

The results from the model were found to be quite accurate with the IEDf measured by the spectrometer. The results show three different types of behavior depending on the frequency applied to the biased electrode. For frequencies below 1MHz, the IEDfs depended only on the sheath voltage waveform since the ions effectively traversed the sheath instantaneously with respect to the frequency. For an intermediate frequency range between 1MHz and 10MHz, a bimodal peak distribution was still observed but the peaks began shifting closer to one another. This is due to the ion flux arriving at the electrode surface being dependent on the RF cycle since the mass of the ions is preventing them from responding to the instantaneous sheath modulation. Lastly, at frequencies above 10MHz, the peaks continued to shift closer to one another until it was impossible to distinguish the high and low energy peaks. For these sufficiently high frequencies, the ions are only able to respond to the time averaged electric field in the sheath which is why the IEDf becomes a single peak distribution. This behavior is consistent with the results presented by Panagopoulos and Economou.

The last common method used to measure the IEDf of a plasma is to use a retarding field energy analyzer (RFEA) [ 1 - 7, 23, 24, 27 - 34, 39, 41, 46, 57 - 60, 64 - 83]. Also known as retarding potential analyzers, velocity analyzers, or electrostatic particle analyzers, these probes use a series of grids and a collector plate to measure the incoming ion current (See Fig. 8). By sweeping the potential of a grid (discrimination grid) in front of the collector plate, it is possible to gradually reducing the incoming current to the collector. By measuring the instantaneous current and matching it with the instantaneous potential of the discrimination grid, it is possible to construct a current-voltage (IV) curve (See Fig. 9). The rate at which the IV curve decreases is directly proportional to the IEDf of the plasma [ 1 ]. By taking the first derivative of the IV curve, one is able to produce the IEDf for the plasma (See Fig. 9).

Because of the simplicity and size of RFEAs, they have been used with multiple configurations. Rafalskyi, Dudin, and Aanesland used a magnetized retarding field energy analyzer (MRFEA) to measure the IEDf of both positive and negative ions [ 71 ]. In a traditional RFEA, the second grid is biased negative to reject plasma electrons. This method works well to keep electrons out of the measurement, but it will also reject negative ions. By modifying the RFEA so that a magnetic field is created above the discrimination grid, the electrons will become trapped in the magnetic field due to their mobility while negative ions will still be able to pass through to the discriminator grid. In the studied performed by Rafalskyi, Dudin, and Aanesland, they presented data that compared the IEDfs of a traditional RFEA and a MRFEA from a positive ion source. The data showed in all cases that the use of the magnetic barrier increased the energy resolution of the probe in reference to the RFEA making the peaks in the IEDf

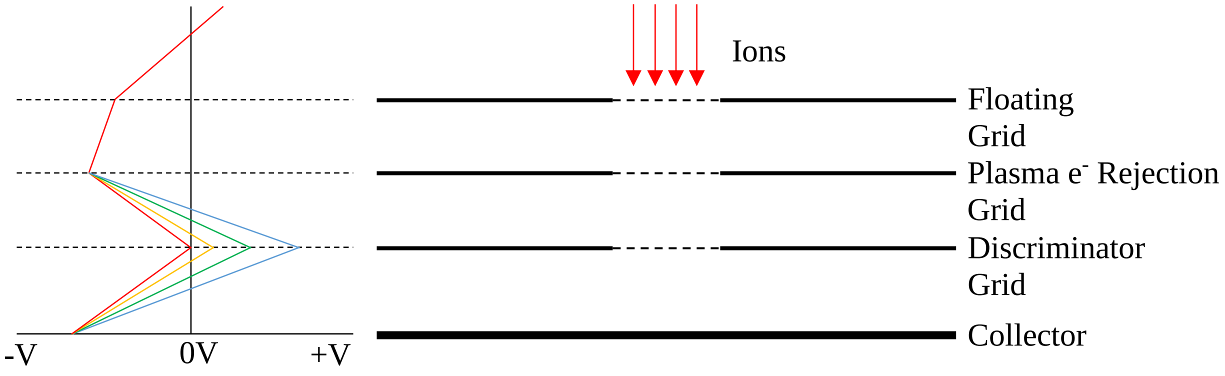

*Fig. 8*: Diagram of an RFEA. This is a three-grid design and each grid is labeled. The plot on the left represents how the potential changes between each grid as the discriminator scans. The color of the lines represents the amount of ion current passing to the collector where red is the highest and blue is the lowest.

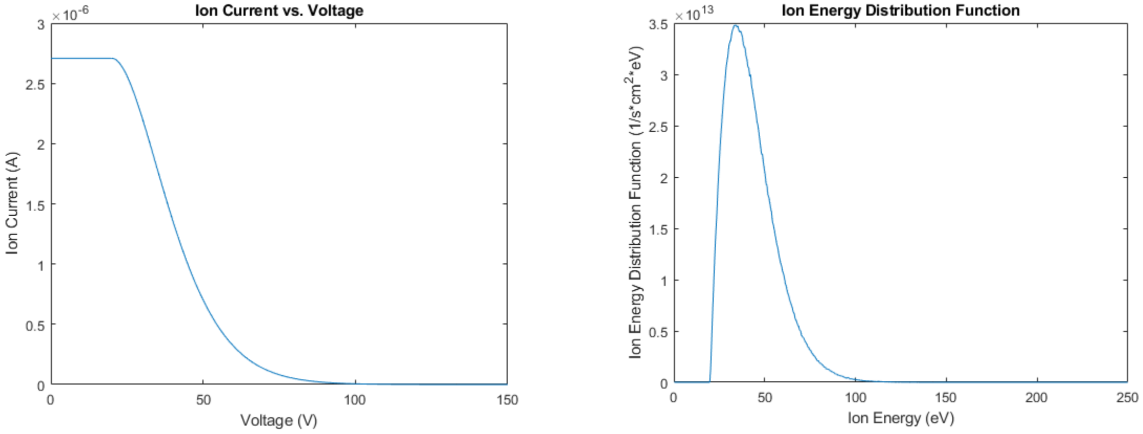

*Fig. 9*: Example of an IV Curve from an RFEA and the corresponding IEDf.

sharper. They also compared the energy distribution functions obtained by the RFEA and MRFEA from a negative ion source. The measurement from the MRFEA created a single narrow peak from the ions while the measurement from the RFEA had the narrow ion peak washed out by three energetic groups of electrons drastically changing the shape of the distribution.

RFEAs have also been used outside industrial plasmas such as measurements in the ionosphere [ 64, 68, 69, 73] and in fusion devices [ 72, 81, 84]. The measurements inside the fusion device presented by Brunner *et al.* was particularly challenging [ 81 ]. They designed an RFEA for the Alcator C-Mod reactor. This reactor is challenging due to the limited materials allowed inside the ultra-high vacuum to limit outgassing and the extreme heat fluxes on the probe surface from high plasma temperature and density. To overcome these challenges, the RFEA was designed using molybdenum, tungsten, stainless steel, silver, and beryllium copper as the metal components. The insulators used consisted of boron nitride, alumina, mica, Teflon, and PEEK. While in use, the RFEA operated as expected even when pushed to the point of melting the outer shield. It was able to measure both the ion energy and electron energy. Based on the fits to the current collected, the ion temperature was 90.9 eV and the electron temperature was 24.0 eV. It was noted that the ion current was lower than expected but it was attributed to ions being attenuated due to high perpendicular energy.

As each diagnostic previously described has advantages and disadvantages (See Table 1), it is necessary to pick which is most capable of fulfilling the goals of this research. The diagnostic probe that best fits this work is the RFEA. The probe can be compact so that it can fit inside a cavity of the biased electrode, it provides a direct measurement from which the IEDf can be obtained (IV curve), and the design can be easily modified to handle the new operating conditions. The circuit model method would do well because the required probes are already in

*Table 1*: This table compares the advantages and disadvantages of each of the different probes or measurement methods.

| Probe | Advantages | Disadvantages |
|---|---|---|
| Energy Analyzer-Mass Spectrometer | - Direct ion velocity measurement<br>- Can differentiate ion peaks based on mass<br>- Can differentiate multi-charged ions | - Very large and difficult to float to the RF bias<br>- Limited spatial and energy resolution<br>- Prone to sputtering<br>- High cost |
| Circuit/Sheath Model | - Indirect measurement does not perturb the plasma<br>- Other probes providing necessary data for the model can provide a broader array of measurements<br>- Cost effective | - Dependent on the accuracy of the model<br>- Unable or difficult to account for collisions<br>- May have complex and long solution times |
| Retarding Field Energy Analyzer | - Direct ion velocity measurement<br>- Small, robust, and flexible probe design<br>- Cost effective | - Unable to directly differentiate peaks based on mass<br>- Unable to differentiate between multi-charged ions |

line with the RF signal (VI probe) or could possibly be modified to fit inside the biased electrode (Faraday cup and capacitive probe). However, these probes do not provide a direct measurement that contains the information of the IEDf. The information gained from the VI probe, Faraday cup, or capacitive probe are used as input parameters for the sheath circuit model and particle transport equations. Here in lies the problem. The IEDf obtain would only be as good as the model used and is limited by the assumptions made when developing the model. Lastly, the mass spectrometer would do well because like the RFEA, it provides a measurement from with the IEDf can be obtained. However, it fails to meet the project objective of fitting inside a cavity of the bias electrode [ 71 ]. Mass spectrometers have been attached to an orifice of grounded electrodes [ 17, 18 ]. In these instances, the apparatus stretched out farther below the grounded electrode because they need to provide an area in which to divert the ion trajectories and another area to collect the screened ions. This makes it impractical to try and fit the probe inside the cavity of the biased electrode and would require significant modification of the lower part of the industrial chamber to house the rest of the mass spectrometer. Therefore, the RFEA is the best diagnostic to use for this work.

To determine the necessary design changes and modifications to make to a RFEA for operation at these process conditions, it is necessary to understand the current designs and capabilities of RFEAs. As mentioned previously, RFEAs consist of a series of grids and a collector plate used to measure the incoming ion current (See Fig. 8). These probes typically have three to four grids in front of the collector plate that measure the ion current. The first grid is referred to as the floating grid as its purpose is to match the potential on whatever surface the RFEA sits. The grid is set at the potential by having a direct line of contact to the biased electrode. This is done to reduce any perturbation of the sheath above the RFEA so the IEDf obtained by the RFEA is generated by the biased electrode and not the probe itself. The second grid is used as a high energy electron rejection grid. This grid is used to screen out any high energy electrons that enter the probe so that they do not screen the ions as they pass through the discrimination grid. This prevents electrons from artificially inflating the current measured at a particular potential. The third grid is the discrimination grid. As mentioned previously, this grid sweeps through a potential range to discriminate ions with energies below the grid potential. Lastly, a fourth grid is sometimes included to act as a secondary electron rejection grid. As ions impact the collector plate, if they are of sufficient energy, they can cause the collector to emit secondary electrons. Since the collector plate is biased negatively with respect to the discrimination grid, these electrons will travel away from the collector plate and be lost. This artificially increases the current of the IV curve. Hence, a fourth grid which is biased negative with respect to the collector plate is sometimes inserted in the probe to force the secondary electrons back to the collector plate.

Insulator sheets are also placed in between each of the grids and collector plate so that all but the first grid are able to float at the RF potential along with the DC bias. The RF potential is coupled to the grids and collector plate of the RFEA by the capacitance between the grids and the electrode itself. Without the RF potential on the other grids and collector plate, it would not be possible to accurately measure the IEDf [ 5, 15, 29, 50, 70 ]. In general, most current RFEAs in an RF plasma system have these design elements in common. For a more comprehensive review of the design of current RFEAs, one is referred to the following [ 2 - 6, 34, 41, 60, 66, 73, 77, 80, 85].

In relation to this work, installing a RFEA in the electrode of an RF plasma system is not something new [ 1, 6, 23, 31, 34, 41, 80]. Kortshagen and Zethoff, Woodworth *et al.*, Bohm and Perrin, Toups and Ernie, Ingram and Braithwaite, Landheer *et al.*, and Rakhimova *et al.* each installed a RFEA in the grounded electrode at surface level of their plasma chambers. All but Woodworth *et al.* used a planar RFEA while Woodworth *et al.* used an RFEA made of concentric hemispheres. However, each of these electrodes are specially designed for the specific purpose of housing the RFEA. In each case, they were not designed for or suitable for industrial systems. Mizutani and Hayashi, Kuypers and Hopman, and Edelberg *et al.* all installed RFEAs at the surface of RF biased electrodes [ 3, 29, 60, 70]. The first two sets of authors did not use an industrial chamber and their RFEAs were on the larger side. The Edelberg *et al.* experiment was different though because they used a slightly modified electrostatic chuck for a Lam TCP reactor. They also biased the electrode with a 4MHz signal allowing for an IEDf measurement from a biased electrode. In this instance, the electrode was designed and used in an industrial system. Nevertheless, the chuck was modified so that the detector was mounted at the surface which displaces many of the other vital systems of an electrostatic chuck (e.g. liquid cooling channels and helium channels for wafer cooling). The goal of this work is to build on this concept and implant the RFEA below the surface of the electrode so as to minimize any redesign of the other systems in the electrode.

Along with installing a RFEA in an industrial electrode, another goal is to increase the operating range of the RFEA. For a RFEA to operate at higher voltages, there are some specific things to consider in the design of the new device. Since the device will be in installed inside an electrode, the device should be compact. With a compact device, there are added benefits in that the device will not need differential pumping [ 32, 41, 60 ] or any issues with space charge distortion in the measurement [ 75, 81 - 83, 85, ]. In order to avoid these issues was why many of the previous referenced designs were made to be compact. However, with a more compact RFEA, the potential magnitude at which the probe can operate is limited. Most current commercial RFEAs have an upper operational bound at 2kV [ 86 ]. A more compact device reduces the thickness of the insulator sheets between the grids. With thinner insulator sheets, the voltage difference between the grids the sheets can withstand before breakdown is reduced. This means that to obtain the higher operating potentials needed for high aspect ratio etch or ion implantation, the dielectric thickness needs to be larger than current RFEAs.

As the dielectric thickness increases, this leads to larger distances between the grids which reintroduces issues avoided with more compact probes. With a large gap comes possible collisions [ 32, 41, 60 ] and light-up within the probe for specific voltage differences, ion energies [ 72 ], gases, and pressures based on Paschen’s law. To prevent Paschen breakdown, the RFEA can be designed for differential pumping so that the pressure between the grids remains in or below the single millitorr range. When comparing the grid gaps to comparable electrode gaps, the required fields for Paschen breakdown exceeds several 10’s of kV $cm^{-1}$ at this pressure range

[ 87 ]. This means that differential pumping of the RFEA becomes necessary for proper operation.

Since the gap between the grids is larger, this also means there are more ions between the grids at any one time. This increases the net charge along the ion path length resulting in possible space charge effects during the measurement [ 75, 81 - 83, 85 ]. The effect of space charge distortion on RFEA measurements has been studied by Jones, Green, and Donoso and Martin [ 75, 82, 83, 85 ]. Jones presented work that systematically compared the extension of theoretical models he developed with calibration experiments. He specifically focused on the measurement of electrons and the resulting electron energy distribution function (EEDf). Jones's analysis showed that if current were to exceed the Child-Langmuir value found from

$$J = \frac{4}{9}\varepsilon_0 \left(\frac{2e}{m_i}\right)^{1/2} \frac{W^{3/2}}{d^2} \qquad 8$$

where $m_i$ is the ion mass, $W$ is electron energy, and $d$ is the grid spacing, a potential valley will be created that will cause space charge distortion. Experimentally, he compared the EEDf for different first grid voltages and varied beam current (See Fig. 10). The results showed that space charge distortion occurred for potentials below 150 V or $J \geq 1.46x10^{-2}$ A cm$^{-2}$ which is in good agreement with Eq. 8. Green performed a similar theoretical analysis investigating the strength of electric fields created by space charge in an RFEA. By using the Poisson's equation, the 1D momentum equation, and continuity equation, he was able to develop an equation to determine when space charge build-up will distort the signal. His results show that when

$$n_o \geq \frac{mu^2}{18e^2Z^2L^2} \qquad 9$$

where $n_o$ is ion density, $m$ is ion mass, $u$ is ion velocity, $Ze$ is charge, and $L$ is length all in CGS units, that the space charge build-up in between the grids will cause distortion to the RFEA electric field. Donoso and Martin also investigated space charge issues using an RFEA with a discrimination grid that has variable gap distance. By taking measurements with different distances, they obtained multiple IV curves and plotted them together to show the variation in the IV characteristics due to space charge build-up (See Fig. 11). By using a theoretical analysis that they previously developed [ 88 ], they created a model to obtain the ion temperature using a correction factor for space charge distortion. From all of their work, the results show that space charge distortion becomes an issue depending on the grid gap distance and incoming particle flux. Therefore, with a new design for high voltage operation of RFEAs, space charge distortion must be considered and analyzed.

The previously mentioned issues are specific to designing a new high voltage RFEA sensor but there are other design considerations that also must be taken into account that are common to all RFEAs. The following considerations may distort the shape of the IV curve or may affect the energy resolution of the detector. The grid plane potential non-uniformity and the electric field uniformity between the grids also has an effect on the measurements. Many studies have shown that for a potential put across a metal grid there is a potential drop between the metal surface and holes of a grid [ 4, 7, 27, 34, 68, 69, 74 -75 76, 78, 80, 85, 89, 90]. This potential drop from metal surface to grid hole will also occur in a high voltage RFEA. Jones, Donoso and Martin, and Landheer *et al.* each investigated the amount of potential variation between the grid surface and grid hole. Their results show that the energy resolution performance of the RFEA is limited by the potential drop in the grids. Jones [ 85 ] investigated the effect for randomly oriented grids made of parallel and perpendicular cylindrical wires. He studied the dependence of the potential difference on the ratio of the wire radius to the distance between hole centers and the ratio of grid gap distance to distance between hole centers. He estimated the difference using

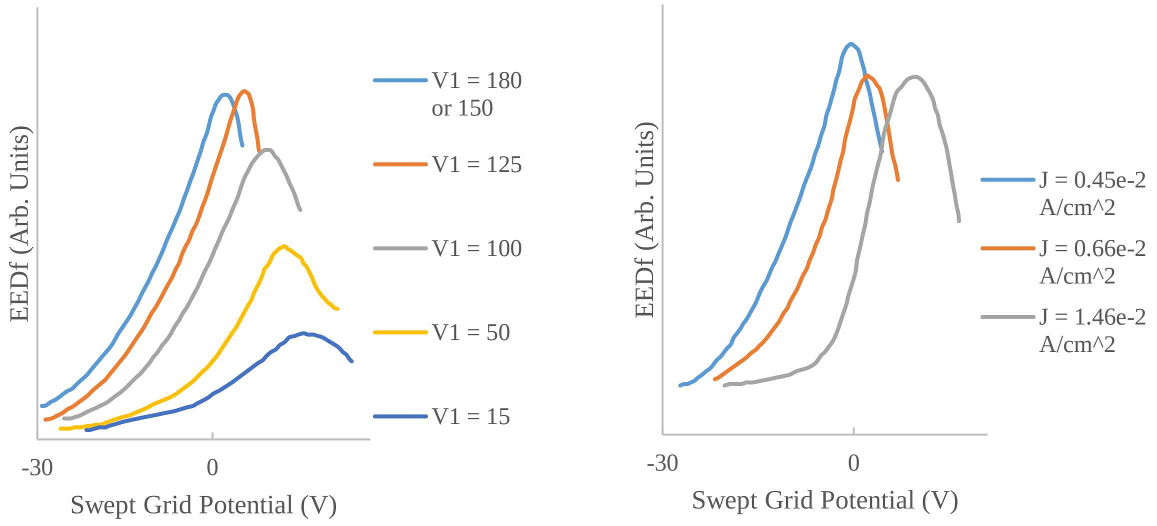

*Fig. 10*: Plots recreated from data presented by Jones [ 85 ]. These plots show that space distortion occurred for $V1 < 150$ V or $J \leq 1.46\ x\ 10^{-2}\ \mathrm{A/cm^2}$.

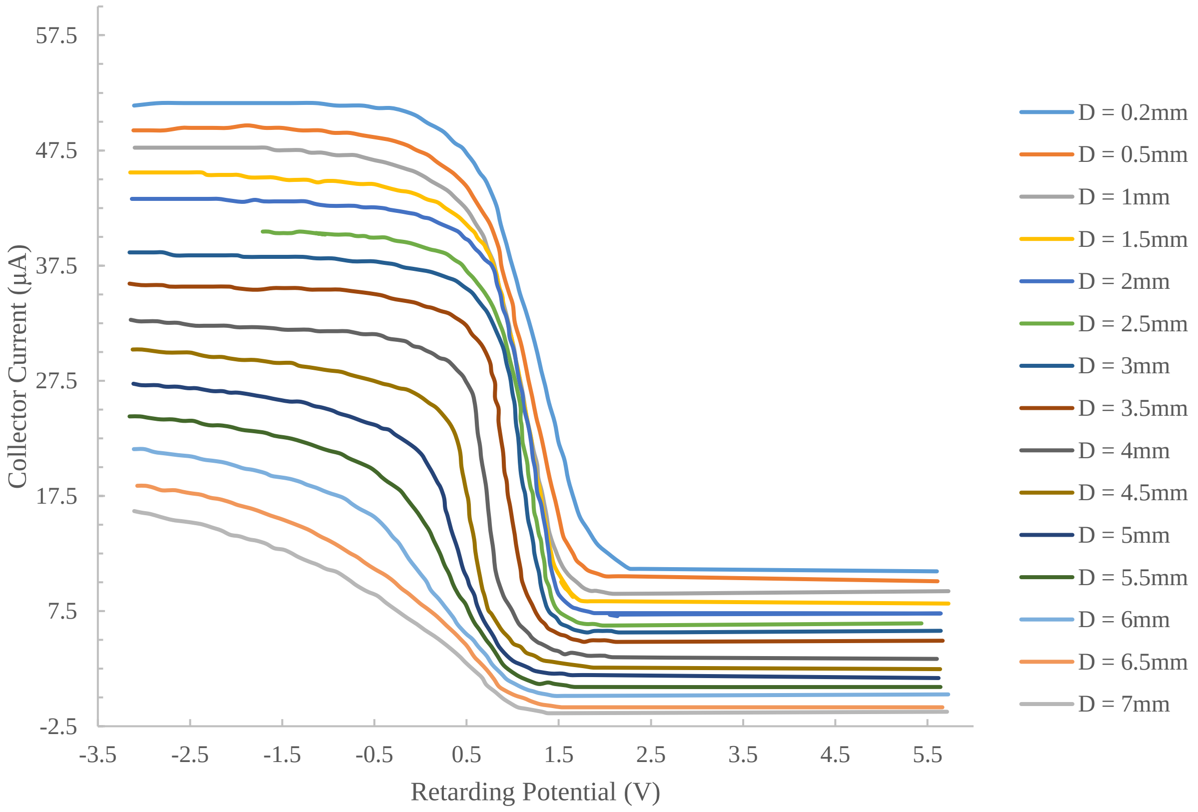

*Fig. 11*: A plot recreated from data presented by Donoso and Martin [ 83 ]. This plot shows IV characteristics for different grid distances in the RFEA. The curves are displaced vertically to avoid pile-up.

Spangenberg's [ 91 ] treatment as well as compared it to measurements. His results show that, for higher ratios of both, better energy resolution was achieved. He also notes that the grid gap distance is limited by space charge build-up like previously mentioned.

Donoso and Martin [ 76 ] also studied a grid of parallel and perpendicular cylindrical wires. In their theoretical analysis, they simplified the shape of the grids by removing the set of orthogonal wires. They then used the Schwarz-Christoffel transformation to obtain an analytical equation for the potential drop. They then showed that by varying the distance between the grids, the potential difference between the grid hole and wire changed (See Fig. 12). Their findings are in agreement with Jones's results that by increasing the gap distance, the potential difference is reduced. Their results were also validated by looking at the IV curves resulting from their variable gap distance RFEA used in the space charge study [ 75 ]. In this case, they were operating within a regime that ruled out space charge distortion. Their results show that as the gap distance increases, the IV curve shape shifts to lower energies (See Fig. 13).

Lastly, Landheer *et al.* [ 34 ] investigated the potential drop using laser cut molybdenum grids. While discussing the design conditions to increase the ion through put of the detector, such as grid alignment [ 34, 73 ], they mention that packing the grids closer together when aligned will cause more electric field penetration of the grids [ 34, 77 ]. This penetration will drastically affect the potential within the grid holes. To study the potential sagging, they simulated the resulting IV curve and IEDf using a mono-energetic beam of 22 eV $H_3^+$ ions when sweeping the discrimination grid from 0 to 50 V. The results presented show that due to a lower potential in the center of the grids, a peak shift of +3eV resulted in the IEDf (See Fig. 14). The shift in peak energy is consistent with the findings of Donoso and Martin. Landheer *et al.* also estimated the potential drop in the grid holes using analytical formulas of Henneberg [ 92 ]. When comparing the simulation results to the analytical results for multiple potentials and stack configurations, they calculated a consistent analytical result of approximately 1.5 times the simulated potential drops. By understanding their work, it is clear to see that to obtain good RFEA performance the geometric design of the RFEA must be taken into account.

The electric field uniformity between the grids also has a significant dependence on the RFEA geometry. The shape of the electric field above the grids will be affected by the proximity of the dielectric insulator. If the insulator is too close to the grid holes, it can alter the field above the grid and contaminate the ion energy as they travel through the detector. The field uniformity will also be affected by geometric design on the inside of the RFEA. With the compact RFEA probes, the space between the grids was symmetrical causing no change to the electric field

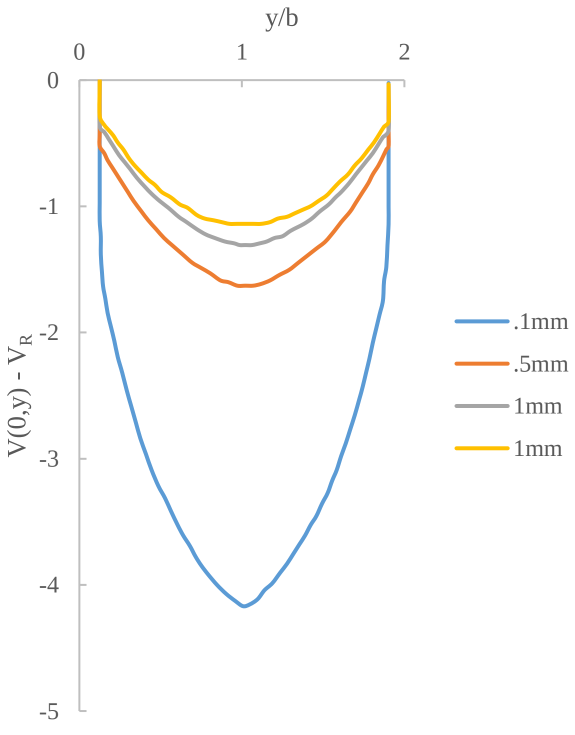

*Fig. 12*: This is a plot recreated from data presented by Donoso and Martin [ 76 ]. This plot shows the change in the grid hole potential based on the grid gap distance.

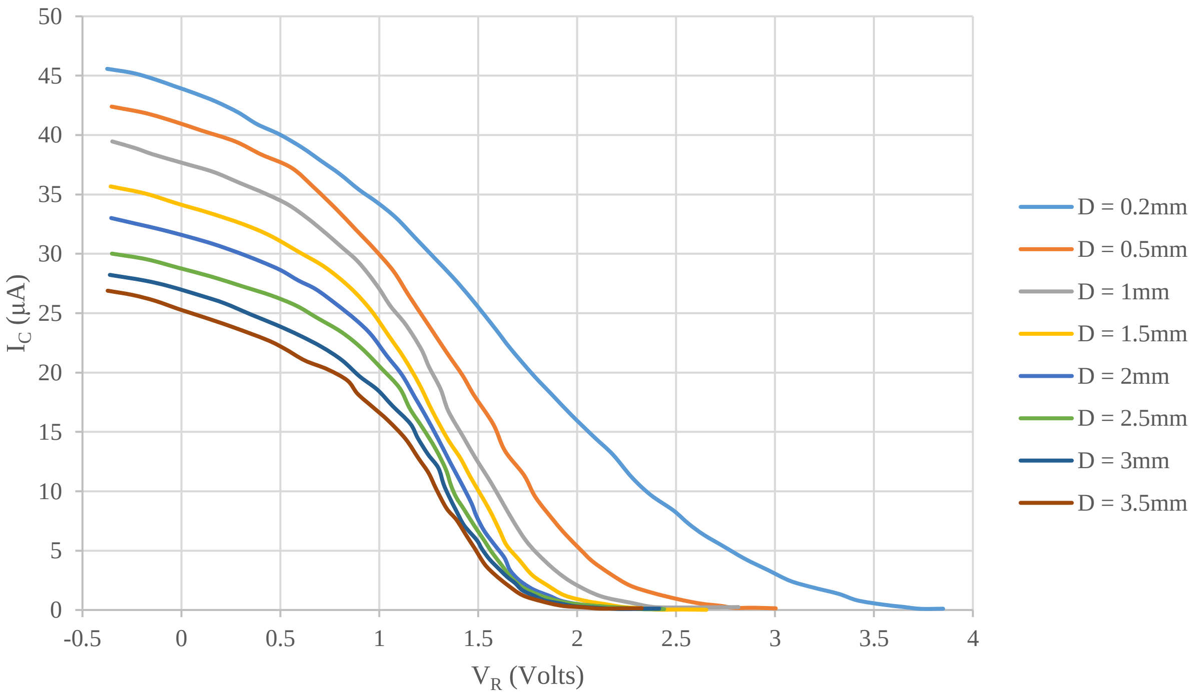

*Fig. 13*: Plot recreated by data presented by Donoso, Martin, and Puerta [ 75 ]. This plot shows the IV curves obtained when adjusting the grid distance. The shift in the IV curve shape is due to a decrease in the potential drop in the grid holes.

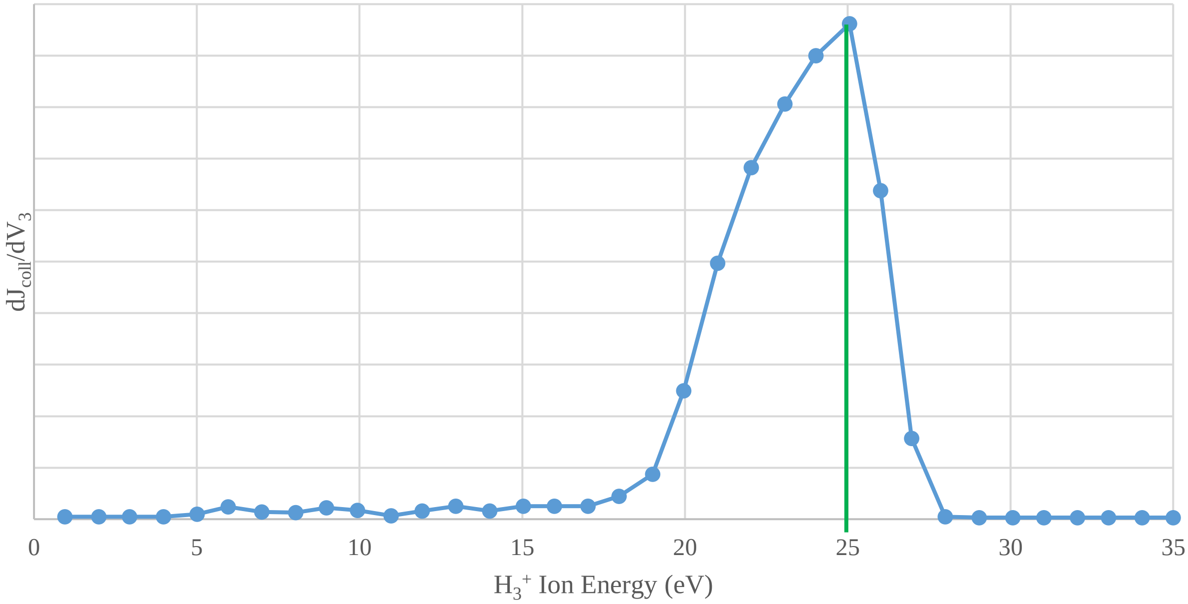

*Fig. 14*: Plot recreated from data presented by Landheer et al. [ 34 ]. This plot shows the IEDf created by scanning a monoenergetic beam of 22 eV $H_3^+$ ions across the potential field in the grid holes on a retarding grid for a sweep from 0 to 50 V. The expected peak energy is at 22 eV but the IEDf gives a peak energy at 25 eV. The 3 eV shift is due to the potential sagging in the grid holes.

between the grids. However, with the high voltage RFEA, differential pumping ports may be added to the side of the detector to reduce internal pressure. These pumping ports make the internal geometry of the probe asymmetric causing a change to the internal electric fields. Therefore, it is necessary to investigate how the changes to probe geometry affect the electric fields in between the grids of the probe and to obtain an optimized design that reduces non-uniformity.

The previously discussed design specifications and issues cover the most significant considerations that must be made when designing a high voltage RFEA to be installed inside the cavity of a biased electrode. However, these issues are not meant to be an exhaustive list. There are many other issues that can also raise complications when making a measurement such as secondary electron emission [ 27, 34, 66, 77, 80, 85], side wall charge build-up, sputtering of the grid material, and corrosive chemical attack [ 34 ] or particle deposition caused by gases used in the semiconductor manufacturing process.  Bohm and Perrin [ 80 ] provided a troubleshooting section to help identify issues in the IV curve characteristics due to plasma electrons or secondary electron emission in the probe. They found a linear increase in the current after rejecting all ions is likely caused by ionization inside the probe from plasma electrons. They also identified a peak near the 0V condition of the discrimination grid likely due to secondary electron emission from the collector. Another indication of secondary electron emission is that the collector current never reaches 0A. Bohm and Perrin explain that this current at high discrimination potential is the result of secondary electron emission caused by neutral species (e.g. photons, metastables, atoms, molecules, etc.). Landheer *et al*. [ 34 ] address the idea of accounting for corrosive chemical attack by changing the material used to make their grids. They explain that grids are commonly made out of nickel or stainless steel. However, they decided on using molybdenum because of its resistance to chemical attack of plasma process gases, paramagnetic, and suitable for laser cutting. As Bohm and Perrin and Landheer *et al*. show, there are more things to consider when designing an RFEA but the main focus will be on the accuracy of the detector and its operation at higher voltages.

Once the design of the RFEA is complete, it will be necessary to check its performance under manufacturing process conditions. To test the applicability of the RFEA in the industrial bias electrode, gases similar to process gases will be used when taking measurements. In this instance, argon (Ar) will be run with a mixture of carbon-tetrafluoride ($CF_4$) or $CF_4$ and oxygen ($O_2$). $CF_4$ and $O_2$ are a common gases used in semiconductor fabrication and have been extensively studied when mixed with Ar [ 17, 18, 20, 24, 56, 93 - 97]. Donko and Petrovi [ 93 ] investigated the IEDfs of Ar, $CF_4$, Ar – $CF_4$ mixtures using particle in cell (PIC/MCC) simulations in single and dual frequency CCP sources. As they used simulations, they were able to separate out the IEDf for the different species. They comprehensively studied the effects of the choice of the high frequency, high frequency voltage, low frequency, and low frequency voltage. Their results showed that with the proper choice of source parameters, it is possible to independently control the ion flux and energy in low pressure plasma discharges. Work such as this and the others referenced will allow for confirmation that the RFEA in the cavity of the biased electrode is working properly.

An extensive review of previous and current RFEA and industrial system has been discussed in the previous paragraphs. Now that the starting point is understood, the importance of this work is apparent. The main objective of this work is to develop a high voltage RFEA located in the RF biased electrode of an industrial plasma system. This consists of analyzing the design of an RFEA to modify it for high voltage performance and optimizing the device for accurate measurement. It also encompasses designing an RF biased electrode on which the substrate would sit and house the high voltage RFEA. This electrode must be easily swapped into an industrial plasma chamber. Lastly, the measurements and resulting IEDfs will be analyzed for different configurations of the chamber for single and dual frequency industrial process conditions.

Chapter 2 will consist of a description of the experimental industrial chamber. It will also discuss the modifications to the RFEA for high voltage operation in section 2.1 and the design of the electrode that will house the detector in section 2.2.1.

Chapter 3 will investigate the conditions at which space charge distortion affects the measurement for the design RFEA. It will also investigate options for space charge distortion compensation through post analysis of the IV curve to recover the true IEDf in section 3.2.

Chapter 4 presents a parametric study using the modified RFEA when located at the wall of the chamber for pure Ar plasma discharges. It will also present a parametric study for the RFEAs located in the low frequency biased electrode of the system for single (section 4.1) and dual frequency (section 4.2) pure Ar CCP discharges. For single frequency discharges, the top electrode will be powered by a 60 MHz RF generator while the biased electrode containing the RFEAs is grounded. During dual frequency operation, the upper electrode will be powered by the 60 MHz generator and the biased electrode will be powered by a 13.56MHz RF generator.

Chapter 5 will present data from a parametric study for single (section 5.1) and dual frequency (section 5.2) CCP discharges for an Ar-$CF_4$ or Ar-$CF_4$-$O_2$ mixture using the electrode probes. Data from the wall probe will also be presented from an Ar-$CF_4$ mixture for single and dual frequency CCP discharges. In these cases, the frequencies used will be the same as those mentioned above for the studies in chapter 4.

Chapter 6 provides a discussion of the results and provides the necessary considerations for future work to continue development of the sensor.

## CHAPTER 2: EXPRIMENTAL CHAMBER AND RFEA DESIGN

### 2.1 RFEA Design

The RFEAs used in this work must be able to operate at higher potentials while still being compact so that they fit within the electrode. To meet these design criteria, a planar three grid design with two plates making up the collector designed by Tokyo Electron Limited (TEL$^{TM}$) was chosen (See Fig. 15 - Fig. 17). The TEL RFEA design is based on and modification of previous designs used in previously mentioned work [ 2 - 6, 34, 41, 60, 66, 73, 77, 80, 85, 98, 99]. In this design, the first grid acts as the floating grid (See Fig. 16 a), the second grid is the electron rejection grid (See Fig. 16 b), and the third grid is the discriminator (See Fig. 16 c). To electrically isolate the grids and the collector, a polyimide sheet was inserted in between each. A center hole was cut out of each to allow the ions to pass through. Screws were connected to each grid and the collector to hold the sensor together. Polyimide sleeves were also used to electrically isolate the screws from the other grids. Dimensions for the plates and polyimide sheets can be found in Table 2.

Each grid consists of a group of holes drilled into each plate in a honeycomb pattern (See Fig. 15). For ease of manufacturability, the grids and plates were made out of aluminum. Aluminum is not the best material choice for the grids and collector as it is susceptible to sputtering and secondary electron emission. However, it is easier to handle when making microstructures (grid holes) and more economic. In a final RFEA design, it is more likely that the grids would be made by electroforming nickel [ 99 ], photolithography on stainless steel [ 98 ], or laser cut out of molybdenum [ 34 ]. Nickel is often used to coat grids and meshes made out of other metals to provide better corrosion resistance. Stainless steel is also corrosion resistant, stronger than nickel, and is less susceptible to secondary electron emission than aluminum. It may have less conductivity than the metal coated in nickel though. Molybdenum is also an advantageous metal because it is resistant to chemical attack, has a very high melting point, low coefficient of thermal expansion, and high thermal conductivity. Nonetheless, it can be brittle and difficult to manufacture. The key purpose of all these materials though is their resistance to chemical attack and sputtering when exposed to the harsh industrial plasma conditions.

The TEL RFEA was also designed with differential pumping ports in each of the grids to provide better pumping access to the center of the sensor. These ports were machined into each of the grids for multiple purposes. The first reason is to prevent collisions and possible light-up (light-up issues discussed in section 4.1.2). To avoid collisions in the RFEA, the ion mean free path $(\lambda_i)$ must be longer than the length of the detector [ 32, 41, 60, 99 ]. $\lambda_i$ for a beam of ions is found by

$$\lambda_i = \frac{1}{n_g \sigma} \qquad 10$$

where $n_g$ is the neutral gas density and $\sigma$ is collisional cross-section with neutral gas particles. The neutral gas density is used for the ion mean free path instead of ion or electron densities because the background neutral gas density is much larger than the ion or electron density. As an example, for argon (Ar) ions, the mean free path as a function of pressure simplifies to

$$\lambda_i = \frac{1}{330p}\ cm \qquad 11$$

where $p$ is the pressure in Torr and the resulting mean free path is given in centimeters. By differentially pumping, the pressure inside the detector will remain low keeping the mean free path larger than the detector. As mentioned in chapter 1, it is also possible to cause light-up in

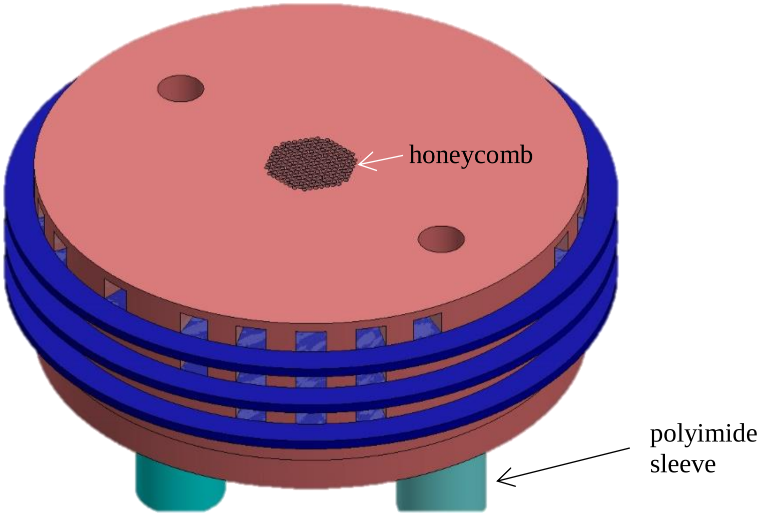

*Fig. 15*: Model of the RFEA design in an isometric view. See Fig. 17 for a detailed view of the honeycomb structure.

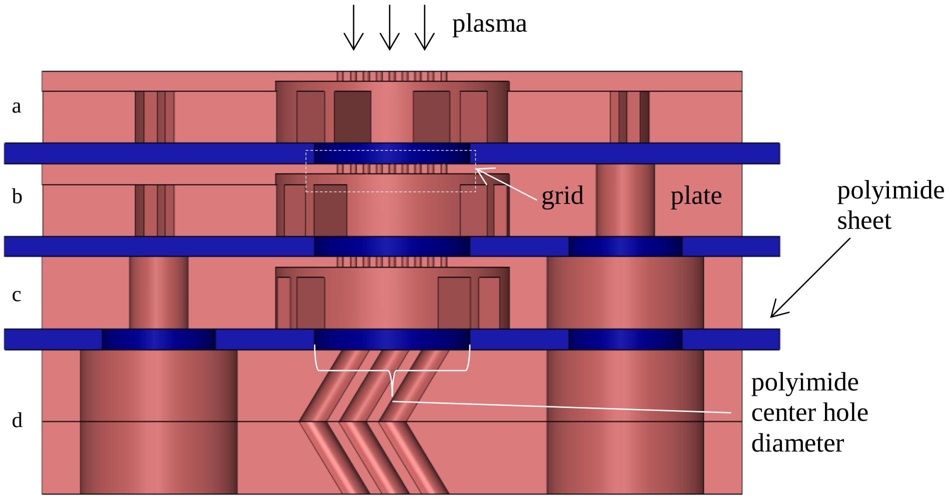

*Fig. 16*: Slice of the RFEA model. This shows the internal structure as well as labels each grid and the collector. (a) Floating grid (b) Plasma electron rejection grid (c) Discrimination grid (d) Collector.

the detector for specific voltage differences, ion energies [ 72 ], gases, and pressures based on Paschen’s law. Differential pumping can keep the pressure below the threshold of Paschen breakdown.

The second purpose to adding pumping ports to the grid is to extend the life of the sensor. By adding pumping ports, additional exits are created that will remove reactive species when the probe is in process environments. These reactive species could corrode the grids or attack the insulator separating the grids resulting more frequent replacement of the RFEA components. Deterioration of the RFEA components from chemical attack by reactive species is a major struggle for current commercial probes. This is why, along with the pumping ports, a silicon (Si) wafer with grids (discussed in section 2.2.1) that helps protect the RFEAs from reactive species is placed on top of the electrode. With the differential pumping ports added, a reduction in the amount of reactive species in the detector will result. Therefore, it becomes advantageous to include differential pumping ports in the design of the detector. On that basis, the collector of the RFEA was made out of two plates because holes were drilled through the plates creating a chevron pattern (See Fig. 16 d). This feature provides one more access point for pumping while still preventing any ions from passing through the sensor without being collected.

Since pumping ports were added to the grids, asymmetry is introduced internally in the detector which affect the electric field on top of any effects caused by the proximity of dielectric

*Table 2*: Dimensions for the RFEA plates and polyimide sheets. See Fig. 15 - Fig. *17* for a refence for where to apply the dimension.

| Metal Plate | Polyimide Sheet |
|---|---|
| Plate Thickness: 0.035" (0.889 $mm$) | Thickness: 0.01" (0.254 $mm$) |
| Plate Diameter: 0.563" (14.3 $mm$) | Diameter: 0.623" (15.824 $mm$) |
| Grid Hole Diameter: 0.005" (0.127$mm$)<br>Aspect Ratio 1:1<br>Center to Center Spacing: 0.006" (0.152$mm$) | Center Hole Diameter: 0.125" (3.175 $mm$) |
| Grid Fill Diameter: 0.102" (2.6$mm$) | |

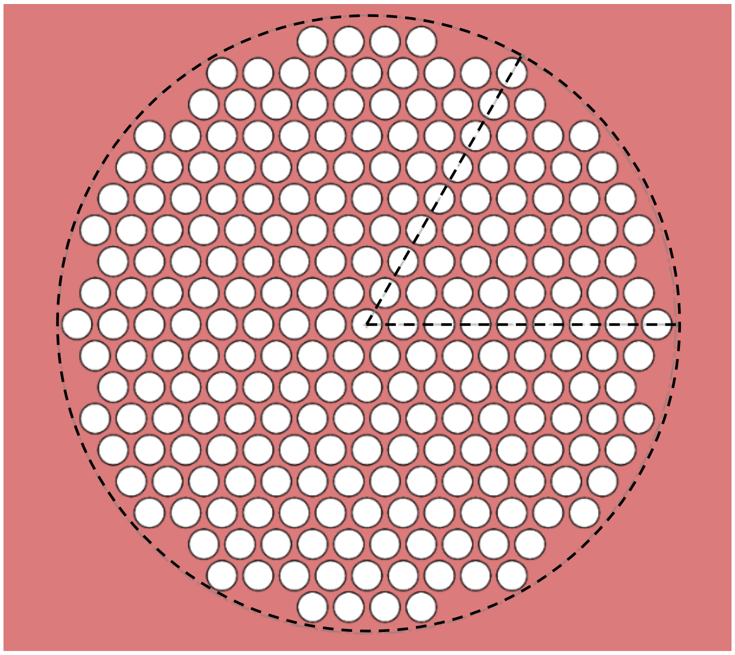

*Fig. 17*: Closeup of the honeycomb grid in the RFEA. The dashed circle represents the grid fill diameter. The dashed lines form a 60° stagger angle to specify how the holes are aligned in the honeycomb structure. The aspect ratio of the grid holes is 1:1.

materials (e.g. polyimide sheet). In a RFEA without pumping ports or close dielectric materials,the electric filed will be completely uniform between each grid as the internal geometry is completely symmetrical and only the grid potential changes. Since the pumping ports introduce asymmetry and the dielectric sheets are in proximity to the ion region, it is necessary to adjust other geometric variables (See Fig. 18) to minimize any variability in the electric field above the grids. These geometric variables that can be changed are the grid gap distance (e), grid fill diameter (f), and grid hole diameter (g). To investigate the changes made to the electric field, a 3D computer aid design (CAD) model was created in the SolidWorks 2016 and 2017 [ 100 ] software packages (See Fig. 15 and Fig. 16). This model was used with the EMWorks 2016 SP2.3 [ 101 ] simulation package. EMWorks is an add-on to the SolidWorks software and the EMS package of EMWorks provides electrostatic and magnetostatic analysis tools using finite element analysis.

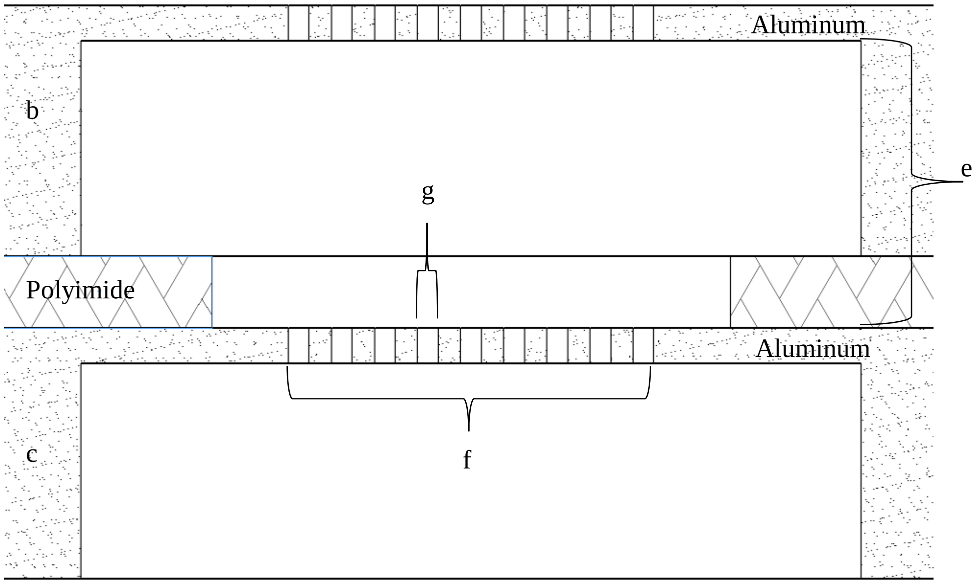

*Fig. 18*: Section outline of the electron rejection grid (b) and discrimination grid (c). (e) Gap distance (f) Grid fill diameter (g) Grid hole diameter.

### 2.1.1 Electric Field

For these simulations and simplicity, it was assumed that no ions were located inside the detector in order to determine how the grid potential and geometry affects the electric field. A more robust model than shown in Fig. 15 and Fig. 16 was used which included design elements for the pumping ports, connection screws, and polyimide sleeves for the screws. The floating grid was set to -1000V (a consistent value with industrial CCP process conditions). The electron rejection grid was set to -1100V. The discrimination grid was set at 500V for all simulations that varied the geometric variables. Lastly, the collector was arbitrarily set to -90V. In traditional RFEAs, the collector must always be negatively biased in reference to the discriminator. Assuming there is no ionization or collisions/charge exchange within the sheath, the discrimination grid can start at -10V for these simulations. Therefore, -90V would always attract ions that are not rejected by the discrimination grid.

For the first simulations, multiple 2D plots were generated on both the vertical axis down the probe (See Fig. 19). The vertical axis plots were generated for the purpose of comparison to the ideal RFEA potential cartoon shown in chapter 1 (See Fig. 8). For the vertical axis, multiple locations (center of the probe, edges of the grid fill diameter, off-axis across the grids) were used to generate the plots. A plot of the vertical component of the electric field down the center of the probe can be seen in Fig. 20. The plot shows that the vertical electric field is effectively uniform in between each of the grids. Sharp slopes are also seen which correspond to transitions through the grids. The shape of the vertical electric field curve is the expected result based on the potential cartoon in chapter 1 and shows the simulation is working correctly. Results from other locations were similar and only showed variation near the edge of the grids.

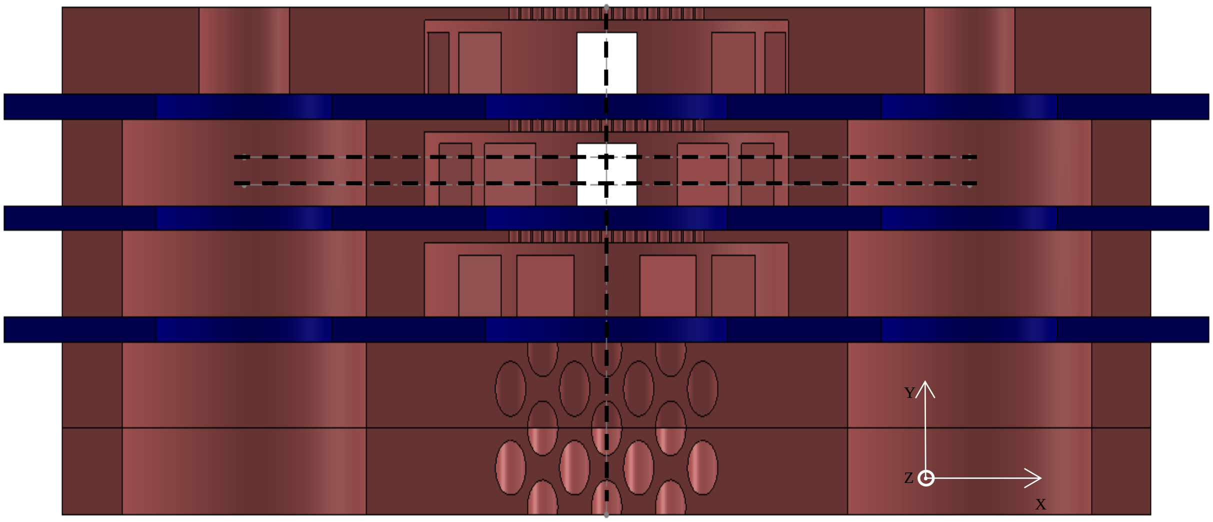

*Fig. 19*: Section cut of the RFEA showing the lines from which the 2D electric field plots were generated. The dashed lines represent the locations at which the electric field was measured in the electrostatic simulations.

It is also important to understand how the vertical component of the electric field compares to the radial component of the electric field. If the radial components are significant or close to the same order of magnitude as the vertical component, it can alter the trajectory of the ions causing them to hit the internal side walls of the sensor. To compare the magnitudes, the vertical component was normalized by the root of the sum of the squares by:

$$\hat{Y} = Y/\sqrt{X^2 + Y^2 + Z^2} \qquad 12$$

where $Y$ is the magnitude of the vertical component and $X$ and $Z$ are the magnitudes of the radial components. The plot (See Fig. 21) shows that the value of the normalized vertical component is effectively 1. The few locations where the normalized component deviates from a value of 1 coincides with the transitions between grids. At these locations, the sign of the vertical electric the vertical electric field looks horizontally across the probe. Again, 2D plots of the vertical electric field were created but looked across the probe horizontally between the electron rejection grid and discrimination grid (example locations seen in Fig. 19). Depending on the location at which the plot was generated, different curve shapes resulted (See Fig. 22). When looking above the polyimide sheet, the vertical electric field increased in magnitude compared to the center (See Fig. 22 a). When the plot was generated within the polyimide sheet region, the vertical electric field decreased in magnitude compared to the center. The variation in these curves is unlikely caused by the pumping ports because of their location. As can be seen in Fig. 16, Fig. 18, and Fig. 19, the edge of the grid is quit far from where the pumping ports start. The variations that are farther outside the ion region in Fig. 22 (specifically in (a)) are more likely due to the pumping ports added to the sensor. This means that as long as enough space is provided, the addition of pumping ports has a negligible affect on the electric field. The varations seen here are more likely caused by the grid edge effects or the proximity of the polyimide insulator.

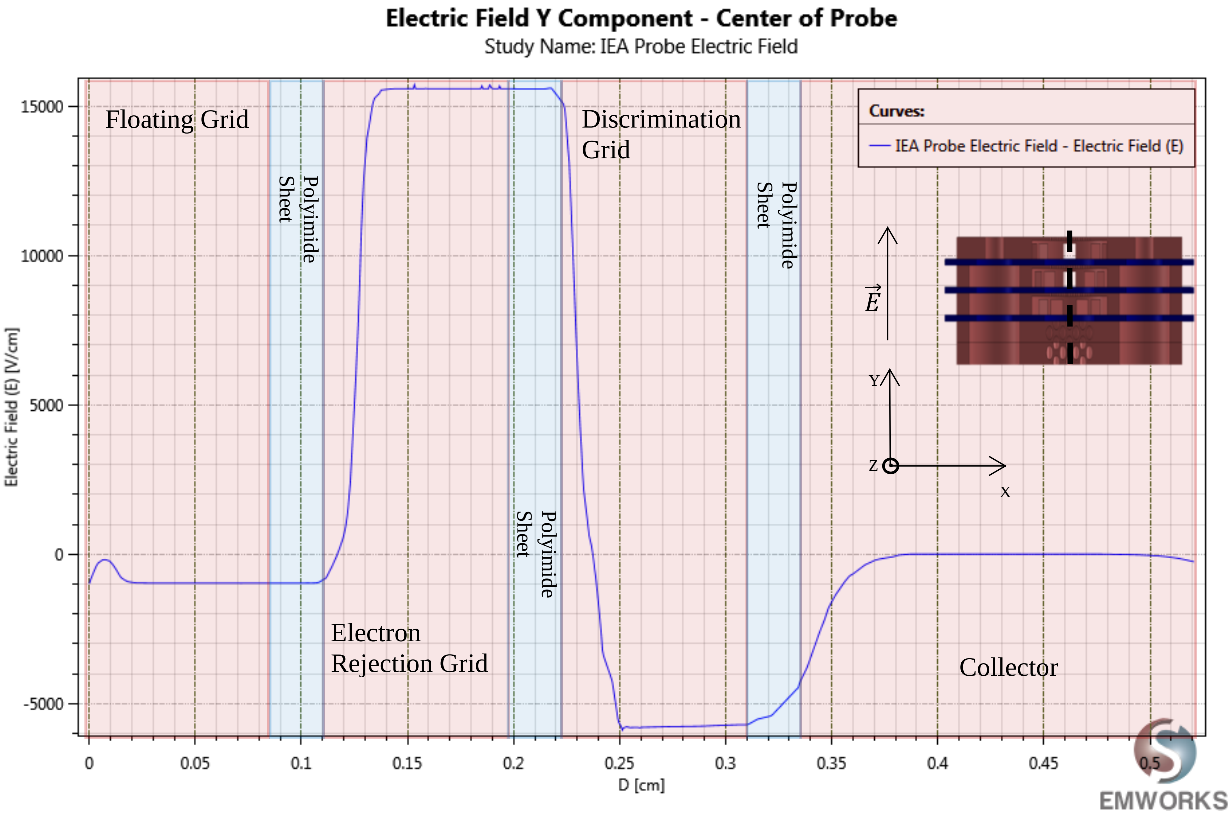

*Fig. 20*: Vertical component (Y) of the electric field down the center of the probe. The electric field magnitude is measured down the vertical dashed line on the RFEA.

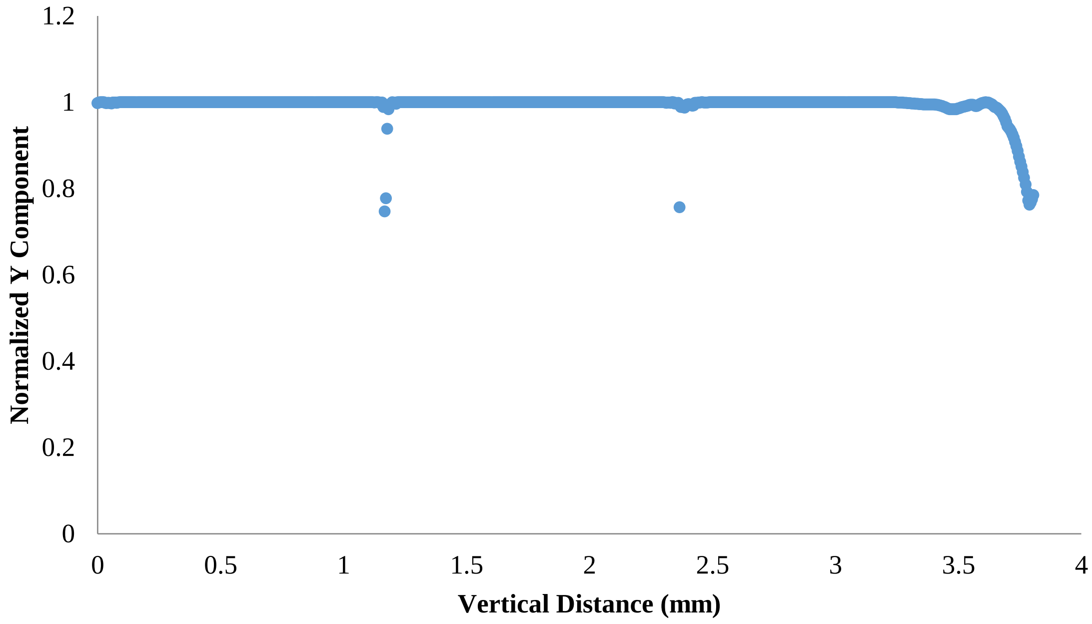

*Fig. 21*: Normalized vertical electric field (Y) to the total electric field using the root of the sum of the squares. The electric field values were taken from a vertical line down the probe.

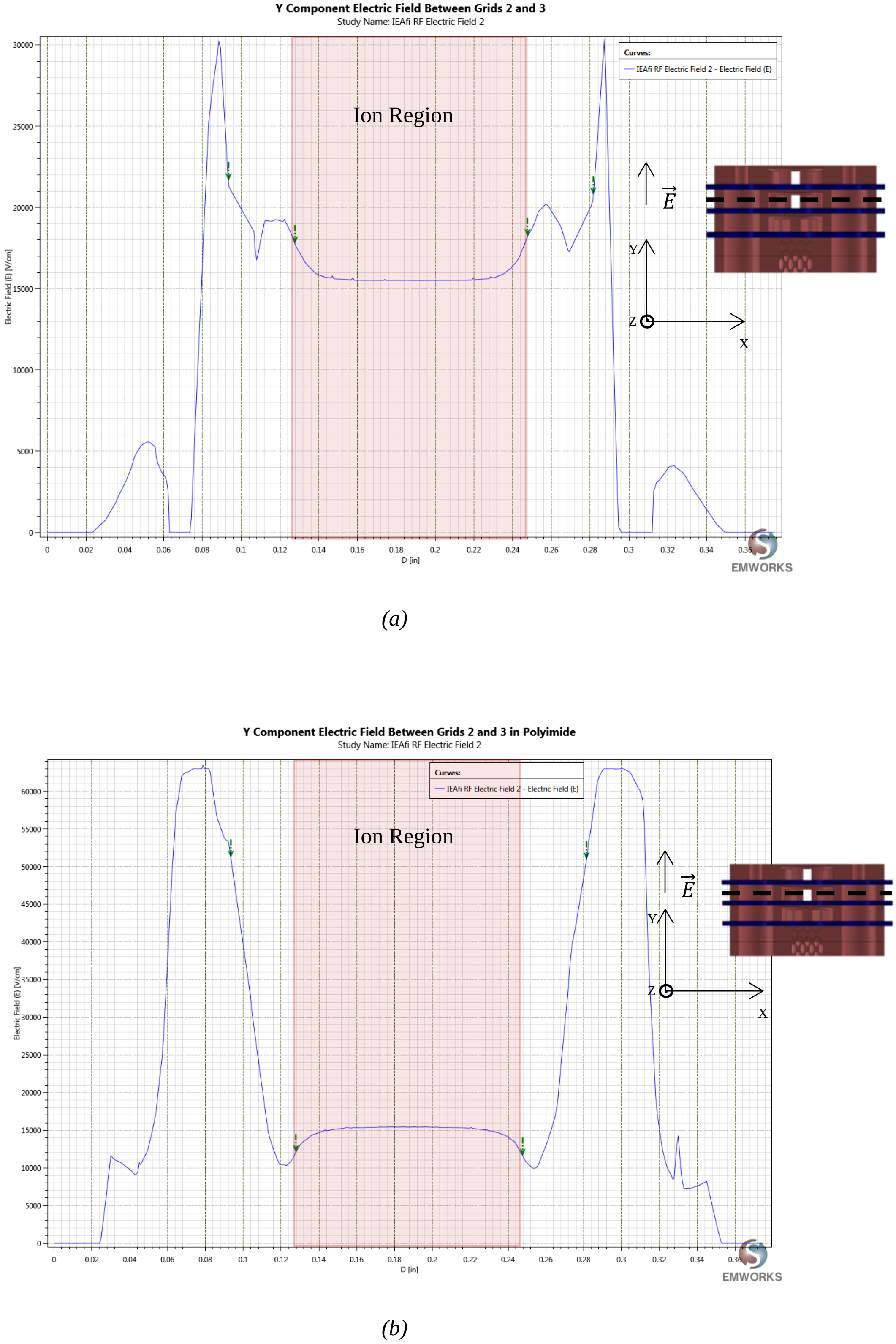

*Fig. 22*: Vertical component (Y) of the electric field between the electron rejection grid and discrimination grid (the black dashed line on the RFEA model). *(a)* This plot was generated at a location above the polyimide sheet. *(b)* This plot was generated at a location within the polyimide sheet.

Again, it is necessary to also compare the vertical electric component to the radial component. By taking the root of the some of the squares of the components and normalizing the vertical (Y) electric field (See Eq. 12), Fig. 23 was created. From the figure, it can be seen that for the ion region, the noramlized vertical electric field has a value of 1. The locations that vary from a value of 1 are caused by material transitions (metal to polyimide) along the horizontal line the field values were taken. Since the value is 1, this means that the radial component horizontally across the probe is negligible through which ions will pass. Again, this means that ions will not be lost to the internal side walls of the RFEA.

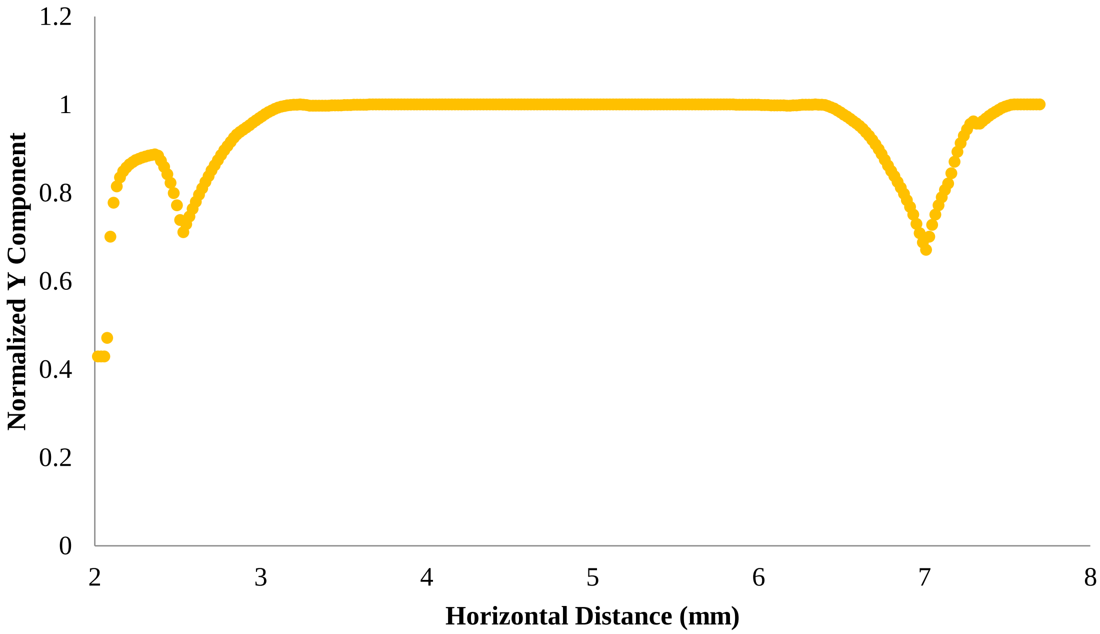

*Fig. 23*: Normalized vertical electrical field (Y) to the total electric field using the root of the sum of the squares. The electric field values were taken horizontally across the probe between the electron rejection grid and discrimination grid.

There is a previously mentioned issue presented by Fig. 22 though. Again an ideal RFEA would have a vertical electric field within the ion region that is completely uniform (horizontal line). However, the shapes seen in Fig. 22 deviate from this ideal. For ions traversing between these grids, the ones near the edges would be accelerated while above the polyimide but be decelerated while within the polymide hole. The edge fields counteract one another but still introduce alteration to the ion energy. It would be better for the ion energy to remain the same than to hope or assume the field shapes will cancel each other out. Since the concavity of the curves changes, it does seem to suggest that it is possible to make a more uniform electric field between the grids by adjusting the parameters (grid gap distance, grid fill diameter, and grid hole diameter) in Fig. 18. Therefore, the optimal values of the design parameters are the ones that produce an electric field that is constant at every location between the grids.

Multiple simulations were performed by adjusting the grid gap distance, grid fill diameter, grid hole diameter, and discrimination grid potential. 2D plots were again generated at two specific locations above the discrimination grid within the ion region (0.5 and 0.75 mm). Generating the plots at the two locations allowed for a comparison of the fields at these locations. In these cases, and ideal vertical electric field is achieved when there is no variation in the field on the left and right side of the plot and no discontinuity in the center (horizontal line across the plot). The only instance where this was not the case was when changing the grid gap distance. In this case, the plot was generated at a point equidistant between the electron rejection grid and discrimination grid. In any case where a parameter was not under investigation, it remained constant. For the grid fill dimaeter, it was set to 2.6mm, the grid hole diameter was set at 0.127mm, and grid gap distance was set at 1mm, and the discrimination grid potential was set at 500 V.

The results for the different simulations can be seen in Fig. 24 and  Fig. 25. For each of the plots, spurious data due to numerical artifacts has been removed. Since the results were generally radially symmetric, especially directly over the discrimination grid, the y-axis of the plots represents the center line down the probe. Since the vertical electric field was generated at two different locations for Fig. 24 (a), (b), and Fig. 25 (b), the left side of those plots shows the field magnitude found at 0.5 mm above the discrimination grid and the right side of the plots shows the field magnitude found at 0.75 mm above the discrimination grid. Fig. 24 (a) shows the change in the vertical electric field when changing the grid fill diameter. Since this adjusts the size of the grid and region in which ions travers though the probe, the dashed and dashed with double dotted lines were added to the plot to show the edge of the 2mm and 2.6mm fill diameter from the center of the probe. For the largest case (3.175mm), the edge of the plot doubles as the edge of the fill diameter as well. The plot shows that as the diameter decreases, the curve within the fill diameter space becomes more uniform (more horizontal). This is seen in a reduction in variation at the edge of the plot. It continues in this fashion until it passes an optimal value in which the vertical electric field begins to vary from the idea (non-horizontal). The departure from the ideal is seen by an increase in the variation at the edge of the fill diameter as well as a change in magnitude at the center (discontinuity).

In Fig. 24 (b), the variation in the vertical electric field due to the grid hole diameter. In this plot, it can be seen that as the grid hole diameter decreases, the variation in the vertical electric field at the edge of the grid fill diameter decreases. This is most notable when changing diameters from 0.254mm to 0.127mm. The grid hole diameter also has an effect on the magnitude of the vertical electric field at the two locations above the discrimination grid. This is seen by the discontinuities or lack thereof in the curves at the center of the plot.

Fig. 25 (a) shows the variation in the vertical electric field due to grid gap distance. Again, only one location was used to generate this plot and it was at the point equidistant between the electron rejection grid and discrimination grid. In general, the curves are pretty

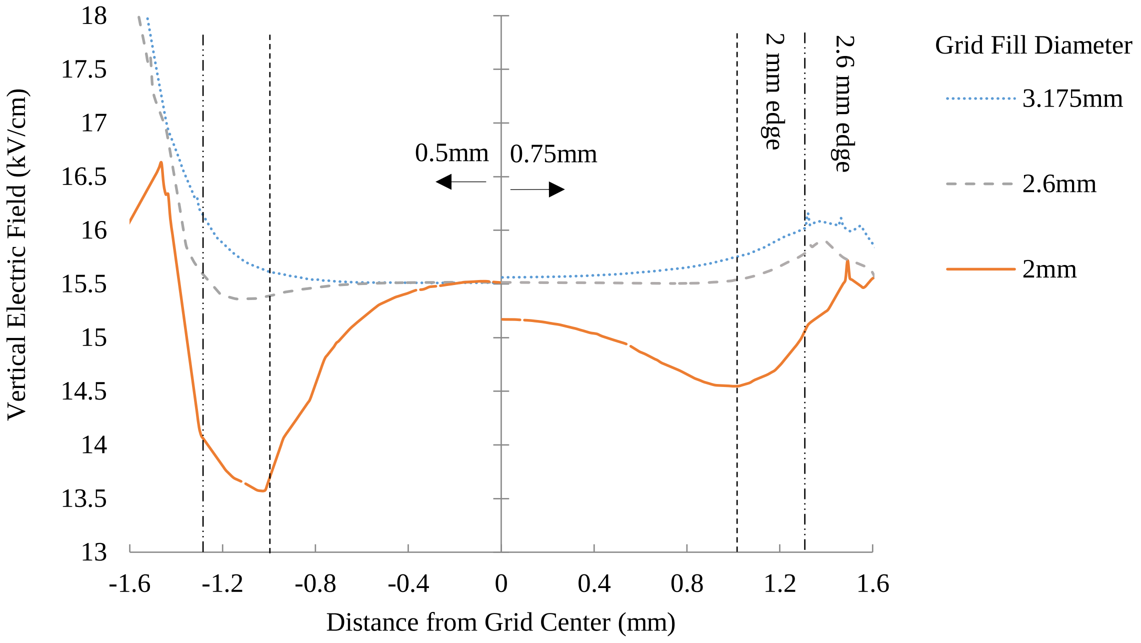

*(a)*

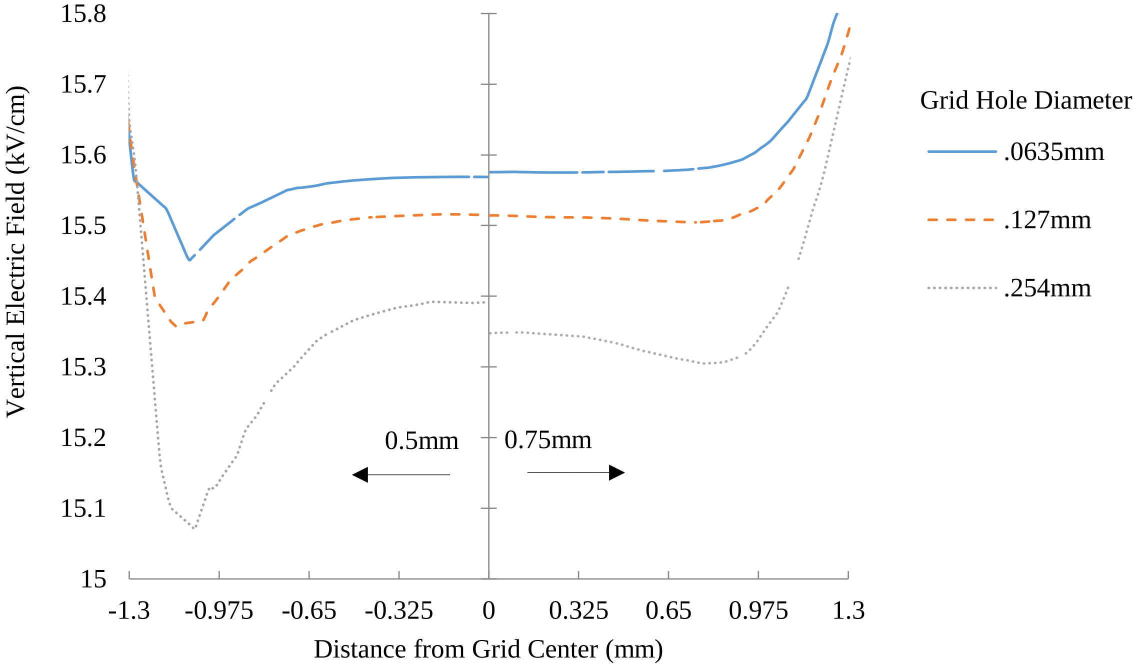

*(b)*

*Fig. 24*: Variations in the vertical electric field above the discrimination grid. Spurious data from numerical artifacts has been removed for clarity. (a) Variations due to the grid fill diameter where the edge of the plot represents the edge of the 3.175mm fill diameter. (b) Variations due to grid hole diameter. In both plots, the left side of the plot represents the electric field found 0.5mm above the discrimination grid while the right side represents the electric field found at 0.75mm above the discrimination grid.

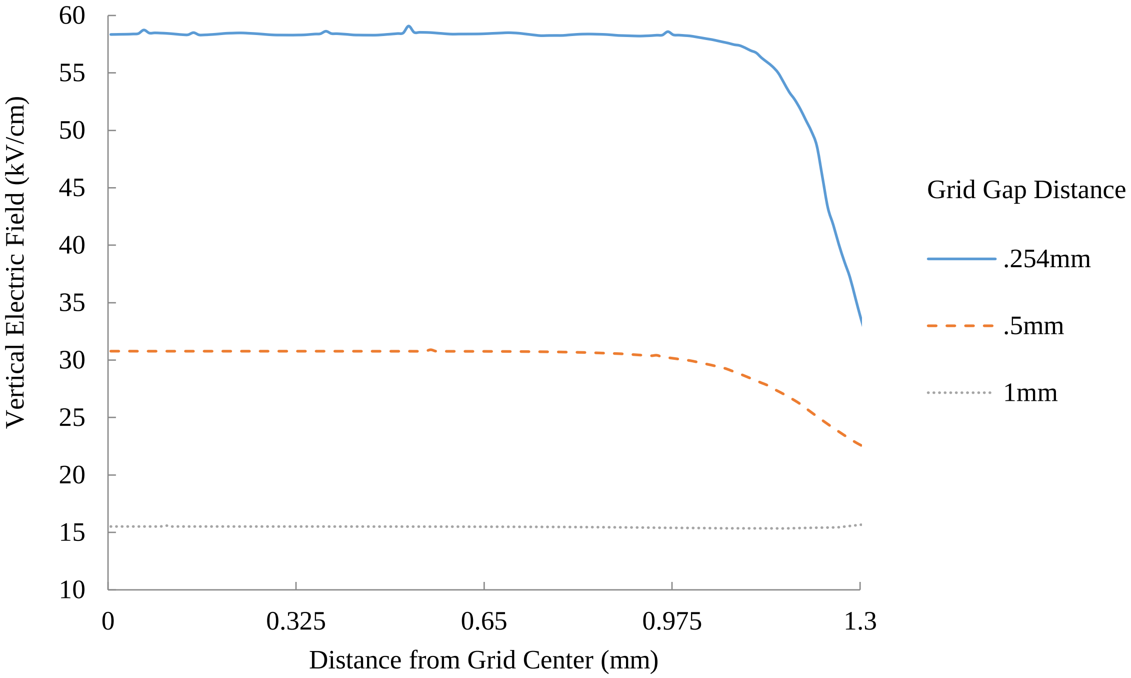

*(a)*

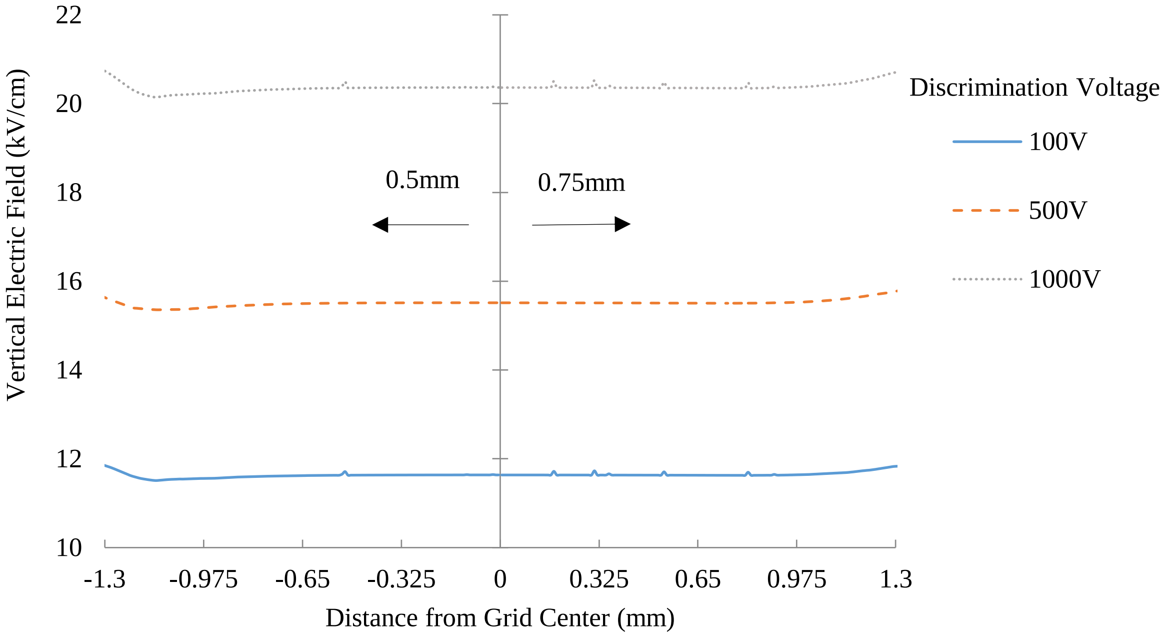

*(b)*

*Fig. 25*: Variations in the vertical electric field above the discrimination grid. Spurious data from numerical artifacts has been removed for clarity. (a) Variations due to grid gap distance. (b) Variations due to the discrimination potential of the discrimination grid. In (b), the left side of the plot represents the electric field found 0.5mm above the discrimination grid while the right side represents the electric field found at 0.75mm above the discrimination grid.

uniform and only deviate from the horizontal near the edge of the grid fill diameter. This deviation gets worse as the grid gap distance decreases.

Lastly, Fig. 25 (b) shows the variation in the vertical electric field due to changes in the discrimination grid potential. As can be seen in the plot for each voltage, very slight variations exist for each of the different potentials, but the overall trend is very uniform as the potential is changed. In general, these curves are very close to the ideal curve showing that the sweeping of the discrimination grid has little effect on the vertical electric field between the electron rejection grid and itself. Also, for all cases, there was always variation in the vertical electric field near the edges of the grid fill diameter between the different locations. This is likely caused by edge effects of the grid or proximity of the polyimide insulator.

By varying the geometric parameters of the RFEA, the shape of the vertical electric field was altered about the discrimination grid. From the results, optimal dimensions of a 2.6mm grid fill diameter, 0.127mm grid hole diameter, and grid gap distance of 1mm were determined. By changing these dimensions, the vertical electric field became much more uniform (See Fig. 26). With a uniform electric field, the RFEA measurements are more reliable because ion energy is not being altered based on the ion travel path. Every ion will be accelerated or decelerated uniformly. The optimal values obtained for this RFEA design are not universal though. If one geometric parameter is changed (e.g. grid hole diameter), then the other two parameters can be changed to restore a more uniform vertical electric field. In this case though, using this optimization prevents the electric field from adversely affecting the measurement.

### 2.1.2 Grid Plane Potential

Since the vertical electric field is altered by these geometric parameters, the next step is to determine how these same parameters affect the resolution of the measurement. For an ideal

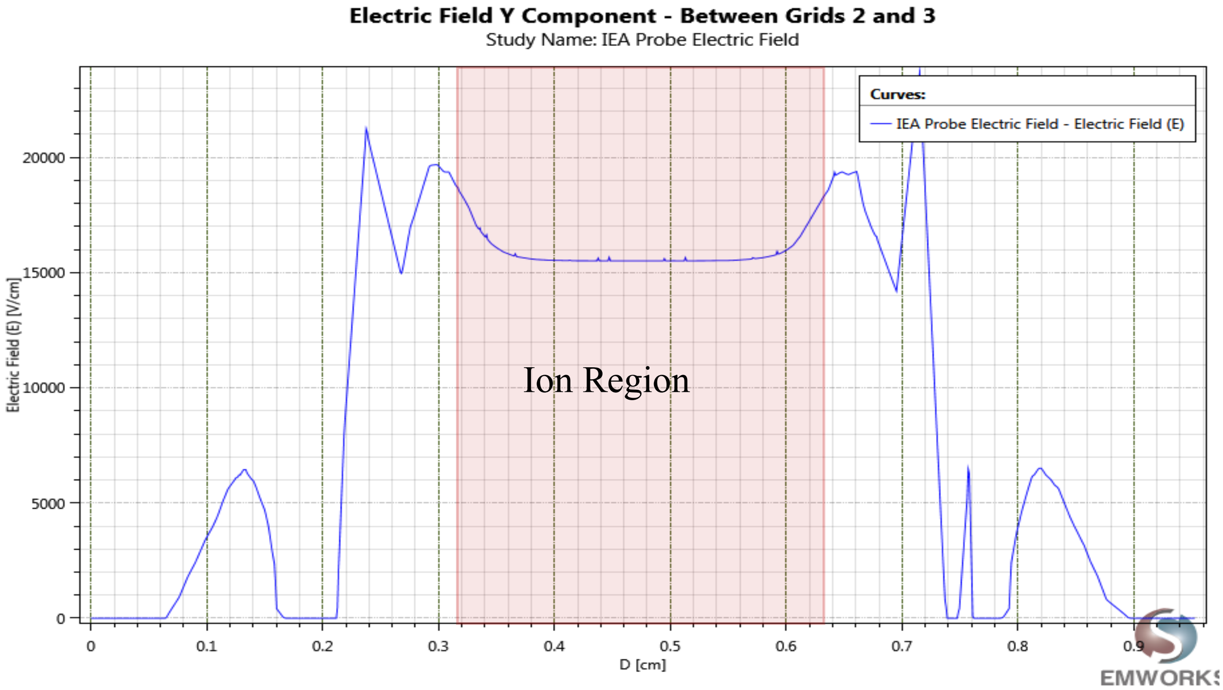

*(a)*

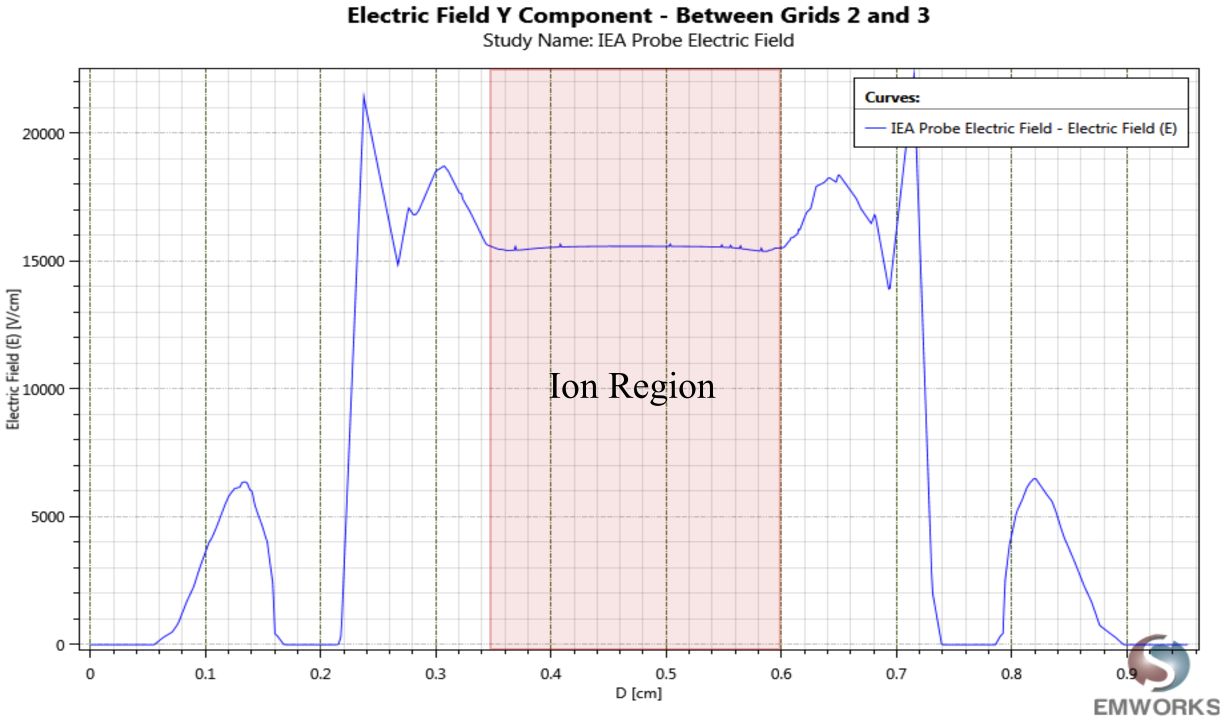

*(b)*

*Fig. 26*: Comparison of the vertical electric field based on original and optimal geometric parameters. (a) Original geometric parameters (b) Optimal geometric parameters.

RFEA and monoenergetic beam, the RFEA instrument function would be measured as a single step function. However, as mentioned in chapter 1, the potential applied to the metal plate decreases when transitioning from the metal to the hole. This same phenomenon is demonstrated in the EMWorks simulations (See Fig. 27). The potential drop causes the instrument function to get smeared out which represents a deviation from the actual ion energy. To determine how the energy resolution is affected by the previously studied parameters, more simulations were run.

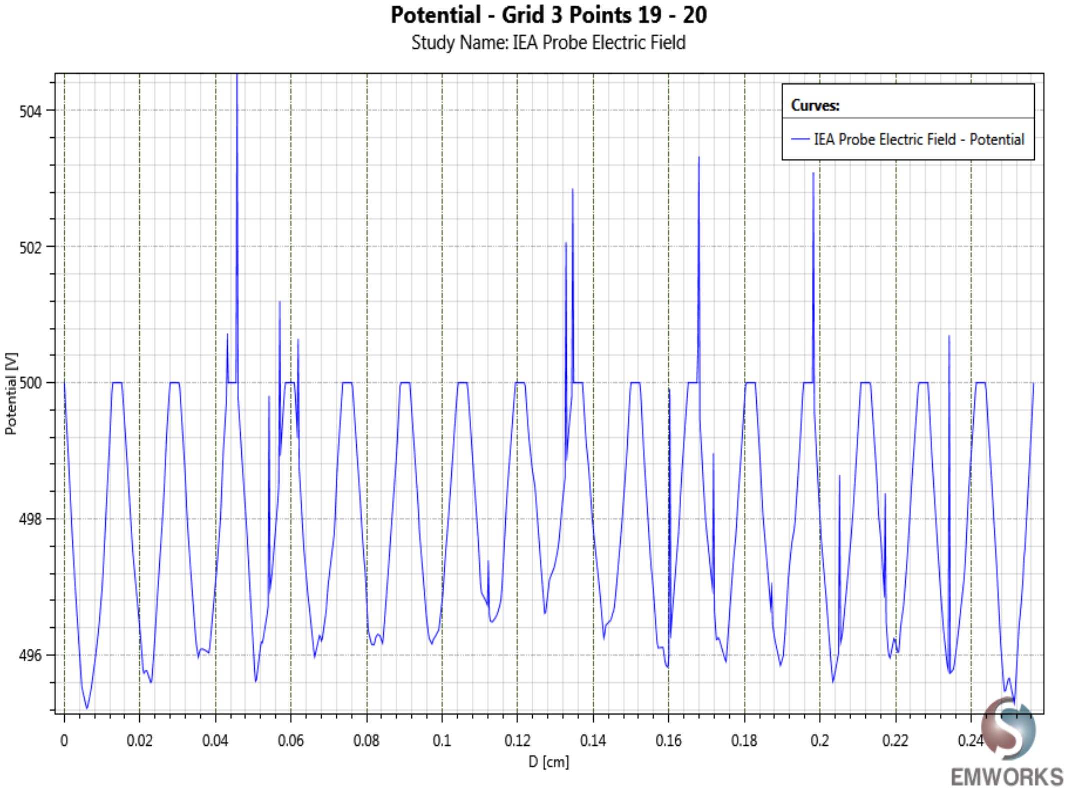

*Fig. 27*: Plot of the potential in the grid holes of the discrimination grid for an applied voltage of 500V. Note – the spikes are spurious data due to numerical artifacts.

These simulations used the same model and potential values from the work looking at the electric fields. For this work, the main focus was on the discrimination grid as this is the grid that determines the ion energy. For the following cases, 2D plots were generated by a line that sat below the surface of the discrimination grid (See Fig. 28). This location was chosen because it is the spot that the grid hole potential varies the least from the applied grid plate potential. Multiple 2D plots of the magnitude difference between grid potential and hole potential were generated at this location when varying the grid gap distance, the grid hole diameter, and the discrimination voltage. As with the vertical electric field cases, unless the specific parameter was under investigation, the grid gap distance was set at 1 mm, the grid hole diameter was 0.127 mm, and the discrimination voltage was 500 V.

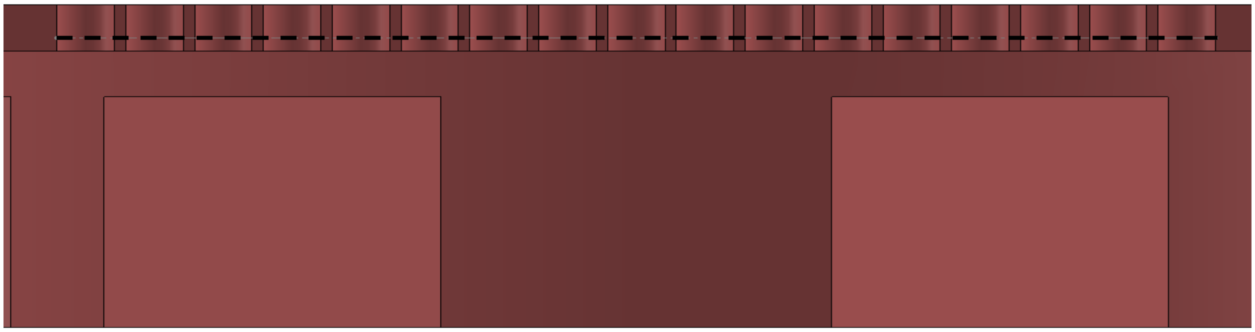

*Fig. 28*: Close-up of the discrimination grid and the location at which the potential was obtained in the grid holes.

As was mentioned in Chapter 1, another design consideration to increase to affect RFEA energy resolution is the grid alignment [1, 34, 77, 99 ]. In altering current RFEA designs for high voltage operation, it is necessary to determine if the grid alignment influences the energy resolution for high voltage RFEAs as well. The grid alignment effect was studied in the during the simulations looking at the changes in grid hole potential due to grid gap distance. It was found that the alignment of the grids only had an effect on the grid hole potential at grid gap distances of 0.5 and 0.254 mm. When the grid was misaligned, the potential difference decreased on average of 1 V for a grid gap distance of 0.5 mm and on an average of 2 V for a grid gap distance of 0.254 mm. Since the grid alignment had no influence on the grid hole potential for a grid gap distance of 1 mm, this optimal value chosen earlier for vertical electric field uniformity is also a good choice when considering this issue. Also, since the other cases looking at grid hole diameter and discrimination potential used a grid gap distance of 1 mm, the effect of grid alignment was not studied. For these cases, the grids were left in perfect alignment.

The results for the different simulations can be seen in Fig. 29 - Fig. 31. In Fig. 29, the potential difference due to the grid gap distance is shown. For this case, the potential profile of each hole was overlaid on top of one another to emphasize the potential drop in each of the holes while still showing the profile variation in each hole. It can be seen that as the grid gap distance decreases, the potential difference increases. This is consistent with previous work discussed in chapter 1 when using analytical solutions and other experiments [ 34, 75, 76 ]. Since the potential drop trend is more dominate than the slight variations between the grid holes, the other plots show only the potential profile for a single consistent hole for each simulation. Fig. 30 shows the potential difference when changing the grid hole diameter. As the grid hole diameter decreases, the results show that the grid hole potential also decreases. Lastly, Fig. 31 shows the potential difference due to changes in the discrimination potential applied to the grid. From these results, it can be seen that as the applied potential increases, the potential difference also increases.

Based on this analysis, the results suggest that the best energy resolution is obtained when the RFEA has a large grid gap distance and small grid hole diameters. This conclusion is presented more affectively by looking at the RFEA instrument function when varying the parameters. For sake of an example, instrument functions of the RFEA were generated for the simulations when the grid gap distance was varied. To obtain the instrument function, it was assumed that a monoenergetic beam of ions at 500 eV was entering through the electron

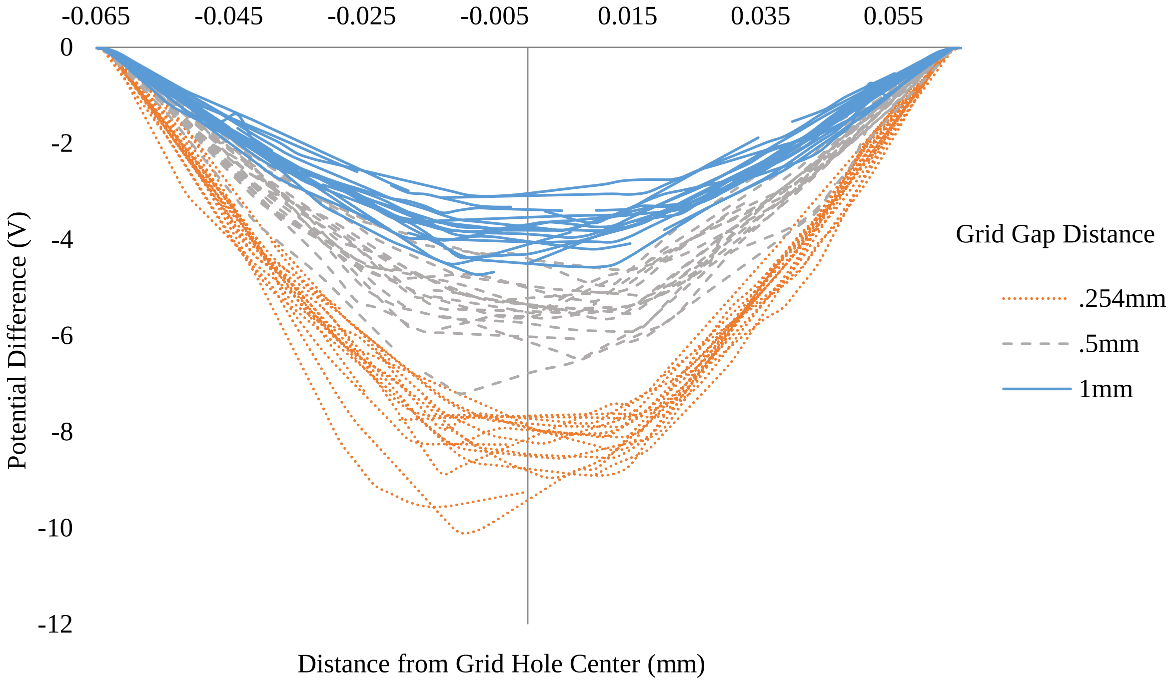

*Fig. 29*: The potential difference between the grid plate and grid holes due to the grid gap distance. Spurious data resulting from numerical artifacts has been removed for clarity.

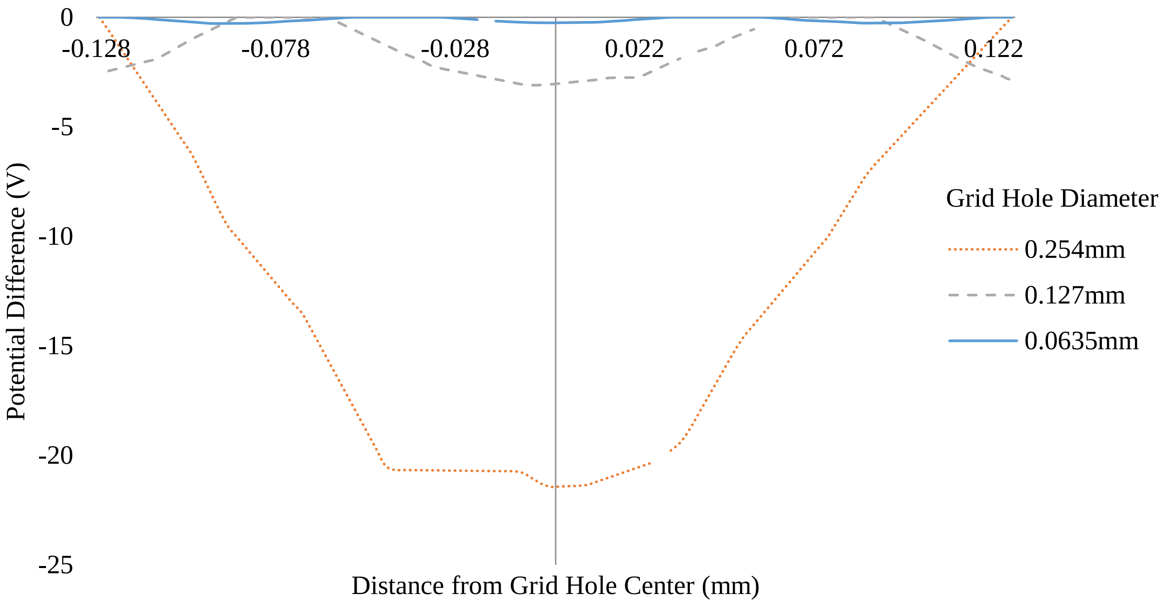

*Fig. 30*: The potential difference between the grid plate and grid holes due to the grid hole diameter. Spurious data resulting from numerical artifacts has been removed for clarity.

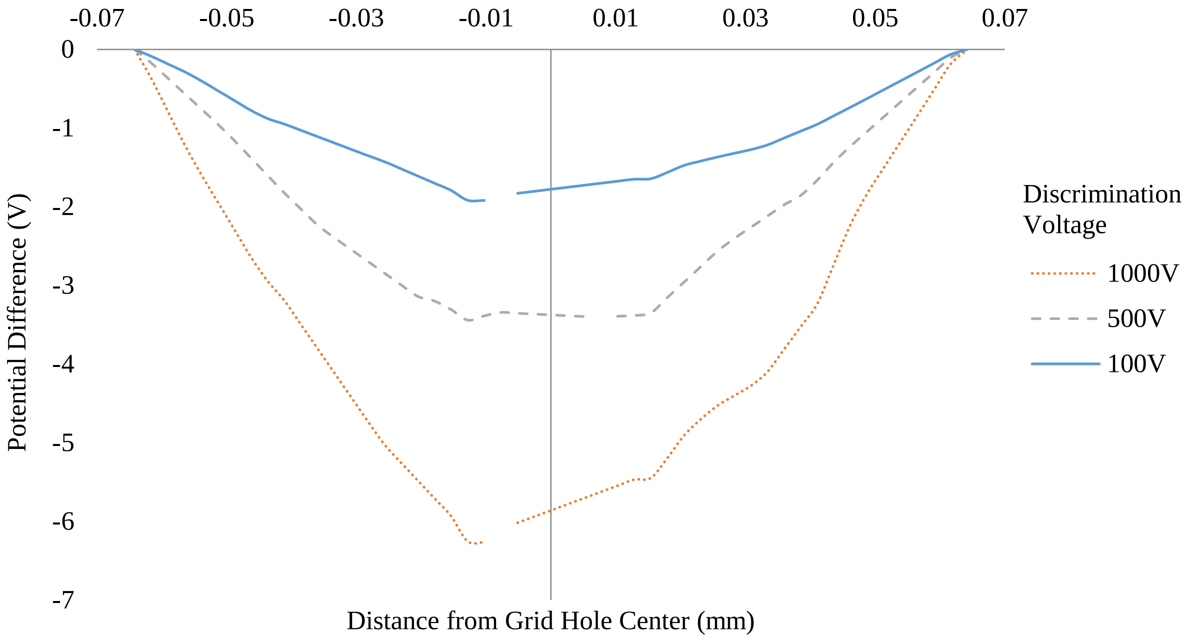

*Fig. 31*: The potential difference between the grid plate and grid holes due to the discrimination potential. Spurious data resulting from numerical artifacts has been removed for clarity.

rejection grid. By varying the discrimination grid potential between 499 – 511 V, the location at which 500 V intersected the potential profile of the grid holes would change. By comparing the valley width (entrance diameter) of the profile at 500 V to the physical diameter of the grid hole, an approximation of the percentage of the ions that would pass through the discrimination grid was obtained (See Fig. 32). By stitching the percentages of ions that pass through the discrimination grid together, instrument functions were created for different grid gap distances (See Fig. 33). The ideal case (step function) was also plotted in the figure for comparison. As can be seen in Fig. 33, as the grid gap distance increases, the instrument function moves closer to the ideal function. This represents an increase in energy resolution because the measured IV curve will be more accurate. Similar instrument function plots could be generated for the grid hole diameter case and the discrimination grid potential case as well. Each would show that energy resolution increases as the grid hole diameter or discrimination potential decreases.

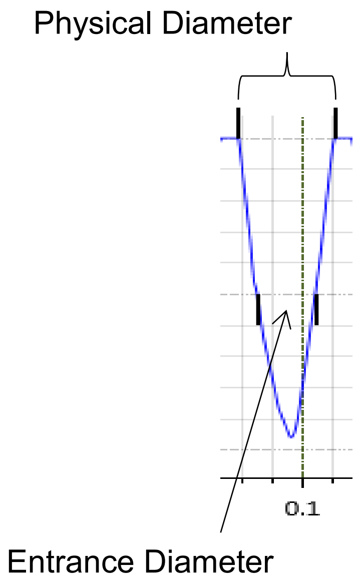

*Fig. 32*: Potential profile of a grid. The entrance diameter is where the valley crosses a value of 500 V while the physical diameter is the physical diameter of the grid hole.

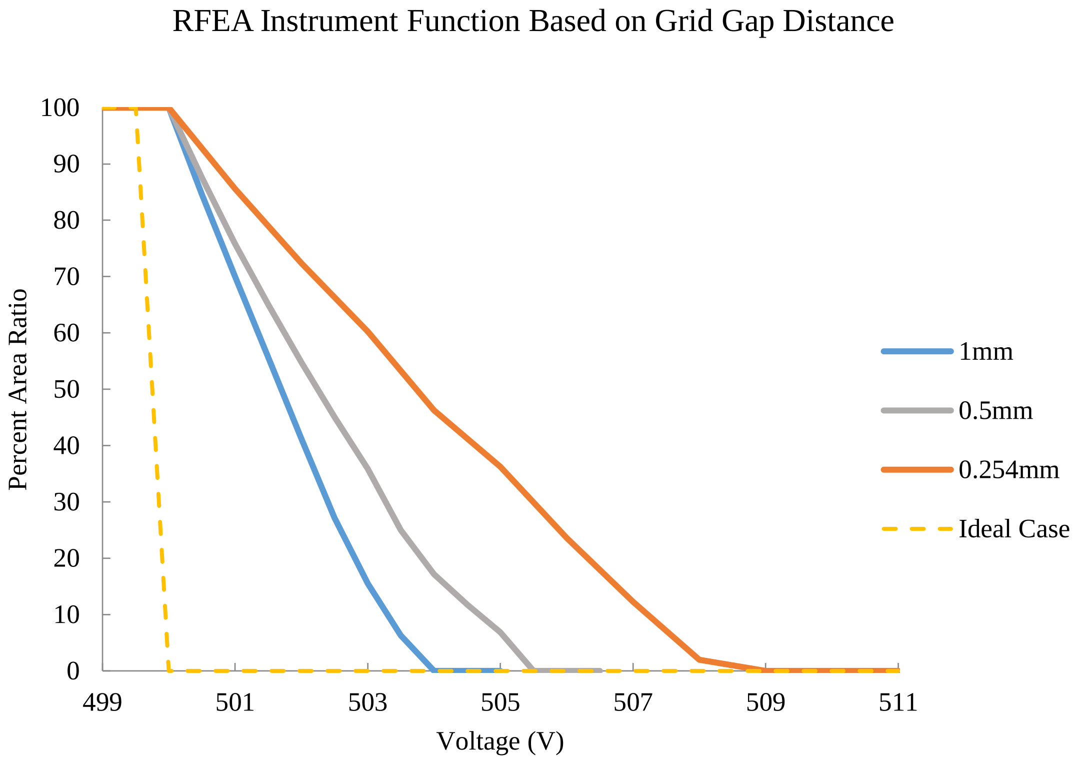

*Fig. 33*: Instrument functions of an RFEA for a monoenergetic (500 eV) ion beam based on changes in the potential drop in the grid holes. Separate functions were created for the different grid gap simulations.

For a high voltage RFEA, some of the advantages of increased energy resolution are inherently included (larger gap distance) but there are some apparent disadvantages as well. When looking at the grid hole diameter, increased energy resolution is obtained for smaller diameters, but the smaller diameters also limits the ion current through the detector. This decreases the signal to noise ratio which makes getting accurate measurements more difficult. Another issue is the decrease in energy resolution for higher discrimination grid potentials. A high voltage RFEA will be going to even higher potentials which will decrease the energy resolution even more. Also, there is no design fix for this issue. The decrease in energy resolution due to higher voltages will always be the baseline even if all other energy resolution considerations were perfect. Lastly, with an increase in gap distance, the pressure inside the detector may also increase. This can be handled using differential pumping, but the line integrated number of particles will still increase which may cause space charge distortion to the IV curves. Therefore, it is necessary to consider if space charge build-up will be an issue for the high voltage RFEA which will be addressed in chapter 3.

## 2.2 Experimental Chamber

To take the RFEA measurements, a dual frequency capacitively coupled (CC) plasma source was built. The chamber parts came from two different older Tokyo Electron Inc. commercial chambers. The bottom portion of the chamber (e.g. chamber body and frame, bias electrode assembly, etc.) mainly came from a 200 mm DRM commercial chamber (See Fig. 34). The top portion of the (e.g. the upper electrode/shower head and gas box) came from a 200 mm SCCM chamber (See Fig. 35). In general, the stock chamber parts were left as manufactured in order to keep the system as standard as possible. To mate the two different types of chambers together, a piece was made that mated two the two chambers (See Fig. 36). This mating piece

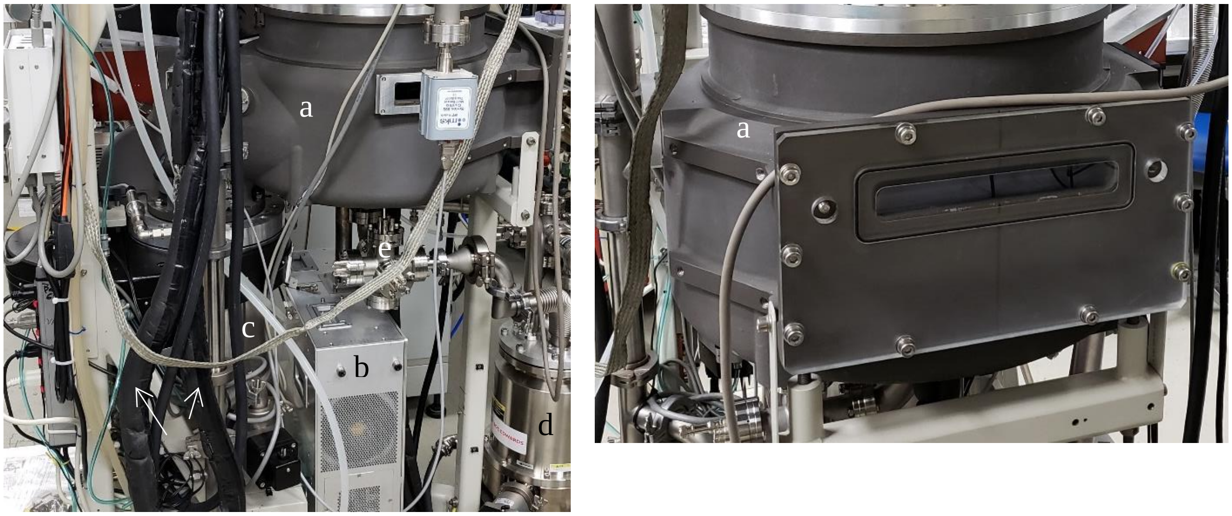

*Fig. 34*: Pictures of the TEL 200mm DRM chamber. (a) 200mm DRM chamber housing (b) 13MHz matching network (c) Main chamber turbomolecular pump (d) Diagnostic differential turbomolecular pump (e) Feedthrough for RFEAs in the bottom electrode (f) Bottom electrode cooling lines.

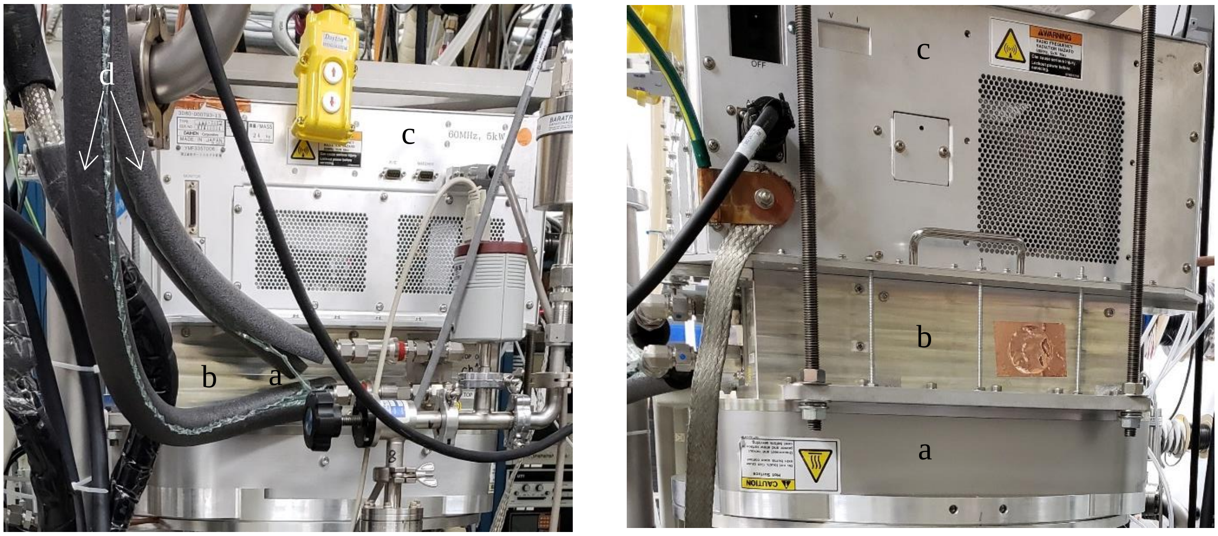

*Fig. 35*: Pictures of the TEL 200mm SCCM chamber. (a) 200mm SCCM electrode housing (b) gas box (c) 60MHz matching network (d) Upper electrode cooling lines.

*Fig. 36*: Pictures of the mating piece used to combine the components of the two TEL chambers.

was used as the main plasma chamber and was also designed with eight ports around the outer wall to provide locations for other diagnostics. The lift pin assembly of the 200mm DRM was not installed and the bellow that operated in connection with the lift pin assembly was replaced with a solid shaft so that the bottom electrode reached the bottom of the mating piece. The pumping baffle of the bottom electrode system was also replaced with a new baffle that connected the grounded section of the bottom electrode to the outer chamber wall and bottom of the mating piece (See Fig. 37). A 60 MHz generator was used to drive the top electrode and a corresponding matching network was installed on top of the gas box. A 13.56 MHz generator was used to power the bottom electrode with a corresponding matching network installed in between. Gas lines were run to the top of the chamber where they connected to the plumbing to the shower head. Three different gases were installed: Ar, oxygen ($O_2$), and carbon tetrafluoride ($CF_4$). Each was fed through a leak valve to control mass flow rate and were connected to a single line to allow for gas mixing when entering the gas box.

The above paragraph summarizes the main components of the plasma chamber, but some modifications were necessary to make it possible to install the RFEA sensors inside the bottom electrode. An overview 3D computer aided design model shows the modifications made to the bottom portion of the electrode (See Fig. 37). The majority of the components were only slightly altered (e.g. ground plate and ceramic insulator). Some were added to the assemble (inner ground shaft and Teflon sleeve) and the RF service plate and stock electrode were replaced with a custom electrode designed to the same geometric restrictions as the originals. These more significant changes will be described in the next few paragraphs.

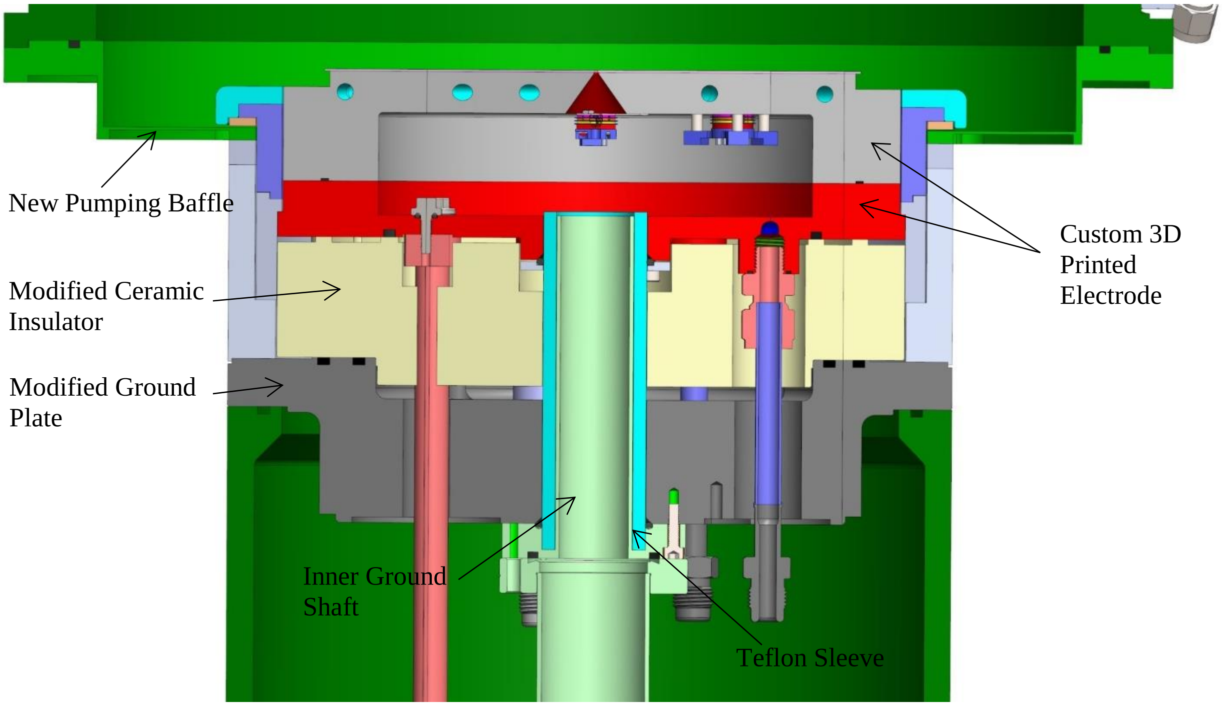

*Fig. 37*: Lower 200mm DRM electrode housing SolidWorks model. This shows the different components that were added or modified for the RFEA sensors.

### 2.2.1 Custom Electrode

The most important component and significant change was the custom electrode (See Fig. 39 - Fig. 42). To make the new electrode compatible with the commercial chamber, the outer dimensions were kept the same as the stock electrode and RF service plate. The electrode was designed as two parts to make it possible to install the RFEA sensors. To house the RFEA sensors, a cavity was created in the center of the electrode. In order to increase the cavity size, the connections from the RF service plate to the RF transmission rod, the cooling line connections, and bolt pattern were incorporated into the bottom half of the electrode (See Fig. 42).

To keep the electrode design simple, the electrostatic chuck was not included for the custom designed chuck. Instead, 4-40 taped screw holes were put into the top of the electrode to clamp the Si wafer to the electrode. To allow ions to reach the REFAs, a special Si wafer was made in which thin sub-Debye Si grids could be inserted to allow ions to pass through the wafer (See Fig. 38). This wafer will provide some protection from reactive ion species to the RFEA components as it will act as the main entrance to the sensor effectively reducing the current density. Reducing the current density reduces the number of reactive species that reach the RFEAs which will prolong the sensor life. The grid holes are in the same setup as the honeycomb structure as the RFEA grids (See Fig. 17) except with a 0.002” (0.05 mm) grid hole diameter, a 0.003” (0.08 mm) center to center grid hole spacing, and a 0.125” (3.175 mm) grid fill diameter. These grids were created on a thin sheet of Si that fit into cutouts on the Si wafer. The grids were located over 1 mm holes in the Si wafer that sat over 1.5 mm holes that were put into the top of the electrode that connected to internal drift cones (See Fig. 39 and Fig. 40). Four of these drift cones were shaped as traditional cones and made so that the RFEAs could be installed below the drift cone. The fifth drift cone was created as a cylindrical bore that sat 1 mm below the surface of the top of the electrode. This made it possible to attach a RFEA where the 1 mm entrance hole lead directly into the probe. This was done in order to determine any effects

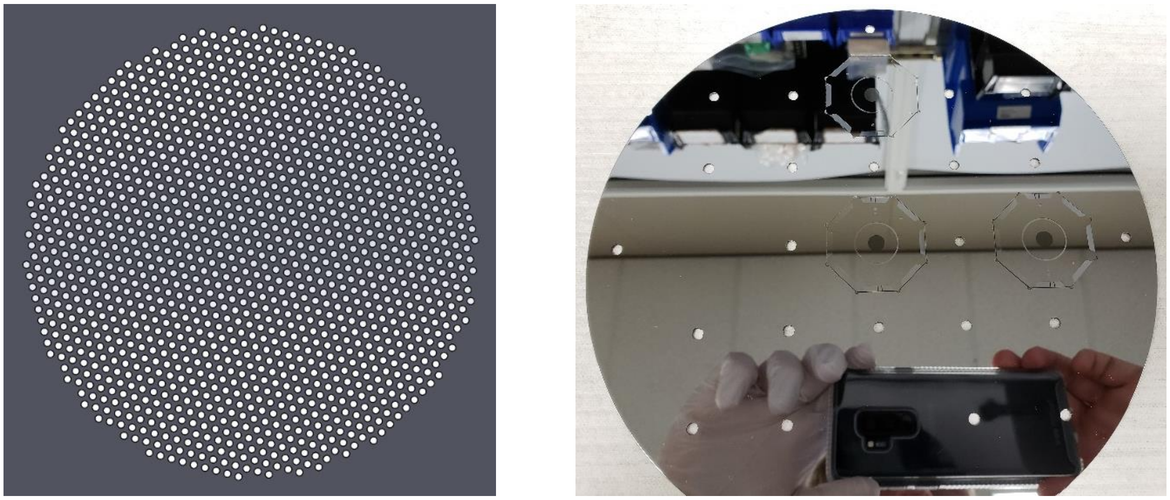

*Fig. 38*: Pictures of the Si wafer and grid used as the entrance to the electrode RFEAs. (Left) SolidWorks model of the Si grid for a 0.002” (0.05mm) grid hole diameter, 1:1 aspect ratio, 0.003” (0.08mm) spacing, a 60° stagger angle, and 0.125” (3.175mm) fill diameter (Right) Picture of one of the Si wafers similar to the one used in the following experiments.

introduced by the drift cones above the other RFEAs. To measure the pressure inside the drift cones, an internal channel was designed that lead to the top of one of the drift cones.

To provide access to the cavity of the electrode and provide differential pumping, an opening was designed in the center of the bottom portion of the electrode. This position traditionally housed part of the lift pin assembly to remove wafers after etching. Since this system was removed from the chamber, this was the ideal location for differential pumping and a wire feedthrough for the RFEAs.

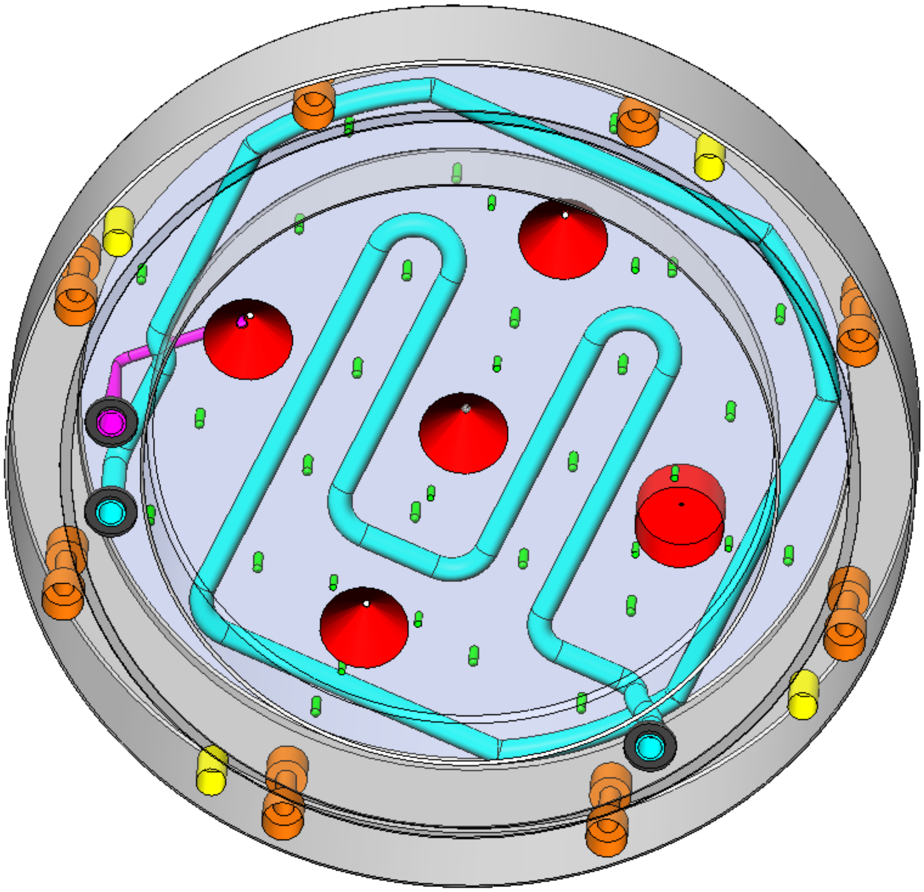

*Fig. 39*: SolidWorks model of the top portion of the electrode. This picture shows the drift cones (red), cooling channel (teal), drift cone pressure channel (purple), and tapped holes for wafer and probe connection (green).

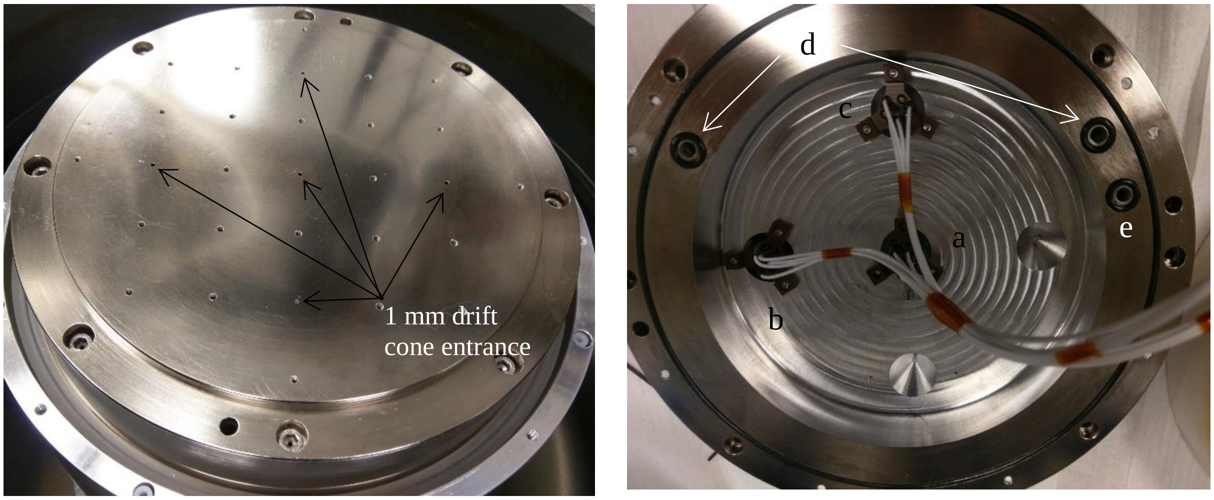

*Fig. 40*: Pictures of the top half of the actual 3D printed electrode. It shows the drift cones and screw holes for the silicon wafer. (a) Top mount (TM) RFEA (b) Surface mount (SM) RFEA (c) Floating mount (F) RFEA (d) Electrode cooling channels (e) Pressure measurement channel

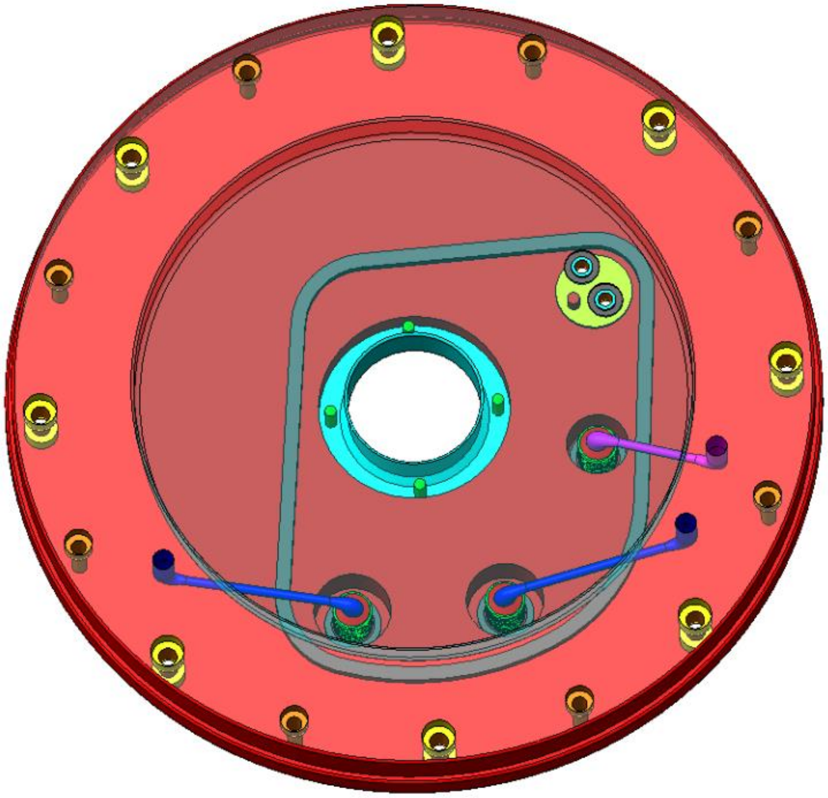

*Fig. 41*: SolidWorks model of the bottom half of the electrode. The face was made transparent so the cooling channels (blue), drift cone pressure channel (purple), and RF transmission rod connection location (green).

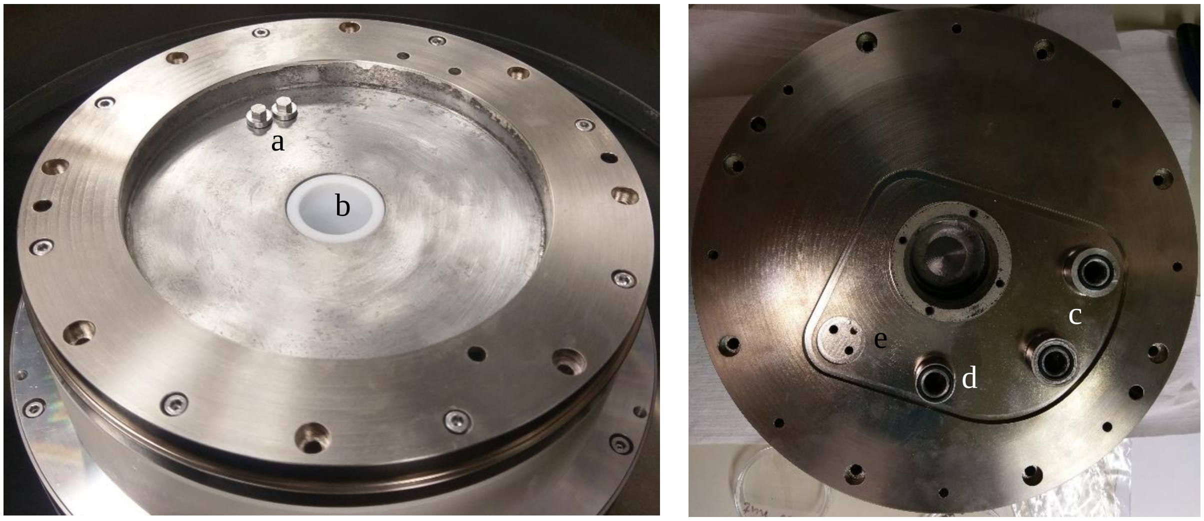

*Fig. 42*: Pictures of the bottom half of the electrode. (Right) (a) Screws attaching the RF transmission rod (b) Teflon sleeve (Left) It also shows the incorporation of the RF service plate connections and O-ring seal location (c) Cooling channels (d) Pressure measurement channel (e) RF rod connection slot.

Simple cooling channels were also designed into the electrode to keep both it and the Si wafer cool (See Fig. 39 and Fig. 41). However, temperature uniformity was not crucial, so it was not considered when designing the channels. The only purpose was to keep the components cool. When designing the cooling channels and pressure measurement channel, consideration was also given to the manufacturing process. To make the process more economical, it was determined that 3D printing the electrode would be the best option.

### 2.2.2 Cavity Electric Fields

Both the top portion and bottom portion were 3D printed using an aluminum-silicon alloy. Since a cavity and openings were created in the electrode, RF from the 13.56MHz generator would be introduced to the inside of the cavity. For better RF conduction and to impede that RF path to the inside of the electrode, the outside of both electrode portions was silver and nickel plated. In order to visualize and estimate the amount of RF entering the electrode, simulations were performed again using SolidWorks with the HFWorks 2016 SP0.2 [

102 ] simulation package. HFWorks was created by the same company as the EMWorks software package and provides analytical modelling tools for high frequency electromagnetic transmission and propagation using finite element analysis.

The HFWorks simulations used a reduced down model from Fig. 37 (See Fig. 43). For this simulation, a frequency of 13.56 MHz at 1 kW was used to drive the electrode. The power and frequency were applied at the end of a transmission rod that was attached to the electrode. Material properties of aluminum were assigned to the electrode, ground plate, and inner ground shaft while the RF transmission rod was assigned the properties for silver. The ceramic insulator was assigned the material properties of alumina and the Teflon sleeve was given material properties of Teflon. A stationary cylindrical plasma was created 10 mm above the electrode to simulate the as much as possible the electrical properties of a plasma. A boundary region was also created surrounding the electrode assembly and cathode to fill in any gaps and provide an outer boundary. This boundary region was given vacuum electrical properties.

The resulting RF electric and magnetic fields can be seen in Fig. 44 and Fig. 45. From both figures, it is readily apparent that there is only a small portion of the cavity in which RF electric and magnetic fields propagate. The 1 mm entrance holes to the drift cones are small enough to prevent 13.56 MHz from entering the cavity so it is only able to propagate at the differential pumping exit. Since the RFEA probe wires will also be traveling through the differential pumping exit, these wires will be exposed to an RF electric and magnetic field. As such, they will capacitively couple to the electrode and pick up some of the RF waveform on the signal lines. This will be in addition to any RF that the grids pick up from capacitively coupling to the electrode as well. This is ideal for the ions because the instantaneous RF potential will be the same everywhere inside the cavity. This means that the only electric fields that will influence

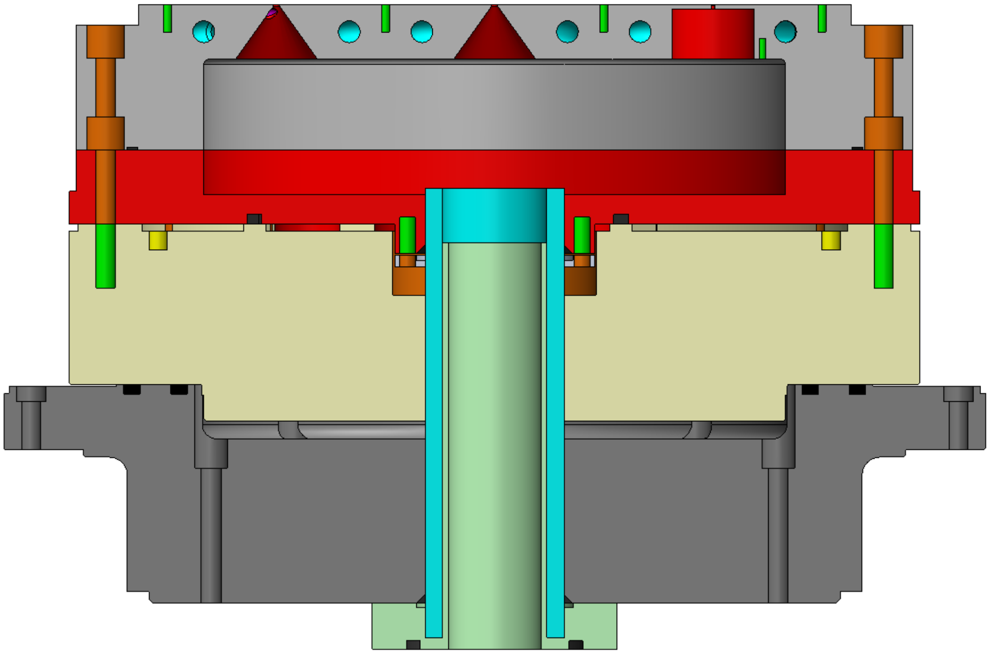

*Fig. 43*: Reduced SolidWorks model for the HFWorks simulations looking at electric and magnetic fields. Things added to the model not pictured are a propagation volume given the properties of vacuum and a stationary plasma above the electrode assigned typical plasma electrical properties.

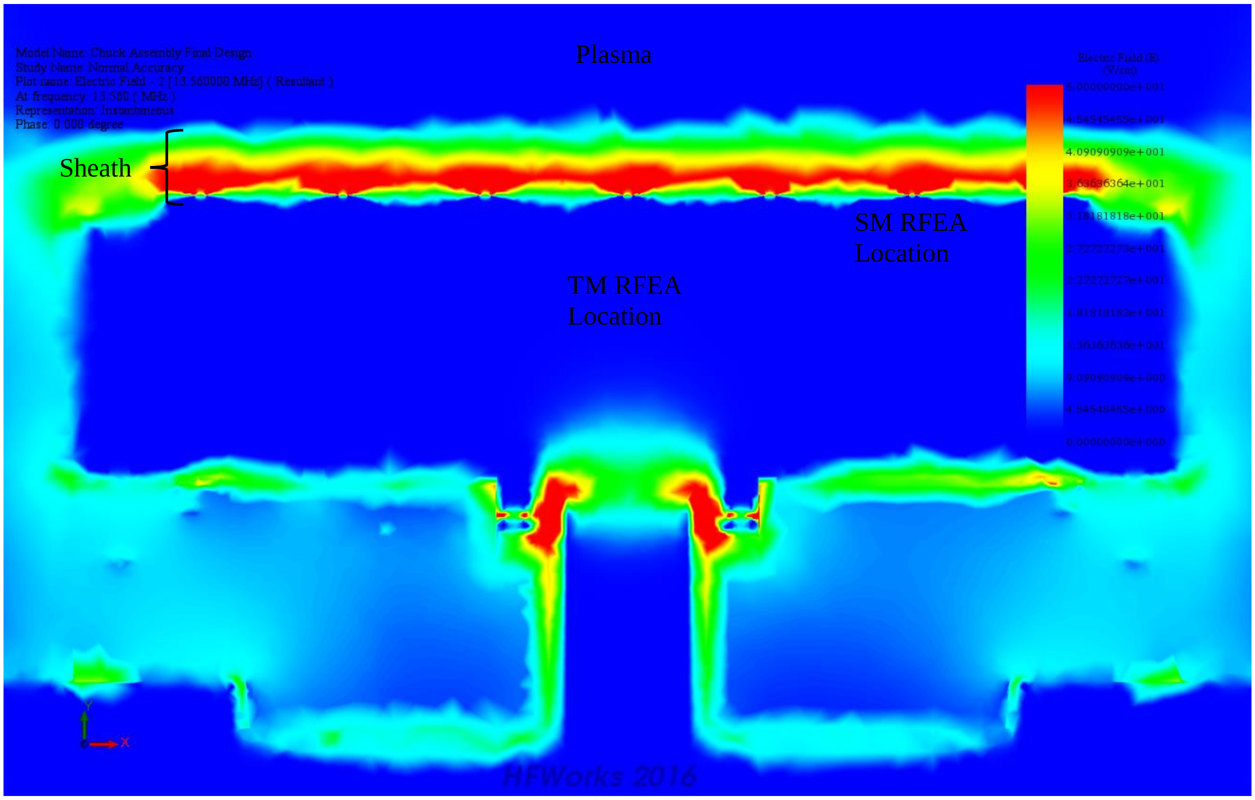

*Fig. 44*: RF electric field from the HFWorks simulation at 13.56 MHz and 1 kW of power. SM stands for the surface mount and TM stands for top mount

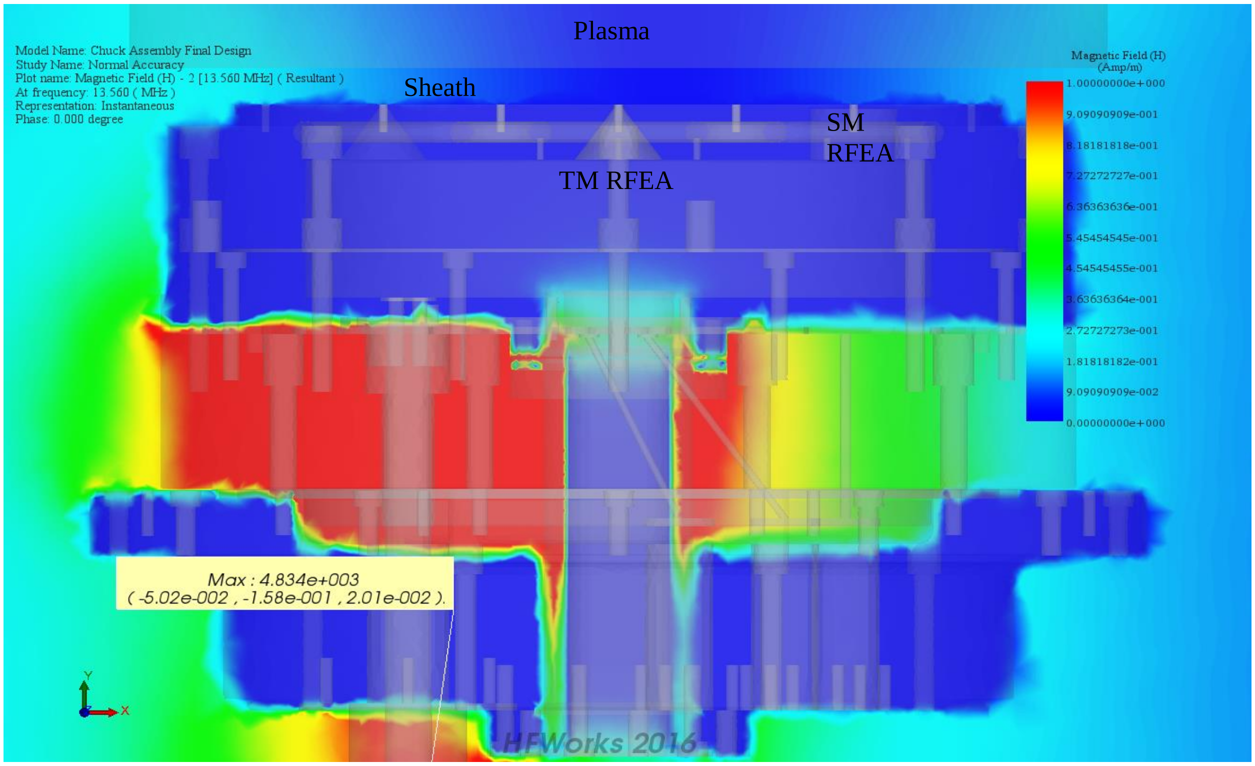

*Fig. 45*: RF magnetic field from the HFWorks simulation at 13.56 MHz and 1 kW of power. A transparent version of the electrode and stationary plasma assembly is visible. SM stands for surface mount and TM stands for top mount.

the ions will be fields resulting from direct current (DC) potential differences. However, when taking the signal out of the chamber and to the system electronics, this 13.56 MHz noise will need to be filtered out leaving only the DC current so that the RF noise does not affect the electronics or IV curve.

Since the RF is not generating fields in the cavity near the detectors, the only other concern will be DC fields that develop in the electrode cavity. The probes themselves create DC fields but these ones are desired. The only other field that will develop is near the exit of the electrode for differential pumping. The DC fields here will not have any effect on the wires traveling through the pumping exit. However, if the field is strong enough, it may reach areas where the probes are located. In that instance, the DC field could adversely affect the RFEA measurements (See Fig. 46).

To check for the strength of the DC field, the same SolidWorks model used in the HFWorks simulations (See Fig. 43) was used in the EMWorks software package. For this simulation, the plasma was set at 60 V, the electrode was given a DC bias of -1 kV, and the grounded components were set to 0 V. These are typical values for a plasma system. The results from this simulation can be seen in Fig. 47. As is apparent from the plot, the DC field is not strong enough to reach the location of any of the detectors. This means that it will not be adversely affecting the RFEA measurements.

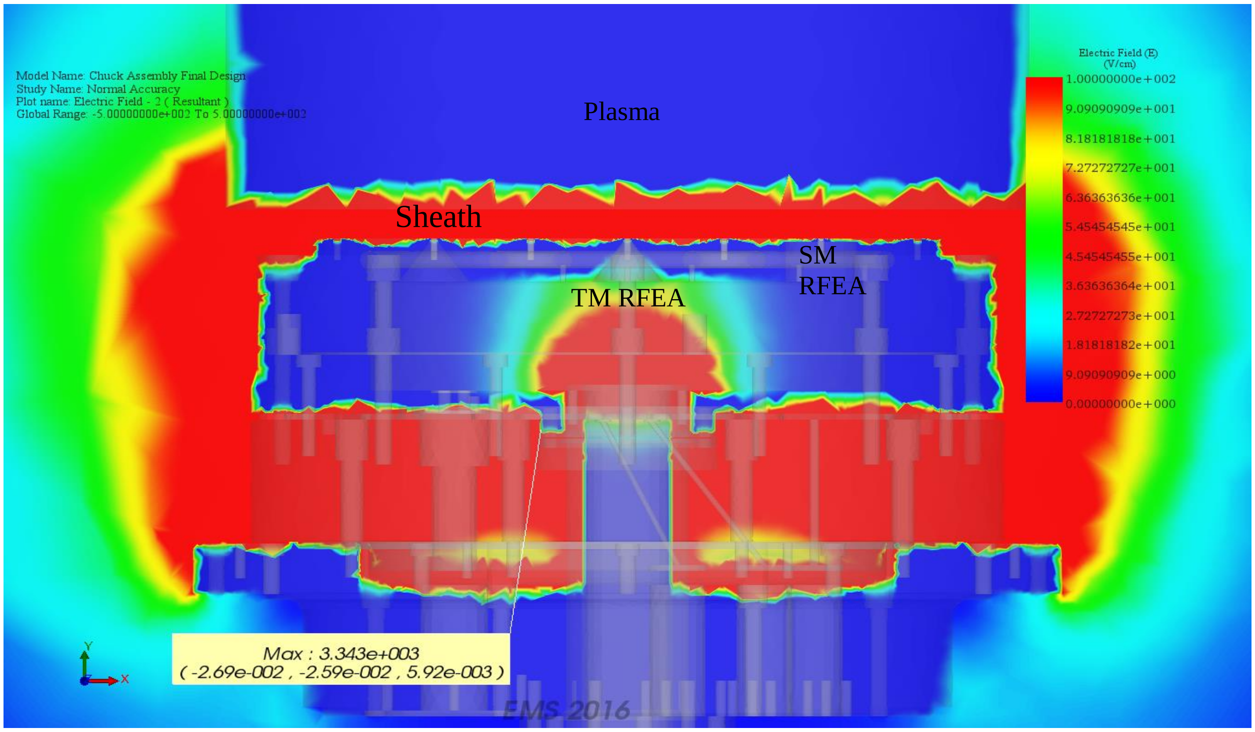

*Fig. 46*: Electrostatic results for an older differential pumping feedthrough design. Here the electric field is strong enough that it will adversely affect the operation of the center RFEA probe. SM stands for surface mount and TM stands for top mount.

### 2.2.3 Drift Cone Pressure

Since the high voltage RFEAs need to be differentially pumped and that the ions will be traveling through the drift cone before reaching the detector, it is necessary to approximate the

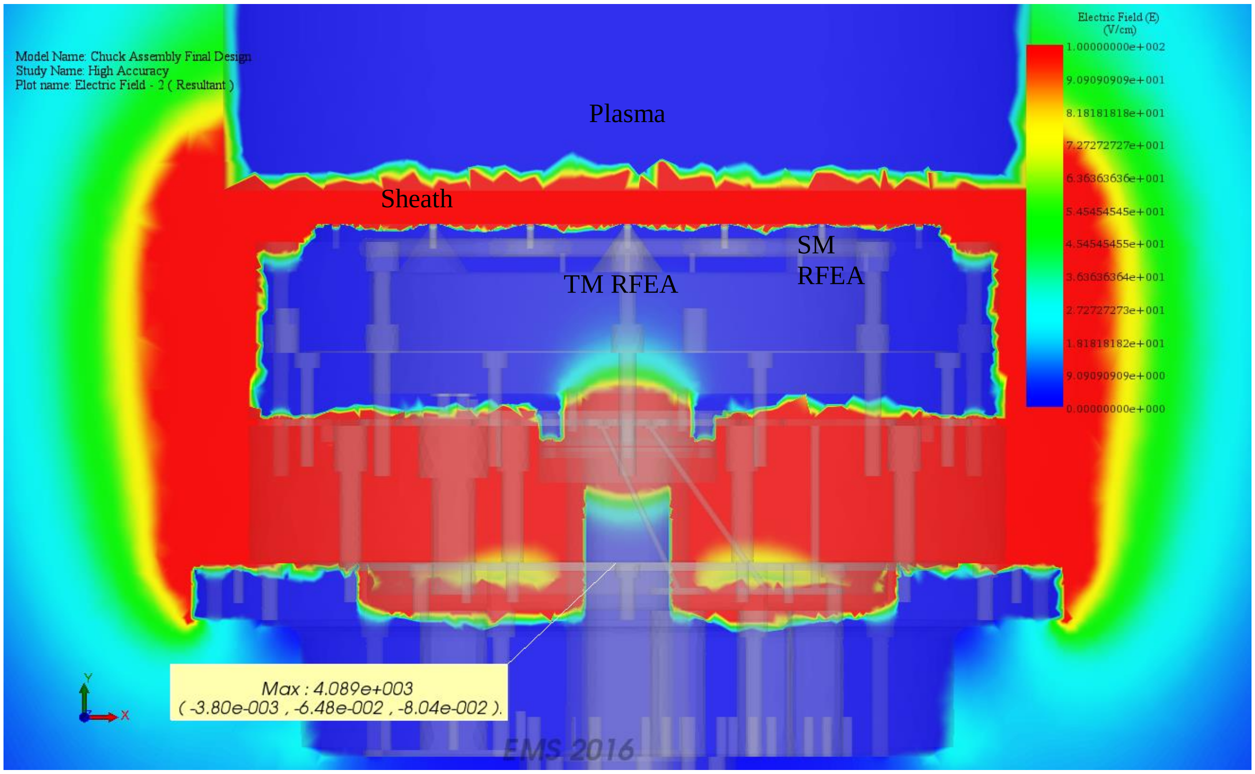

*Fig. 47*: Electrostatic fields for the DC simulation of the current differential pumping feedthrough design. Here, the field is not strong enough to reach any of the detectors to adversely affect their operation. SM stands for surface mount and TM stands for top mount.

pressure in the drift cones and around the RFEAs. To do this, conductance calculations from a formular by Zheng [ 103 ]. This formular gives the derivation of equations to determine the conductance $(C)$ for straight pipes (See Eq. 13) as well as tapered tubes (See Eq. 14) for molecular flow.

$$C = 3.81\sqrt{\frac{T}{M} * \left(\frac{D^3}{L}\right)} \tag{13}$$

$$C = 7.62\sqrt{\frac{T}{M} * \left(\frac{D_1^2 D_2^2}{(D_1 + D_2)L}\right)} \tag{14}$$

In Eq. 13, $T$ is the gas temperature, $M$ is the molar mass, $D$ is the tube diameter, and $L$ is the tube length. These variables are the same in Eq. 14 with $D_1$ and $D_2$ are the entrance and exit diameters. The coefficients at the front of Eqs. 13 and 14 come from a multiplication factor assuming the drift and random velocity of a molecule are proportional, two times the value of the Boltzmann constant, and for coefficients of geometric conversions. Once the conductance of each piece has been calculated, the values can be used with the plasma pressure and pumping speed of the turbomolecular pump (See Eq. 15 and Eq. 16) to determine the pressure at different locations in the system.

$$W = SC \tag{15}$$

$$W = C(P_2 - P_1) \tag{16}$$

In these equations, $W$ is the throughput which is constant throughout the whole system, $S$ is the pumping speed of the pump, and $P_1$ and $P_2$ are the entrance and exit pressures of the component for a specific conductance value. Using these equations, it is possible to approximate the pressure in the drift cone and around the detector.

The resulting pressure, throughput, and ion mean free path for the drift cone and electrode can be seen in Table 3 for a 20mTorr Ar plasma. The pressure calculations in Table 3 were validated by comparing the calculated pressure at a location in the differential pumping line to the pressure measured by a 20mTorr Baratron at that same location. When varying the

*Table 3*: Pressure, throughput, and ion mean free path for the differential pumping assembly and electrode.

| Location | Pressure (mTorr) | Throughput (W) | Mean Free Path (cm) |
|---|---|---|---|
| Silicon Holes - Plasma | 20 | 1.07566541 | 0.151515152 |
| Silicon Tube - Silicon Holes | 6.930226424 | 1.07566541 | 0.437258878 |
| Drift Cone Top - Silicon Tube | 2.044734445 | 1.07566541 | 1.48200322 |
| Corrected Drift Cone Bottom - Drift Cone Top | 0.470385975 | 1.07566541 | 6.442162797 |
| Electrode - Corrected Drift Cone Bottom | 0.434634665 | 1.07566541 | 6.972069365 |
| Teflon Insulator - Electrode | 0.434542346 | 1.07566541 | 6.973550589 |
| Ground Tube – Teflon Insulator | 0.428130227 | 1.07566541 | 7.077993653 |

pressure between 5 – 40 mTorr, the calculations had a maximum error of 1.9% referenced to the Baratron measurement. This means that the conductance calculations for the differential pumping line give a good estimate of the pressure in the electrode and drift cones.

As can be seen in the table, the throughput is constant throughout the whole assembly signaling that the calculations were performed correctly. The pressure where the RFEAs are mounted below the drift cones is well below the minimum single millitorr range required to prevent light-up that was mentioned in chapter 1. Also, the mean free path at each location is much larger than the feature length meaning the likelihood of collisions is very small. The only area of concern is that the current drift cone design would displace or interfere with the cooling channels and helium channels of an industrial electrode. For these systems, the drift cone design would need to become less obtrusive.

As the current drift cone design creates an issue for other important components in the electrode, it is necessary to investigate how the pressure changes in the drift cone when making the top portion of it less obtrusive. To limit the foot print of the drift cone, the cone can be separated into two different halves (See Fig. 48). The slope of the top half can then be varied based on the half angle θ between a vertical line and the drift cone wall. By changing this top portion of the drift cone more space is created for other systems in the electrode but the conductance of the drift cone also changes. To determine how the pressure in the drift cone is affected by the conductance changes, a plot comparing the pressure to the half angle was created (See Fig. 49). To keep the likelihood of collisions in the drift cone low, the pressure needs to remain below about 4 mTorr. This guarantees a mean free path of Ar that is longer than the distance of the top portion of the drift cone. From Fig. 49, this corresponds to a half angle of about 15°. The current drift cone angle is about 36° so this decrease in angle would provide quite a bit more space for the other internal electrode components.

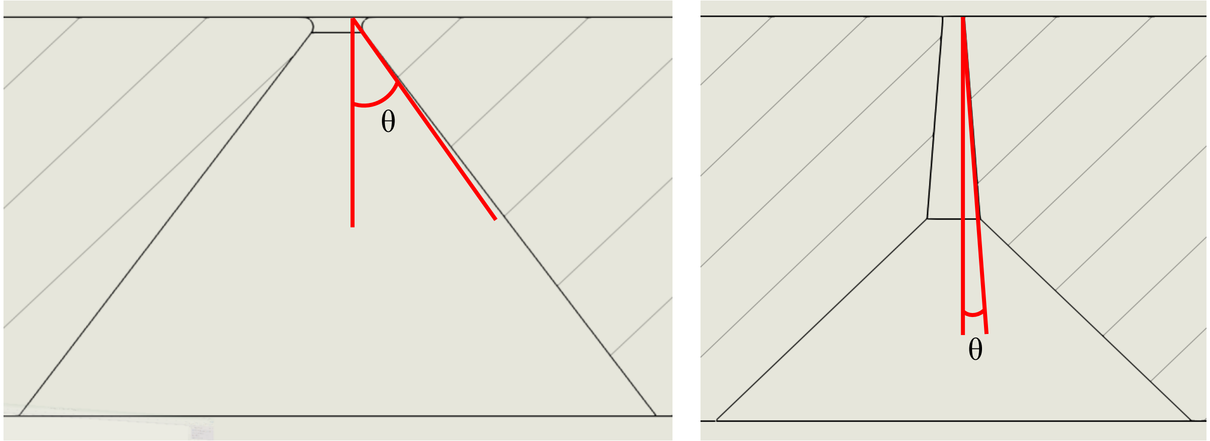

*Fig. 48*: Diagrams of the current (left) and less obtrusive (right) drift cones. Here, θ represents the half angle for the top portion of the drift cone.

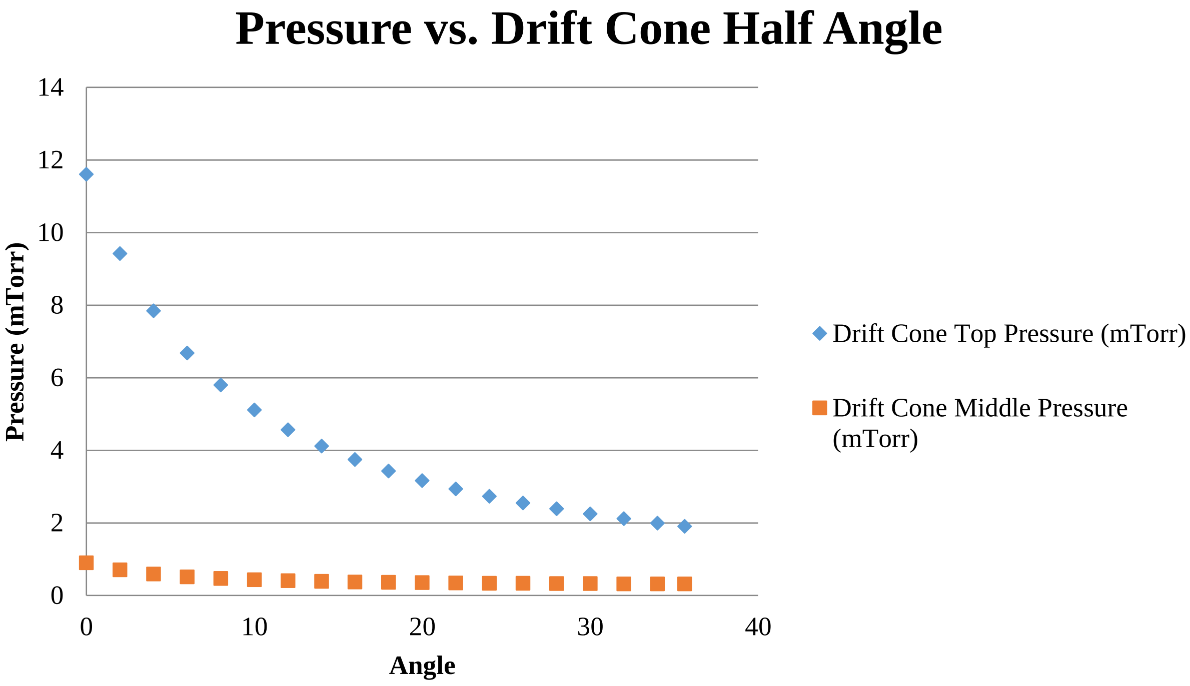

*Fig. 49*: Plot comparing the drift cone pressure to changes in the drift cone half angle θ.

## 2.3 Measurement Electronics

The electronics used for the measurement also have a significant impact on the RFEA measurements. A National Instruments PXI-1042 chassis was used as the main data acquisition device. It was also used as the main control computer by a PXI-6289 digital to analog converter (DAC) to set the electron rejection grid potential and the sweep profile and potential of the discrimination grid. Two PXI-4071 digital multimeters were used to measure the voltage being applied to the discrimination grid and the voltage drop across a 3 kΩ resistor. The 3 kΩ resistor is connected in series with the collector so that the ion current could be obtained using Ohm's law.

Fig. 50 is a diagram of the control electronics for the RFEA measurements. Two Ultravolt HVA series amplifiers were used to amplify the signal from the DAC to be applied to the electron rejection grid and the discrimination grid. The Ultravolt connected to the electron rejection grid was a 500:1 amplifier while the Ultravolt connected to the discrimination grid was a 1000:1 amplifier. Both were powered by a 24V DC power source. A high voltage probe was connected in parallel to the output of the amplifiers for measurement and for connection back to the high voltage return. The potential applied to the collector was also provided by a parallel connection to the discrimination grid Ultravolt output. A 9V battery was applied in series to the collector grids to keep biased negative in reference to the discrimination grid. This is also done so that as ions pass the discrimination grid, they are not excessively accelerated so as to cause secondary electron emission and distort the measurement. Lastly, different types of low pass filters were used to remove any 60 MHz or 13.56 MHz noise that is passed to the RFEA signal lines from entering the PXI chassis or amplifiers. The different types of filters include some low-power low pass Minicircuit filters, an Impedances filter box for an Impedans Semion probe, and some high-power low pass filters from Allen Avionics.

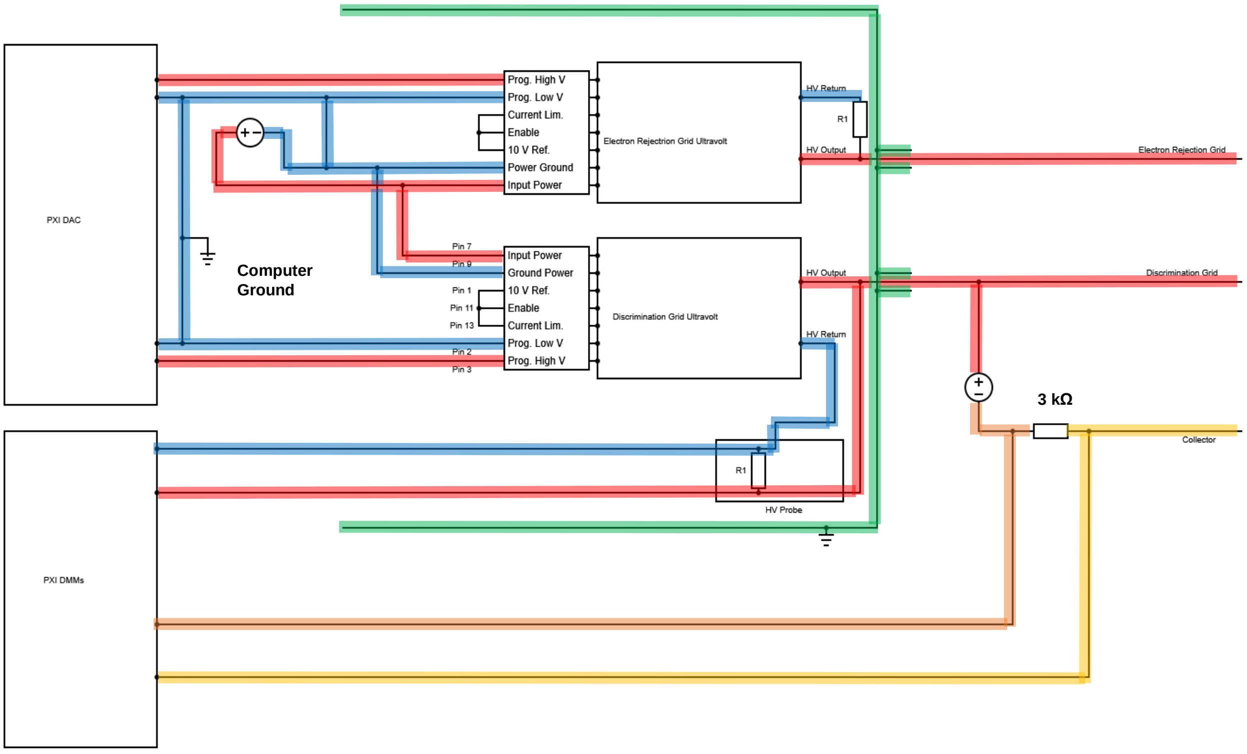

*Fig. 50*: Diagram of the control electronics for the RFEA measurements. The color code specifies the voltage on the line. Red - high voltage signal, Blue - computer ground, Green - rack ground, Yellow - Collector voltage, Orange - high voltage minus battery bias.

## 2.4 Regularized Least-Squares Solution Method

Since the measurement from the RFEA is an IV curve, it is necessary to perform a post analysis on the measurement to obtain the IEDf. The post analysis process is dependent on how the current relates to the desired information (i.e. the IEDf). The current $(I_c)$ obtained from the collector during an RFEA measurement is found by the following relationship to the IEDf

$$I_c(V_d) = eA\int_{eV_d}^{\infty} IEDf\ dE \tag{17}$$

where $A$ is the collector area, $e$ is elementary charge, and the lower bound of the integral is determined by the potential $(V_d)$ applied to the discriminator. $V_d$ is multiplied by $e$ to give the energy at this potential as the IEDf integral relationship to $I_c$ is dependent on the differential energy $(dE)$. As such, to obtain the IEDf, it is necessary to differentiate the IV curve with respect to $eV_d$. Since, at a minimum, the IV curve measurement is full of random noise this makes traditional numerical differentiation schemes (e.g. backwards difference differentiation method) ill-suited to calculate the IEDf. This is due to the fact that the random noise in the measurement will manifest as large changes in slope which will completely washout the more gradual change in current throughout the entire IV curve. This fits in with a class of ill-posed problems that must be solved by a different method.

The regularized reconstruction methods are a common means to obtain a solution to these types of ill-posed problems [ 104, 105 ]. This regularization method has been used for optical emission spectroscopy and Langmuir probe analysis [ 106 - 109 ]. A regularized least-squares (RLS) solution with L-curve optimization was the specific method used here to obtain the IEDfs. This method uses the following equation:

$$f = [K^T K + \alpha D^T D]^{-1} K^T I_c \tag{18}$$

where $f$ is the IEDf, $K$ is the system matrix, $\alpha$ is the regularization parameter, $D$ is the conditioning matrix, and $I_c$ is the current measured at the collector. For this work, $D$ and its transpose make up a square differentiation matrix. $K$ is composed of a model that is used to approximate the IV curve. In this case, it consists of step functions at each energy the measurement was taken (See Fig. 51). The regularization parameter is used to regulate the amount of smoothing caused by $DD^T$.

The choice of the $\alpha$ is chosen using an L-curve optimization scheme. In this method, the semi-norm of the solution is plotted against the norm of the residual. The semi-norm of the solution and norm of the residual are both dependent on the $\alpha$ (See Fig. 52). The different semi-norm of the solution and norm of the residual values are created by multiple $\alpha$ values. The L-shape to the curve is created by two competing mechanisms of the solution method. The first mechanism is the exact differentiation of the IV curve (i.e. level of accuracy of the solution) and the smoothing of noise in the IV curve (See Fig. 53). The optimized $\alpha$ is the one that finds a balance between these two mechanisms. This $\alpha$ is the one that created the point the bend of the L-curve that is closest to the bottom right corner of the plot. Using this optimized $\alpha$ and Eq. 18, it is possible to obtain an accurate representation of the IEDf from the IV curves measured by

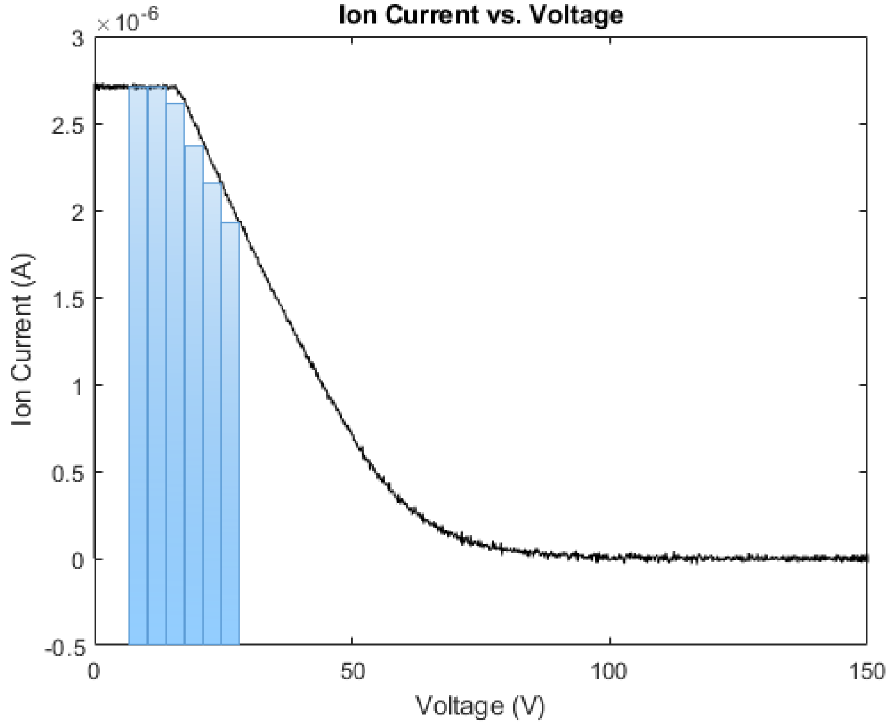

*Fig. 51*: Plot of an IV curve and how step functions are used to approximate the IV curve. These step functions are used in the system matrix $(K)$ in the least squares regularization method.

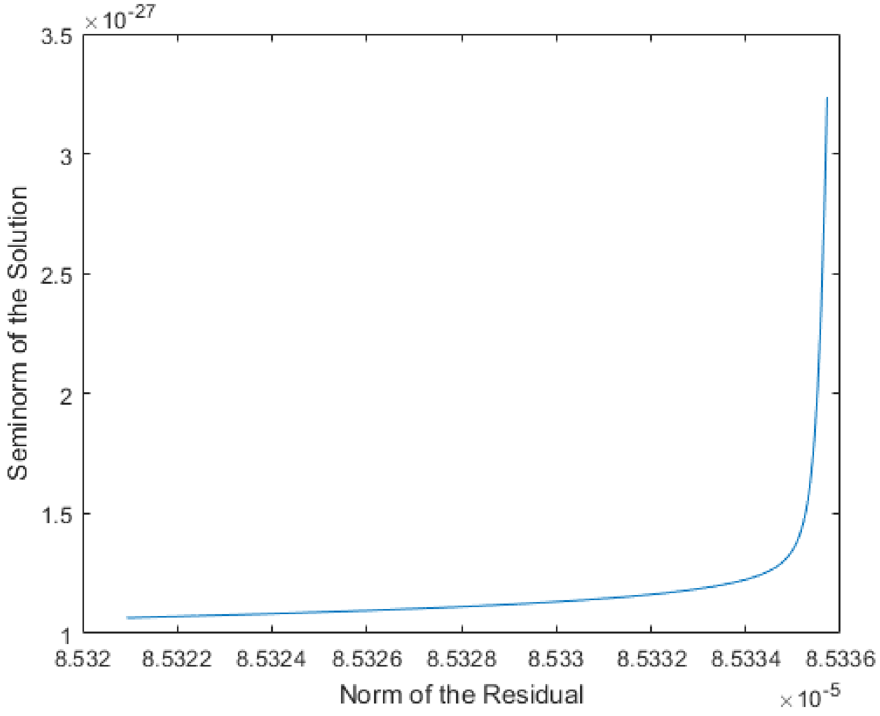

*Fig. 52*: Plot of the L-curve created using multiple regularization parameter $(\alpha)$ values. The curve represents the influence of two competing mechanisms: the exact differentiation of the IV curve and smoothing of the noise in the IV curve. The optimized $\alpha$ is the $\alpha$ value used to create the point in the bend in the L-curve that is closes to the bottom right corner of the plot.

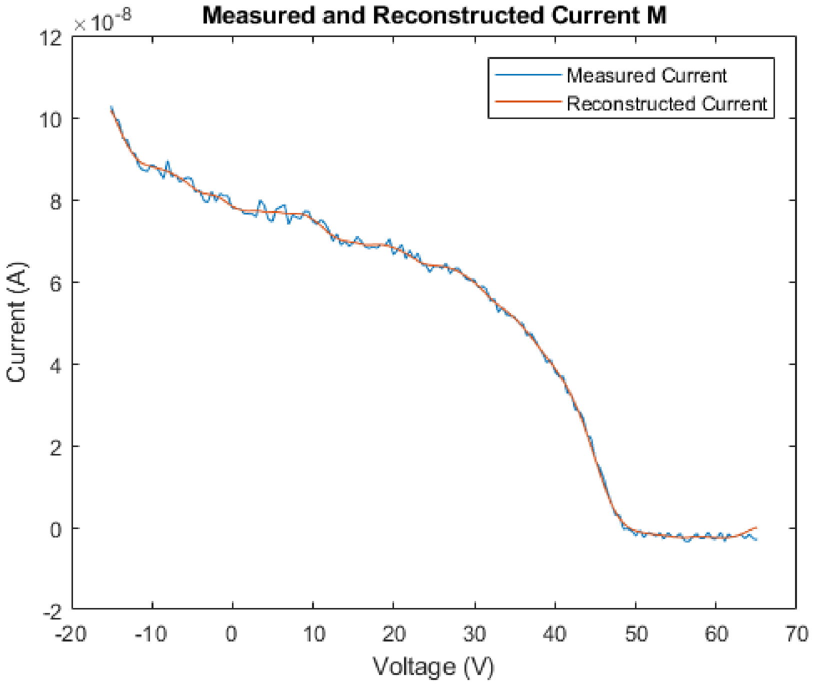

*Fig. 53*: Plot of the original IV curve and the IV curve created from the reconstructed IEDf. This plot shows how the noise in the original IV curve is smoothed by the regularization parameter.

RFEAs. For example, using a simple Maxwellian distribution (See Fig. 54) in a particle-in-cell code called XPDP1 [ 62 ], the current measured by an RFEA was simulated. From this IV curve, the RLS method was used to obtain the IEDf based on the simulated IV curve (See Fig. 54). It can be seen in Fig. 54 that the RLS solution reproduces a distribution very similar to the original distribution used by XPDP1. The slight variations (oscillation at the sharp rise and peak height) in the reconstructed solution are the result of the $\alpha$ parameter used, and numerical artifacts created by the numerical method. Overall, this shows that the RLS method provides an accurate IEDf from an IV curve and was used to generate all the IEDfs in the following chapters.

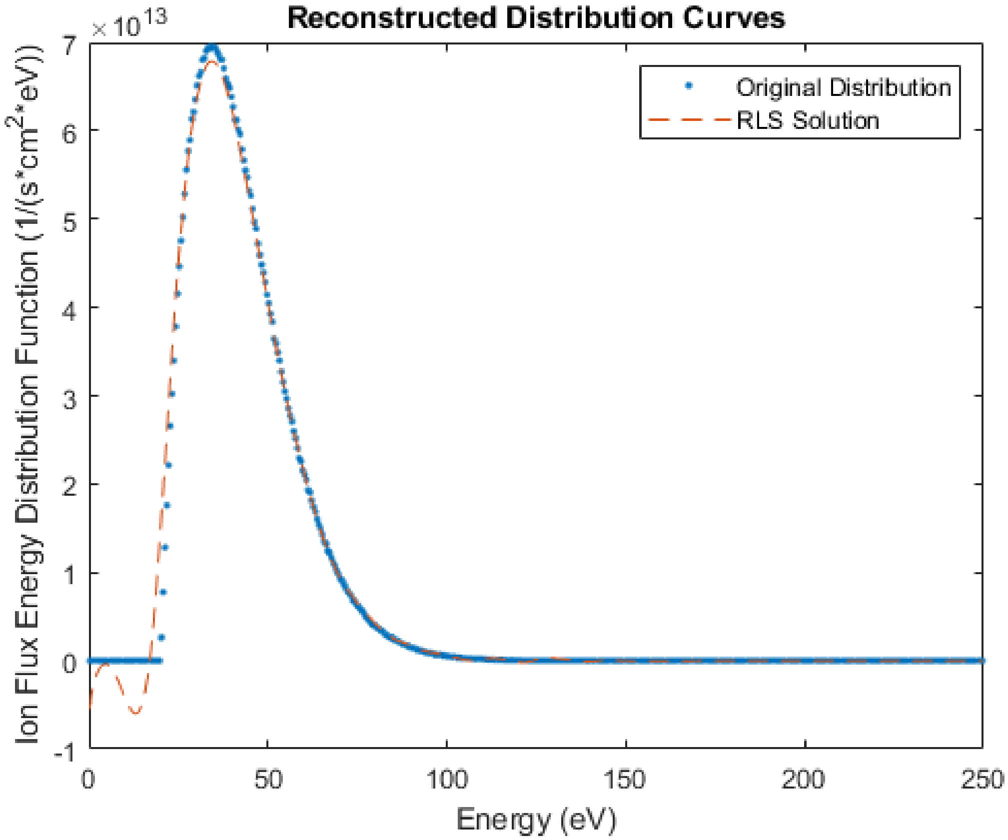

*Fig. 54*: Comparison of an original IEDf distribution used in XPDP [ 62 ] and the RLS solution obtained from an IV curve created by the XPDP1 simulation. This plot shows that the RLS method provides an accurate solution of the original distribution.

# CHAPTER 3: SPACE CHARGE DISTORTION AND COMPENSATION

## 3.1 RFEA Space Charge Distortion

In chapter 2, electrostatic simulations were used to look at the changes in the electric field due to design changes in the RFEA to allow it to operate at higher potentials. It was shown that by adjusting the geometric dimensions of the grid fill diameter, grid gap distance, and hole diameter, it was possible to minimize variations in the electric field between the grids and minimize the potential drop in the grid holes. By optimizing these design features, it is possible to obtain better resolution. Increasing the grid gap distance, which is inherently included in high voltage RFEA operation, increases the energy resolution by decreasing electric field variations and reducing the potential sagging within the grid holes. Nevertheless, this increase in grid gap distance will also increase the line integrated number of particles between the grids. Since the flux is constant within the RFEA, an increase in the line integrated number of particles does not necessarily present a problem as long as the density of the ions between the grids remains small [ 82, 85 ].

In general, the density of ions in the RFEA remains low. As ions traverse through the sheath, the ion density decreases from the plasma density due to the ion acceleration that occurs within the sheath. This means that the density is low as the ions enter the RFEA. As they enter the space between the floating grid and the plasma electron rejection grid (See Fig. 8), the ions continue to accelerate due to the negative potential applied to the plasma electron rejection grid to repel plasma electrons reducing the ion density even further. Ion acceleration also occurs between the discrimination grid and the collector due to the lower potential applied to the collector in reference to the discriminator. This ensures that ions that pass through the discriminator are picked up by the collector but also reduces the ion density from the ion acceleration. This space will also have lower ion density in general because as the discrimination potential increases, fewer ions will pass through the discriminator effectively reducing the line integrated number of particles in this space. The one location that the density may become a problem is between the plasma electron grid and the discrimination grid. As the ions pass through the plasma electron rejection grid, they are decelerated in order to discriminate between the different energies of the ions. As they are decelerated, this increases the ion density between the grids which also increases the space charge.

As mentioned by Green and Jones [ 82, 85 ], if the density (or current density) increases too much before a grid, it can distort the potential and electric field between the grids. During the potential sweep when taking a measurement with an RFEA, the potential between the plasma electron rejection grid and the discrimination grid changes shape. Initially, when the potential applied to the discriminator is equal to 0 V, the space charge of the ions will create a natural maximum at the midpoint between the grids. Typically, this is on the order of a couple of electron volts which is less than the minimum energy gained by the ions as they traverse through the sheath. As the potential on the discriminator rises, the maximum of the potential should shift towards the discriminator until the point that the discriminator overtakes the maximum from the space charge. This shift changes the shape of the potential from a convex curve to a straight line when plotting potential versus position. An example of this phenomenon was created using the following 1D Poisson's equation and the associated boundary conditions

$$\frac{d^2\Phi}{dx^2} = \frac{ne}{\varepsilon_o} \qquad B.C\colon \Phi(0) = 0, \Phi(d) = 100\left(1 + \sin\left(\omega t + \frac{3\pi}{4}\right)\right) \tag{19}$$

where $\Phi$ is the potential, $x$ is the location between the grids, $n$ is the ion density, $e$ is elementary charge, $\varepsilon_o$ is the permittivity of free space, $d$ is the total distance between the grids, $\omega$ is the angular frequency of the scan, and $t$ is the time of the scan. For the example, $n$ was uniform between the grids at 5 x $10^{15}$ $m^{-3}$, $d$ was 1 mm, and the scan frequency was set to 1 Hz. The resulting curves can be seen in Fig. 55 and the plot shows how the potential curve transitions from being convex to linear. The arrow shows the direction of the shift of the maximum potential as the discriminator potential increases.

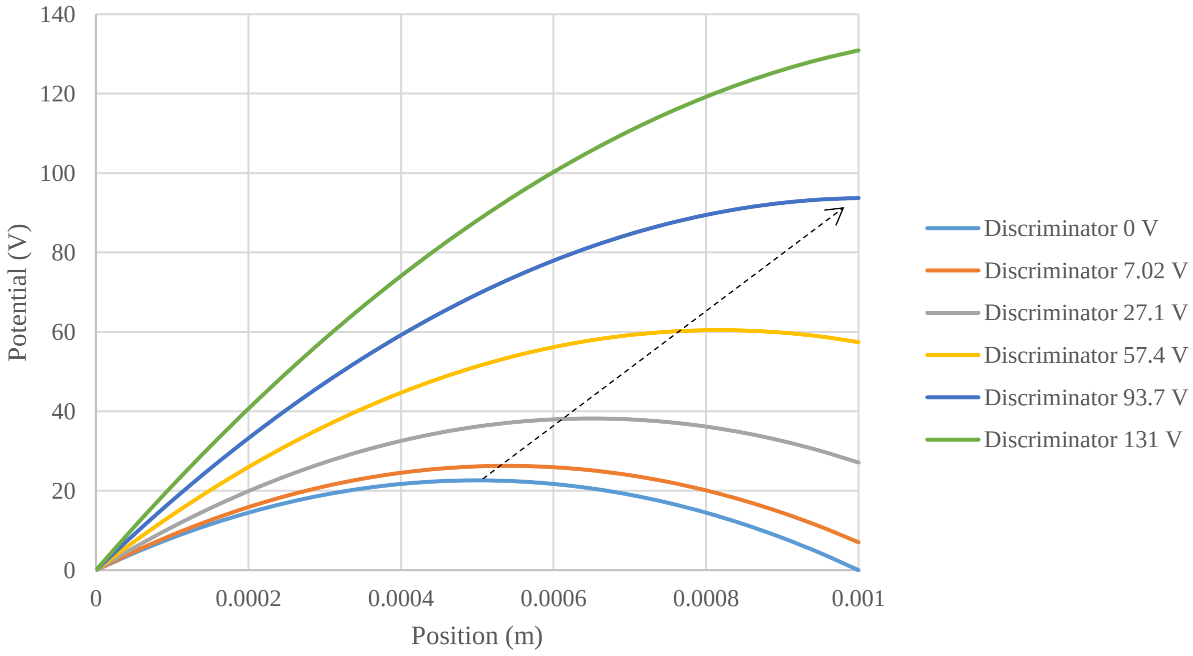

*Fig. 55*: Example of how the shape of the potential in between the plasma electron rejection grid and the discrimination grid change as the potential changes on the discriminator. In the plot, the discriminator is the far right side and the plasma electron rejection grid is the far left side. Since the potential within an RFEA is a state function, the value assigned to the plasma electron rejection grid is arbitrary and has been set to 0 V for this example. The arrow shows the shift in the maximum potential as the discriminator potential changes.

This local maximum in the potential curve is not normally an issue, but if the density between the grids is too high, the space charge build-up can make the potential curve retain its convex shape. This means that a maximum in the potential remains between the grids that is greater than the potential applied to the discrimination grid (See Fig. 56). As long as the ions have sufficient energy to overcome the potential maximum created by the space charge, the space charge build-up isn't a problem. There is a possibility though that some of the ions will not have enough energy to overcome the potential barrier. In this case, the ions will be reflected back towards the plasma electron rejection grid even though they should have been able to pass through the potential set by the discrimination grid (See Fig. 57). The premature rejection of ions causes a distortion the current measured meaning the resulting IEDf will be incorrect. As this distortion could occur for high voltage operation of RFEAs, it is necessary to determine its effects. It is also necessary to look at how to fix the distortion when it does occur.

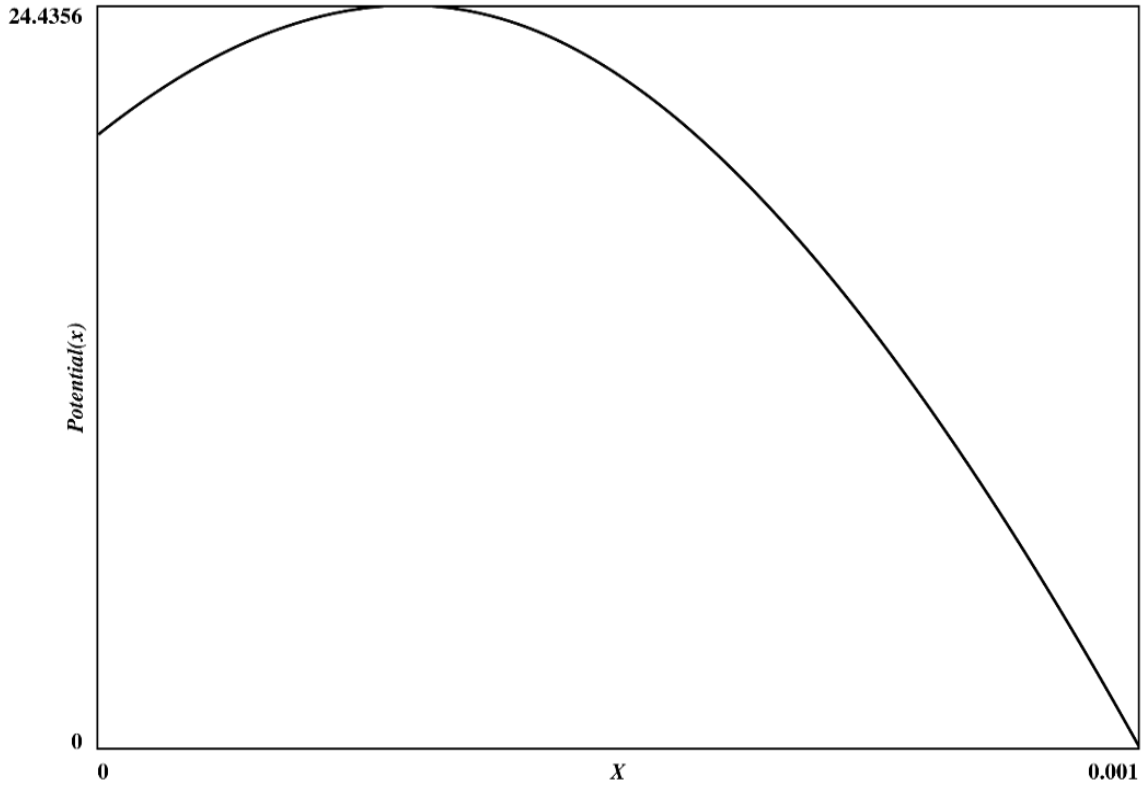

*Fig. 56*: Plot of the potential maximum between the plasma electron rejection grid and the discriminator caused by space charge build-up. The discriminator is located at the left vertical axis and the plasma electron rejection grid is located at the right vertical axis. Since the potential within an RFEA is a state function, the value assigned to the plasma electron rejection grid is arbitrary and has been set to 0 V for this example. This plot was created using XPDP1 [ 62 ]. This curve was created for Ar ions with an incoming current density of 6.8971 A/m$^2$, grid gap distance of 1.5 mm, drift velocity of 20 eV, and thermal velocity of 5 eV.

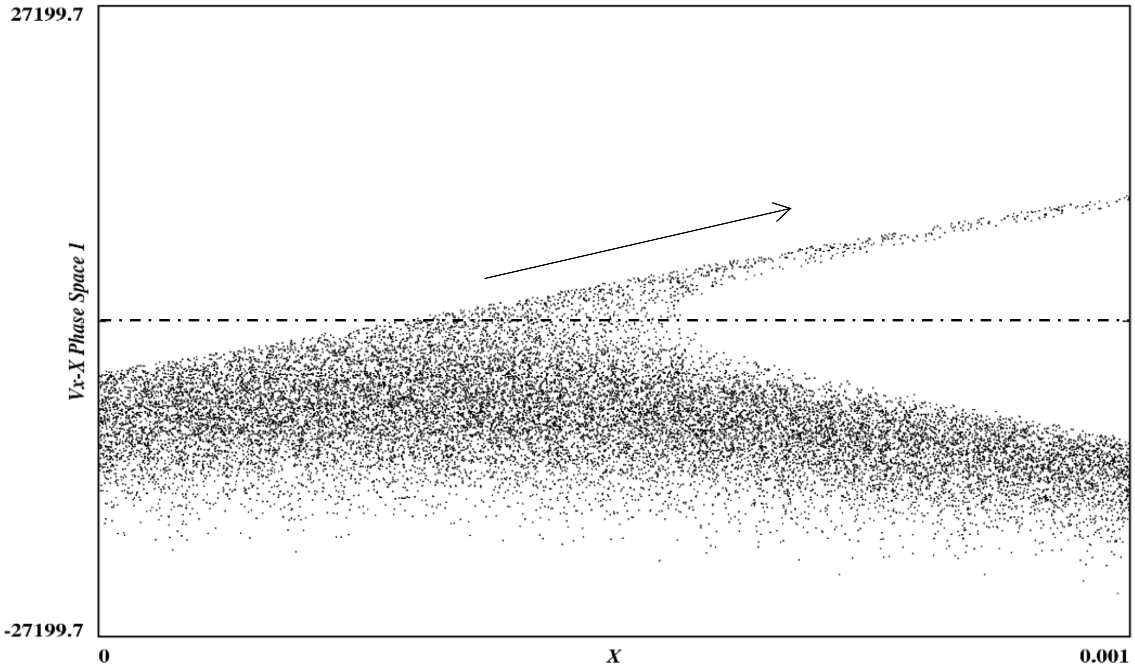

*Fig. 57*: This is a plot of the Vx-X Phase Space of ions plotted against their position in between the plasma electron rejection grid and the discriminator. In the plot, the discrimination grid is the far left side and the plasma electron rejection grid is the far right side. All the ions below the dashed line are moving to the left while those above are moving to the right. In this instance, the space charge build-up created a potential maximum that was larger than some of the ion energies traversing the space between the grids. Ions with insufficient energy were reflected back even though they had enough velocity to make it through the discriminator. This plot was created from an XPDP1 [ 62 ] simulation. This phase space profile was created for Ar ions with an incoming current density of 6.8971 A/m$^2$, grid gap distance of 1.5 mm, drift velocity of 20 eV, and thermal velocity of 5 eV.

### 3.1.1 XPDP1 Simulation

In order to analyze the effects of space charge on the IEDf from and RFEA IV curve, particle in cell (PIC) simulations were used to model the motion of ions as they traverse the space between the plasma electron grid and the discrimination grid. The PIC code used for these simulations was XPDP1 [ 62 ]. This is a 1D PIC code that simulates charged particle motion in between two electrodes. A 1D code was chosen for multiple reasons. The first is that electrostatic simulations were performed on the TEL RFEA CAD model to find the optimal geometric dimensions to minimize the radial electric fields and minimize fluctuations in the vertical electric field in the probe. As the manufactured RFEA is based off this CAD model, it is safe to start with a model that only looks at the 1D motion of the ions due to the minimal radial electric fields. A 1D PIC code also provides a faster and simpler analysis of the problem. As this was the first attempt to analyze space charge distortion in the TEL RFEA design, it was better to start with a simpler model that would provide quick results. This makes it easier to quickly grasp the main effects of space charge distortion while also providing clues for new areas of focus with more complex models. As just mentioned, for simplicity and keeping the focus on space charge distortion effects, secondary electron emission was disable as it can also distort the IV curve. Multiple simulations were performed, from which an IV curve was created from which an IEDf could be obtained. The IEDfs were reconstructed from the IV curves using a regularization algorithm that will be discussed in the next subsection (See section 3.1.2).

The XPDP1 simulations were set up so that an ion beam was created and injected from the right electrode. This electrode represented the plasma electron rejection grid (See Fig. 16). The beam diameter was set to the entrance diameter (1 mm) of the silicon (Si) wafer as this was the most constricting feature on the ion beam and was used in the RFEA electrode experiments. The injected ions were given a drift velocity of 20 eV with an additional thermal velocity of 5 eV assigned in the x-direction. The drift velocity creates a monoenergetic beam of ions all with the specified energy. The thermal velocity is used to create a Maxwell-Boltzmann velocity distribution at the specified energy. Each ion is given a drift velocity and then randomly assigned an additional thermal velocity added on top of the drift velocity. This creates a velocity distribution spread for the ions in the beam that is more consistent with an actual plasma measurement.

In order to study the space charge effects, the gap distance between the electrodes (RFEA grids) and incoming current density were varied.  The gap distance was changed between 0.5 –

15 mm. The incoming current density for an Ar plasma was calculated using a self-consistent model, equation for flux $(\Gamma)$, and the transparency ratios of each of the grids. For the self-consistent plasma model, the sheath voltage $(V_o)$ was set at 1 kV, the pressure $(p)$ was set at 10 mTorr, and the chamber radius was 150 mm with a height of 300 mm. Three different plasma densities of 1x$10^{10}$ cm$^{-3}$, 1x$10^{12}$ cm$^{-3}$, and 2x$10^{12}$ cm$^{-3}$ were assumed. Using these initial values and following the example presented by Lieberman and Lichtenberg [ 12 ] in chapter 11 of their book, the electron temperature and the density at the sheath entrance were obtained using a numerical solution (See Appendix A). For these conditions, the electron temperature $(T_e)$ was calculated to be 2.18 eV and the density at the sheath entrance $(n_s)$ was 8.324x$10^{8}$ cm$^{-3}$, 8.324x$10^{10}$ cm$^{-3}$, and 1.665x$10^{11}$ cm$^{-3}$. Using the equation for Γ and Bohm velocity $(u_B)$

$$\Gamma = n_s u_B \qquad 20$$

$$u_B = \left(\frac{eT_e}{m_i}\right)^{1/2} \qquad 21$$

where $e$ is elementary charge and $m_i$ is the ion mass, it was possible to solve for the incoming Γ at the sheath entrance. Since Γ is always conserved, the Γ entering the sheath is the same as the Γ at the Si wafer grid entrance. From here, the incoming Γ was reduced based on the transparency of the Si wafer grid, the floating grid, and the plasma electron rejection grid. The transparency of each of the grids was calculated by taking the area ratio between the grid holes and the total ion beam area. Using the transparency ratios and the incoming Γ, it was determined that the incoming current density from the plasma electron rejection grid was 3.4486x$10^{-2}$ A/m$^2$, 3.4486 A/m$^2$, and 6.8971 A/m$^2$ respectively.

The left electrode acted as both the discrimination grid and the collector. This electrode was scanned at a frequency of 1 kHz. It is possible to adjust the scan frequency in XPDP1. This value was chosen by finding a compromise between the experimental scan frequency and the runtime of the simulations. The voltage range of the scan was from 0 to 150 V. Simulations were run for all combinations of different gap distances, current densities, and multiple scan frequencies. For the scan frequencies, it was found that the speed of the scan had no difference on the IV curves produced from the simulation as long as the current from the AC source was accounted for in the IV trace. To do this, for each simulation run, a second simulation was run without any ions injected into the system. The IV curve produced from these ion free simulations was the pure AC source current. Since the current measured from the simulations with ions was a combination of the AC source current and ion source current, the AC source current from the ion free simulations was subtracted off of the total current (AC plus ions) to obtain the pure ion current for the IV curve.

The IV curves obtained from the simulations can be seen in Fig. 58 -Fig. 60. In each of these figures, an IV curve with no space charge distortion (0.5mm case) is compared to one with space charge distortion (various gaps). As can be seen from the plots, depending on the incoming current density, the gap distance when space charge distorts the IV curve changes. In Fig. 58 where the plasma density was set to $1x10^{10}$ $cm^{-3}$, the IV curve was distorted for a 15 mm gap distance. For the higher plasma density cases (See Fig. 59 and Fig. 60), space charge distortion occurred at gap distances of 1.5 mm and 1 mm. For all of these cases, the IV curves that were distorted by space charge began to drop off sooner and a more gradual slope than its non-distorted counterpart. It can also be seen in the plots that at a specific voltage (approximately 50V in these cases) the distorted IV curves meet back up with the non-distorted curves and both follow the same trend from then on. This means that the potential sweep on the discrimination grid overcame the potential caused by the space charge build-up.

Since space charge distortion has been observed for specific gap distances, a density

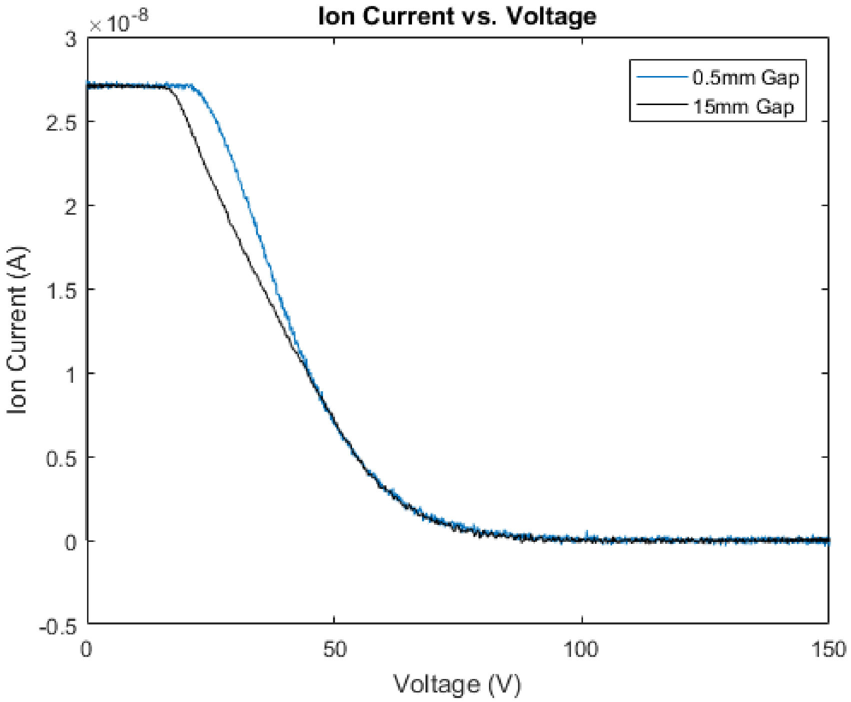

*Fig. 58*: IV curves obtained from the XPDP1 simulations for an incoming current density from a 1x10$^{10}$ cm$^{-3}$ plasma density.

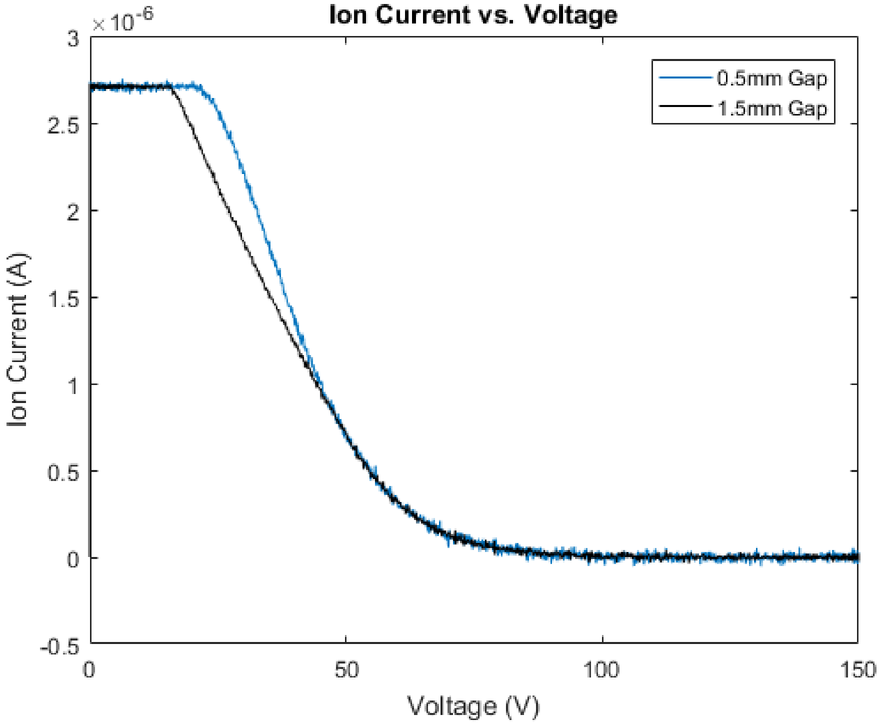

*Fig. 59*: IV curves obtained from the XPDP1 simulations for an incoming current density from a 1x10$^{12}$ cm$^{-3}$ plasma density.

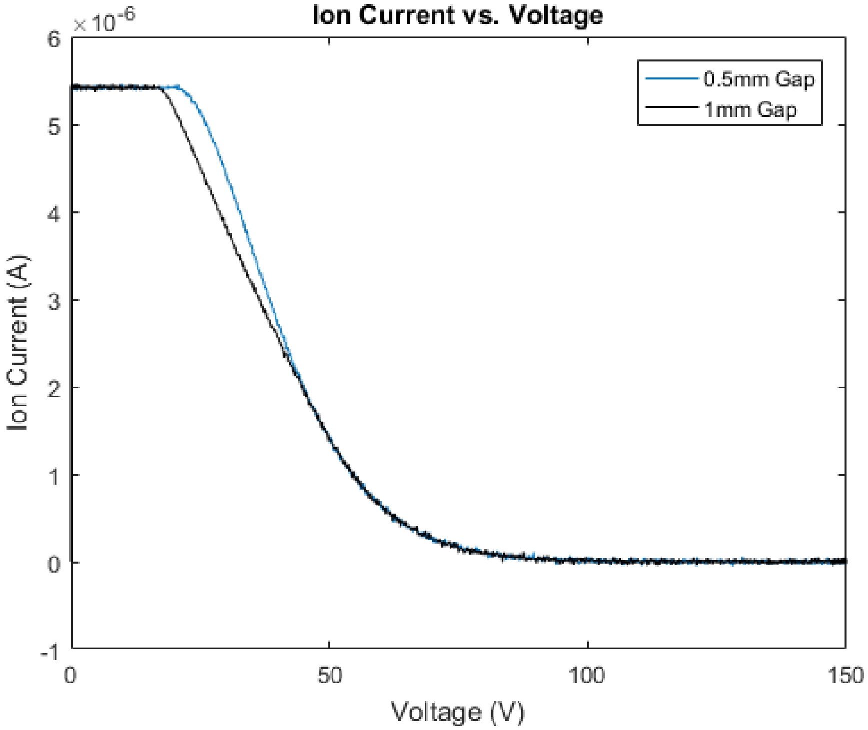

*Fig. 60*: IV curves obtained from the XPDP1 simulations for an incoming current density from a 2x10$^{12}$ cm$^{-3}$ plasma density.

value can be obtained using Eq. 9 in chapter 1 presented by Green [ 82 ]. Using the incoming current density ($J_{2nd}$) at the plasma electron rejection grid (2$^{nd}$) and the drift velocity ($u_{2nd}$) of the ions entering the 2$^{nd}$ grid, the density of the ions at this point can be calculated using

$$n_{2nd} = \frac{J_{2nd}}{u_{2nd}} \qquad 22$$

$$u_{2nd} = \left(\frac{2V_i}{m_i}\right)^{1/2} \qquad 23$$

where $m_i$ is the mass of the ions and $V_i$ is the drift velocity in electronvolts used in the simulations. The drift velocity was chosen as it is the minimum energy of the distribution and these ions will experience space charge repulsion first. These density values can then be compared to the density value found from Eq. 9 assuming an ion energy of 20 eV and single ionization. The density values entering the 2$^{nd}$ grid and from Green's equation can be seen in

Table 4. Based on the density values calculated, the density entering the 2nd grid is slightly larger than the density values calculated using Green's equation but still on the same order of magnitude. Based on these density values, it would signify that space charge distortion should start occurring immediately as the ions enter past the send grid. However, because only a single energy value was chosen in the calculation of the 2nd grid entrance density, the 2nd grid entrance density is artificially high. Since some of the ions will have a higher energy, this density value would drop for the entrance flux.

Table 4: Density values entering the plasma electron rejection grid compared to density values from Eq. 9 in chapter 1 presented by Green [ *82* ].

| Plasma Density ($cm^{-3}$) | Gap Distances (mm) | Green Density Equation (20eV) ($cm^{-3}$) | 2nd Grid Entrance Density (cm^-3) |
|---|---|---|---|
| 1.00E+10 | 15 | 8.89E+06 | 2.44E+07 |
| 1.00E+12 | 1.5 | 8.89E+08 | 2.44E+09 |
| 2.00E+12 | 1 | 2.00E+09 | 4.89E+09 |

Another reason for the discrepancy in the density values may be due to the grid gap distance used. In Fig. 58 - Fig. 60, a significant amount of space charge distortion to the IV curve has occurred. The distortion will not be as bad at smaller grid gap distance. A smooth transition of space charge distortion shown by multiple IV curves for a plasma density of $2x10^{12}$ $cm^{-3}$ from different gap distances can be seen in Fig. 61. The IV curve for a gap of 0.7 mm is a non-distorted IV curve just as the 0.5 mm cases in Fig. 58 - Fig. 60. Therefore, 0.7 mm can be used as the gap distance in Eq. 9 for a better estimate of the density necessary for space charge distortion. Using this gap distance, a density of $4.08x10^{9}$ $cm^{-3}$ is calculated. This density value is in even better agreement with the 2nd grid entrance density (which is still artificially high). This shows that gap distances showing space charge distortion in the XPDP1 simulation is consistent with previous work.

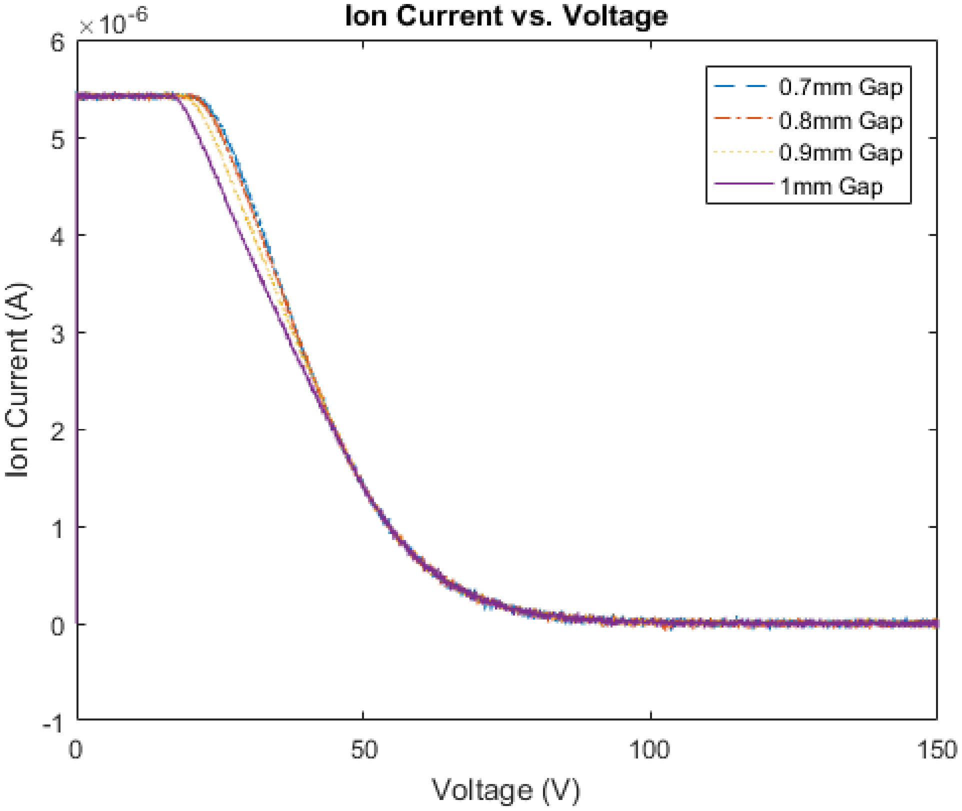

Fig. 61: Multiple IV curves for a plasma density of 2x10$^{12}$ cm$^{-3}$ showing a smooth transition as space charge distortion occurs at increasing gap distances.

### 3.1.2 Simulation IEDfs

The regularized least-squared (RLS) solution method described in section 2.4 was used to obtain the IEDfs for the XPDP1 simulation IV curves. The reconstructed IEDfs obtained from the IV curves presented in Fig. 58 - Fig. 60 can be seen in Fig. 62 - Fig. 64. These IEDfs were also plotted against the original Maxwell-Boltzmann distribution that XPDP1 used to assign energies to the ions in the simulations. For each case, the IEDf solution from the 0.5 mm gap IV curve are in very good agreement with the XPDP1 original distribution. This agreement is

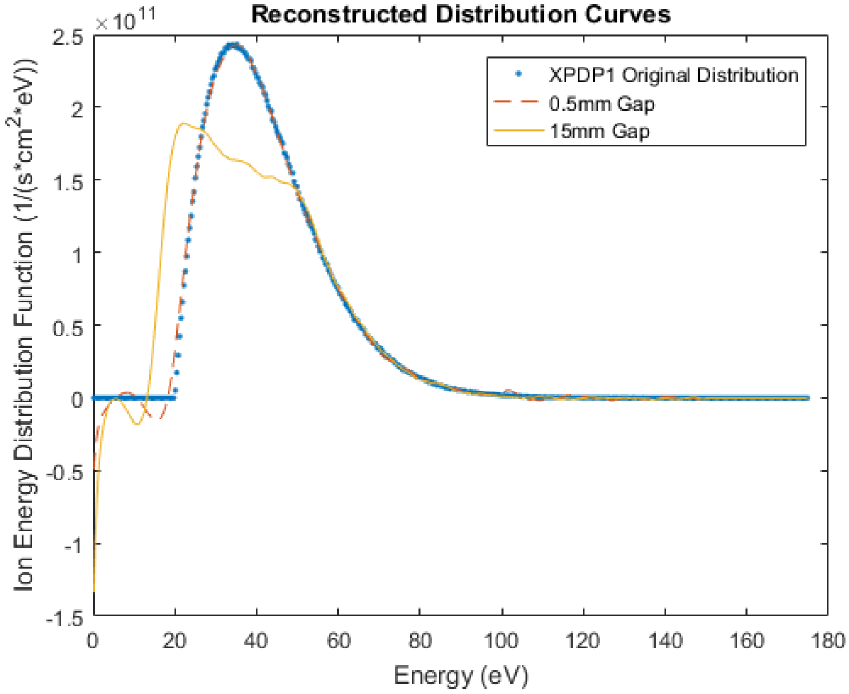

*Fig. 62*: Plots the reconstructed IEDfs from the IV curves presented in Fig. 58 for a plasma density of 1x10$^{10}$ cm$^{-3}$. The reconstructed IEDfs are plotted along with the original distribution function that XPDP1 used in assigning energies to the ions in the simulation.

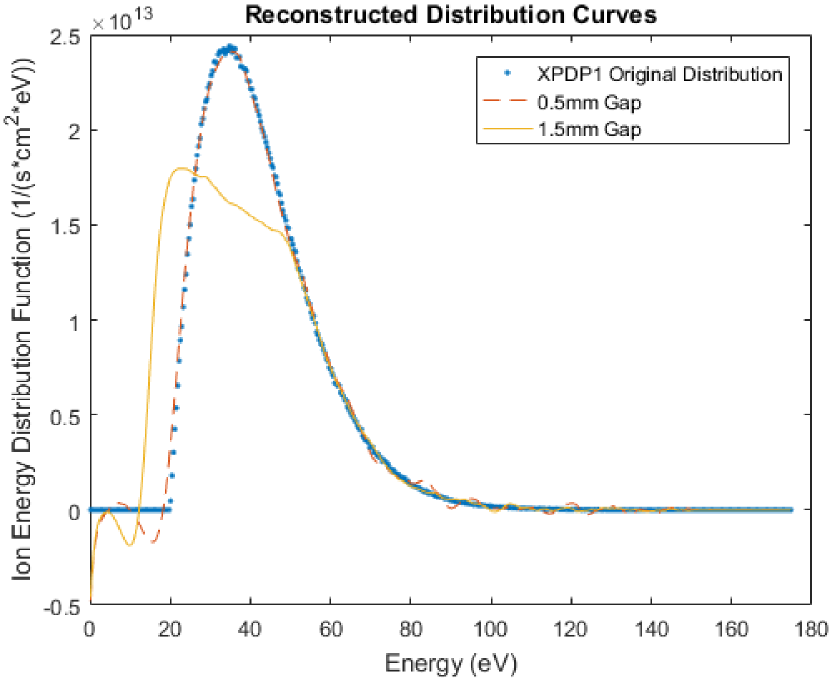

*Fig. 63*: Plots the reconstructed IEDfs from the IV curves presented in Fig. 59 for a plasma density of 1x10$^{12}$ cm$^{-3}$. The reconstructed IEDfs are plotted along with the original distribution function that XPDP1 used in assigning energies to the ions in the simulation.

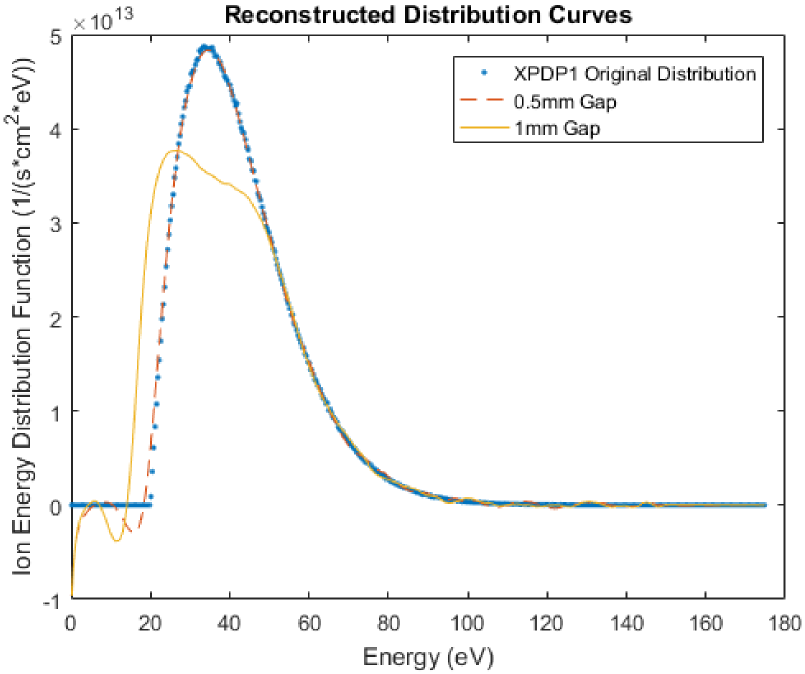

*Fig. 64*: Plots the reconstructed IEDfs from the IV curves presented in Fig. 60 for a plasma density of 2x10$^{12}$ cm$^{-3}$. The reconstructed IEDfs are plotted along with the original distribution function that XPDP1 used in assigning energies to the ions in the simulation.

expected as there was no space charge distortion in the 0.5 mm gap IV curves. This signifies that the regularization reconstruction method being used to calculate the IEDfs is working properly and accurately so the IEDf solutions from the space charge distorted IV curves is correct.

In each of the cases, the space charge distorted IEDfs follow a similar shape. The rise of the IEDfs starts sooner than the non-distorted IEDfs. The maximum peak location of the distorted IEDfs is also located at a lower energy than the non-distorted IEDfs. The distorted peaks approximately linearly decrease until about 50 V at which point the distorted IEDfs and non-distorted IEDfs have little to no discrepancy. It is important to note that the space charge distortion in the IEDfs does not change the area under the curve. Hence the ion saturation current ($I_{sat}$) of the distorted IV curves is the same as the non-distorted IV curves. It also limits space charge distortion identification to the IV curve characteristics as opposed to the RFEA geometry.

The IEDfs for a 2x10$^{12}$ cm$^{-3}$ plasma density from the IV curves presented in Fig. 61 can be seen in Fig. 65. These IEDfs show a similar trend to the IEDfs shown in Fig. 62 - Fig. 64. As this plot also presents how the space charge distortion changes as gap distance increases. The 0.7 mm gap case had no space charge distortion and is in good agreement with the XPDP1 original distribution. As the gap distance increases, the peak location gradually shifts to lower energies and the initial rise also starts at lower energies. These are expected trends for the distorted IEDfs based on the measured IV curves. During the scan of the discrimination-collector grid in the simulations, the space charge potential created by the ions maintains a potential that is about 10 V higher than the potential applied to the discrimination-collector grid. This higher space charge potential remains until the discrimination-collector grid reaches about 40 V. From this point, the discrimination-collector grid potential begins to overtake and exceed the space charge potential. In other simulations with different gap lengths and current densities, this trend of space charge

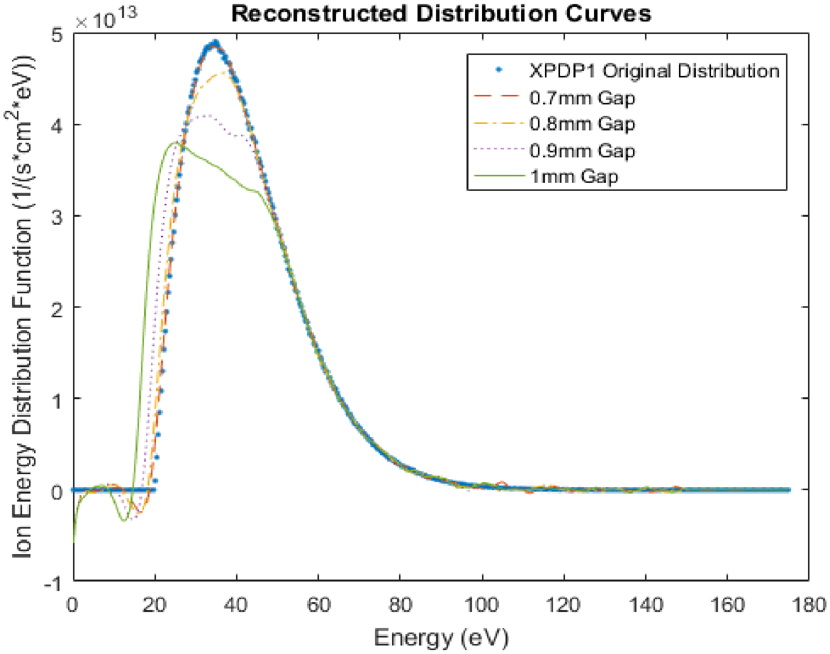

*Fig. 65*: Plot of the IEDfs for a 2x10$^{12}$ cm$^{-3}$ plasma density for the IV curves presented in Fig. 61. These IEDfs are also plotted with the original energy distribution used in XPDP1 in assigning energies to the ions in the simulation.

distortion only occurred for discrimination-collector grid potentials below about 100 V. This signifies that space charge has the most significant impact at lower ion energies. This then becomes a design criterion for high voltage RFEAs. If the high voltage RFEA will be used in plasma conditions where low energy ions are not expected or if low energy resolution is not of interest, then the space charge distortion is not an issue and need not be considered. However, if an accurate IEDf with good low and high energy ion resolution is needed, then space charge distortion will need to be considered.

### 3.2 Space Charge Compensation

To solve the issue of space charge, there are two options. The first option is to limit the flux of ions that enters the probe. This could be done by limiting the transparency of the entrance of the probe. Reducing the flux would reduce the number of ions between the grids which would effectively reduce the space charge build-up between the grids. There is a downside to this method. By reducing the flux, the current measured by the collector is also reduced so the signal to noise ratio will get smaller. For cases that have a large incoming signal, this is not a problem. However, for cases that already have a limited incoming signal, reducing the flux would cause the signal to be completely lost in the noise. This means, especially for low signal situations, another method would need to be used to account for space charge distortion. As industrial processes move toward higher plasma density for increased process rate and higher ion energy for increased process anisotropy, the trend with regard to ion flux and ion energy flux begins to approach a condition where these parameters cannot be measured without accounting for space charge.

The other option is to account for space charge is account for space charge distortion in the post analysis process when calculating the IEDf. For this option and since the RLS method is used to calculate the IEDf, it is proposed that the space charge distortion can be accounted for by truncating the system matrix $(K)$ in the RLS equation (See Eq. 18). By truncating $K$, it is possible to accurately represent the early loss of current due to space charge build-up. Nevertheless, this is a more difficult process than it seems because one does not know what the exact shape of the IEDf is supposed to look like. This means that this method can only use very limited information when accounting for space charge distortion. It is possible that the initial truncation of $K$ will correct for some of the space charge distortion but not all of it. In this instance, it may be necessary to implement an iterative solution in which the space charge profile is generated from the IEDf, $K$ is then truncated again based on the space charge profile, and then a new IEDf is found with the updated $K$. This process could be repeated until it reaches a convergence criterion. It is possible though that this iterative process might not actually converge and would have to be tested. Whether an iterative solution is used or not, in order to truncate $K$ with limited information on the IEDf, it is necessary to create a model to help truncate $K$.

### 3.2.1 Compensation Models

In building a model to truncate $K$, it is necessary to go back to the characteristic relationship between the collector current $(I_c)$ and the IEDf (See Eq. 17). Before, the lower limit of integration was based on the potential applied to the discrimination grid $(V_d)$. When accounting for space charge, $V_d$ is not necessarily the lower limit of integration. For a portion of measurement, the relationship between $I_c$ and the IEDf is

$$I_c(V_c) = eA \int_{eV_{scp}}^{\infty} IEDf\ dE \tag{24}$$

where $V_{scp}$ is the peak potential generated by space charge build-up. This is the proper relationship until the point where $V_d$ overtake and exceeds $V_{scp}$. Knowing the value of $V_{scp}$ is necessary in truncating $K$. Again, this is where the difficulty arises because $V_{scp}$ is dependent on the IEDf but very little information about the true IEDf is known. In trying to estimate $V_{scp}$ with limited assumptions about the IEDf, it is necessary to try and simplify the space charge distribution (or density distribution) based on the measured IV curve. The simplest method to do this is to assume that the density distribution is a simple step function between the minimal ion energy $E_{min}$ and the maximum ion energy $E_{max}$ (See Fig. 66). Since that saturation current $I_{sat}$ of the IV curve is equal to

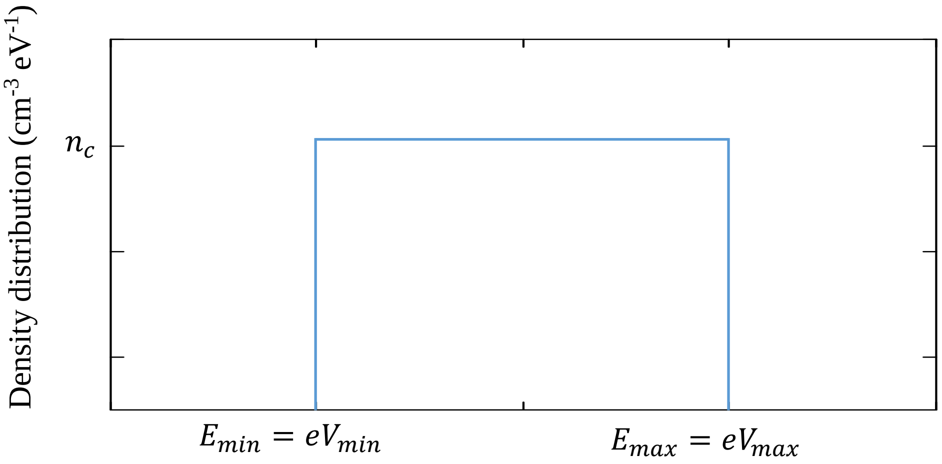

*Fig. 66*: A plot of the density distribution used in creating a model to truncate the system matrix $(K)$ of the RLS method. To start, a simple step function was used to represent the density distribution to keep complexity of the model low.

$$I_{sat} = n_m A e \bar{v} \qquad 25$$

where $n_m$ is equal to the total ion density and $\bar{v}$ is the average ion energy, then $n_c$ in Fig. 66 is equal to

$$n_c = \frac{I_{sat}}{Ae\bar{v}(E_{max} - E_{min})} \qquad 26$$

From Eqs. 25 and 26, a piecewise density distribution can be constructed that is dependent on $V_d$ as follows

$$n(V_d) = \begin{cases} \dfrac{I_{sat}}{Ae\bar{v}}, & eV_d < E_{max} \\ \dfrac{I_{sat}}{Ae\bar{v}} - \dfrac{I_{sat}(eV_d - E_{min})}{Ae\bar{v}(E_{max} - E_{min})}, & E_{min} \leq eV_d < E_{max} \\ 0, & E_{max} < eV_d \end{cases} \qquad 27$$

Since $n$ is also dependent on $\bar{v}$, it is necessary to estimate this value based on the limited information from the IV curve. A simple estimate for $\bar{v}$ can use $V_d$ at the point where the $I_c$ is equal to half the value of $I_{sat}$ so that

$$\bar{v} = \sqrt{\frac{2eV_d(I_{sat}/2)}{m_i}} \qquad 28$$

where $m_i$ is the ion mass and $e$ is elementary charge. Now that a density distribution is created, it is possible to obtain an equation for the potential with the respect to location between the plasma electron rejection grid and the discriminator-collector using the 1D Poisson's equation. Thus the potential is equal to

$$\phi(x) = \begin{cases} -\dfrac{n_m e x^2}{2\varepsilon_o} + C_1 x + C_2, & eV_d < E_{max} \\ C_1 \exp\left(\sqrt{\dfrac{n_c e}{\varepsilon_o}} x\right) + C_2 \exp\left(-\sqrt{\dfrac{n_c e}{\varepsilon_o}} x\right) + \dfrac{V_{max}}{e}, & E_{min} \leq eV_d < E_{max} \end{cases} \qquad 29$$

Since $n$ is equal to 0 for the regime where $E_{max} < eV_d$, the potential equation for this portion is inconsequential because all the ions are being rejected at this point. Therefore, in Eq. 29, only the potential equation in the first two regimes was determined. Also, in Eq. 29, the values of $C_1$ and $C_2$ are constants determined by the boundary conditions at the electron rejection grid and the discriminator-collector. Before the values of these constants is determined, it is necessary to understand how $\phi(x)$ can be used to truncate $K$.

To illustrate how $\phi(x)$ is useful in truncating $K$, it is best to refer to Fig. 67 during the explanation. The plot in Fig. 67 shows how the lower limit of the integral in chapter 2 Eq. 8 or

Eq. 24 changes depending on $V_d$. In the case that there is no space charge distortion, the lower limit of the integral follows the red line which is just the original relation presented in Eq. 17. If space charge distortion does occur, then the lower limit of the integral (when $V_d = 0$) would start at one of the green dots on the vertical axis. The green dot, or intercept voltage ($V_{int}$), used depends on the flux entering the detector. The larger the flux, the higher $V_{int}$ will be as it is equal to $V_{scp}$ created by the space charge build-up. As $V_d$ increases during the scan, the lower intercept of the integral will trace a path to one of the blue dots on the red line. This path is dependent on the shape of the IEDf and is represented by the orange curve in Fig. 67. The blue dot, or convergence voltage ($V_{con}$), is the potential where the $V_d$ equals and exceeds the $V_{scp}$. This point

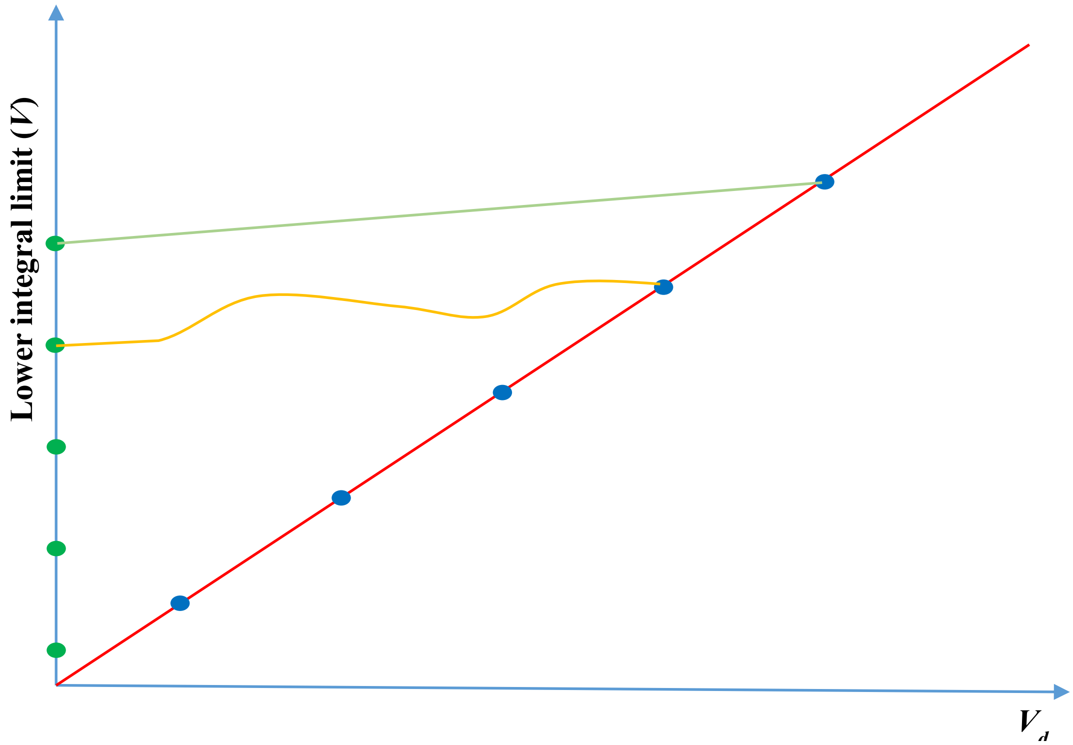

*Fig. 67*: Plot of how the lower limit of integration changes with the potential applied to the discrimination grid with and without space charge distortion. In the case there is no space charge distortion, the lower integral limit follows the red line. If there is space charge distortion, the lower integral limit would start at one of the green dots on the vertical axis and trace a path (dependent on the shape of the IEDf) to one of the blue dots on the red line (represented by the orange curve). Knowing the potential $\phi(x)$, it is possible to find the intercept voltage ($V_{int}$) (green dots) and the convergence voltage ($V_{con}$) (blue dots). The lighter green line is a simple linear model between the two potentials that can be used to truncate the system matrix ($K$).

is the same point where the space charge distorted IV curve begins to follow the same trend as the non-distorted IV curve in Fig. 58 - Fig. *61*. This point has a strong dependence on the shape of the IEDf while $V_{int}$ has only a weak dependence on the IEDf. The curve that the IEDf creates between these two points is what is needed to truncate $K$.

As the exact shape of the curve between $V_{int}$ and $V_{con}$ is not known, so an estimate must be used to truncate $K$. The simplest model to assume is a linear dependence between the two points which is represented by the light green line in Fig. 67. Using this linear line, it would be possible to truncate $K$ to try and account for space charge distortion. The only unknowns for this model would $V_{int}$ and $V_{con}$. This is where the equation for $\phi(x)$ comes into play. Using the proper boundary conditions, values for $V_{int}$ and $V_{con}$ could be estimated using Eq. 29. In general, the boundary conditions for $V_{int}$ and $V_{con}$ can be seen in Table 5. In these boundary conditions, the plasma electron rejection grid is located at x = 0 and the discrimination grid is located at x = d. Using these boundary conditions, the constants in Eq. 29 can be found (See Eqs. 30 and 31) where $\phi(x)$ now becomes the space charge peak potentials $V_{int}$ and $V_{con}$. These two equations show why $V_{int}$ has a weak dependence on the IEDf and that $V_{con}$ has a strong dependence. The only dependence that $V_{int}$ has on the IEDf is through $\bar{v}$. On the other hand, $V_{con}$ is dependent on the IEDf through not only $\bar{v}$ but also through $V_{max}$ and $V_{min}$. It is important to note though that as both are dependent on $\bar{v}$, the estimate of $\bar{v}$ will have a significant effect on the accuracy of $V_{int}$ and $V_{max}$. These two equations can next be used to create the linear model for $V_{scp}$ used to truncate $K$ (See Eq. 32). Now that an equation for $V_{scp}$ has been found, the integral relationship can be rewritten to account for space charge build-up (See Eq. 33). Given this model, $K$ could be truncated to account for space charge distortion in the IV curve.

*Table 5:* Boundary conditions used in Eq. 29 to find values for $V_{int}$. *and* $V_{con}$. In these equations, the plasma electron rejection grid is located at x = 0 and the discriminator is located at x = d.

| B.C. for $V_{int}$ | B.C. for $V_{con}$ |
|---|---|
| $x = 0, \phi(0) = 0$<br>$x = d, \phi(d) = 0$ | $x = 0, \phi(0) = 0$<br>$x = d, \left.\frac{d\phi}{dx}\right\|_{x=d} = 0$ |

$$V_{int} = \frac{I_{sat} d^2}{8A\varepsilon_o \bar{v}} \qquad eV_d < E_{max} \tag{30}$$

$$V_{con} = \frac{V_{max}}{e}\left(1 - \frac{1}{\cosh\left(\sqrt{I_{sat} e d^2 / A\varepsilon_o \bar{v}(V_{max} - V_{min})}\right)}\right) \qquad E_{min} \leq eV_d < E_{max} \tag{31}$$

$$V_{scp} = \frac{I_{sat} d^2}{8A\varepsilon_o \bar{v}} + V_d \frac{\frac{V_{max}}{e}\left(1 - \frac{1}{\cosh\left(\sqrt{I_{sat} e d^2 / A\varepsilon_o \bar{v}(V_{max} - V_{min})}\right)}\right) - \frac{I_{sat} d^2}{8A\varepsilon_o \bar{v}}}{\frac{V_{max}}{e}\left(1 - \frac{1}{\cosh\left(\sqrt{I_{sat} e d^2 / A\varepsilon_o \bar{v}(V_{max} - V_{min})}\right)}\right)} \tag{32}$$

$$I_c(V_d) = \begin{cases} eA\int_{eV_{scp}}^{\infty} IEDf\, dE, & V_d \leq \frac{V_{max}}{e}\left(1 - \frac{1}{\cosh\left(\sqrt{I_{sat} e d^2 / A\varepsilon_o \bar{v}(V_{max} - V_{min})}\right)}\right) \\ eA\int_{eV_d}^{\infty} IEDf\, dE\,, & V_d > \frac{V_{max}}{e}\left(1 - \frac{1}{\cosh\left(\sqrt{I_{sat} e d^2 / A\varepsilon_o \bar{v}(V_{max} - V_{min})}\right)}\right) \end{cases} \tag{33}$$

Since this space charge work has been done using XPDP1 simulations, the exact values of $V_{int}$ and $V_{con}$ are known for those simulations. This makes it possible to compare how well the model accurately estimates these values as they are vital to truncating $K$. To do this, values for $V_{int}$ and $V_{con}$ were recorded from XPDP1 for multiple drift and thermal velocities. When the drift velocity was varied, the thermal velocity was held constant and vice versa. The comparison between the model $V_{int}$ and $V_{con}$ to the XPDP1 values can be seen in Fig. 68 and Fig. 69. A comparison for the $V_{int}$ can be seen in Fig. 68. To estimate of $\bar{v}$ for this comparison, the velocity was found at $.5I_{sat}$. These plots show that the model gives an estimate for $V_{int}$ on the same order of magnitude as the values obtained from XPDP1. The trend of the model is also consistent with the trend produced from XPDP1 except when the drift energy drops below 13 eV. The reason the shape of the measured data changes here is due to the fact that at drift velocities of 13 eV or less, the space charge build-up is large enough to cause ion rejection immediately. This means that the IV curve does not have a $I_{sat}$ region and only has the fall off region (See Fig. 70). This is a limiting constraint of the model but with energies above this regime, the model gives a good estimate for $V_{int}$.

As mentioned, a comparison for $V_{con}$ can be seen in Fig. 69. For this case, two different methods were used to provide an estimate for $\bar{v}$. The same method that was used for the $V_{int}$ case was the first. The other method was to use the first moment of the step distribution to estimate $\bar{v}$. Again, for both the drift and thermal velocities, the model gives a decent estimate for $V_{con}$. The values are on the same order of magnitude but not quite as close as the $V_{int}$ comparison. It is interesting to note that the $V_{con}$ values associated with the $\bar{v}$ estimate used in the $V_{int}$ gives a better estimate than the first moment of the step distribution. This is consistent with the idea that $\bar{v}$ has a strong dependence on the skew of the distribution. In XPDP1, a Maxwell-Boltzmann distribution is used, and this type of distribution is going to be skewed towards lower velocities. The estimate for $\bar{v}$ from the $V_{int}$ case results in lower velocity values than the first moment of the step distribution. This confirms the dependence of the model accuracy on a good estimate for $\bar{v}$. Nevertheless, on a first order approximation for $\bar{v}$, the model gives a decent estimate for $V_{con}$.

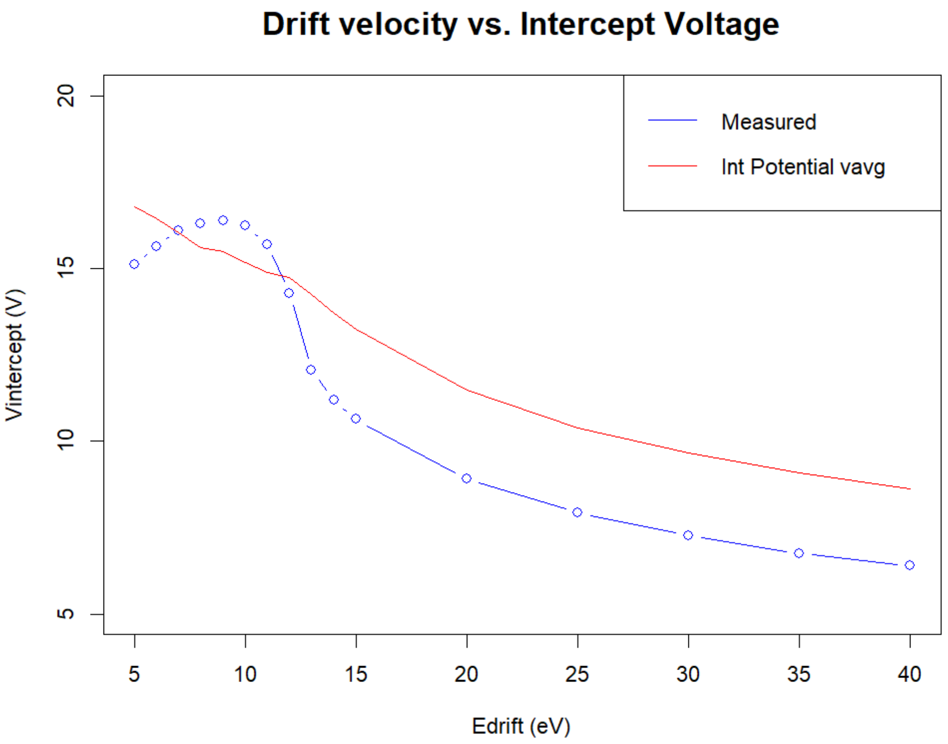

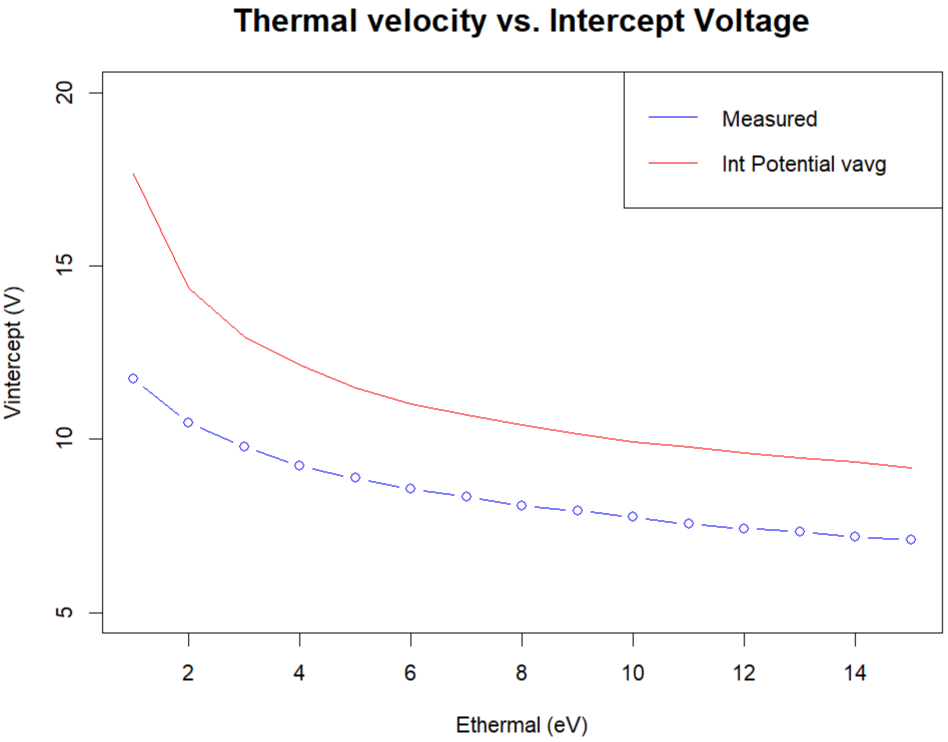

*Fig. 68*: Comparison of the XPDP1 potential values to the potential values predicted by the model equation for $V_{int}$. For this case, a constant thermal energy of 5 eV or a constant drift energy of 20 eV was used when varying the other parameter.

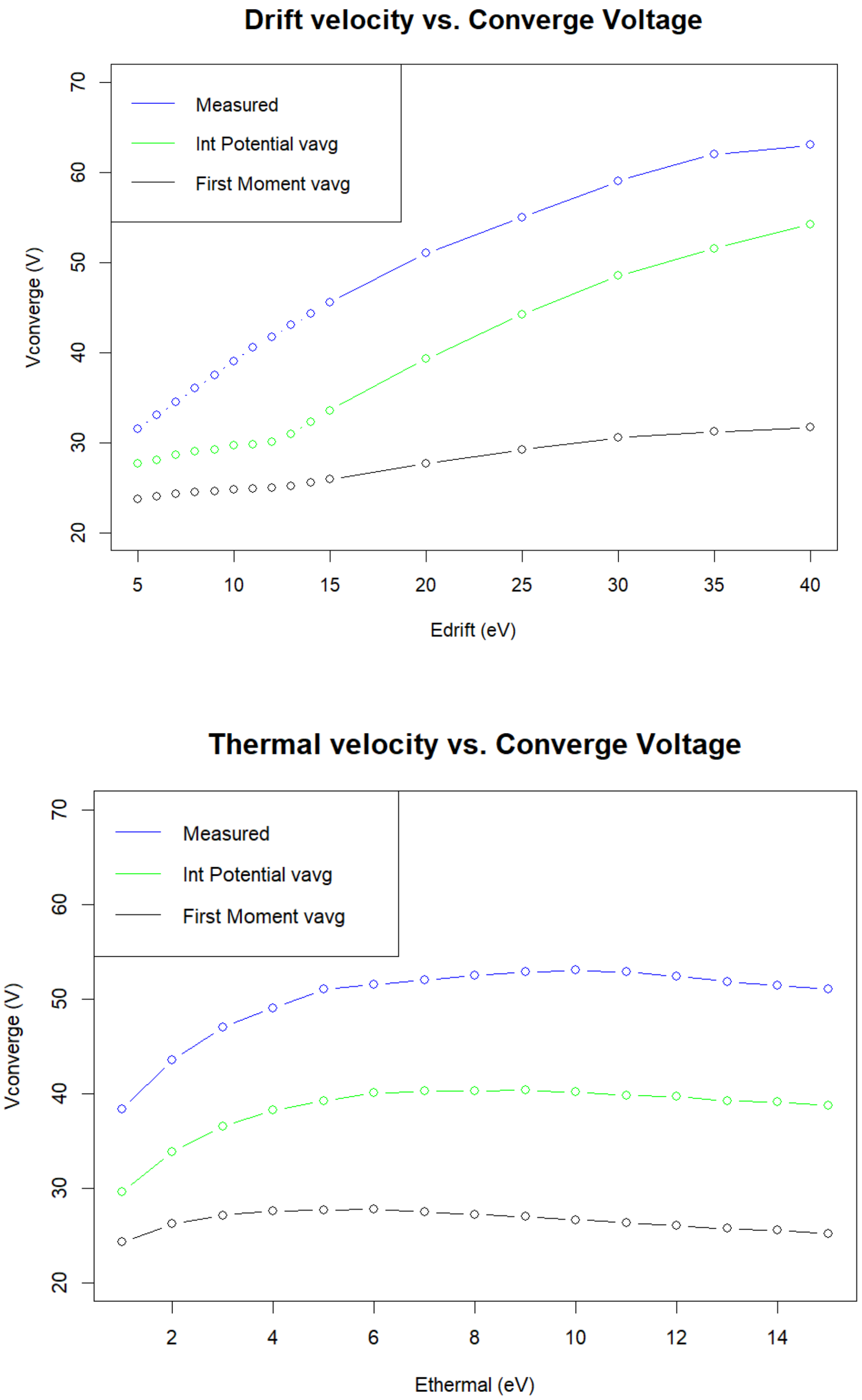

*Fig. 69*: Comparison of the XPDP1 potential values to the potential values predicted by the model equation for $V_{con}$. For this case, a constant thermal energy of 5 eV or a constant drift energy of 20 eV was used when varying the other parameter.

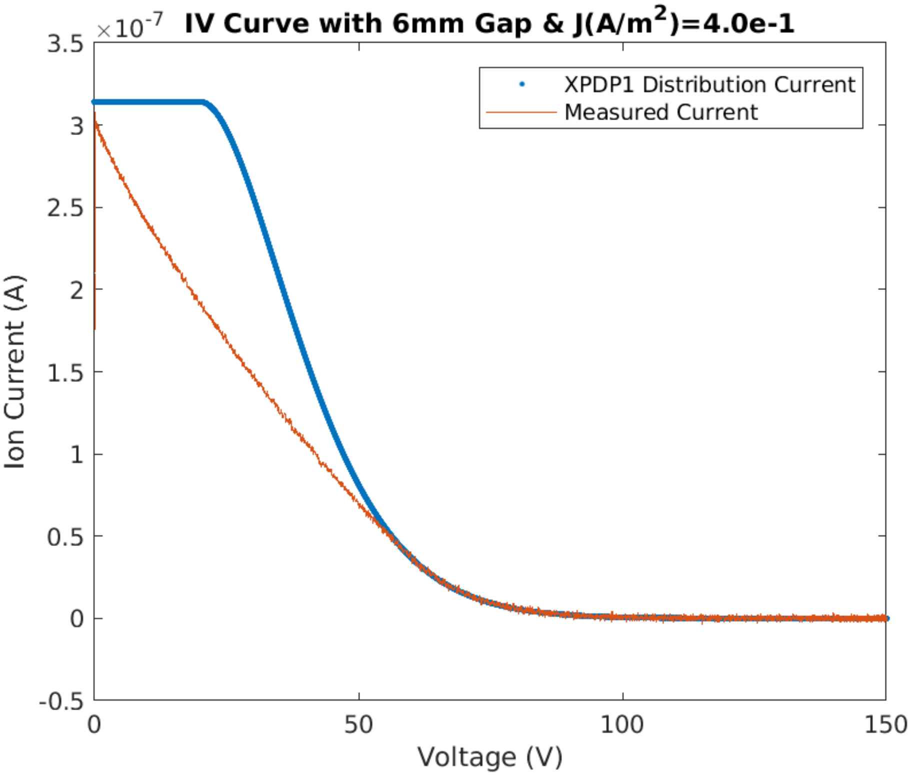

*Fig. 70*: Plot of the space charge distorted IV curve measured in XPDP1 compared to the IV curve that should have been measured based on the XPDP1 distribution. The space charge build-up here was large enough that ions were rejected immediately and no $I_{sat}$ was reached.

### 3.2.2 Compensation Results

A general discussion of the theory behind accounting for space charge distortion has been given, but it is also important to test whether truncating $K$ can actually provide the correct IEDf. As mentioned earlier, because these IV curves were obtained using XPDP1, it is possible to obtain the maximum potential generated by space charge as the discriminator-collector is swept. A comparison of the maximum space charge potential to the applied grid potential can be seen in Fig. 71. By using the initial measured potential and the measured convergence potential, it is possible to create a linear model to truncate $K$ to check how much it can compensate for space Charge (See Fig. 72). A more complex model (four-point model) can also be generated using more points from the measured maximum potential with linear fits in between each of the points.

In order to truncate $K$ using these models, the columns that correspond to the space charge potential are adjusted. For columns that are associated with an energy less than the space charge potential, the values in them are replaced with zeros (See Fig. 73). This truncation makes $K$ properly represents the idea that any ion with energy below the space charge potential is rejected. Using this truncated $K$, it is now possible to create the IEDfs.

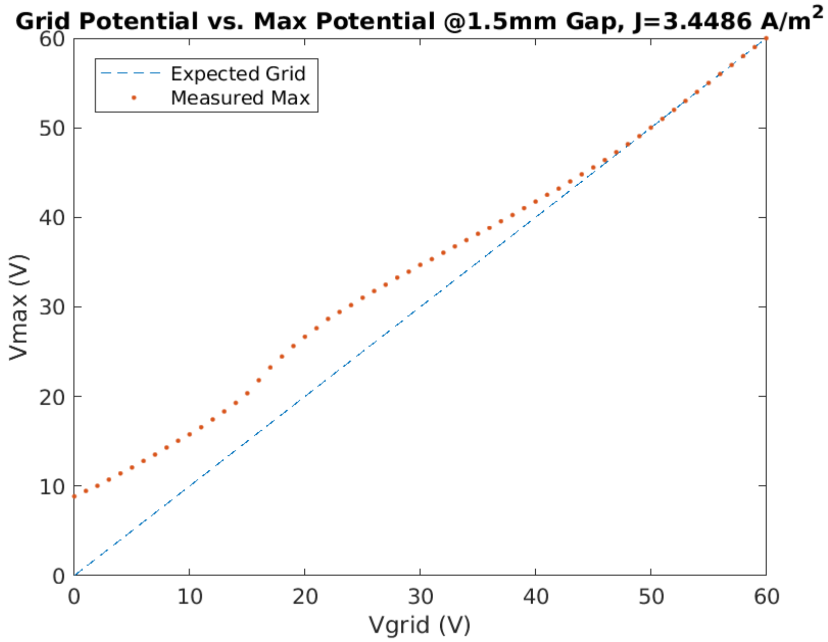

*Fig. 71*: Plot of the maximum space charge potential compared to the applied discriminator-collector potential for a space charge distortion case. As expected at lower grid potentials, the space charge potential dominates until the applied grid potential is able to overcome the potential produced by space charge build-up.

A plot of the reconstructed IEDfs can be seen in Fig. 74. This plot shows the original IEDf with the original $K$. It also presents IEDfs that were generated from a truncated $K$ using the linear model, four-point model, and the exact space charge potential measured from XPDP1. These are all plotted against the original distribution used in XPDP1. When using the linear model to truncate $K$, the results show an increase in peak energy and height closer to the actual distribution used in XPDP1. The location of the initial rise is also shifted to a higher energy that

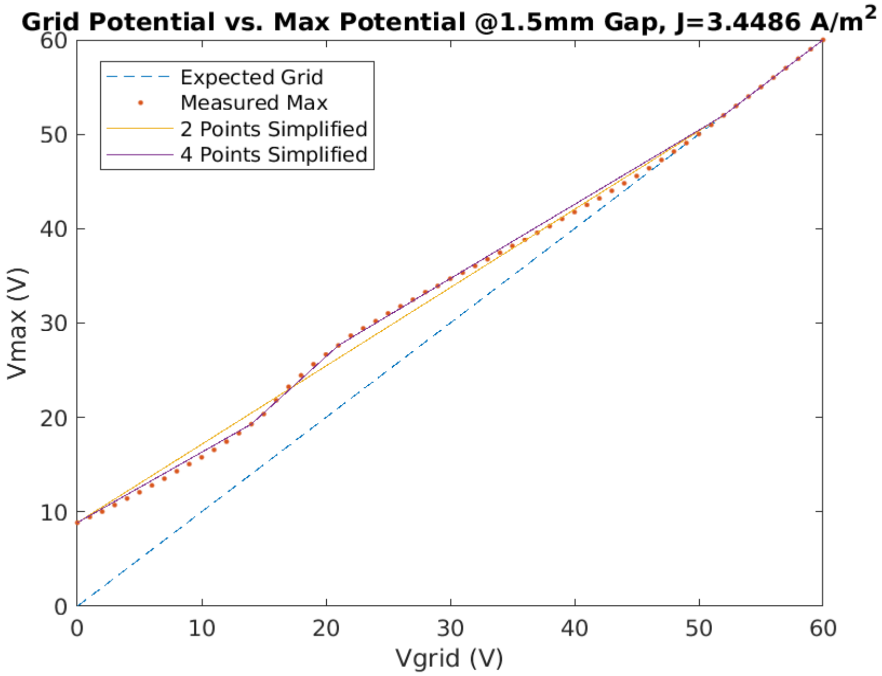

*Fig. 72*: Plot of the maximum space charge potential compared to the applied discriminator-collector potential for a space charge distortion case. The linear estimation model and four-point estimation model used to truncate $K$ that use points from the measured maximum potential are also plotted.

$$K = \begin{bmatrix} 1 & 1 & & 1 & 1 \\ .5 & 1 & \cdots & 1 & 1 \\ 0 & .5 & & 1 & 1 \\ \vdots & & \ddots & & \vdots \\ 0 & 0 & & 1 & 1 \\ 0 & 0 & \cdots & .5 & 1 \end{bmatrix} \qquad K = \begin{bmatrix} 1 & 1 & & 1 & 1 \\ 0 & 0 & \cdots & .5 & 1 \\ 0 & 0 & & 0 & .5 \\ \vdots & & \ddots & & \vdots \\ 0 & 0 & & 0 & 0 \\ 0 & 0 & \cdots & 0 & 0 \end{bmatrix}$$

*(a)* *(b)*

*Fig. 73*: Example of how $K$ is truncated using the space charge potentials to compensate for space charge distortion. (a) Original system matrix (b) Truncated system matrix.

matches the location of the actual distribution. As expected, the four-point model follows the same trend and is slightly more accurate than the linear model as it used more points from the actual space charge potential. Lastly, when truncating $K$ with the exact space charge potential measured from XPDP1, the resulting IEDf matches perfectly with the actual distribution used to assign ion energies. These results show that it is possible to account for space charge distortion

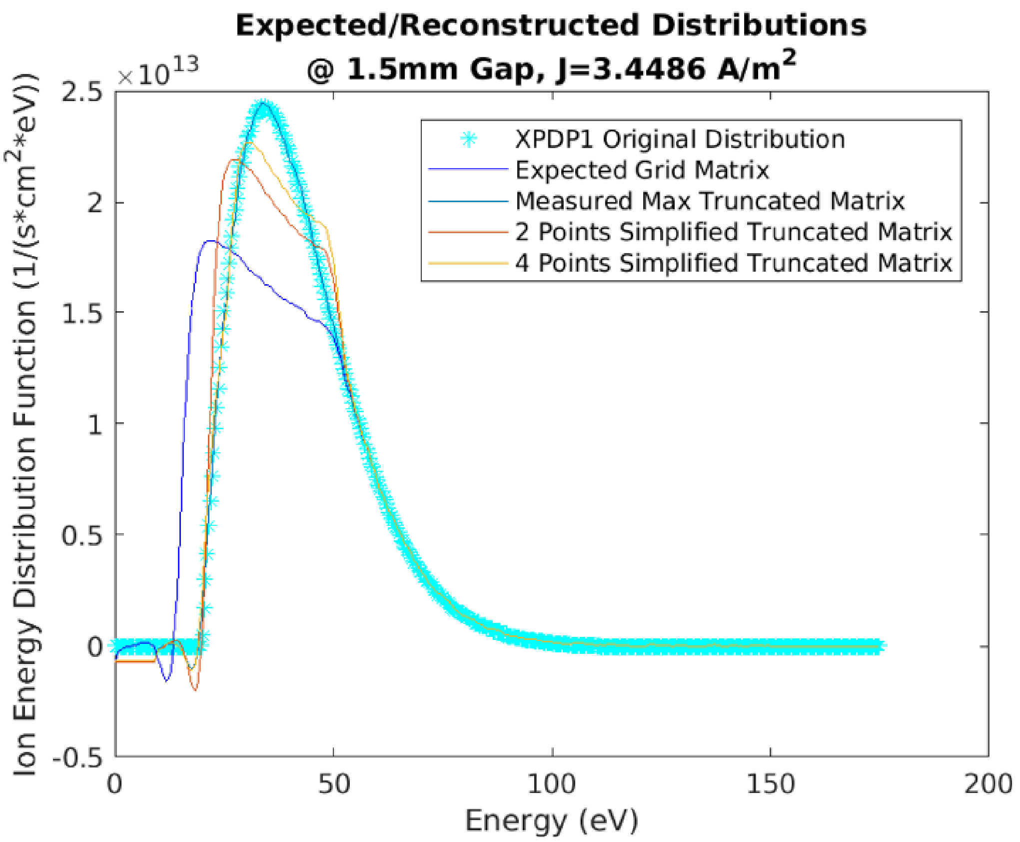

*Fig. 74*: Plot of the reconstructed IEDfs. This shows the original IEDf created from the original $K$. It also shows IEDfs generated from truncating $K$ with the linear and four-point models. An IEDf generated from truncating $K$ with the exact space charge potential is also shown. These are compared against the original distribution used by XPDP1.

in post processing by truncating $K$. By using this new capability, the RFEA is now a more robust diagnostic that can be used in a broader set of plasma and ion beam conditions.

## CHAPTER 4: RFEA WALL AND ELECTRODE MEASUREMENTS

### 4.1 Single Frequency Measurements

Where chapters 2 and 3 looked at the theoretical design analysis of RFEAs, it is also necessary to test the new RFEA design. In order to make sure the probes are working correctly, measurements under the simplest conditions were taken to compare diagnostic measurements to predictable experimental conditions. For these experiments, the top electrode was powered at 60 MHz while the bottom electrode was grounded. This made it possible to make a one to one comparison between the wall probe and the electrode probes embedded in the cathode. In this setup, the resulting IEDf is the simplest form as it is a single peak per gas species. A single peak in an RF driven plasma is not necessarily expected since the plasma potential $(V_p)$ oscillation should cause a sheath oscillation at a grounded surface. Sobolewski, Wang, and Goyette [ 15 ] used an energy analyzer-mass spectrometer to measure the IEDf from a grounded surface. Their results show that, at sufficiently low frequency, a RF potential forms across the grounded sheath creating a dual peak bimodal IEDf. The single peak in this work is likely the result of two factors. The first is that the RF potential across a powered sheath decreases with increasing drive frequency. The second is that there is large chamber asymmetry since everything but the powered electrode and alumina or quartz insulators reside at ground (e.g. bottom electrode, chamber wall, pumping baffle, etc.) With a 60 MHz RF source in combination with the chamber asymmetry, the RF potential across the grounded sheaths is likely small so the ion acceleration is caused only by the difference between $V_p$ and ground. Hence, single species peak IEDfs are measured by the RFEAs at grounded surfaces. Having a single species peak is advantageous though, as makes it easier to compare the shape and peak locations of the IEDfs measured by not only the electrode probes but also with a commercial RFEA system such as the Impedans Semion Probe [ 5, 32, 86 ].

A single frequency experimental configuration also simplified the filter requirements for the measurement signal. With only the 60 MHz electrode powered and the probes surrounded by ground, only a small amount of the 60 MHz signal (0.1 – 1 V amplitudes) was able to make it on to the RFEA signal lines. As the 60 MHz signal was small and low power, it was easily removed from the RFEA signal lines using commercial in-line non-dissipative low pass filters (MiniCircuit BLP-1.9+). These filters were added to the plasma electron rejection grid and discrimination grid lines as these lines and the attached electronic equipment seemed to be affected the most by the 60 MHz signal. Most notably, the signal would affect the Ultravolt amplifier operation by changing the initial offset on the output of the amplifiers. The 1000:1 amplifier typically output 5 V and the 500:1 amplifier output 1.5 V when not sweeping voltage. When the plasma was turned on with the 60MHz RF generator, these values would jump up into the tens of volts. This did not represent a huge problem as the offsets could be accounted for in measurement software. In addition, DC offsets are easily factored out since the extraction of the IEDf is essentially a differentiation of the IV characteristic that is immune from DC offsets, but it was better to remove the signal so as to not cause any other issues. Additionally, observation of trends of the DC offsets may indicate additional capabilities of this diagnostic. One such possibility is the estimation of fast neutral flux via secondary electron emission current from the collector generating an additional DC offset. Therefore, there is motivation to minimize these drifts. The 60MHz signal on the collector line appeared to have no effect on the IV curve and very little effect on the Ultravolt amplifiers so a filter was not added to this line.

Lastly, to keep the measurement simple, the plasma generated consisted only of argon (Ar) at pressures typically between 5 – 40 mTorr. This noble gas is easy to strike and forms a stable plasma over a wide operating regime. It has also been used extensively in previous work to analyze plasma and plasma chamber characteristics [ 1 2 3, 5, 6, 23, 29, 32, 41, 60, 75, 77, 80 ]. Using a single gas simplifies the IEDf even more to just one single peak as there are no other ions accelerated at different rates caused by mass differences. By keeping the IEDf as simple as possible, it makes it easier to verify that the RFEAs are working properly and providing the correct information. Additionally, the non-reactive nature of Ar gas mimimized component erosion, particularly in the RFEA, eliminating any potential drift due to hardware degradation.

The downside of Ar, in comparison to conditions that this system would normally operate under, is that it is not generally representative of the combination of density and ion energy flux that more complex process gases present during operation. Additionally, as will be shown in other experiments, Ar's non-reactive characteristics lend itself to sputter deposition on low potential surfaces under conditions with substantive powered bias potentials.

### 4.1.1 RFEA Validation

In order to validate the measurements from the TEL RFEAs, it was necessary to compare the IEDfs they measured to the measurements from a commercial RFEA system (Impedans Semion RFEA). The IEDf comparison consists of using the TEL RFEA wall probe (WP) (See Fig. 75), the TEL RFEA surface mount (SM) (See Fig. 40) probe, and the Impedans Semion probe. For this setup, the Impedans Semion probe was mounted along the wall of the chamber to give the best comparison to the WP (See Fig. 76). When mounting it to the wall, it also ensured a chamber ground connection for the probe housing and floating (1st grid) since the WP and SM 1st grids are both at chamber ground. The filter and measurement electronics from this probe were also attached to the WP to see how the TEL RFEA works with a commercial measurement system (See Fig. 77). This setup is labeled as the "Hybrid". For this validation measurement, a 5 mTorr Ar plasma was generated and multiple measurements were taken at different 60 MHz powers.

The resulting IEDfs from the measurements can be seen in Fig. 78 and Fig. 79. In these plots, the IEDfs were normalized by their respective peak energies so that the peak location and curve shape could be more easily compared. As expected, the IEDfs measured contain a single peak. The peak energies are also reasonable for the plasma conditions. Since the probes are taking the IEDf measurement at chamber ground, the energy that is measured should be

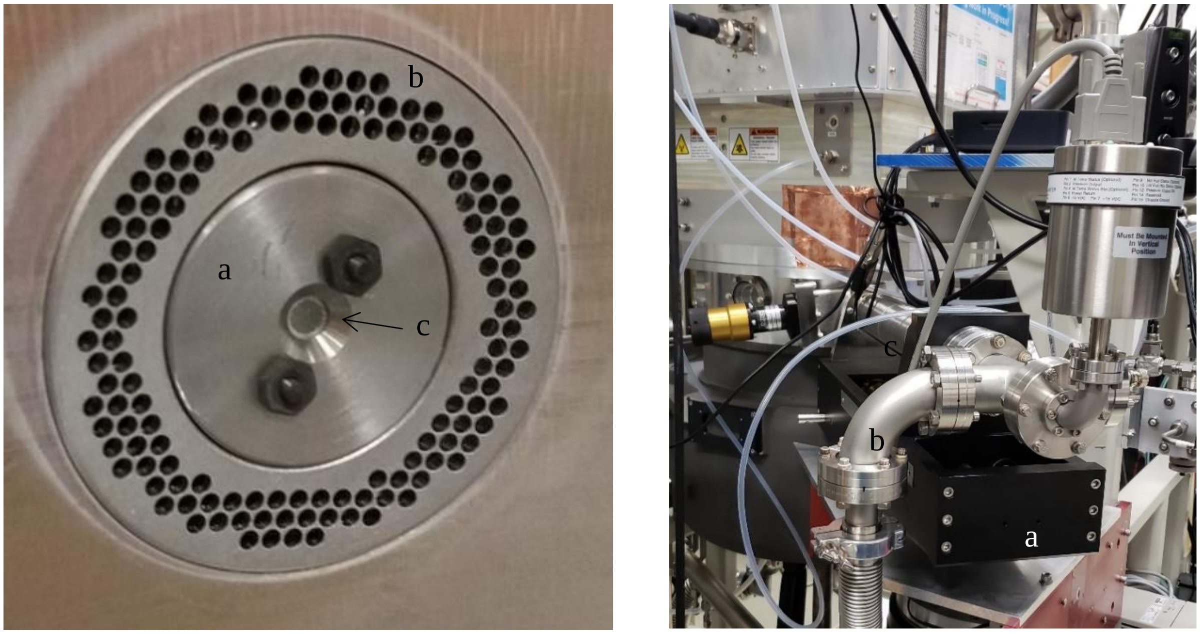

*Fig. 75*: Pictures of the TEL RFEA wall probe (WP). (Left) Picture of the front of the grid in the wall of the chamber (a) Ground cover that covers the probe and attaches to the differential pumping shaft (b) Port cover to prevent light-up down the outside of the differential pumping shaft (c) Floating (1st) grid (Right) Picture of the WP housing on the outside of the chamber (a) Linear stage that moves the probe in and out of the chamber (b) differential pumping line (c) Bellow that covers the differential pumping shaft on which the RFEA is mounted.

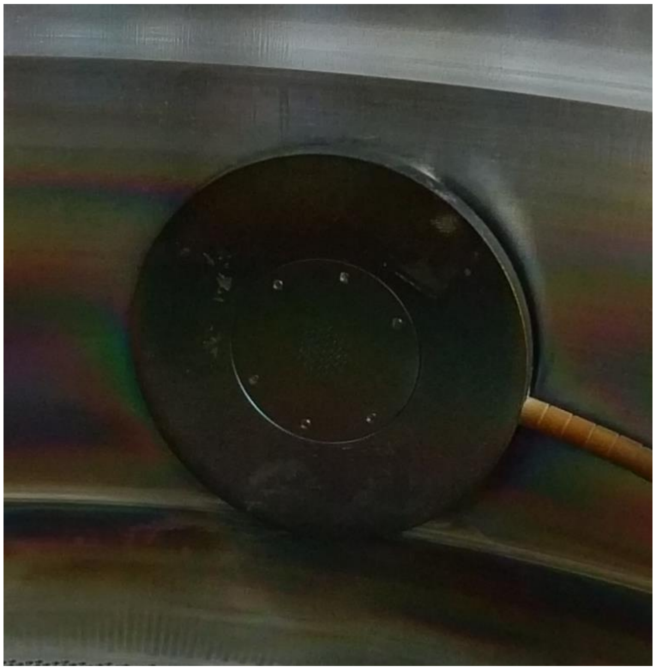

*Fig. 76*: Picture of the Impedans Semion probe attached to the chamber wall

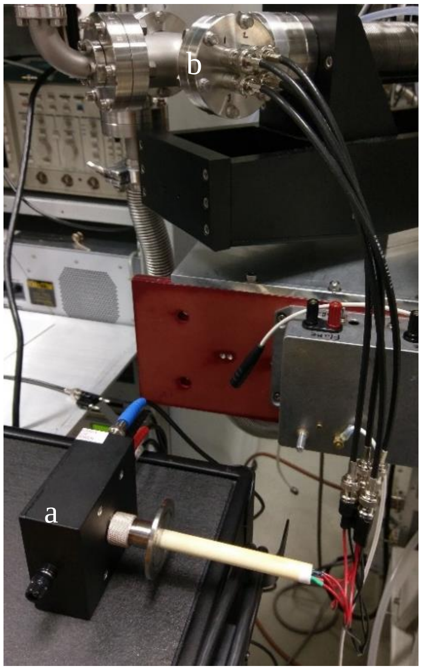

*Fig. 77*: Picture of the Impedans Semion filter box rigged to the WP (a) Impedans Semion filter box (b) WP vacuum transition

comparable to the plasma potential. Between the different probes, the peak locations vary somewhat from one another. The peak locations in the other measurements not shown also varied but as in this case, the variation was always less than 10 eV from one another. The variation in these peak locations may be due to plasma non-uniformity as the probes are located in different locations around the chamber. The Impedans Semion probe setup is also slightly different because it is not completely enclosed by the chamber ground. Because the probe is a flat disc and the chamber wall is curved, the probe was not completely flush with the wall. In some instances, plasma was able to form in the space between the probe and the wall. This may have had an effect on the measurement. There also seems to be a little variability in the measurement electronics as the hybrid probe and the WP measurements don’t match exactly. As expected, when power was increased from 400 W to 700 W, the peak energy increased. It was

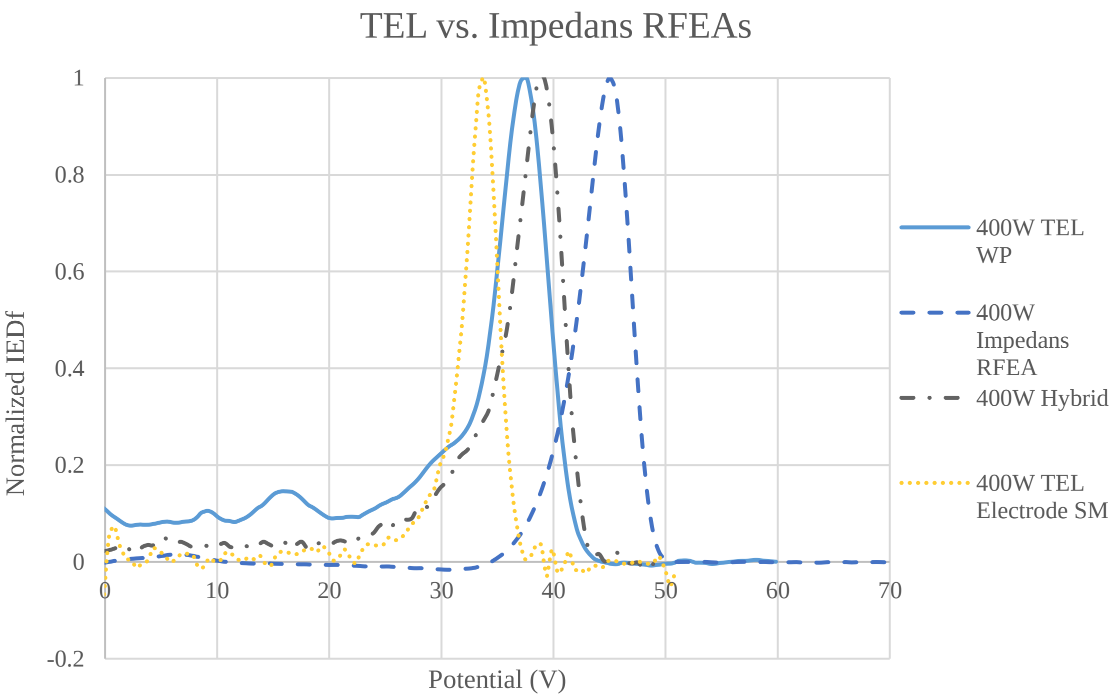

*Fig. 78*: Normalized IEDfs from the TEL RFEAs and the Impedans Semion probe. These measurements were obtained from a 5 mTorr Ar plasma for 400 W 60 MHz RF. The probes were taking measurements at chamber ground.

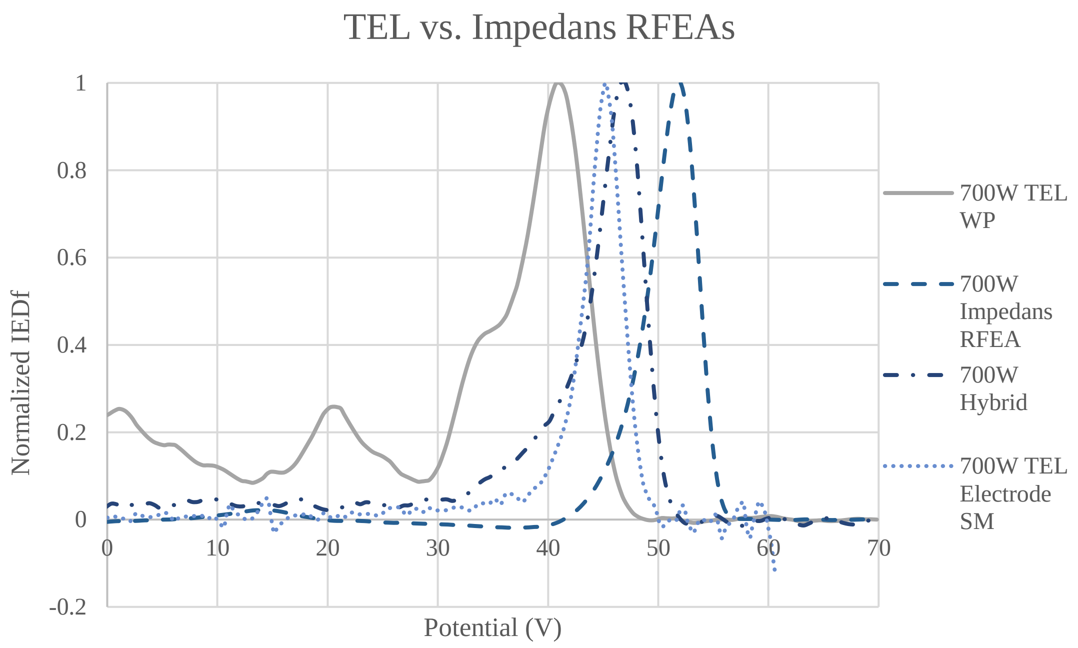

*Fig. 79*: Normalized IEDfs from the TEL RFEAs and the Impedans Semion probe. These measurements were obtained from a 5 mTorr Ar plasma for 700 W 60 MHz RF. The probes were taking measurements at chamber ground.

not a substantial increase, but the peaks did shift anywhere from about 5 eV to the extreme case with the SM probe that shifted about 11 eV. Again, the variation in the shifts is likely due to plasma uniformity issues.

The shapes of the IEDfs are also quite similar. Each IEDf is slightly asymmetric with a larger low energy tail. Since the pressure is at 5 mTorr, collisions are unlikely but not completely nonexistent. This could be the cause of the asymmetric low energy tail. The post processing used to obtain the IEDfs will also have an effect on the shape. The Impedans Semion electronics take care of producing the IEDf from the IV curve. With the TEL electronics, only the IV curve is measured and then a regularized least squares (RLS) solution method (See Section 2.4) was used to obtain the IEDf. The difference in the analysis methods used will cause a slight variation the shape of the curves. This is also evident in the fact that the shape of the hybrid IEDf is almost exactly the same as the shape of the Impedans Semion probe. As they both used the same electronics and post analysis, this is expected. In general though, these IEDfs are consistent in shape and peak location. This signifies that the TEL RFEAs and electronics are operating correctly and can provide a correct IEDf.

### 4.1.2 IV Curve Characteristics

Having the confirmation that the TEL RFEAs are operating correctly makes it possible to take a closer look at the characteristics of the IV curves generated by the TEL RFEA. As this is a newly designed probe and housing system (differential pumping shaft and 3D printed electrode), there will be issues that were unaccounted for in the theoretical analysis. These issues were found in the characteristics of the IV curve after measurement. Some characteristics pointed to major problems that needed to be address while others were observations to note about the measurement. By analyzing these characteristics, a better understanding of the plasma and the RFEA was obtained. A knowledge about the plasma and the RFEA helps further the understanding of measurements taken in dual frequency operation or complex gas mixtures. It also aids when making recommendations for future iterations of probe design.

The first interesting IV curve characteristic found was during measurements with the WP. When taking measurements with the WP using the 60MHz RF source, the IV curves showed a double drop-off feature that one would expect from an RFEA measurement taken at a powered electrode (See Fig. 80). The first drop-off occurred when the discriminator was at negative voltages. One other characteristic about these drop-offs was that it would track with the voltage applied to the plasma electron rejection grid. To understand the mechanism between the grids to cause this phenomenon, conductance calculations were performed to estimate the pressure between the grids. The conductance calculations showed that pressure between the 1st grid and 2nd grid was approximately 30 mTorr. For accuracy, when comparing the conductance

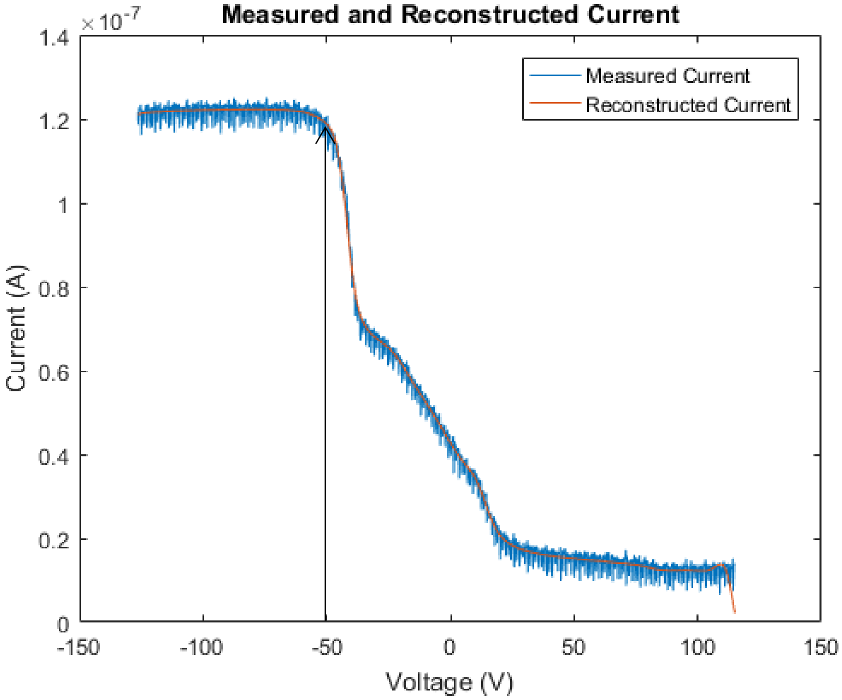

*(a)*

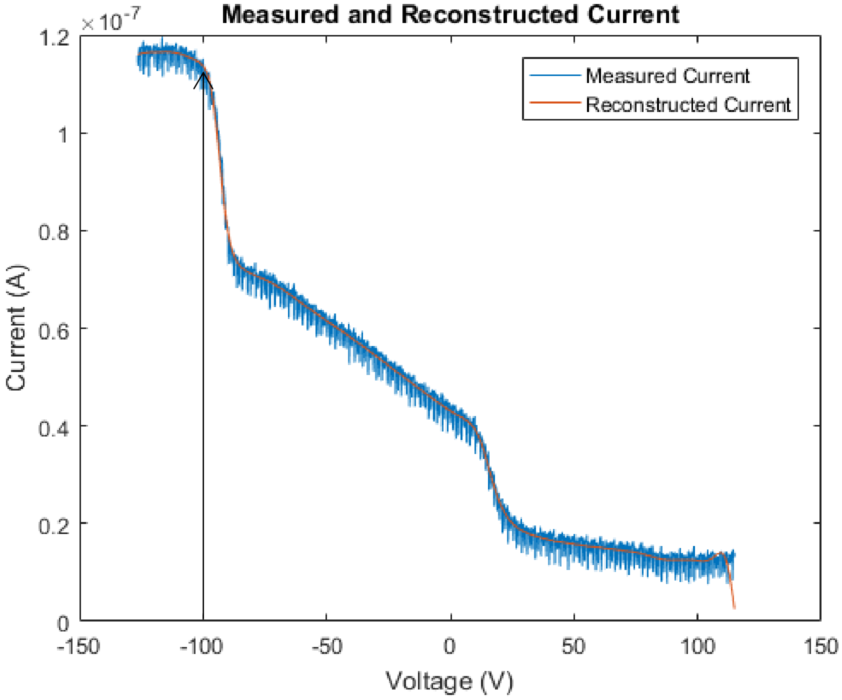

*(b)*

*Fig. 80*: IV curves taken with the WP for a 40 mTorr Ar plasma for 300 W 60 MHz RF source. (a) In this measurement, the plasma electron rejection (2nd) grid was set to -50 V. (b) In this measurement, the 2nd was set to -100 V. The first drop-off tracked with the 2nd grid voltage. It was determined this was due to plasma light-up in the probe.

calculations at a specific location in the differential pumping line to a Baratron measurement, the calculations were only about 8% off from the measured value. Therefore, 30 mTorr is a good estimate of the pressure between those grids.

The pressure between the grids was that high due to the way the RFEA housing was designed. The probe was mounted on the end of the differential pumping shaft and the ground cover was placed over the RFEA with the floating grid as the only entrance to the probe and differential pumping shaft (See Fig. 75 (a)). Since the 1st grid is the only entrance to the RFEA and differential pumping shaft, everything had to be pumped through the probe which made the pressure high between the grids. At that pressure, the mean free path is about 1 mm for Ar. The probe itself from the 1st grid to the collector is 0.135" (3.43 mm). This means that there are collisions occurring in between the grids. Since collisions are occurring in the RFEA, it was determined that this first drop-off was likely due to light-up. When there was no plasma in the chamber, the IV curve generated from a voltage sweep only showed the noise resolution of the DMMs used. Since no current from a plasma was being sent to the collector, this is the expected result. Thus, the potential difference across the grids was not causing the light-up. This IV curve characteristic only occurred when a plasma was in the main chamber and at high pressure between the grids. This points to light-up likely being caused by ionization due to secondary electron emission from the grids.

The light-up of the probe was a major issue. Due to the mean free path limitation of the Ar ions, the probe could only be run up to a chamber pressure of about 10 mTorr. This is a very limiting threshold as many industrial processes run at higher pressures than this. To fix this problem, there were two options. The first was to reduce the number of grid holes in the 1st grid. This was attempted but the current entering the probe became negligible, so it was not possible to make a measurement. The second option, which was implemented, was to adjust the ground cover and the differential pumping shaft. In this process, the diameters of the both the ground cover and differential pumping shaft were increased (See Fig. 81 and Fig. 82). In the initial design, the ground cover diameter was large enough so that it snuggly fit around the RFEA base and the differential pumping shaft diameter was small to limit plasma perturbation in the event the probe is extended into the bulk plasma for a measurement. Both designs limited the conductance and pumping that could occur through the probe. In the new design, the ground cover height was also increased so that it no longer attaches to the 1st grid of the RFEA. Grid holes were machined into the ground cover with the same hole diameter and pattern as the grid holes in the RFEA (See Table 2 and Fig. 17). The only difference is that the fill diameter was decreased to 0.069" (1.75 mm). The grid was created in the ground cover so it, and not the RFEA

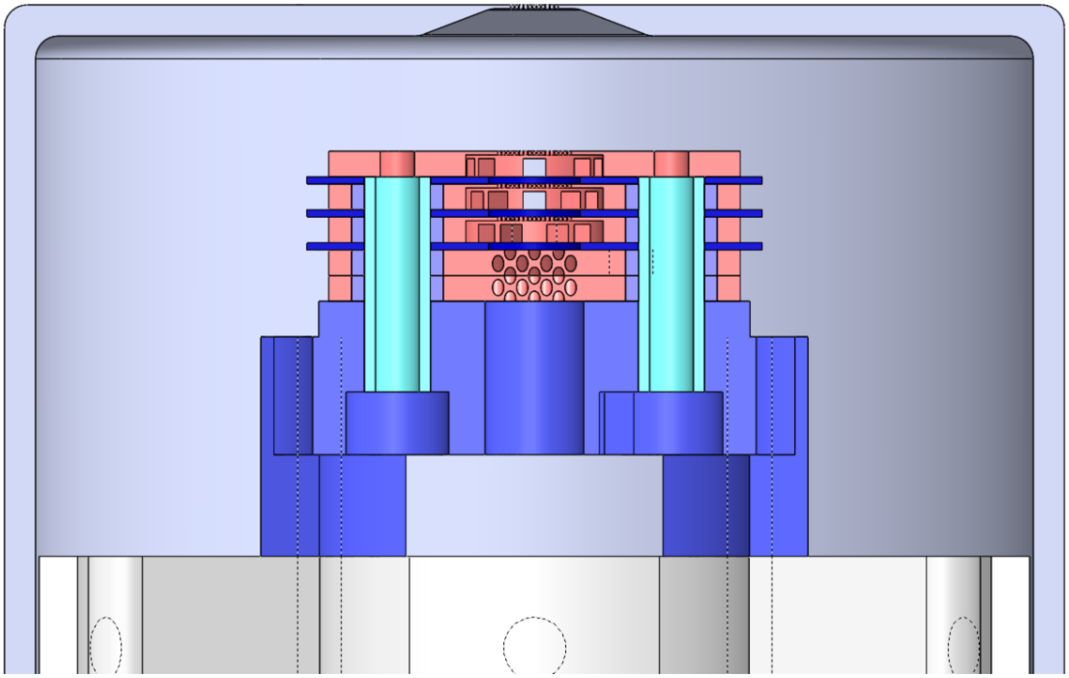

*Fig. 81*: SolidWorks model of the new WP assembly. It shows the expanded ground cover so now differential pumping does not have to occur through the probe but can pass around it.

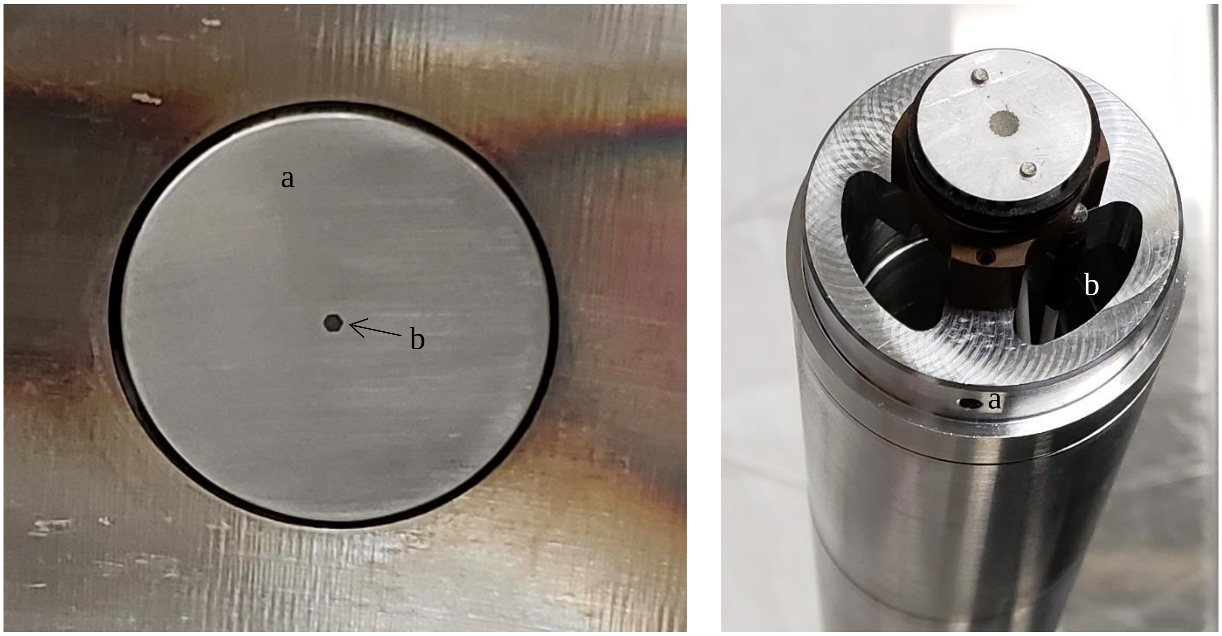

*Fig. 82*: Pictures of the new WP. (Left) Picture of the new WP at the inner chamber wall (a) New ground cover that no longer requires the port cover to prevent light-up down the outside of the differential pumping shaft (b) Grid machined into the ground cover that acts as the main differential pumping limiter (Right) Picture of the RFEA mounted to the modular differential pumping shaft (a) Screw connection to attach the ground cover (b) Openings to allow for pumping around the probe.

grids, would become the main conductance limitation in the pumping path. As opposed to the original design, this new one does not force the pumping through the detector but can pump around the detector. This made it possible for the WP to operate at higher chamber pressures.

Conductance calculations were also performed on this new design. For a 40 mTorr Ar plasma, where the calculated pressure was approximately 30 mTorr between the 1st and 2nd grids, the calculated pressure for the new design was approximately 4 mTorr. Based on the ion mean free path for Ar and the additional length added by the new WP design, the WP could operate up to 40 mTorr and retain a remote chance of collisions. To determine the accuracy of these calculations, Baratron measurements were used as a comparison just as with the old WP design. Multiple Baratron measurements were made for a pressure range of 5 – 40 mTorr. When compared to the pressure from the conductance calculations, the average error in the calculated pressure to measured pressure was about 11%. The error got larger as the pressure increased but the conductance calculations always overestimated the pressure meaning the actual pressure around the RFEA was likely less than what was calculated. This error measurement provides good confidence that the conductance calculations provide a reasonable estimate of the pressure around the new WP design. Unless otherwise stated, all future WP measurements presented were done using this new WP design.

Another interesting IV characteristic involved the electrode probes below the drift cones (i.e. top mount (TM) and floating (F) probes). When taking measurements with the probes below the drift cones, a linear trend was found in the ion saturation current $(I_{sat})$ region (See Fig. 83). This linear trend would only occur to a specific voltage at which point the $I_{sat}$ would level off until the discrimination grid started limiting the current to the collector. The point at which the linear trend would stop seemed to track with the magnitude of the offset applied between the

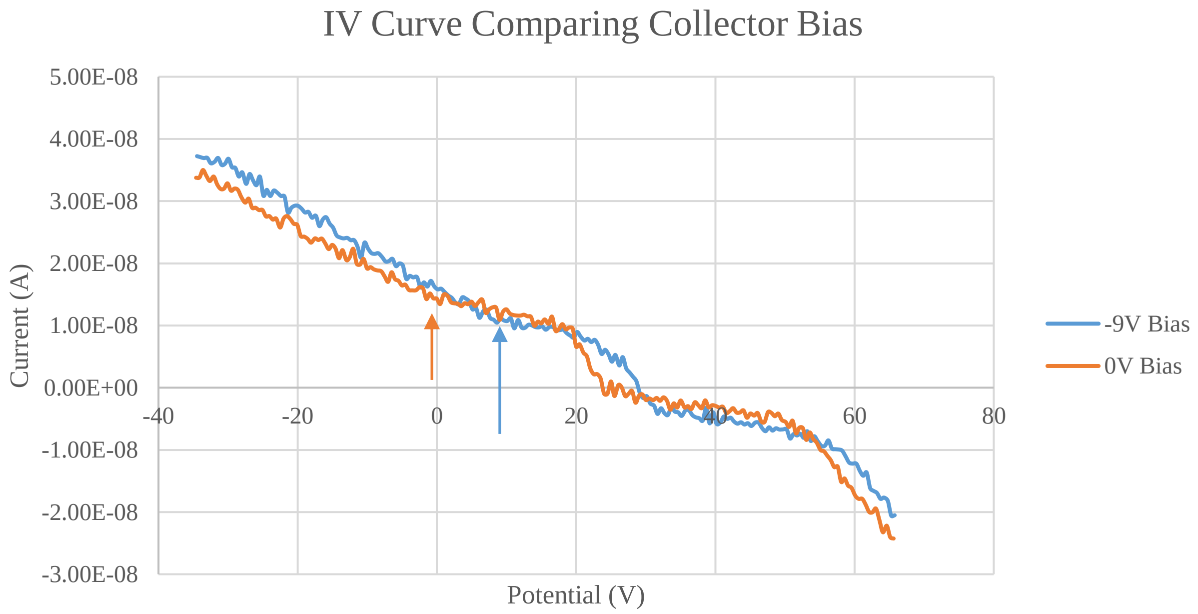

*Fig. 83*: Plot of two IV curves based on the bias applied between the discrimination grid and the collector. A linear trend is seen in the ion saturation current region up until 0 V or 9 V. The arrows approximately point to these two locations. These are the moments that the collector becomes positive so ions outside the probe are no longer attracted to the collector.

discrimination grid and the collector. As was mentioned previously in section 2.3, the discrimination grid and the collector were tied together so that the potential to one was applied to the other. A battery was then added in series with the collector to offset the potential of the collector in reference to the discrimination grid slightly. This created an electric field between the two grids that would accelerate ions toward the collector at any potential but only provide a minimal amount of acceleration.

The reason the trend tracked with this offset was because it was caused by ion current collection from outside the RFEA. Initially, when designing and planning out the drift cone concept, the ions entering the drift cone were always imagined as a uniform beam. However, in reality, any beam as it travels will have a certain amount of expansion, especially when the particles of the beam are all the same charge. This means that as the ions enter into the drift cone cavity, they will begin to expand whether due to an initial radial velocity component or from Coulomb repulsion. As the beam expands and travels down the drift cone, some of the ions will enter through the 1st grid of the RFEA, some will collide with the solid surfaces of the RFEA or its mounting apparatus, and some will travel through an opening around the outside of the RFEA (See Fig. 84). As ions travel around the outside of the RFEA, they will still experience electric fields generated by the different potentials applied to the grids because they are exposed. As a result, ions will be attracted and collected from outside the RFEA when the discriminator sweep is in a regime where the offset makes the collector negative. When the potential becomes more negative, it will attract more ions which is why a linear trend was created.

There was a simple solution to fix this issue. The polyimide insulator between the discrimination grid and the collector was replaced with a Vespel SP-1 insulator that not only separated the discriminator and collector, but also covered the collector (See Fig. 85). A step was

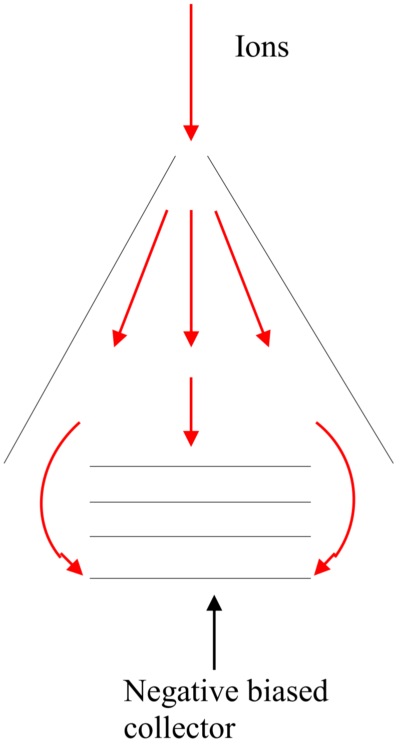

*Fig. 84*: Picture of the ion beam expansion around the drift cone. It also represents that ions outside the RFEA will be picked up by the collector when it is negatively biased.

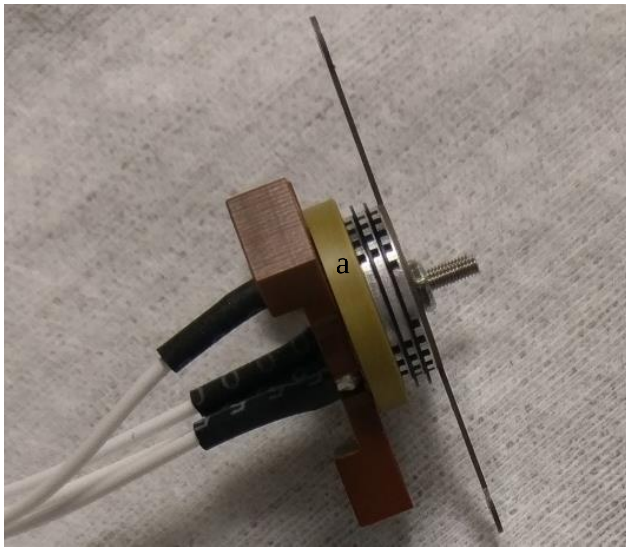

*Fig. 85*: Picture of the top mount (TM) probe with a Vespel SP-1 cover (a) around the collector. These covers were placed not only on this RFEA, but also the floating probe (F) and new wall probe (WP) to prevent ion current from being collected outside the detector.

made in the cover so that a portion of it would also cover the polyimide base of the RFEA. Hence, there was not a simple straight path to the collector and any ions attracted to the collector would hit the Vespel SP-1 insulator. As the new design of the WP also allowed ions to travel around the RFEA, one of these covers was also placed over the collector of this sensor as well. Using these covers, the linear trend in the $I_{sat}$ region that tracked with the offset potential of the collector of the IV curves was removed.

The next consistent trend found in the IV curves deals with the region at which all ions are rejected by the discriminator. In this regime, an ideal IV curve from a RFEA will be flat with a current value measured at 0 A (or at least the minimum current the measurement equipment can resolve). An example of this can be seen in Fig. 58 - Fig. 60. However, in the case of the TEL RFEA, this current region was flat but typically was offset from 0 A. An example of this can be seen for the new WP in Fig. 86. Since this current is positive, it must be the loss of electrons from the collector. Since the discrimination potential is high enough to reject all the ions, the loss of electrons cannot be due to ion collection. The only other option that could cause electron loss from the collector is secondary electron emission due to neutral particles. Since they are neutral, these particles are not affected by any of the electric fields in the RFEA. Böhm and Perrin [ 80 ] discussed this offset found in RFEA measurements for a 27 mTorr Ar plasma. They also claimed the offset was caused by neutral particle and identified possible culprits as photons, fast neutrals, and metastables.

To determine which particle was likely the cause of the secondary electron emission, the solid angle from the 1st grid from the collector was determined. This calculation was helpful because other than the fast neutrals, the other neutral particles are isotropic. If the solid angle to the collector is small, then it would be unreasonable for a sufficient number of photons or

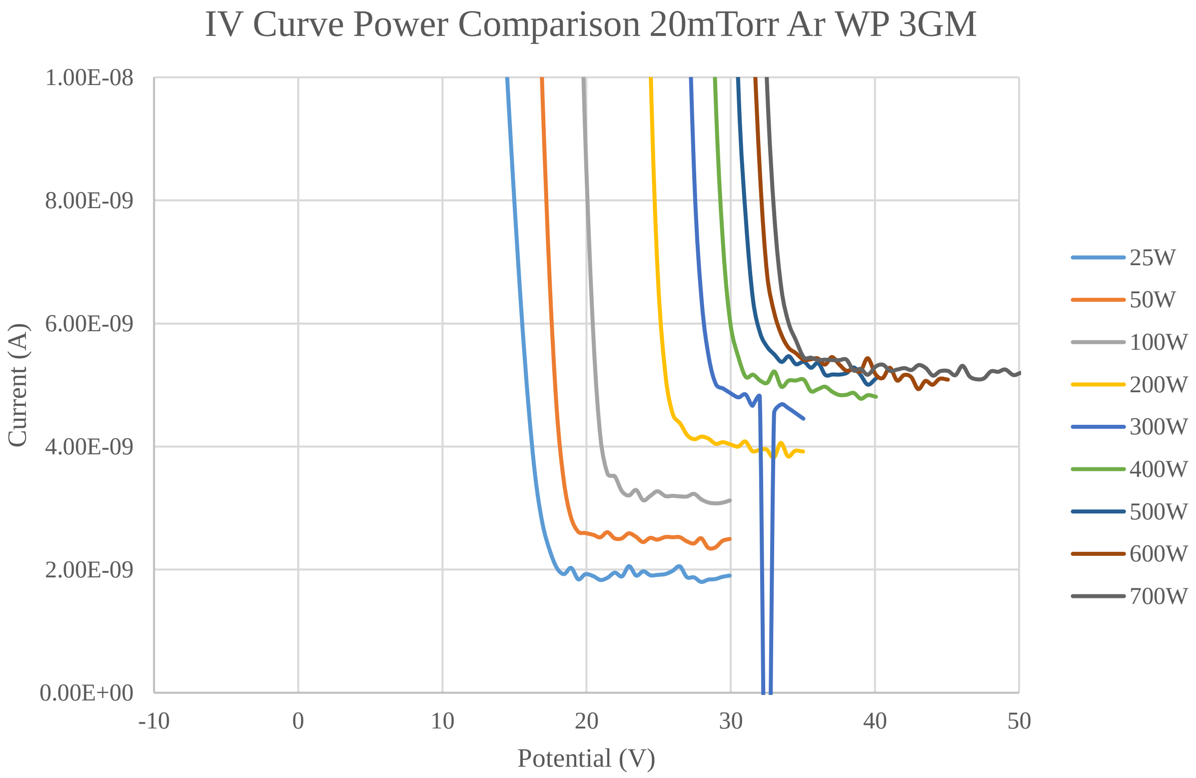

*Fig. 86*: Zoomed in plot of IV curves obtained with the new WP for 20 mTorr Ar at different 60MHz RF powers. It can be seen here that the no ion current region is relatively flat but there seems to be an increasing offset of the IV curve from 0 A. This offset is due to secondary electron emission off the collector due to fast neutrals entering the probe.

metastables to cause a measurable amount of secondary electron emission. The solid angle from the 1$^{st}$ grid to the collector is 0.116 steradians. This is very small and only 0.93% of a full solid angle represented by isotropic motion. This leads to the conclusion that the secondary electron emission is due to fast neutrals.

Fast neutrals are formed when an accelerated ion heading towards the collector experiences resonant charge exchange with a neutral atom [ 49, 54, 55, 110 - 112 ]. In this process, the fast ion leaches an electron from the neutral atom becoming a fast neutral. The cross-section for this process is dependent on the energy of the ions. It typically occurs at lower energies but charge exchange cross-sections have been measured at energies from 82 eV to 100 keV [ 54, 111 ]. As the fast neutral retains its motion, it eventually reaches the collector retaining its high energy and causes secondary electron emission. This emission is consistent no matter the potential applied to the discriminator and the plausible cause of the offset in the IV curves.

To check if this is the case, some simple calculations were performed to compare two different WP measurements at different pressures. The IV curves used can be seen in Fig. 87. The IV curves were obtained from a 300 W Ar plasma with a grounded bottom electrode at two different pressures. For the 20mTorr case, the three-grid mode (3GM) described in this work was used. For the 5mTorr case, a four-grid mode (4GM) was used which means a secondary electron rejection grid (4th) was inserted between the discriminator and collector. This 4th grid repels any secondary electrons from the collector back to the collector. Therefore, the $I_{sat}$ for the 5 mTorr case was not altered due to secondary electron emission. By accounting for secondary electron emission in the 20 mTorr case, the total $I_{sat}$ for this case should be somewhat similar to the $I_{sat}$ in the 5 mTorr case. To account for the secondary electron emission, the first step was to determine the neutral current $(I_n)$ reaching the collector. This was estimated by:

$$I_n = \frac{I_{off} - I_{res}}{\gamma} \tag{34}$$

where $I_{off}$ is the 20 mTorr offset current, $I_{res}$ is the DMM current resolution, and $\gamma$ is the secondary electron emission coefficient. Values for the DMM current resolution and secondary electron emission coefficient for aluminum [ 80 ] can be seen in Table 6. Once $I_n$ is determined, this value was added to the $I_{sat}$ measured in the 20 mTorr case in order to obtain the total 20 mTorr $I_{sat}$ (See Table 6). This value was compared to the 5 mTorr $I_{sat}$. From this analysis, the total 20 mTorr $I_{sat}$ is on the same order of magnitude as the 5 mTorr $I_{sat}$ and reasonably close for a first order estimate. This analysis provides confidence that the offset is caused by secondary electron emission from the collector due to fast neutrals.

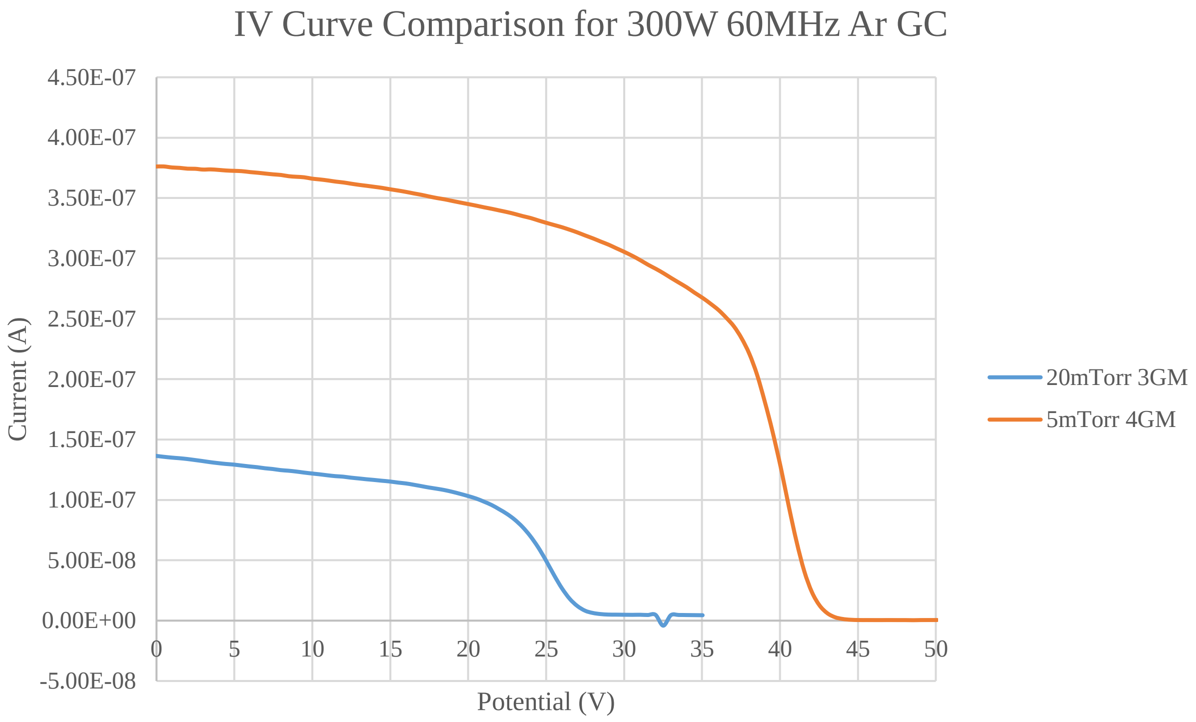

*Fig. 87*: IV curve comparison for WP measurements at two different pressures and different RFEA operation modes. The 4GM stands for four grid mode where a secondary electron rejection grid was used in between the discriminator and the collector. The 3GM stands for three grid mode which is the normal operation used in this work.

*Table 6*: Values used in the estimation of the true $I_{sat}$ for the 20 mTorr WP measurement. It also presents the values for the 20 mTorr neutral current $I_n$, the total 20 mTorr $I_{sat}$, and the 5 mTorr $I_{sat}$.

| | |
|---|---|
| DMM Resolution | 6 x $10^{-10}$ A |
| Secondary Electron Emission Coefficient for Aluminum | 0.05 |
| 20 mTorr $I_n$ | 7.9 x $10^{-9}$ A |
| Total 20 mTorr $I_{sat}$ | 2.2 x $10^{-7}$ A |
| 5 mTorr $I_{sat}$ | 3.8 x $10^{-7}$ A |

Another analysis method that was also used was to estimate the portion of the 5 mTorr $I_{sat}$ that would experience a charge exchange collision traveling from the entrance of the WP to the collector. To do this, the charge exchange cross-section from Lieberman and Lichtenberg

[12, 112, 113] was used with the conductance calculations for the WP (See Table 7). Using the pressure in the WP and the charge exchange cross-section, the mean free path was calculated (See Table 7). This mean free path was compared to the distance the ions must travel from the entrance of the WP to the collector in the RFEA. In this analysis, it was assumed the sheath distance was negligible compared to the distance from the entrance to the probe collector. Since the mean free path represents the idea that an ion will have had a collision over that distance, it was compared to the probe distance to calculate the probability that an ion will have had a charge exchange collision while traversing the probe. From the values in Table 7, the probability of collision was 18.5%. Multiplying this by the 5 mTorr $I_{sat}$ gave an estimate for $I_n$ (See Table 7). The $I_n$ calculated in this method is also on the same order of magnitude as the $I_n$ shown in Table 6. These values are only off by approximately 12% again showing that the offset is likely due to secondary electron emission from fast neutrals colliding with the collector.

*Table 7*: Values used in the estimation of the neutral current ($I_n$) from the 5 mTorr $I_{sat}$ based on the charge exchange collision percentage. This shows the WP pressure, the charge exchange cross-section, the mean free path of the Ar ions, and the distance to the collector of the WP.

| | |
|---|---|
| WP Pressure | 2 mTorr |
| Charge exchange cross-section for Ar at 25 eV [ 12 ] | 3.40 x$10^{-15}$ cm$^2$ |
| Mean Free Path | 4.5 cm |
| Distance from WP entrance to the collector | 0.828555 cm |
| $I_n$ based on collision percentage | 6.9 x $10^{-8}$ A |

The discrepancy between these calculations and measured $I_{sat}$'s has a couple probable causes. The first is that for the second analysis, the calculations are based off of the conductance calculations. These calculations also have some error in relation to experimental pressure measurements. The slight adjustment of the pressure will have a large effect on the mean free path and, in essence, the probability of charge exchange collisions. The same issue can be applied to other coefficients used in this analysis (e.g. $\gamma$ and the charge exchange cross-section). Another possible cause for the discrepancy arises from the IV curves used in the analysis. The IV curves were obtained using the same 60 MHz RF power but were at different pressures. This pressure difference will generate plasmas with different characteristics. The 20 mTorr plasma will have a higher plasma density but also be a little more collisional than the 5 mTorr case. The difference in plasma characteristics at the different pressures and the error inherit in the coefficients used in the analysis provide an explanation for the discrepancy between the calculated currents.

One of the causes for error mentioned in the previous paragraph is related to the last interesting characteristic observed in the IV curves. As mentioned above, a 20 mTorr Ar plasma will have a higher density than a 5 mTorr Ar plasma. However, the $I_{sat}$'s measured at higher pressures was typically lower than the $I_{sat}$'s at lower pressures no matter the probe used (See Fig. 88). Some of the reasoning behind this was just explained through charge exchange collisions but even the total 20 mTorr $I_{sat}$ in Table 6 was still lower than the 5 mTorr $I_{sat}$. If the plasma density increases, the current to the probes should also typically increase. This discrepancy needed to be investigated.

In previous work, the concept that the incoming flux (or current) should increase with increasing plasma density (or pressure) for an Ar plasma is not exactly clear. The results of Lee and Lieberman [ 61 ], Wang and Olthoff [ 51 ], and Janes and Huth [ 45 ] all showed that the incoming current should increase with increasing pressure. The results of Toups and Ernie [ 31 ] show that the ion flux is proportional to the square root of the RF frequency but was completely

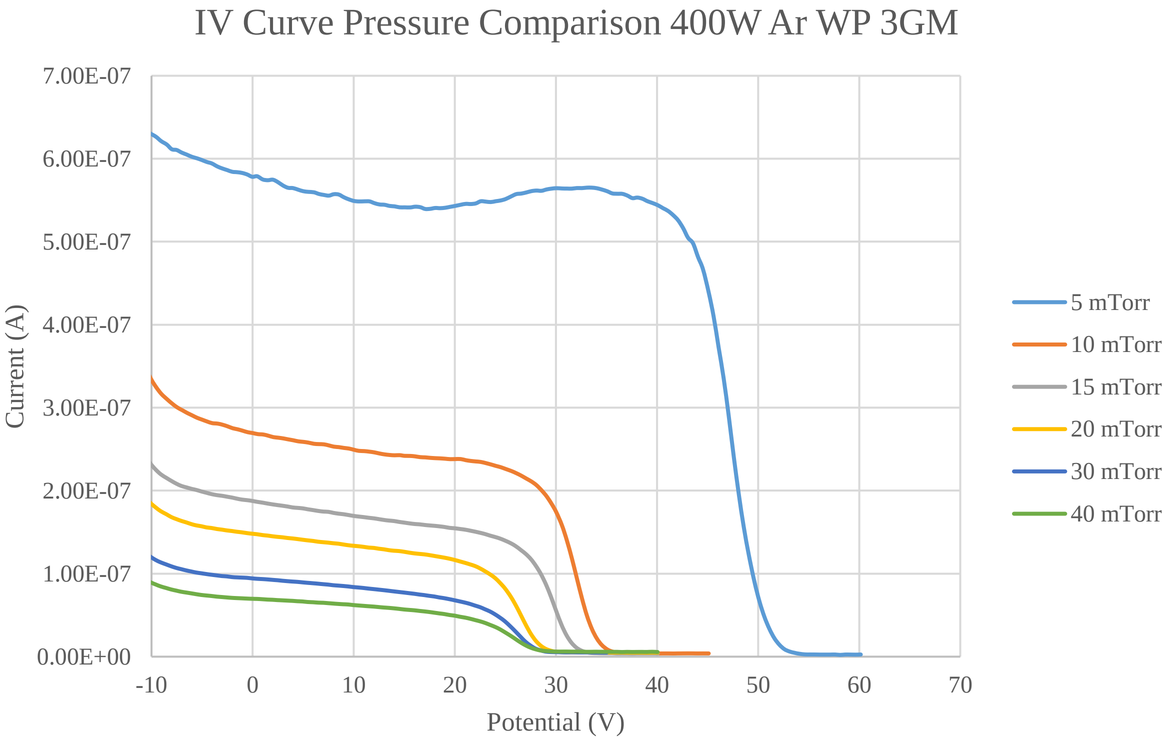

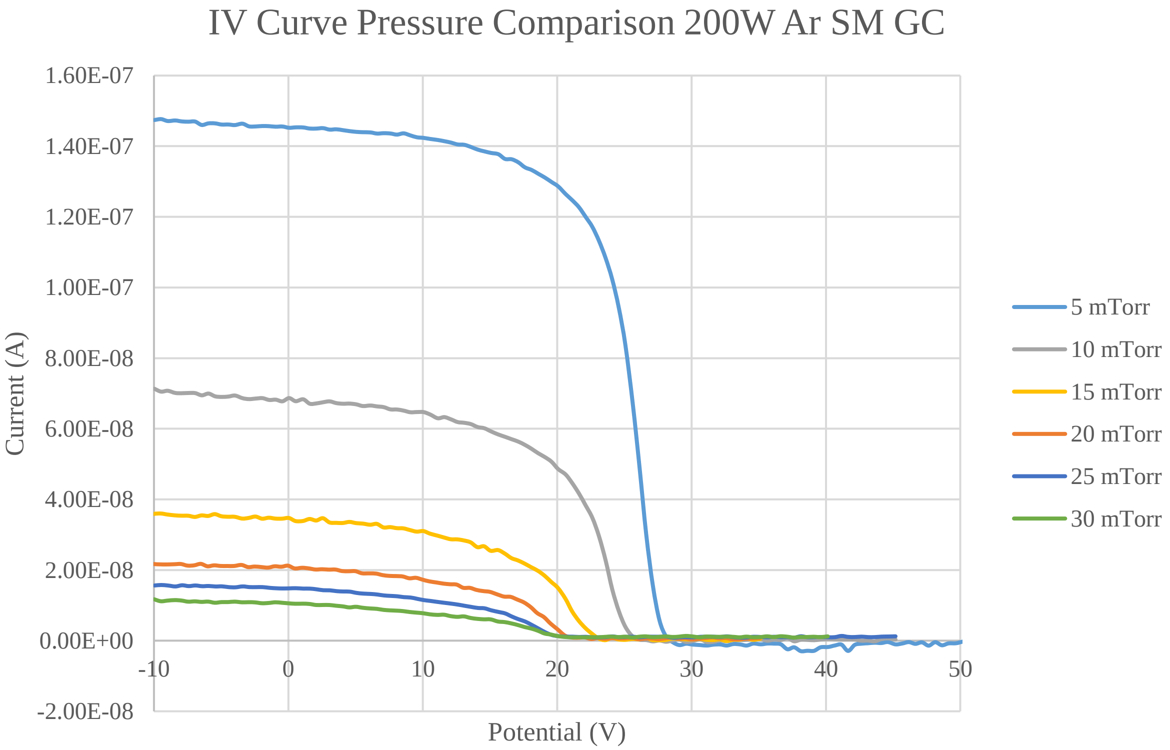

*Fig. 88*: Plot of the IV curves obtained from for an Ar plasma at different pressure and constant power (Top) IV curves measured using the WP for an Ar plasma generated by 400 W 60 MHz RF. (Bottom) IV curves measured using the SM probe for an Ar plasma generated by 200 W 60 MHz RF. In both cases, the $I_{sat}$ decreases with an increase in pressure.

independent of pressure. Lastly, the results of Olthoff *et al.* [ 47 ] and Seeböck *et al.* [ 53 ] show that the incoming current will decrease with increasing pressure. There may be a couple of reasons for the conflicting results. The first is that the chamber setups between each of the works and even the chamber for this work were not the same. The plasma reactor will have an effect on the plasma characteristics. Whether an ICP [ 51, 61] or CCP [ 31, 45, 47, 53 ] is used and the reactor dimensions will have an effect on the plasma produced. The number of frequencies used to power the plasma is another possible cause for the different results. Lastly, the location where the measurement was taken can produce different results. Taking all of these into consideration, the setup used in this work is most similar to the setup used by both Olthoff *et al.* and Seeböck *et al.* The results presented in these publications is consistent with the results in Fig. 88.

As the presented results are consistent with some of the previous work, the next step is determining what the cause of the decrease in current to the chamber walls and grounded electrode is. The most probable reason behind the drop in the current is the constriction of the plasma towards the powered electrode at these higher pressures. It makes sense that as the chamber pressure increases, the distance to which the power coupling to the gas can propagate is reduced. This would be caused by the power being absorbed more quickly due to a higher concentration of atoms, so the signal dissipates more quickly. If the plasma is more confined to the powered electrode at higher pressures, a smaller current will reach the chamber walls and grounded electrode.

To test this idea, a hairpin resonator (or just hairpin) probe was used to measure the density of the Ar plasma at the center of the chamber. A hairpin probe works by using a transmitting coil and resonating antenna to look for a resonance shift when the plasma is on and off. This shift is due to changes in the permittivity in the space between the transmitting coil and the resonance antenna. Since the frequency shift represents the permittivity change, which is linked to the plasma density, a value for the plasma density can be obtained. The equation used to calculate the density $(n)$ is as follows:

$$n = \frac{f_r^2 - f_o^2}{0.81} x10^{10}\ cm^{-3} \qquad 35$$

where $f_r$ and $f_o$ are the resonance frequencies in GHz when the plasma is on and off. For a more detailed description of the probe, its design, and its uses, one is referred to [ 114 - 121 ].

The hairpin used for this work was located in the center of the chamber (approximately 4 cm above and below the electrodes). Measurements were taken for pressures at 5, 10, 20, and 40 mTorr. The number of points taken at these pressures was dependent on how quickly the resonance was lost in other resonances caused by the measurement circuit when the plasma was on. Once the resonance frequencies were obtained, Eq. 35 was used to calculate the plasma density. A plot of the density results at the different pressures can be seen in Fig. 89. As expected, as the source power increases the plasma density also increases. The more interesting revelation is how the density changes with pressure. Going from 5 to 20 mTorr, the results show that the density increases. Nevertheless, the density measured at 40 mTorr decreased below the initial density values. This phenomenon could be explained by two competing mechanisms and the location of the hairpin. At the center of the chamber, as pressure increases, the density also increases as expected. At the same time, the plasma is becoming more localized towards the powered 60 MHz electrode. Initially, the hairpin only sees the density increase because the localization of the plasma has not affected the center of the chamber at this point. However, between 20 and 40 mTorr, there is a point where the localization reaches the center of the chamber, so the hairpin measures a drop in density. This would also explain why the rate of increase in density between 5 to 20 mTorr seems to slow down some. These results seem to point

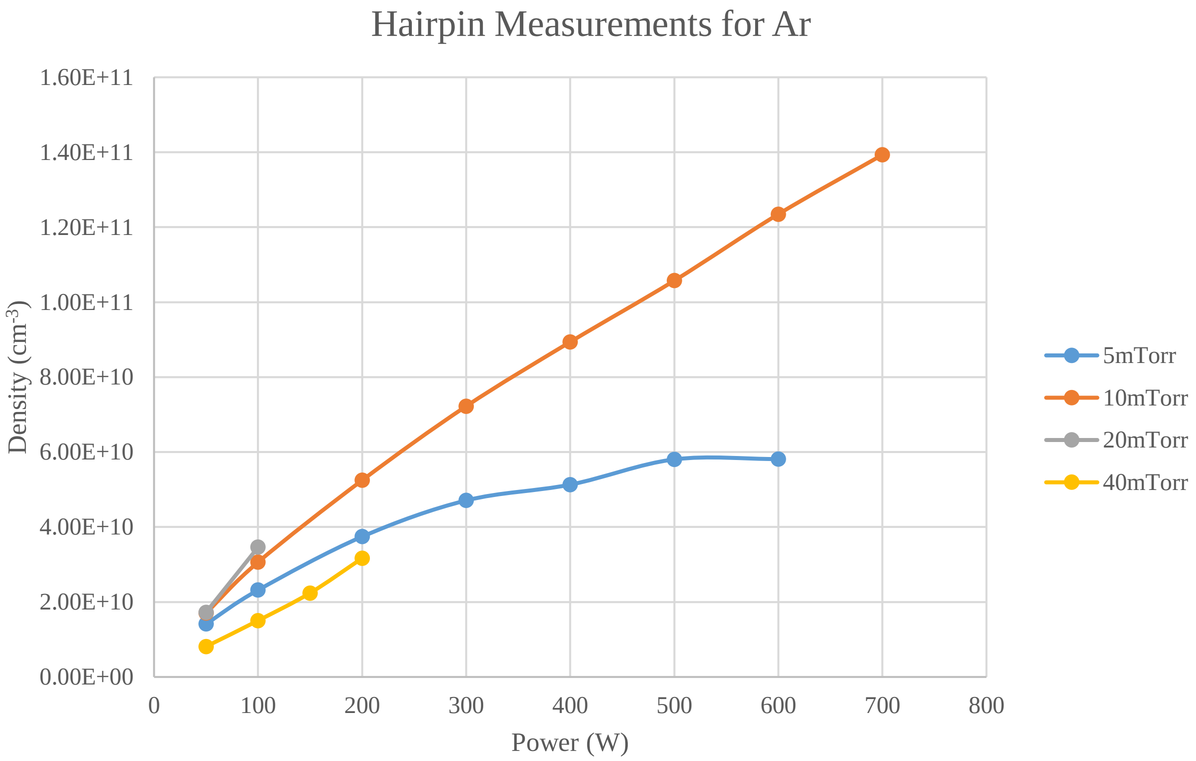

*Fig. 89*: Plot of density vs. power at different pressures obtained through hairpin measurements at the center of the chamber. Plasma was generated using 60 MHz power applied to the top electrode. The results show an increase in density with increasing pressure until the 40mTorr measurements.

to the idea of plasma localization, but a more thorough analysis is needed to provide more confidence that the localization of the plasma is the root cause of current loss at higher pressures.

### 4.1.3 Probe Comparison

After addressing and analyzing some of the issues apparent in the IV curve characteristics, the next step was to look at the IEDfs obtained from the IV curves for a single frequency Ar plasma. The IEDfs obtained from the IV curves from different probes for a 5 mTorr Ar plasma at different 60 MHz RF powers with a grounded bottom electrode can be seen in Fig. 90 and Fig. 91. For these measurements, the F probe 1st grid was externally grounded to match the electrode. The peak energies in these measurements also give a rough estimate of the

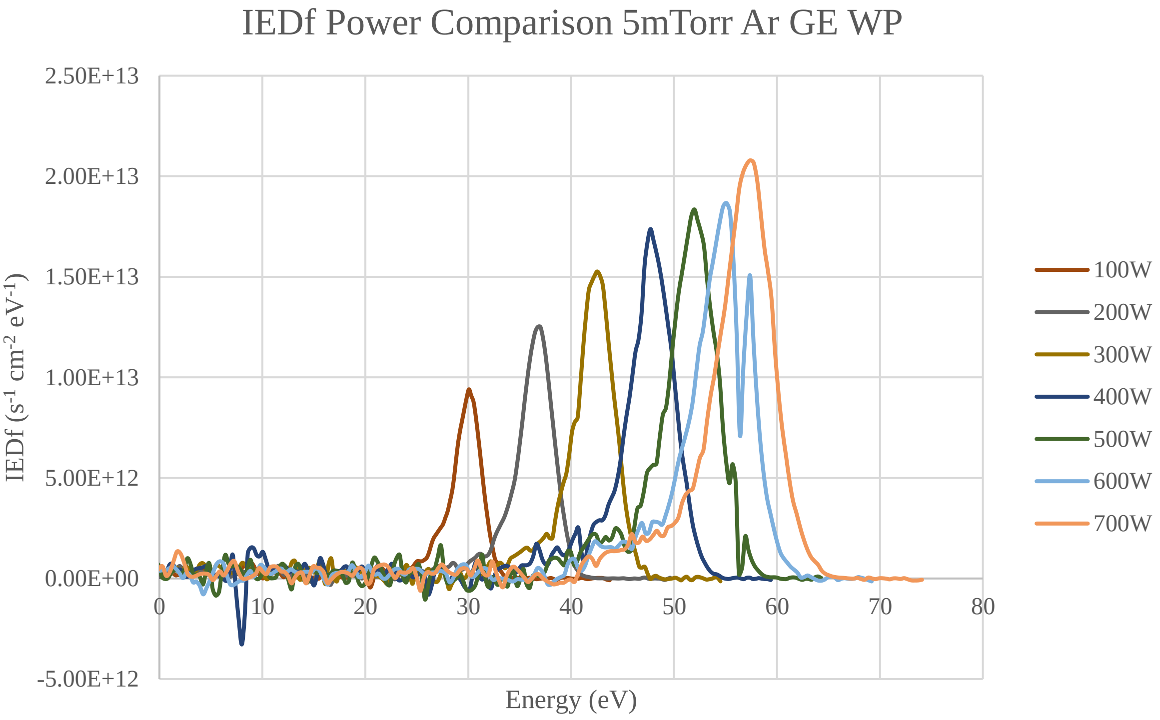

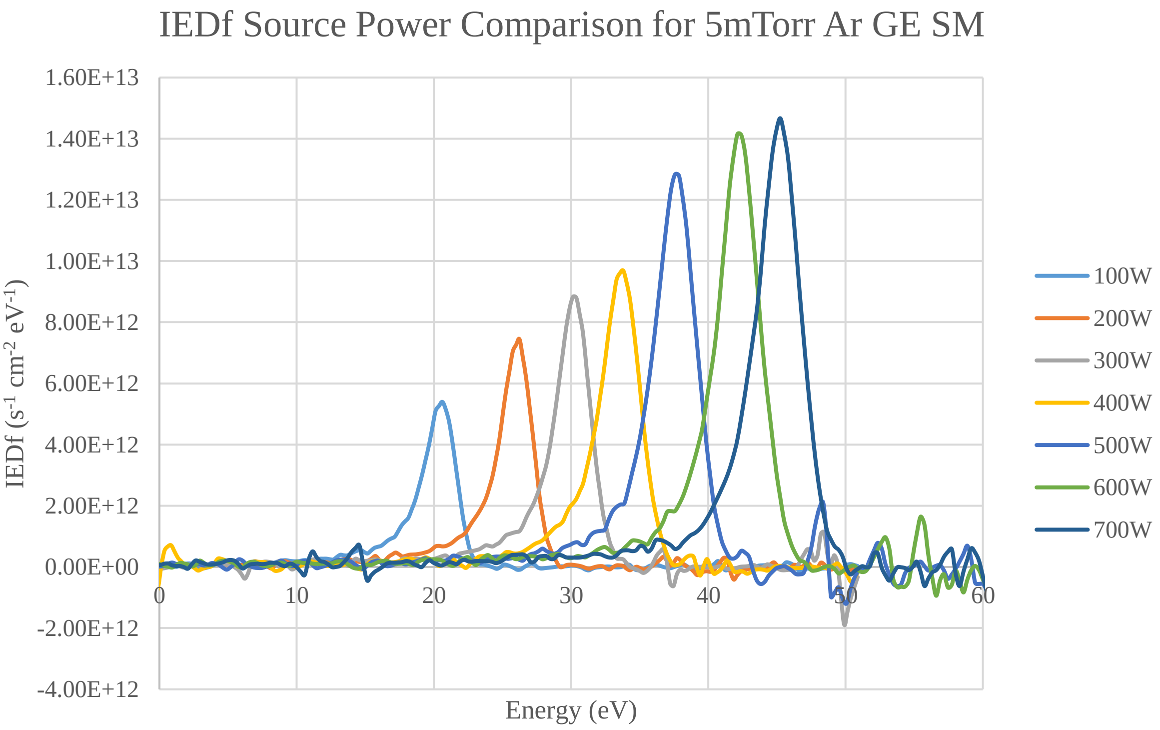

*Fig. 90*: IEDfs from the WP and SM probes for 5 mTorr Ar at different 60 MHz RF powers and a grounded electrode (GE). The SM probe has IEDf peak energies that seem to be about 10 eV lower than the WP probe. The shapes of the IEDfs are generally consistent.

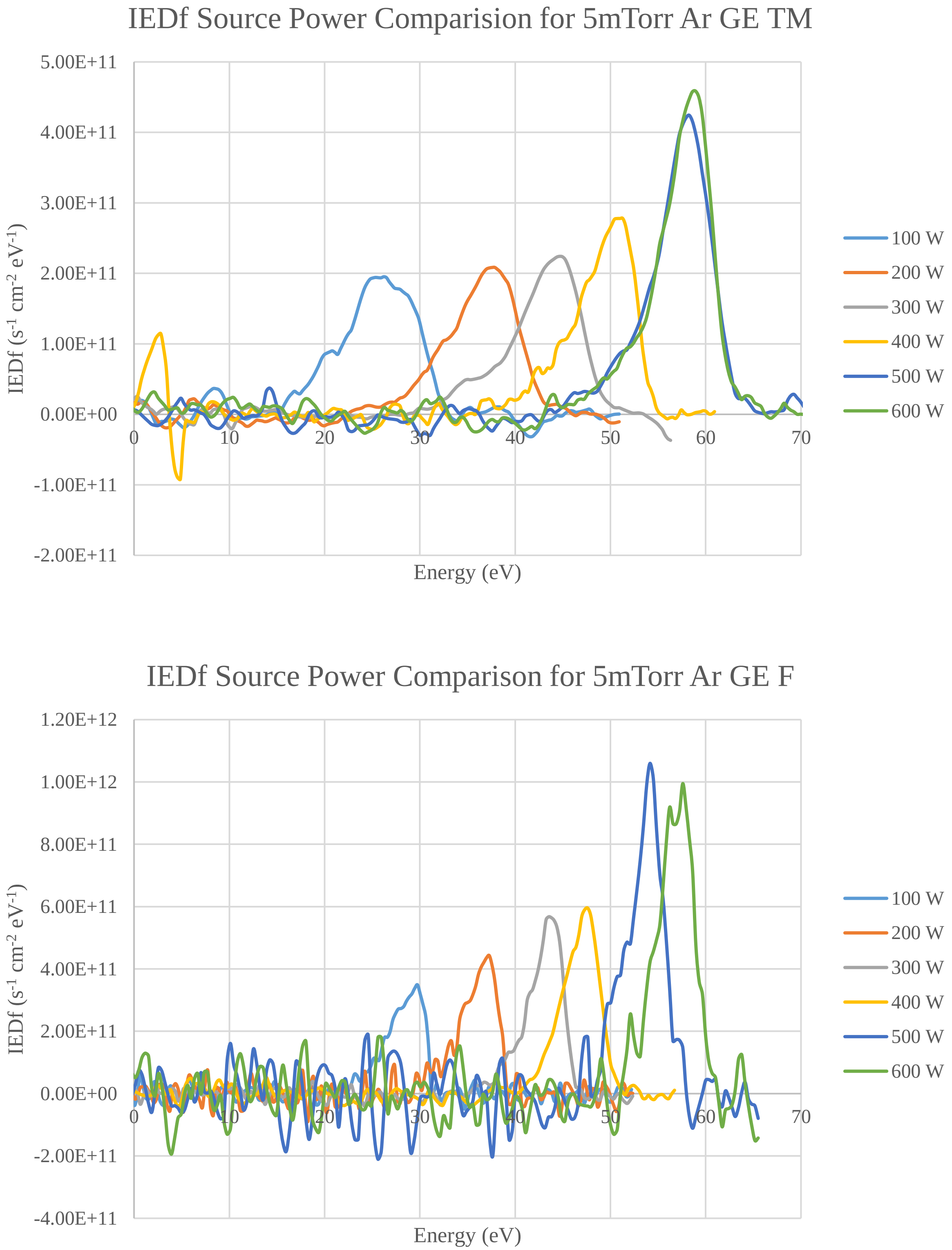

*Fig. 91*: IEDfs from the TM and F probes for 5 mTorr Ar at different 60 MHz RF powers and a grounded electrode (GE). The IEDf peak locations are very consistent between the TM and F probes. The shapes of the IEDfs are generally consistent but the TM and F probes.

plasma potential. These peak values are reasonable and consistent with previous work [ 47, 53 ]. As expected, the results from all the different probes show that as the 60 MHz RF power increases, the IEDf peak location also increases. The peak intensities also increase with increasing source power. The peak locations between the WP, TM, and F probes is pretty consistent. The SM probe IEDf peak locations differ from the other probe peak locations. These peak energies seem to be about 10 eV less than the energies measured by the other probes. This may be due to plasma non-uniformity or slight differences between the runs.

The shapes of the IEDfs between the curves is also consistent. The biggest difference arises in the IEDfs from the TM and F probes. The collisional tail on the lower energy side is larger than the tail measured by the WP and SM probes. The peak intensities of the TM and F probes are also smaller than the other probes. Both of these trends are caused by the drift cones. The larger collisional tail is due to the increased probability of collisions from the extra distance the ions must travel. The ions must traverse an additional 15 mm through the drift cone and the mean free path from the plasma to the RFEA changes from 0.152 mm to 64.5 mm. Based on this range, there is a portion of the drift cone where the probability of collisions is higher. The peak intensities are lower because of the loss of current from beam expansion as well as the collisions in the drift cone.

IEDfs from the WP, SM, and TM probes were also obtained from and Ar plasma at different pressures (See Fig. 92 - Fig. 94). At each of the pressures, 200 W of 60 MHz of RF power was used to generate the plasma. As expected, across all the probes, the peak energy decreases as the pressure increases. This is due to the plasma becoming more collisional with increased pressure. Also, as mentioned in the previous section, the intensity of the IEDfs decreases with increasing pressure. Again, this is likely due to the localization of the plasma

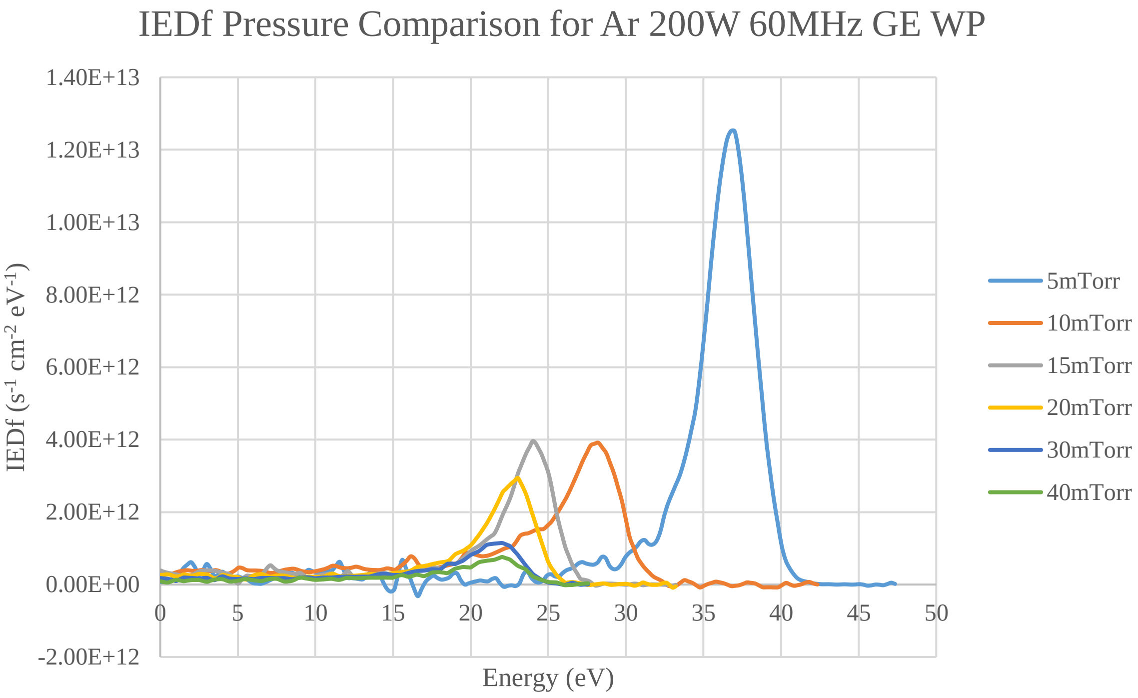

*Fig. 92*: IEDfs obtained from the WP probe from an Ar plasma for 200 W 60 MHz RF and a bottom grounded electrode (GE).

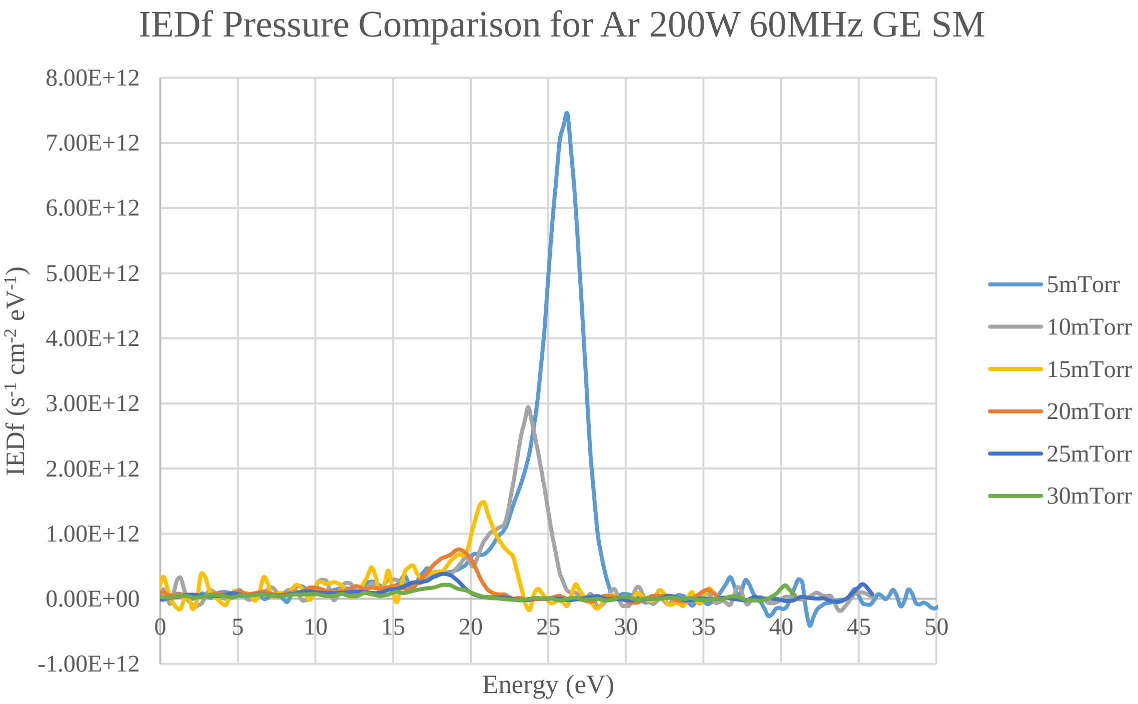

*Fig. 93*: IEDfs obtained from the SM probes from an Ar plasma for 200 W 60 MHz RF and a bottom grounded electrode (GE).

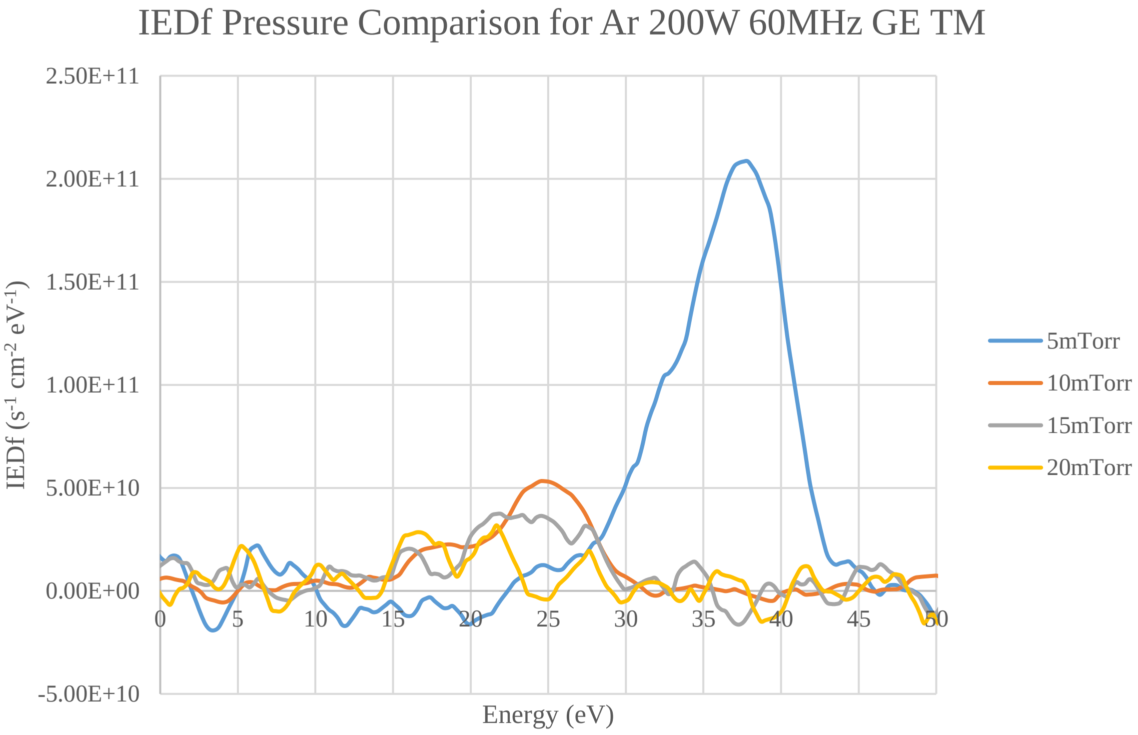

*Fig. 94*: IEDfs obtained from the TM probes from an Ar plasma for 200 W 60 MHz RF and a bottom grounded electrode (GE). The low energy collisional tail of the TM peak is wider again. The IEDf for the TM probe at higher pressures gets lost in the noise after 15mTorr.

towards the 60 MHz source electrode resulting in lower current collected. There is also a slight variation in the IEDf peak location again for the WP and TM probes. The SM probe IEDf peak locations are consistently lower in energy than the other two probes as well. Again, these variations are likely due to plasma non-uniformity and variation between plasma runs. The trends of IEDf intensity and IEDf shape of the WP and SM are similar again. As expected, the collisional low energy tail of these IEDfs increase with increasing pressure. Just as with the previous TM IEDfs, the peak intensities are lower than the other probes due to current losses in the drift cone. The collisional low energy tail is also wider in the IEDfs from this probe than those in the other two probes due to collisions in the drift cone. The beam expansion and collisional losses in the drift cone become so significant at pressures higher than 15 mTorr that the IEDf becomes lost in the noise when using the TM probe. In general, the IEDfs obtained from Ar plasmas at grounded surfaces are consistent between the probes and provide reasonable ion energies consistent with previous work.

## 4.2 Dual Frequency Measurements

The next logical progression in measurements was to increase the level of complexity by adding a second frequency to the plasma. The bottom electrode that was ground in the previous measurements was connected to a 13.56 MHz RF generator. For these experiments, the 60 MHz RF generator was still connected to the top electrode. Having the additional lower frequency on the bottom electrode will alter the IEDf creating a distribution impinging on the bottom electrode that has a saddle, or dual peak, shape. The bimodal IEDf is due to the ions traversing through an oscillating sheath as described in chapter 1. This distribution shape and chamber operation is more consistent with semiconductor fabrication chambers. In order to only look at the differences between a single frequency and dual frequency measurement, an Ar gas was used again to create the plasma.

Since a high-power RF signal was being applied to the bottom electrode, more robust filters were required to filter out the RF noise on plasma electron rejection grid, discrimination grid, and collector signal lines of the RFEAs in the electrode. This fulfilled a twofold purpose. The first was to protect the more delicate components in the PXI chassis and Ultravolt amplifiers. The second purpose was to have a high impedance component on the signal line to make sure that the grids in the RFEA oscillated at the same potential as electrode. As mentioned in chapter 1, to obtain the proper IEDf, the grids of the RFEA need to float at the RF potential with the electrode [ 5, 15, 29, 50, 70 ]. For these measurements, two different filters were used. The first filter used comes from the commercial Impedans Semion probe. Similar to the hybrid case mentioned in section 4.1.1, the signal lines from the grid were sent through the Impedans Semion filter box (See Fig. 95). The only difference in this case was that the sweep and measurement electronics used were the PXI chassis and Ultravolt amplifiers. The other filters used were high power low pass filters from Allen Avionics (See Fig. 96). The specific model number used was HPLP-03P00-B-050-N. These filters removed the 13.56 and 60 MHz signals on the electrode probes lines and provided the impedance to float the grids and collector at the RF potential.

A filter was not attached to the 1st grid of the RFEAs because this line was used to measure the DC potential bias ($V_{DC}$) of the electrode. A measurement of the $V_{DC}$ is necessary to obtain the proper energy values of the IEDf. Since the other grids of the RFEA are referenced to the computer ground, the IV curves obtained by the RFEAs are shifted by the $V_{DC}$ because the ions being collected by the RFEAs are referenced to this bias. To measure the $V_{DC}$ on the electrode a Tektronix 40 MΩ 2.5 pF 1000:1 high voltage probe was attached to the 1st grid of the SM probe. This probe was attached to a Tektronix TDS 684B oscilloscope to measure the RF waveform on the 1st grid. Due to the skin effect, the RF applied to the bottom electrode resides in the outer layers of the electrode. As the SM probe was closest to this layer, the RF waveform on the 1st grid was the one closest to the waveform on the electrode. The DC offset of the RF waveform is equal to the $V_{DC}$ on the electrode. Therefore, by taking the average of the waveform measured by the high voltage probe, a value for the $V_{DC}$ was obtained.

To check the accuracy of the $V_{DC}$ measured using the average of the RF waveform, a second measurement was taken with a high voltage probe through an Allen Avionics filter connected to the 1st grid of the TM probe. The high voltage probe used for this measurement was a Fluke 80K-6 probe because it is capable of measuring DC potentials unlike the Tektronix

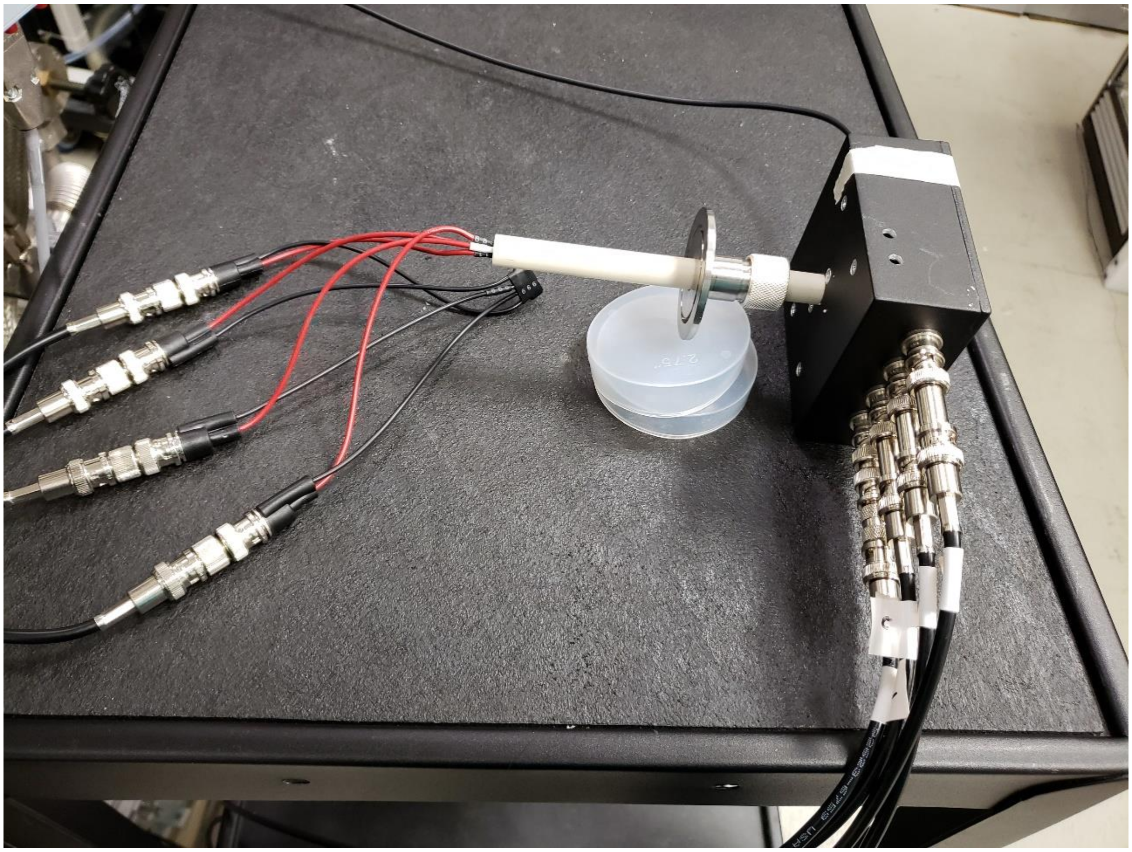

*Fig. 95*: Picture of the Impedans Semion filter box attached the one of the electrode RFEA probes.

*Fig. 96*: Picture of the Allen Avionics filters attached to one of the electrode RFEA probes.

probe. These Fluke probes were also the same probes used to measure the potential output by the Ultravolt amplifiers. Since the TM probe is much farther below the surface of the electrode, the 1st grid does not have good coupling to the RF waveform on the outer surface of the electrode even though it was directly attached to it. Even though it does not have a completely accurate RF waveform, it still sat at the $V_{DC}$ with the rest of the electrode due to that direct connection. The output of the Fluke probe was connected to a Fluke multimeter to get a $V_{DC}$ measurement. The Fluke probe and Tektronix probe were used to analyze the $V_{DC}$ when only the 60 MHz source was on and when both the 60 MHz and 13.56 MHz generators were on. For the case were only the 60 MHz source was on, the percent error of the $V_{DC}$ between the two probes was 0.76%. When both generators were on, the percent error of the $V_{DC}$ between the two probes was 4%. This shows that the average of the RF waveform measured by the Tektronix probe was an accurate measure of the $V_{DC}$. For all the following measurements presented, the average of the RF waveform was used to obtain the $V_{DC}$.

### 4.2.1 IV Curve Characteristics

An analysis of the IV curve characteristics was performed in section 4.1.2 and many of the same characteristics analyzed there are seen in the IV curves from a dual frequency plasma. Nevertheless, with the addition of the second frequency, a few new characteristics appear. Just as with the first analysis earlier in the chapter, it is necessary to analyze these new IV curves to isolate problems and understand the underlying physics of the measurement. It will also provide a better understanding of the measurements taken when more complex gas mixtures are addressed in the next chapter.

The first issue apparent in the new IV curves dealt with the offset of the IV curve. As mentioned in section 4.1.2, the no ion current regime of the IV curves was flat but there was an offset of the curve from 0 A which was larger than the default resolution of the PXI DMMs used. This is caused by a fast neutral current causing secondary electron emission. Just like before, there was an offset of the dual frequency IV curves as well. In this case though, there were times the offset was negative as opposed to positive (See Fig. 97). This change in the offset did not have any noticeable impact on the shape of the IEDf or its peak locations, but it was worth investigating to try and determine the cause.

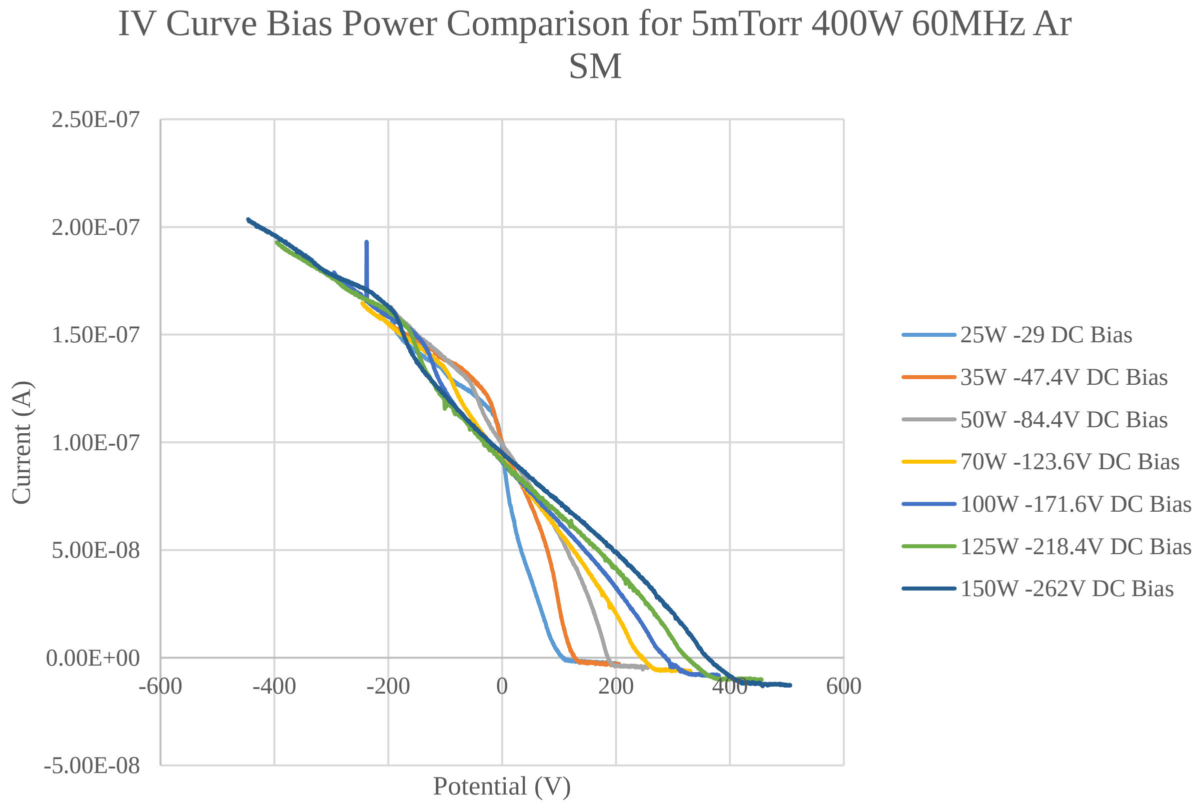

*Fig. 97*: Dual Frequency IV curves obtained using the SM detector for a 5 mTorr 400 W 60 MHz Ar plasma. The Impedans Semion filter box was used in these measurements. As the bias power increased, the offset of the IV curve became more negative.

For the measurements in Fig. 97, the Impedans Semion filter box was used to remove the RF signal from the RFEA signal lines. The relevance of the filter is due to the fact that it seemed to be the cause of the negative offset. This is best illustrated by IV curve measurements obtained from an $Ar\text{-}CF_4\text{-}O_2$ plasma with a 90-5-5 pressure ratio (See Fig. 98). Even though a this was a different gas mixture, the trends between the gas mixtures were the same. In this plot, the IV curve obtained using the Impedans Semion filter has a negative offset while the IV curve obtained using the Allen Avionics filters has the expected positive offset. It appeared that the filters were the cause of the discrepancy because these measurements were taken under the same plasma conditions and the shapes of the IV curves were very similar. There was some variability from run to run which would cause the slight shape changes between the curves but not such a drastic offset difference. The phenomenon also seemed to be affected by an increase in the $V_{DC}$, but this was only the case when the Impedans Semion filter was used as the RF choke. Without taking both filters apart to analyze the circuit components, the only measurable difference

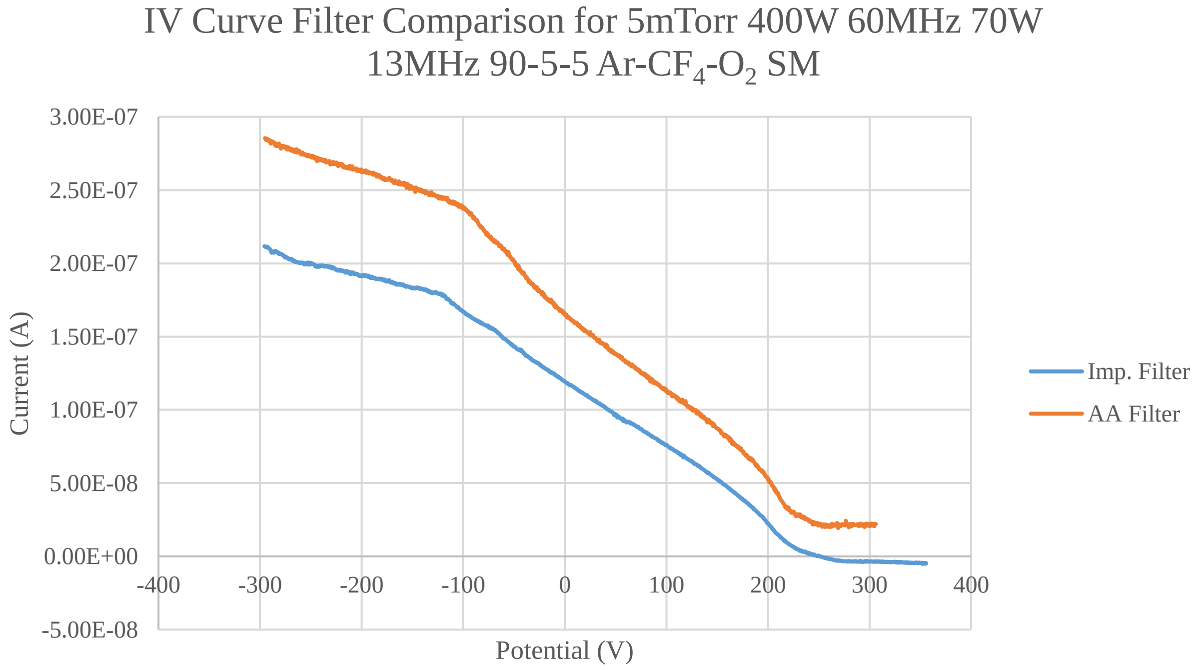

*Fig. 98*: IV curves obtained with the SM probe using two different RF chokes for a 5 mTorr 400 W 60 MHz 70 W 13.56 MHz $Ar\text{-}CF_4\text{-}O_2$ plasma with a 90-5-5 pressure ratio. In the plot, the Impedans Semion filter (Imp.) IV curve has a negative offset while the Allen Avionics (AA) filter IV curve has the expected positive offset for the same plasma conditions.

between them was their circuit resistance. Both filters used reactive elements (capacitors and inductors) to remove and impede the RF signal but the Impedans Semion filter also had a 200 kΩ resistance in its circuit. The Allen Avionics filters only had a circuit resistance of about 10 Ω. It is possible that the interaction of the RF and DC signals with this 200 kΩ resistor may have been the cause of the negative offset. To determine if this really was caused by the filter choice, a more thorough understanding of the filter design as well as more experiments that isolate the filters are needed.

Another IV characteristic of the dual frequency IV curves was that a large portion of the curve, including the ion saturation current $(I_{sat})$ region, is located at negative potentials. This is quite different than the IV curves that were obtained at the grounded electrode (See Fig. 87 and Fig. 88). This shift in the IV curves was caused by the $V_{DC}$ of the electrode. As mentioned in section 4.2, the ions measured by the REFAs are referenced to the $V_{DC}$ while the RFEA grids are referenced at ground. As a result, when taking a voltage sweep with the RFEA, the $V_{DC}$ must be added to the plasma electron rejection grid potential and the sweep potential to ensure collection of ions at all energies. Since the sweep potential was shifted by $V_{DC}$, the DMM that measures the sweep potential measured this shift resulting in the raw IV curve data residing at negative potentials. Hence, it is necessary to shift the IEDf by the $V_{DC}$ to obtain the proper ion energy values. That being said, all future IEDfs presented will be shifted by the $V_{DC}$ unless otherwise stated. This shift will be noted in the label of the energy axis of the IEDfs. Also, any future IV curve data presented for dual frequency plasmas will be the raw data without any shift from the $V_{DC}$.

The next IV characteristic observed in the dual frequency IV curves is the linear trend in the $I_{sat}$ region of the IV curves (See Fig. 97 and Fig. 98). For the measurements taken at the grounded electrode, this region was typically flat (See Fig. 87 and Fig. 88) which is expected. The dual frequency measurements always contained this trend to varying degrees for the SM, TM, and F probes. This trend was not observed in the WP dual frequency measurements. The cause behind this trend is not fully understood. Since the SM probe IV curves displayed this trend and it did not change based on the collector bias, this trend was not caused by ion current collection outside the probe. It is probable that the linear trend is caused by secondary electron emission from the collector. With the electrode biased, the grid potentials of the SM, TM, and F probes are much more negative. Since the ion energies are much higher due to the powered electrode and the $I_{sat}$ region does not significantly slow the ions, it is possible a significant amount of secondary electron emission occurs. This would also explain why the trend was not observed with the WP measurements as the ion energies and grid potentials for these measurements were much lower. To confirm the trend is caused by secondary electron emission, dual frequency measurements from the electrode with an RFEA that has a secondary electron rejection grid between the discriminator and collector are required. However, this linear trend in the $I_{sat}$ region of the IV curves did not have a significant effect on the IEDf, so a fix was left for future work.

The last interesting IV curve characteristic came from measurements taken with the TM and F probes. IV curves obtain with the WP and SM probes presented no major issues like in the single frequency measurements. The curves obtained took on the generally expected bimodal shape for a dual frequency plasma measurement with an RFEA. When measurements were taken with the TM and F probes though, a significant deviation appeared from the measurements taken using the WP and SM probes. The IV curves taken with the TM and F probes had significant portions of their IV curves in the negative current region (See Fig. 99). The no ion current regime was also quite different in shape in that it did not level off like the WP or SM probe measurements.

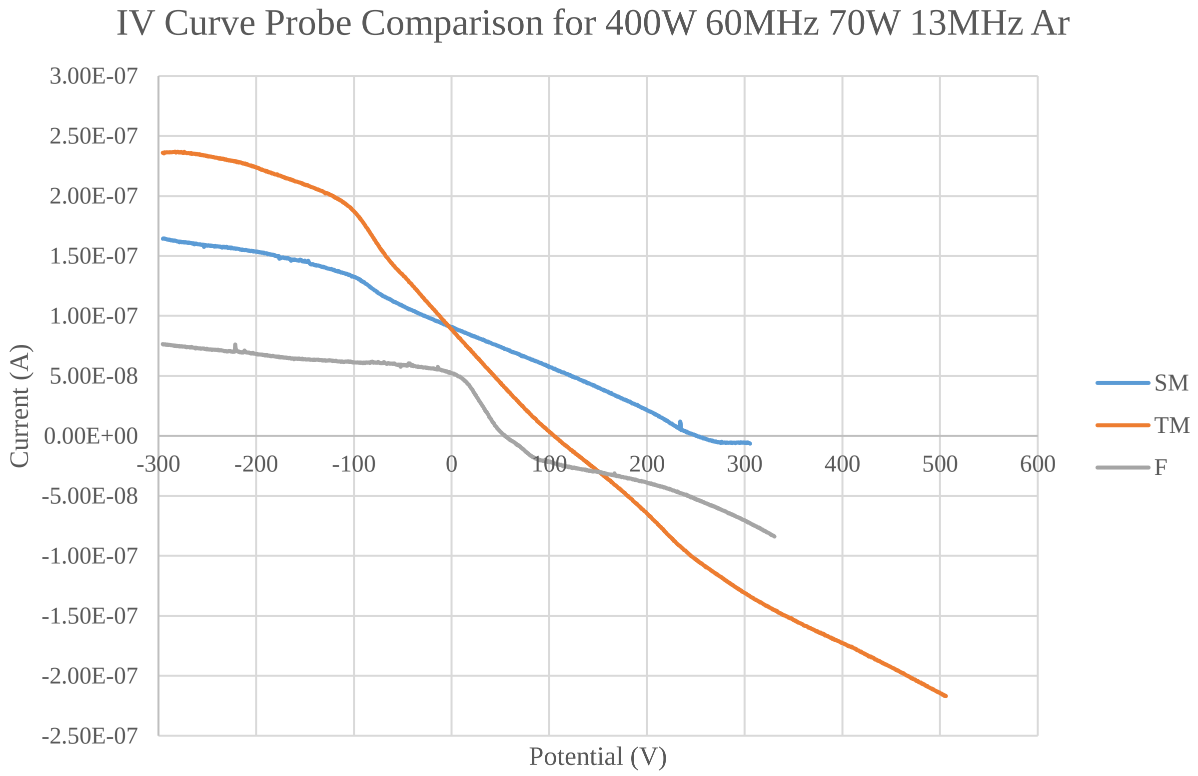

*Fig. 99*: Plot of the IV curves obtained using the SM, TM, and F probes for a 5 mTorr 400 W 60 MHz 70 W 13 MHz Ar plasma. The plot shows that the shape and current values of the TM probe and F probe IV curves deviates significantly from the shape of the IV curve from the SM probe.

Since the current goes negative, this negative portion must represent the collection of electrons. As mentioned in section 4.1.2, when designing the cavity and drift cones in the electrode, it was common to think about only ions entering the drift cone as a uniform beam. However, whether a single or dual frequency plasma, electrons will also be entering the drift cones and electrode cavity. The electrons beam will also expand just like the ion beam and a portion of electrons will travel around the outside of the RFEA. Due to their smaller mass resulting in increased mobility, the electrons travel around the outside of the probe more easily.

Even though this is the case, the collector was covered with the Vespel SP-1 insulator to prevent outside ion current (See Fig. 100). This cover also made it difficult for the electrons to reach the collector. They would have had to travel through the pumping ports of the discriminator or gaps between the Vespel cover and base to reach the collector. However, there was another option. There were screws in the polyimide base that were used to connect the signal lines to the grids. These screws were housed in a recess of the base but not completely covered. The recess was enough to prevent ions from being collected due to their limited mobility but not the electrons. With their higher mobility, the electrons could swing around the backside of the detector and be collected by these screws. This generated the large negative current in the IV curves measured by the TM and F probe. Also, since all the ions and electrons had to travel through the SM probe, it explains why this trend was not observed with the SM IV curves.

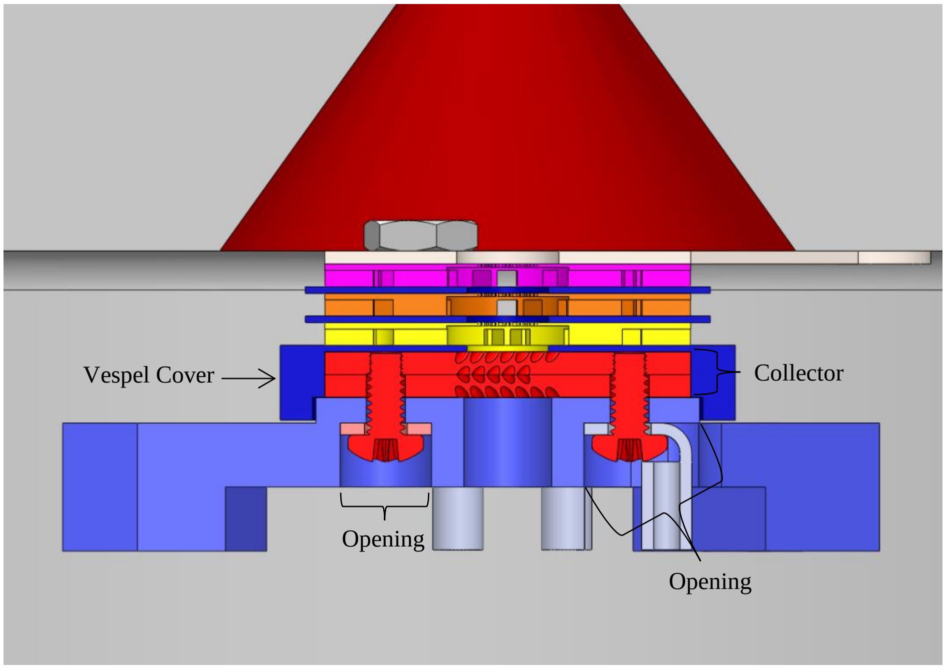

*Fig. 100*: SolidWorks section model of the TM probe below the drift cone. The section shot shows how the collector screws are exposed to the cavity allowing for current collection.

The WP was different from the SM probe because there was a gap that allows ions and electrons to travel around the probe. The difference here may have been due to the potential on the 1st grid. Unlike the TM probe where the 1st grid was determined by the electrode and the F probe 1st grid was floating, the WP 1st grid was biased negative as it acted as the plasma electron rejection grid. This created an electric field that would force any electrons entering the WP towards the ground cover. This field seemed to be strong enough to prevent any electrons from traveling to the back side of the detector. This would explain why the IV curves from the WP follow the expected trend. To fix this issue for any future IV curves from the TM or F probes, it will be necessary to cover the screws with an insulator (e.g. methacrylate) to prevent electron current collection.

### 4.2.2 Probe Comparison

Having analyzed the IV curves from a dual frequency plasma, the next analysis focused on the IEDfs from a dual frequency plasma. As RF power was now applied to the electrode with the SM, TM, and F probes, it was necessary to make sure the probes were operating properly. Based on the IV curves shown in Fig. 99, the SM probe seemed to be providing a correct measurement as its IV curve most closely resembled an IV curve from a dual frequency plasma. The TM and F probes on the other hand may not have been taking a correct measurement based on the IV curve shapes. To confirm this, it was necessary to look at the IEDfs obtained from the IV curves. The IEDf for the IV curves in Fig. 99 can be seen in Fig. 101. These IEDfs have not been shifted based on the $V_{DC}$ measured from the 1st grid of the SM, TM, or F probes. The RF waveform measured by Tektronix high voltage probe was not the same on the 1st grid of each of the probes and provided different $V_{DC}$ values (SM = -116 V, TM = -96.8 V, and F = 6.16 V). Therefore, to see how the IEDfs compare to one another, it was better not shift them.

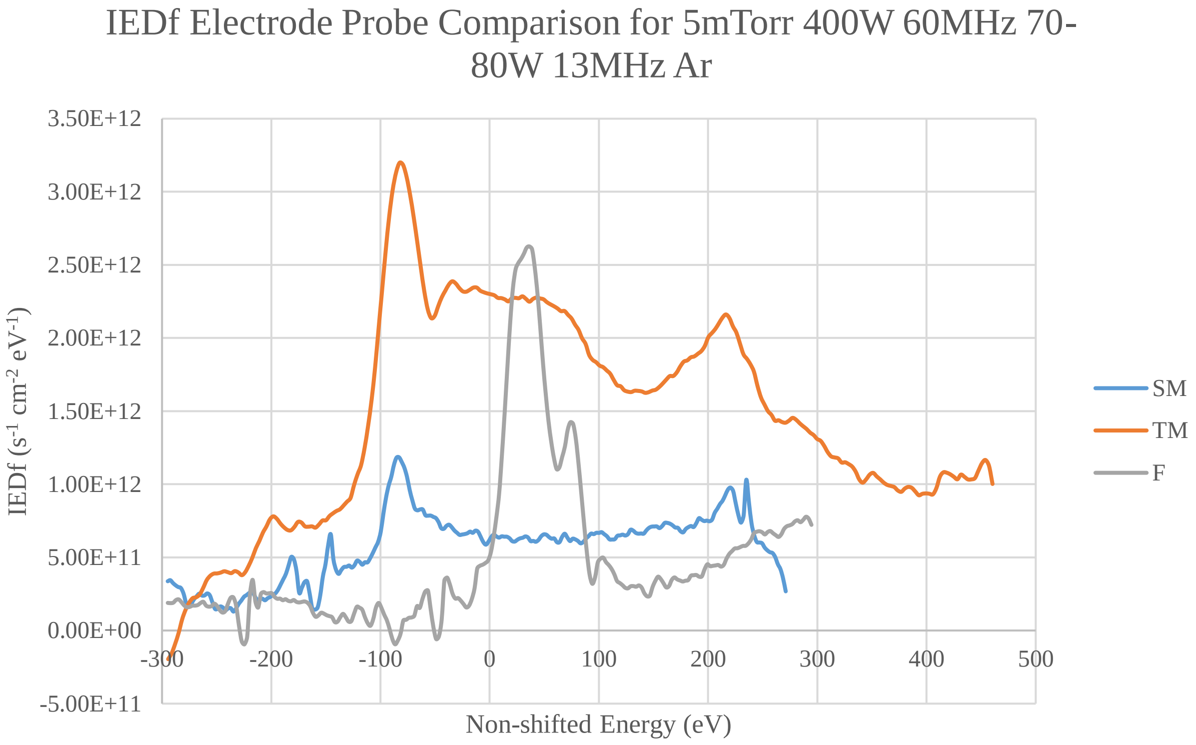

*Fig. 101*: Comparison of the IEDfs not shifted based on $V_{DC}$ from the IV curves in Fig. 99 taken by the SM, TM, and F probes. As expected, the SM IEDf has reasonable peak energy values and shows the typical saddle shape expected of a dual frequency IEDf. The TM probe also shows dual peaks in agreement with the SM IEDf but the saddle shape of the IEDf is slightly off. The F probe has a small saddle shape, but the peak locations are very different from the SM and TM peak locations. This probe does not appear to obtain a correct measurement.

The SM IEDf gives reasonable peak energies based on its $V_{DC}$ and has the expected saddle shape of a dual frequency IEDf. The peak locations of the TM IEDf coincide very well with the peak locations of the SM IEDf. The peak widths also appear larger than the SM IEDf but this is probably caused by collisions occurring within the drift cone. The IEDf intensity and saddle shape of the TM IEDf deviates from the SM IEDf because of the electron current collection that occurs at positive collector potentials. This electron current artificially inflates the incoming flux and prevents the IEDf from trending towards 0 $s^{-1}$ $cm^{-2}$ $eV^{-1}$ at energies above the high energy peak. The $V_{DC}$ from the TM probe would also not provide the proper shift of the IEDf. Like previously mentioned, the RF waveform measured on this grid was not the same as the one on the outer surface of the electrode because the probe was located below the drift cone. Therefore, the average measurement of the RF waveform gave an incorrect value. This will not affect the measured energy though as long as the TM 1st grid follows the same potential as the rest of the drift cone. Based on the peak locations, it seems the TM probe was measuring the correct ion energy. For this exact reason the curves were not adjusted by the probe $V_{DC}$ because the peak locations of the TM probe are correct. Were the TM IEDf shifted, it would have shown a discrepancy compared to the SM IEDf. Hence, the $V_{DC}$ used to shift all the future IEDfs is the value obtained from the measurement of the SM 1st grid. Lastly, the F IEDf shows a slight saddle shape but the peak locations are very different from the SM and TM IEDfs. In this case, the RF waveform and DC potential on the 1st grid are quite different from the RF waveform and DC potential on the electrode. This is evident in the $V_{DC}$ measured on the F probe 1st grid. This shows that there was not good coupling between the electrode and RFEAs below the drift cones unless the 1st grid is directly connected to the electrode. Since the SM and TM probes provide the correct peak locations, the following IEDf analysis will focus on the IEDfs obtained from these probes and the IEDfs measured by the WP.

With the addition of an RF bias added to the system, a discussion of the expected effects on the IEDf caused by the bias is needed. The ion energy impinging on the biased electrode is dependent on the oscillation frequency, waveform shape, and thickness of the sheath. The oscillation frequency controls the IEDf shape due to the ion transit time dependent on the ion mobility as described in chapter 1 and shown in Fig. 2. The waveform shape causes changes in the IEDf shape based on how much time the waveform resides at specific points in its cycle. When considering a sinusoidal waveform for example, most of the cycle is spent at the peaks of the waveform as opposed to the transition region. Therefore, the ion energies that appear more frequently in the IEDf are those generated by the peaks of the sinusoidal waveform (i.e. bimodal IEDf) in the sheath oscillation. Lastly, the energy dependence on sheath thickness is similar to the dependence on frequency. Considering a smaller sheath, the ions are able to traverse the distance more quickly and therefore respond to the instantaneous electric fields. For a larger sheath, because of the increased transit time, the ions respond to an average of the variation in the electric field.

The frequency and waveform shape applied to the sheath are mainly determined by the generator capabilities while the sheath thickness is dependent on the sheath density and bias potential (*V<sub>DC</sub>*) that forms on the RF bias electrode. The sheath dependence can be seen in the Child Law equation for high voltage sheath thickness $(s)$

$$s = \frac{\sqrt{2}}{3}\left(\frac{\varepsilon_o T_e}{e n_s}\right)^{1/2}\left(\frac{2V_o}{T_e}\right)^{3/4} \qquad 36$$

where $\varepsilon_o$ is the permittivity of free space, $T_e$ is the electron temperature, $e$ is the elementary charge, $n_s$ is the density at the sheath interface, and $V_o$ is the potential drop across the sheath. The density of the plasma controls $n_s$ and $V_o$ is traditionally equated to the $V_{DC}$ on the RF biased electrode. For a dual frequency system, as mentioned in chapter 1, the high frequency source mainly controls the plasma density while the low frequency bias source mainly controls the ion energy impinging on the electrode [ 2, 3, 5, 10, 11, 13 - 23 ].

As a result of the additional level of control over the plasma added by the RF bias described above, more experiments were needed to analyze the IEDfs from the SM, TM, and F probes. Using these two controls, the IEDf was obtained when the plasma density or $V_{DC}$ was kept constant and the other parameter varied. By holding the power of the 60 MHz RF generator constant, the density of the plasma was effectively held constant. The $V_{DC}$ can be held constant by adjusting the power applied by both the 60 MHz RF generator and the 13.56 MHz RF generator. The following IEDfs come in two sets, one looking at this constant plasma density (or constant 60 MHz power) and the other looking at a changing 60 MHz source power with constant $V_{DC}$.

The first set of IEDfs were obtained from a 5 mTorr Ar plasma generated from a constant 400 W 60 MHz RF signal when varying the 13.56 MHz RF power applied to the biased electrode (See Fig. 102 - Fig. 104). The WP IEDfs from this set are mainly single peak IEDfs. The IEDf shapes are very similar to the IEDf shapes measured from a single frequency plasma (See Fig. 90 and Fig. 91). The peak locations are quite different though. The addition of the 13.56 MHz signal increased the ion peak energy by about 1.5 times. The intensities of the peaks are pretty uniform which is expected for a plasma where the density is held constant.

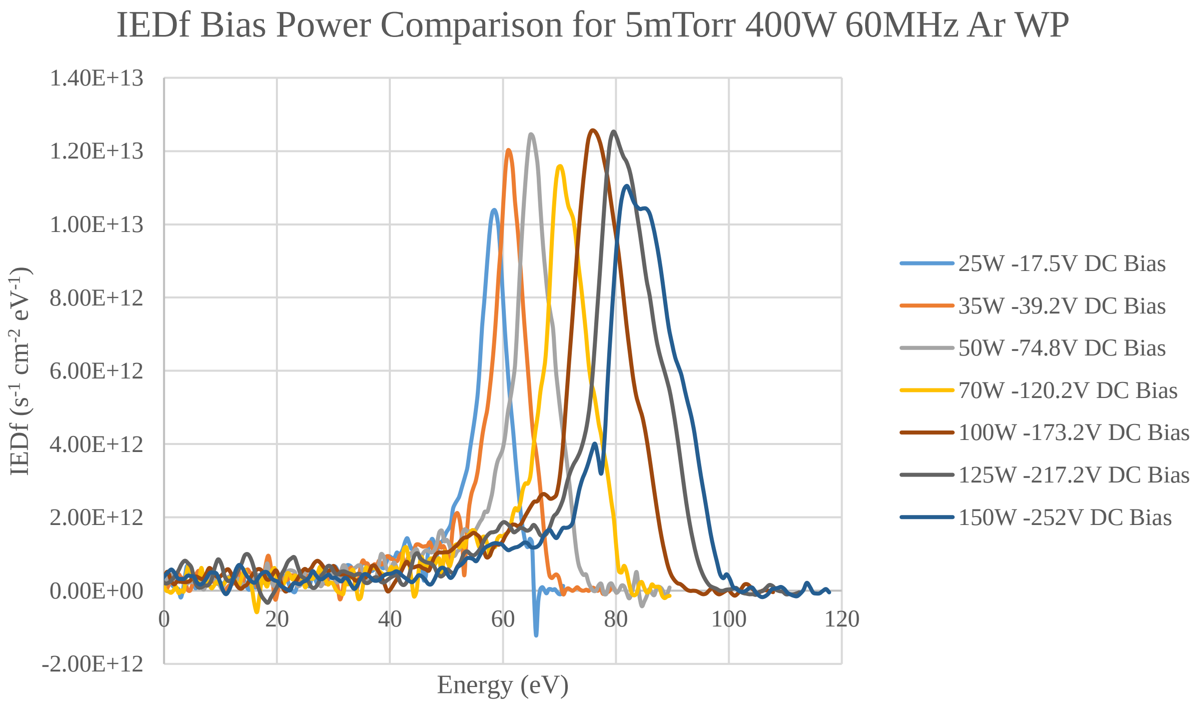

*Fig. 102*: IEDfs from a 5 mTorr Ar plasma generated by a 400 W 60 MHz RF signal when varying the 13.56 MHz bias power. The WP IEDfs are mainly single peak with hints of dual peak formations due to the fact that the measurement was made at a grounded surface.

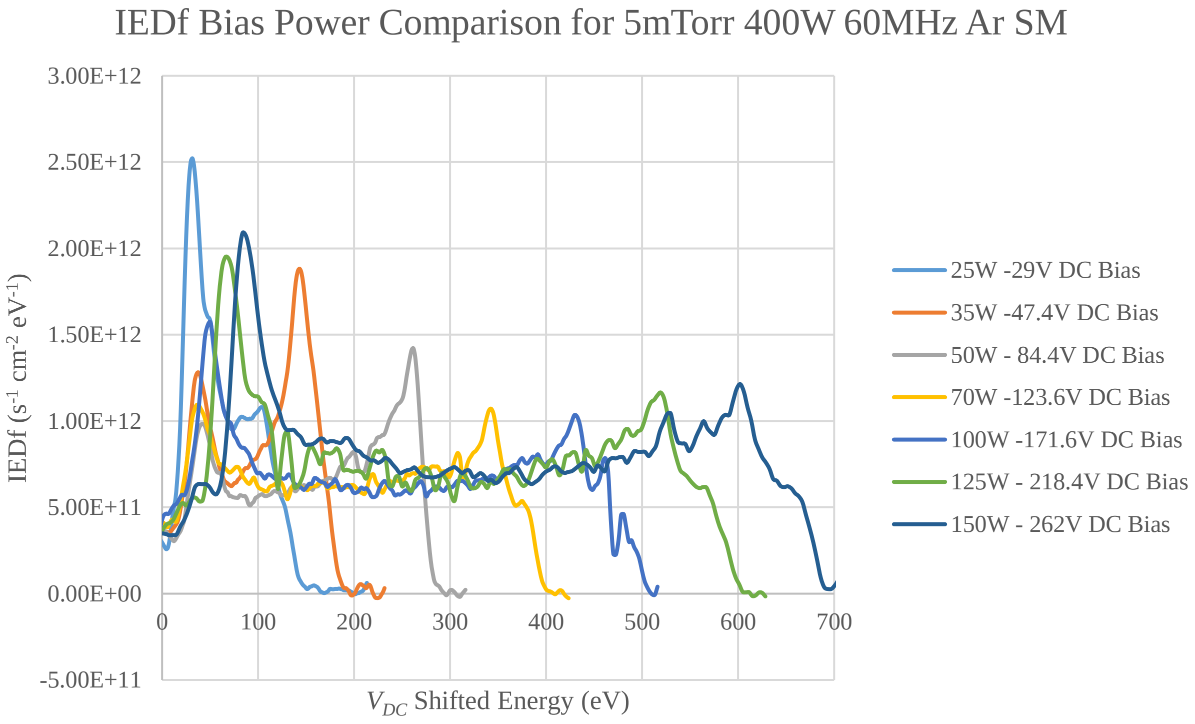

*Fig. 103*: IEDfs from a 5 mTorr Ar plasma generated by a 400 W 60 MHz RF signal when varying the 13.56 MHz bias power. The IEDfs from the SM have dual peaks as the measurement was made at the bias electrode. For a clearer picture of the trends of the SM IEDf plot at lower powers, see Appendix B.

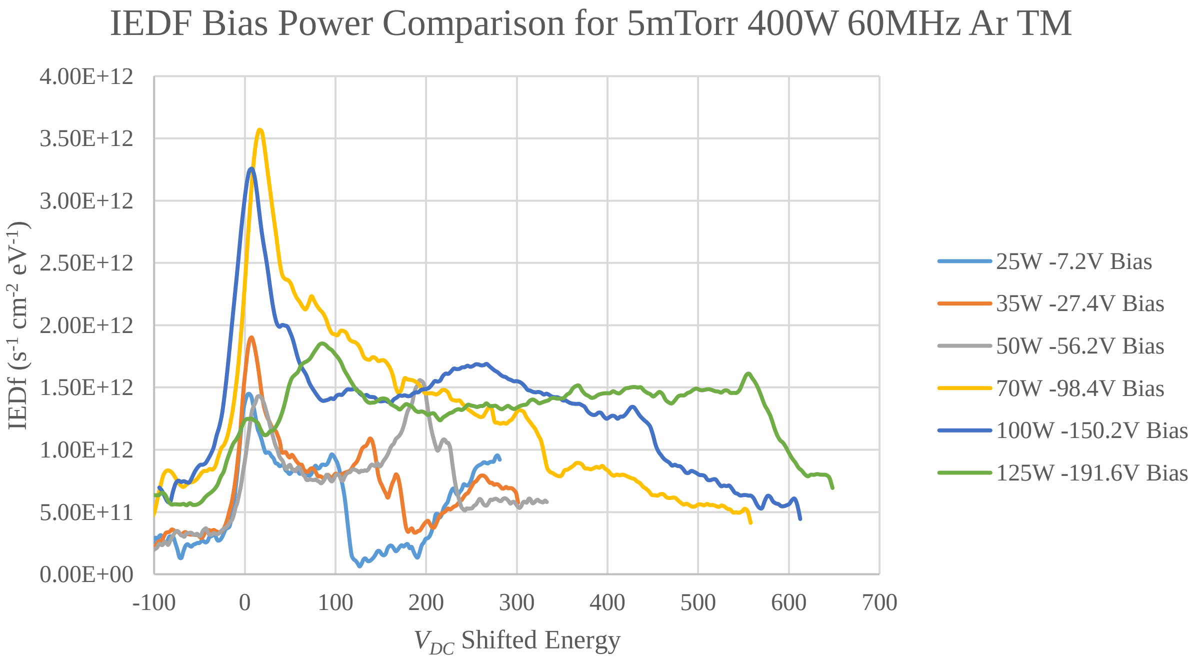

*Fig. 104*: IEDfs from a 5 mTorr Ar plasma generated by a 400 W 60 MHz RF signal when varying the 13.56 MHz bias power. The IEDfs from the TM have dual peaks as the measurement was made at the bias electrode.

The fact that the IEDfs are a single peak seems a little counter intuitive for dual frequency plasma. With a low frequency, the ions should be able to respond to an RF potential across a sheath generated by the 13.56 MHz signal. There are hints of a slight RF potential across the sheath as the 70 W, 125 W, and 150 W cases show a slight second peak in the main peak. However, it is possible that these variations are caused by noised in the IV curve measurement. If a dual peak IEDf does occur at the wall of the ground probe, a finer measurement resolution may be needed.

It is also possible, as mentioned in section 4.1, that the RF potential did not couple very well to the grounded sheath. This would explain why the WP IEDfs appear mainly as single peaks. However, the exact reason the ions seem to only respond to the $V_p$ and ground differential is not fully understood. Most sheath analysis techniques [ 1, 10, 12 ] have been performed under the assumption that the presheath-sheath interface has a potential of 0 V. Following this assumption, this means the peak energy of the IEDfs should match the differential between the $V_p$ and floating voltage $(V_f)$. The IEDfs presented here provide ion energies too high for a differential between $V_p$ and $V_f$. As a result, the analysis of sheath theory at a grounded surface for RF plasmas may need to be revisited (See section 6.3) to explain the single peak.

The SM IEDfs are very typical of IEDfs obtained from a biased electrode. Each of the IEDfs is saddle shaped and all of the energies are quite reasonable. The peak intensities are changing, but it appears that the area under the curves is very consistent. This is an indication of constant density. Since the plasma density (or current) was held constant for these cases, it is possible to determine how the sheath changes with increasing $V_{DC}$. Since the energy gap between the peaks gets larger with increased $V_{DC}$, this points to the sheath above the electrode shrinking with increasing $V_{DC}$. There is also an interesting shift in the peak intensity at lower bias powers between 25 and 70 W. Initially at 25 W, the low energy peak is much higher in intensity than the high energy peak. However, as the bias power increases, the low energy peak shrinks and the high energy peak increase. This change in the skew is typically observed when changing the phase between the bias frequency and an additional third frequency that is a harmonic of the bias. Even though a third frequency was not used in these experiments, harmonics of the bias were generated by nonlinearities in the sheath. It is possible that the phase between the bias and this plasma generated harmonic changed phase as the bias power changed. The waveform measured by the Tektronix high voltage probe was analyzed to look for this phase change. A slight shift in the phases was observed based on the waveform measurement but not to a degree that could cause skew changes. A more thorough measurement and analysis of the electrode waveform is needed to determine whether this skew is due to a phase change.

The high peak energies are quite high but not above the operational limits of typical RFEAs. The goal of these RFEAs was to operate under high voltage conditions. The RFEAs are capable of reaching higher energies, but the limiting factor was the PXI DMMs. The main problem arose from the potential on the collector line. The high voltage line of the DMMs could float at 1 kV above computer ground, but the low voltage line could only float 500 V above computer ground. In this work, the discrimination grid and collector were tied to the same potential and offset by a 9 V battery. Since this collector line also connected to the low voltage input on the DMM, this meant that the scans could only sweep between ±510 V without causing a computer fault.

The TM IEDfs also show the traditional dual peak configuration. The peak energies are somewhat similar to the peak energies measured by the SM probe. Collisions in the drift cone is a possible reason why the peak positions deviate from the SM IEDfs. Another reason for the difference is smaller $V_{DC}$ values in the TM runs. It is possible this is due to run variation but also possible that these smaller values are caused by a change in the electrode impedance based on the probe used. These IEDfs are also different in the intensity values. It is very apparent that, unlike with the SM IEDfs, the area under the curves changes. It seems to change until high bias powers were reached. This is logical because at the lower bias powers, the ions were more susceptible to collisions since they were at lower energies. Since collisions in the drift cone could easily prevent an ion from entering the RFEA, it makes sense that the incoming flux would be lower at lower ion energies. As expected, the peak gap also increases with increasing $V_{DC}$ similar to the SM IEDfs.

There are some differences between the TM IDEfs and the SM IEDfs though. One difference is the lower intensities of the high energy peaks. This is taken to the extreme at the higher bias powers. It is possible that this was due to ion collisions occurring as ions traversed the length of the drift cone. High energy ions experiencing collisions could be washed out into the continuum or low energy peak. This is contradictory to general knowledge though. Traditionally, particles at higher energies are less likely to have collisions. When the bias power is higher, the high energy peak should be higher as well. Another possible cause could be a shift in phase of the bias harmonic. As mentioned earlier, the shift in the phase of the harmonic can affect the skew of the IEDf. A skew change was observed for the SM IEDfs as well, but no significant phase change was observed in that case. Here, the waveform was not analyzed to look for a phase change, but it may be possible that this was the cause of the skew change. As this change was consistent across both the SM and TM IEDfs, it is more likely that the skew change was caused by a phase change between the bias and its harmonic.

The next set of IEDfs were generated from the same pressure and gas compositions but the $V_{DC}$ was held constant while the source power was varied. Keeping the $V_{DC}$ constant required adjusting the bias power after the source power had been adjusted. The IEDfs obtained from the different probe measurements can be seen in Fig. 105 - Fig. 107.

Again, as expected, the WP IEDfs are single peaks with higher energies than the single frequency WP IEDfs (See Fig. 90). The peak energies are very consistent with the energies obtained from the constant source power case (See Fig. 102). The shape between these IEDfs and previous ones presented are very similar. Hints of dual peak formation in these IEDfs are less apparent in this case than the constant source power case. However, as mentioned before, it is possible the small fluctuations in the WP IEDfs for the constant source power case may be caused by noise in the IV curve measurement. Unlike the case where source power was held constant, the intensity the IEDf peaks increased with increasing source power. This is expected

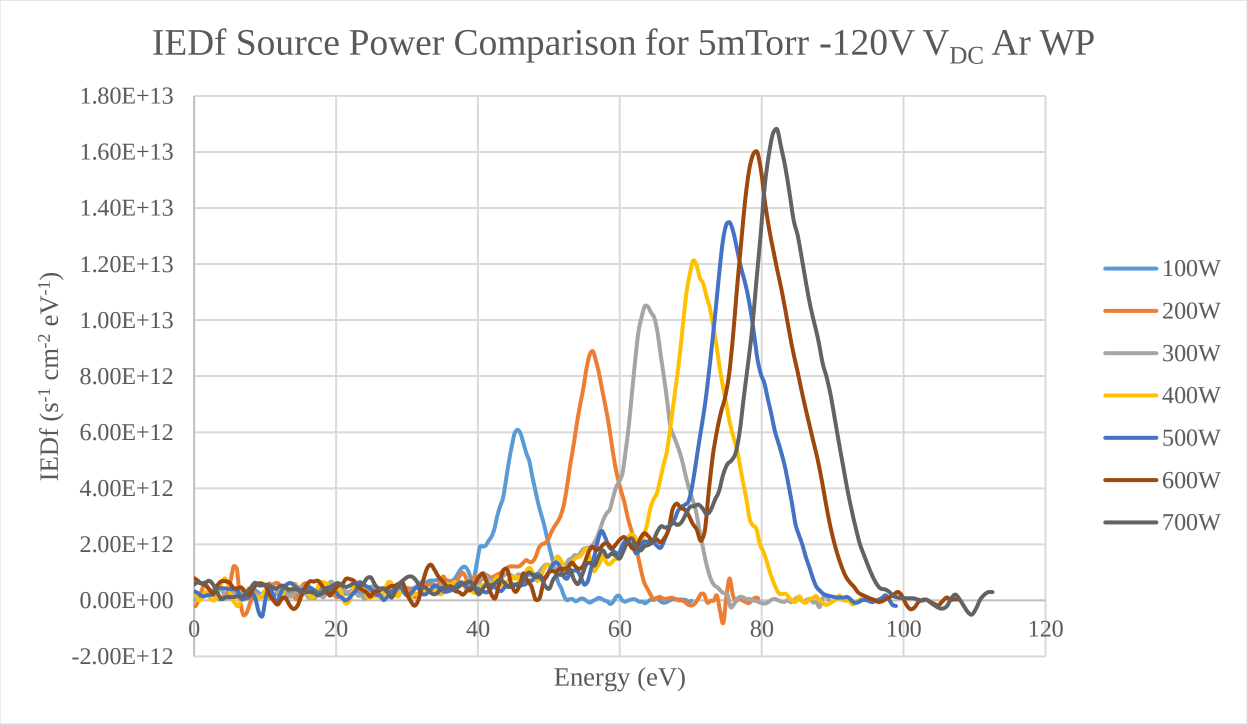

*Fig. 105*: IEDfs from a 5 mTorr Ar plasma generated with a -120 V $V_{DC}$ when varying the 60 MHz source power. The WP IEDfs are mainly single peak due to the fact that the measurement was made at a grounded surface.

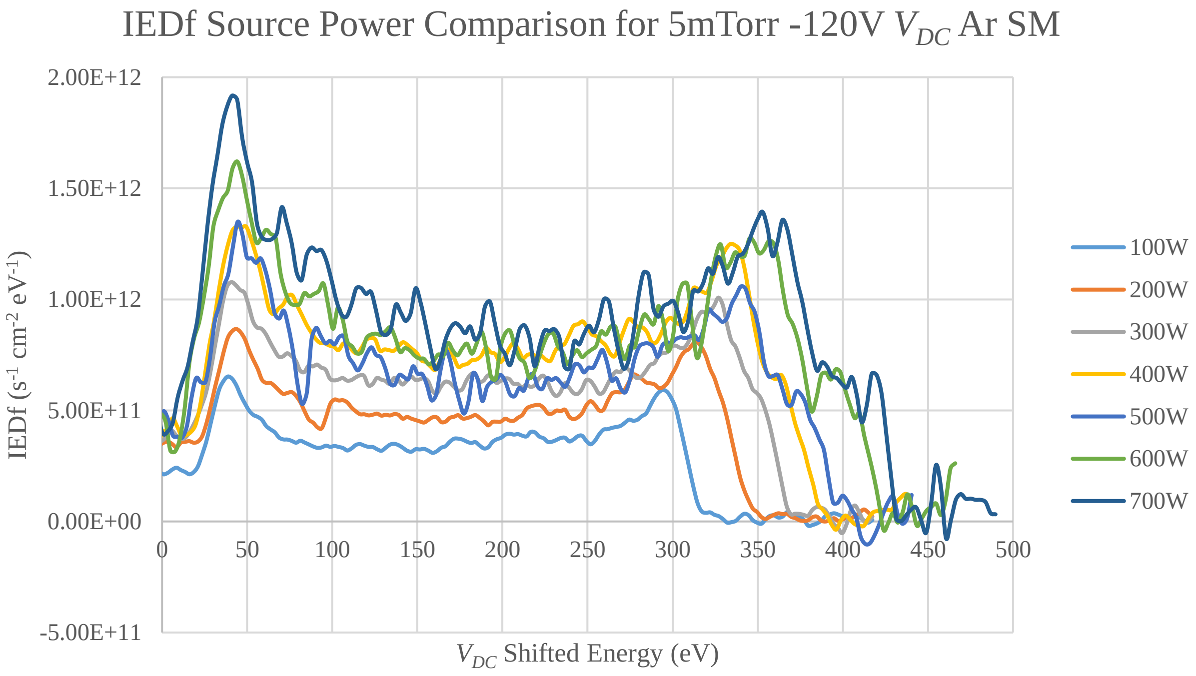

*Fig. 106*: IEDfs from a 5 mTorr Ar plasma generated with a -120 V $V_{DC}$ when varying the 60 MHz source power. The IEDfs from the SM have dual peaks as the measurement was made at the bias electrode.

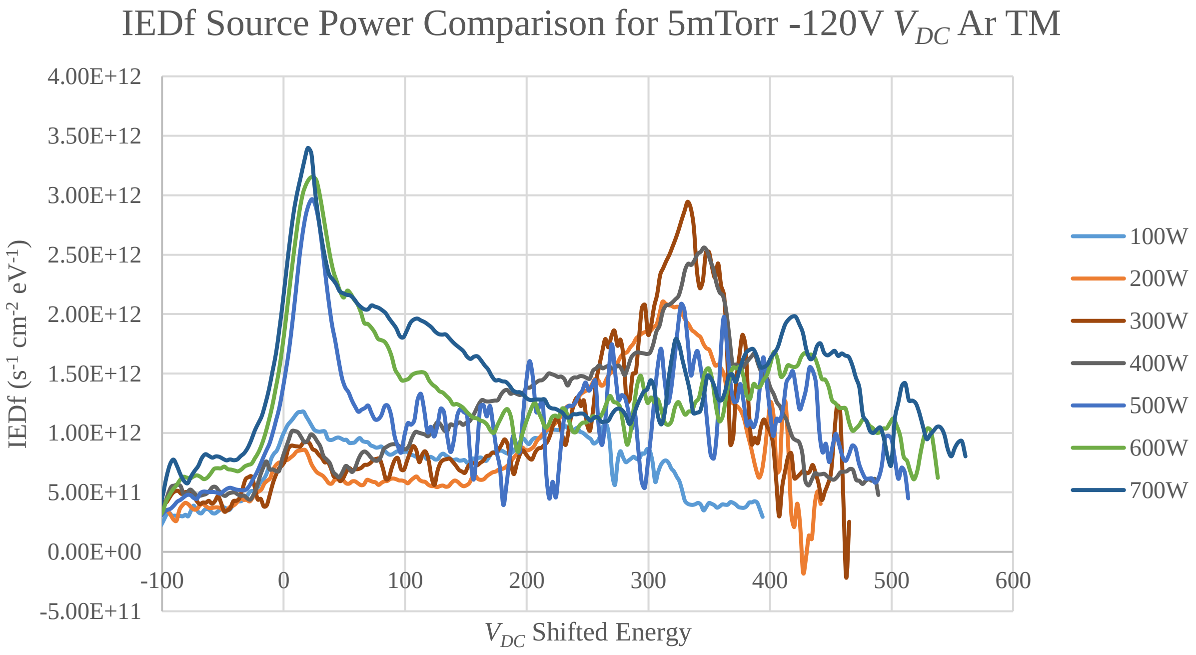

*Fig. 107*: IEDfs from a 5 mTorr Ar plasma generated with a -120 V $V_{DC}$ when varying the 60 MHz source power. The IEDfs from the TM have dual peaks as the measurement was made at the bias electrode. For a clearer picture of the trends of the TM IEDf plot, see Appendix B.

since the source power was increasing, the plasma density should also increase.

The SM IEDfs have very similar trends in this case to the ones obtained for a constant source power (See Fig. 103). The IEDfs have the expected saddle shape. The low energy peak locations are also very similar to the previous case. By holding the $V_{DC}$ constant, an analysis of how the sheath changes with respect to plasma density was performed. As the source power (or density) increases, the peak intensities increase, and the peak energy gap between the peaks also increase. The peak intensity increase is expected due to the increase plasma density. Again, the energy gap increase between the peaks is indicative of a shrinking sheath because the ions are traversing the sheath more quickly allowing them to respond to the instantaneous electric fields.

The TM IEDfs also have some of the same trends observed in the constant source case (See Fig. 104). Again, the peak energy locations are lower than the SM IEDfs. This is likely due to collisions occurring within the drift cone. Another interesting consistency, but is also different from the SM IEDfs, is that the high energy peak gets washed out at higher powers. The difference here though is that the source power was increased as opposed to the bias power. The possible causes mentioned earlier were collisions within the drift cone or a phase change in the harmonic of the bias. In this instance, it seems more likely that collisions are to blame for two reasons. The first is that as the source power increased, the density also increased making ion-ion collisions more likely. The other reason is that this skew change was not observed in the SM IEDfs for this case. If the phase between the bias and its harmonic were to change, it is unlikely that it would affect the IEDfs of one probe but not the other. This makes it seem more likely that collisions are the reason for the reduction in the high energy peak.

Similar to the single frequency cases, the effect of pressure was also investigated for the WP and SM probes. For these measurements, the WP measurements were taken for a consistent set of power and $V_{DC}$ conditions. The source power was set to 400 W and the bias power was adjusted at the different pressures to obtain a -120 V $V_{DC}$. The SM probe conditions were a little different. For the SM IEDf pressure measurements, the $V_{DC}$ was held constant at -120 V but the source power and bias power were varied. The source power was set at 400, 600, or 700 W and the bias power ranged between 58 W to 70 W. Plots of the IEDfs obtained can be seen in Fig. 108.

As expected, for both the WP and SM probes, the IEDf intensities decrease with increasing pressure. This is somewhat due to the increase in collisionality of the plasma at higher pressures but is more likely due to the localization of the plasma toward the top electrode. The evidence for this is the fact that the peak widths don't seem to change very much with increasing pressure. This is most clearly seen with the WP IEDfs. The energies of the IEDfs are also quite reasonable. As expected, as the pressure increases, the peak energies of the WP IEDfs and the energies of the high energy peaks of the SM IEDfs decrease in energy. This trend is likely due to the increase in collisions at higher pressures.

Collisions become such an issue for the SM probe that at 30 mTorr, the peaks have been lost in the continuum or noise. It is possible that this is the expected transition from a dual peak IEDf to a single peak IEDf expected at higher pressures. It may also be a sign though that the SM probe was not being sufficiently differentially pumped at this pressure. Just like with the old WP design (See section 4.1.2), the differential pumping occurs through the probe. The only difference in this case was that the Si grid acted as the main differential limitation. This reduced the pressure the SM probe sees compared to the old WP.

At these high pressures, the SM probe displayed some characteristic signs that the old WP did. The most evident is that there was a peak located around the potential applied to the 2nd

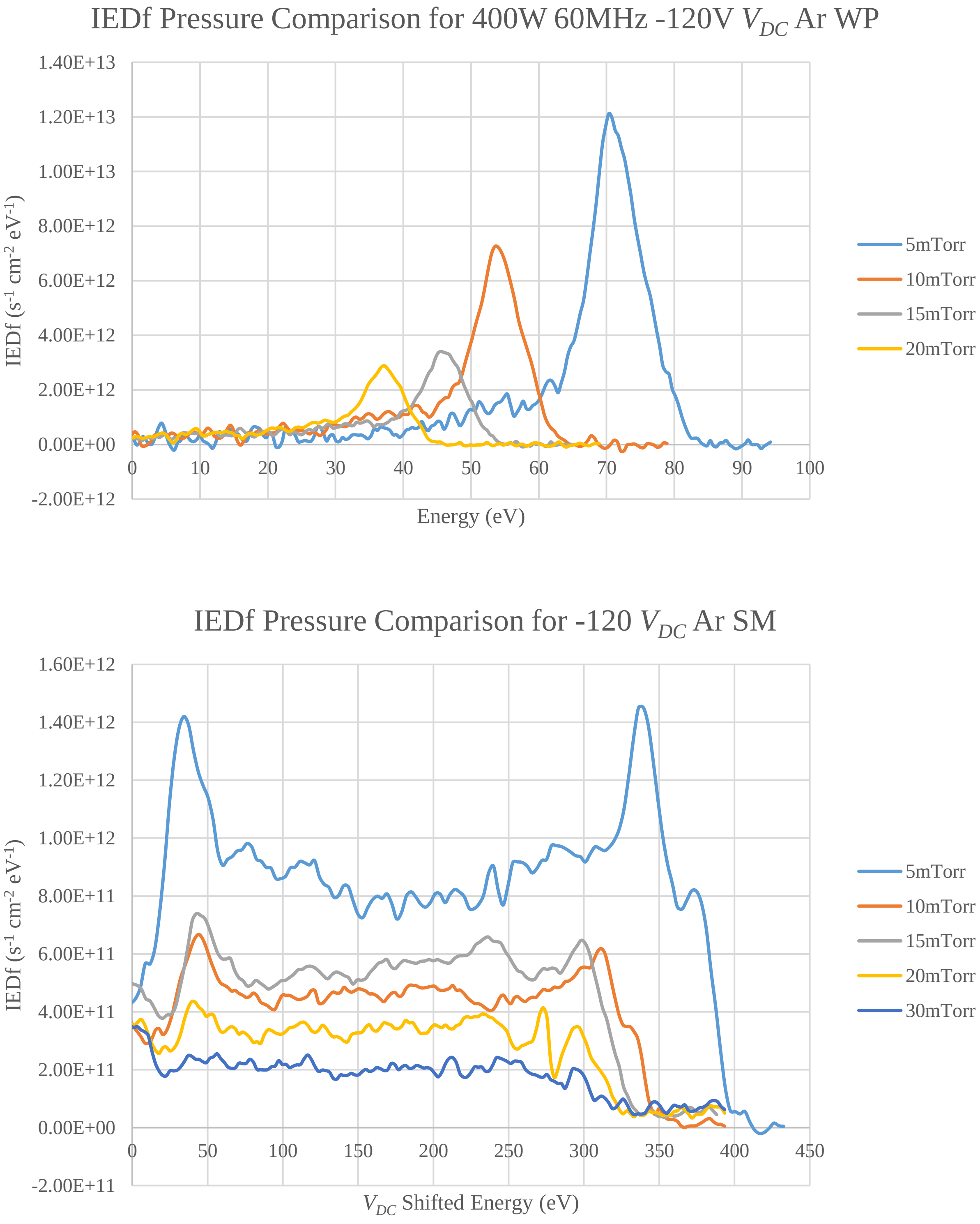

*Fig. 108*: IEDfs obtained from the WP and SM probes when varying pressure. The WP power and $V_{DC}$ conditions were consistent across all measurements. The SM $V_{DC}$ was held constant, but the source power and bias power were both varied between the pressures to keep $V_{DC}$ constant. As expected, in both plots, as the pressure increases, the IEDf intensity decreases likely due to plasma localization. The WP peak energies and SM high energy peaks also decrease in energy with increasing pressure.

grid. This can be seen when the pressure is increased to 80 mTorr where the IEDf should just be a single peak (See Fig. 109). In the plot, it appears that there are two peaks. One located just below -100 eV and one located around -35 eV (the fact that the peaks are both negative will be discussed shortly). This makes it seem like a bimodal peak structure but an 80 mTorr Ar IEDf should be a single peak due to the collisionality of the plasma. This first taller peak was actually an artificial peak dependent on the potential applied to the 2nd grid. This dependence can be seen in Fig. 110 where the measurement was taken at 5 mTorr and the 2nd grid voltage was varied. In the plot, the expected saddle shape peaks are obtained but a third peak was generated in the negative energy region. Based on the potential applied to the 2nd grid, the peaks shifted locations. This peak was probably generated from ionization in the RFEA due to secondary electron emission off the 1st and 2nd grids. Unlike with the old WP though, it does not seem that the

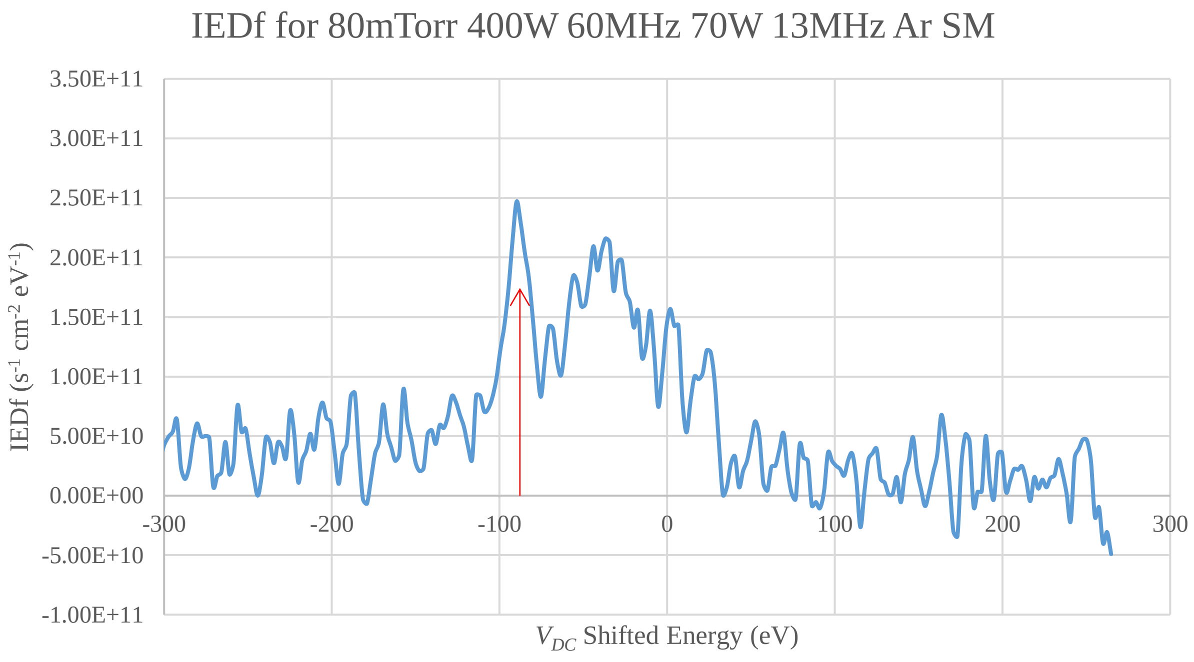

Fig. *109*: IEDf obtained from the SM probe for an 80 mTorr Ar plasma at 400 W 60 MHz 70 W 13.56 MHz. Two interesting characteristics here. The first is that the red arrow points to a peak that is dependent on the 2nd grid potential. The second is that after shifting the curve for the $V_{DC}$, the real peak still appears to be negative.

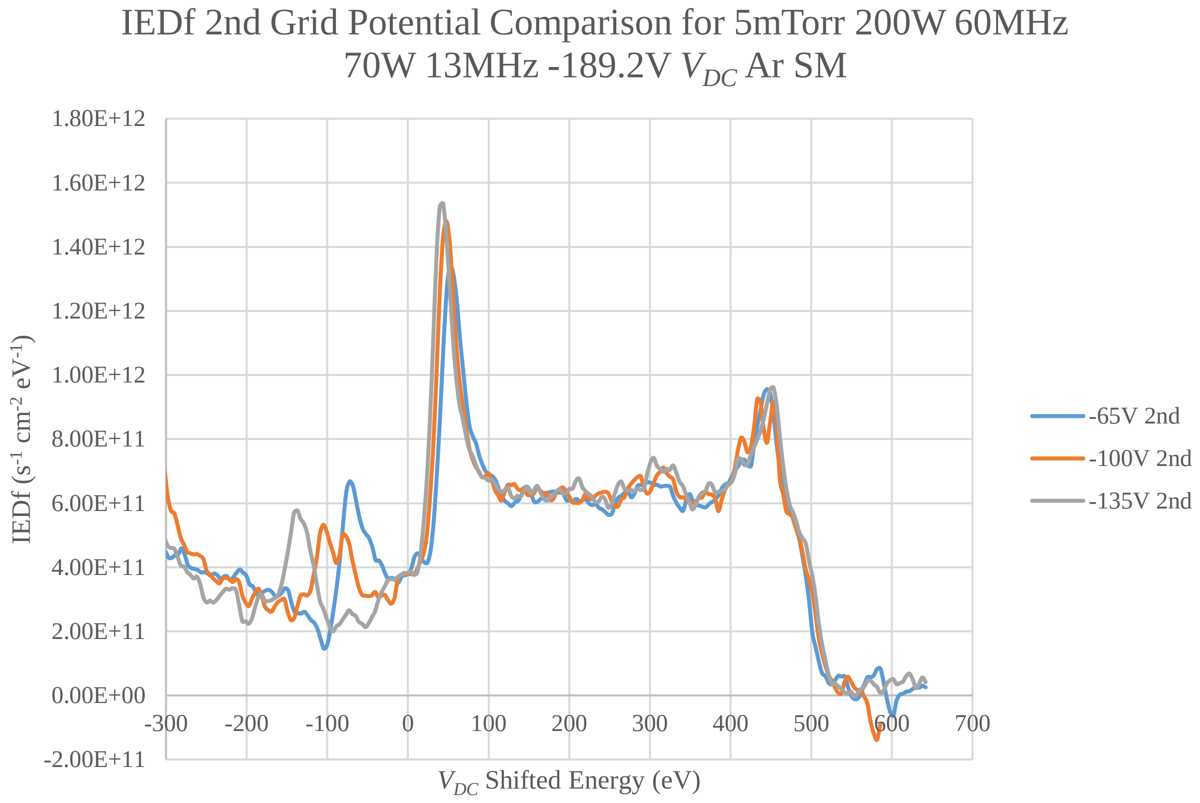

*Fig. 110*: Plot of IEDfs from the SM probe for a 5 mTorr Ar plasma at 200 W 60 MHz 70 W 13 MHz -189.2 $V_{DC}$. The 2nd grid potential was varied for the different measurements. The expected saddle shaped peak is obtained but, based on the 2nd grid potential applied, a third peak is generated at this potential.

ionization was sufficient to cause light up in the probe due to the fact that the expected IEDf is still obtained and the 2nd grid peak intensity is much lower than the real IEDf peaks. In the case with the old WP where light-up occurred, this 2nd grid peak was substantially larger in intensity (See IV current drop in Fig. 80) than any other peak obtained. This indicates that the SM probe is not lighting-up, even at 80 mTorr.

The second peak in the 80 mTorr case was not the only point of interest though. Secondary electrons emission may explain the second peak formation but does not explain why the two peaks in Fig. 109 are still in the negative energy region after being shifted by the measured $V_{DC}$. One possible reason for this is that the measured $V_{DC}$ was incorrect. This is unlikely though because it has been consistent in every other measurement and an increase in pressure should not affect the waveform measured on the 1st grid of the SM probe.

The more likely reason is that the $V_{DC}$ is not the only amount required to properly shift the curve. The $V_{DC}$ represents a shift from 0 V to the negative DC bias potential measured. Nonetheless, the ions initial frame of reference is not at 0 V but at the plasma potential ($V_p$). When the ions move from the plasma to the electrode, they traverse a potential difference ($\Delta V$) equal to

$$\Delta V = V_p - V_{DC} \tag{37}$$

A similar example was looked at for a single frequency plasma with a floating bottom electrode. Using the WP and SM probes, IEDf measurements were taken for a 5 mTorr Ar plasma for 400 W 60 MHz and a floating bottom electrode (See Fig. 111). Both IEDfs look correct except for the fact that the SM IEDf peak is located in the negative energy region even

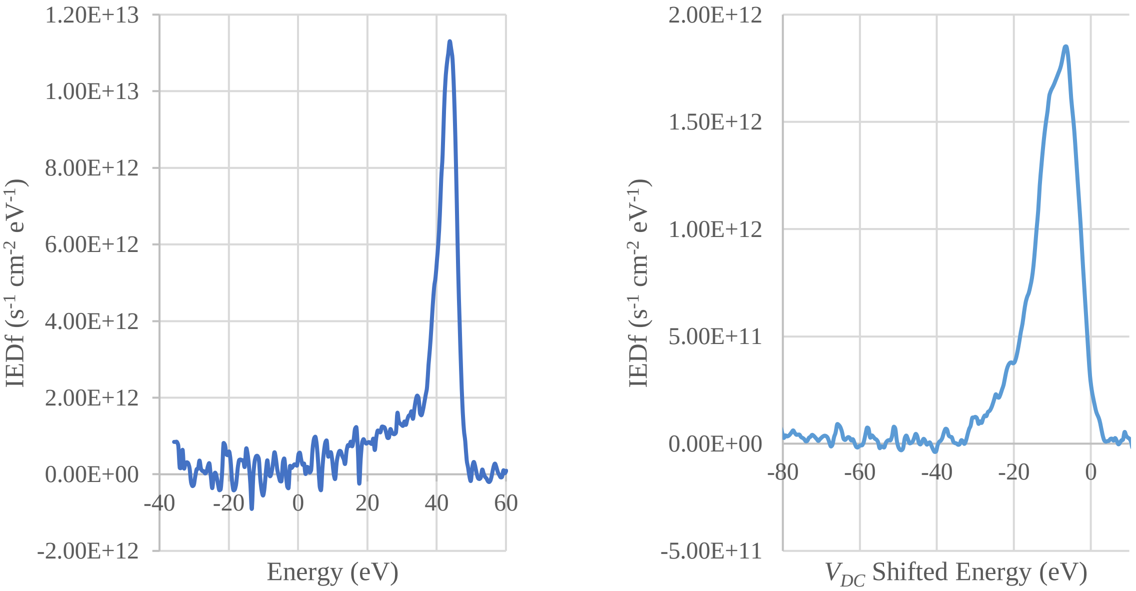

*(a)* *(b)*

*Fig. 111*: IEDfs obtained with the WP and SM probe for a 5 mTorr Ar plasma at 400 W 60 MHz and a bottom floating electrode. (a) WP IEDf that represents the ion energy gained from $V_p$ to ground (b) SM IEDf that was shifted for $V_{DC}$ but is in the negative energy region

after the $V_{DC}$ shift had been applied. In this instance, the $V_{DC}$ was positive because the electrode floated up to the floating potential ($V_f$). However, the ions should have and did gain energy. They gained energy because their initial frame of reference was at $V_p$ which was more positive than $V_f$. That means, to properly shift the SM IEDf, the difference between $V_p$ and $V_f$ must be used. Since the WP IEDf represents the average amount of energy an Ion gains traveling from $V_p$ to ground, the difference between $V_p$ and $V_f$ can be found by

$$V_p - V_f = WP_{peak} - V_{DC} \tag{38}$$

where $WP_{peak}$ is the peak energy in (eV) of the WP IEDf. Shifting the SM IEDf by $V_p - V_f$ gives the IEDf seen in Fig. 112. This new shift puts the SM IEDf in the positive energy region as expected.

This applies to the 80 mTorr SM IEDf because the $V_{DC}$ shift did not include the energy gained by the ions moving from $V_p$ to 0 V. If this extra energy were included in the $V_{DC}$ shift, this

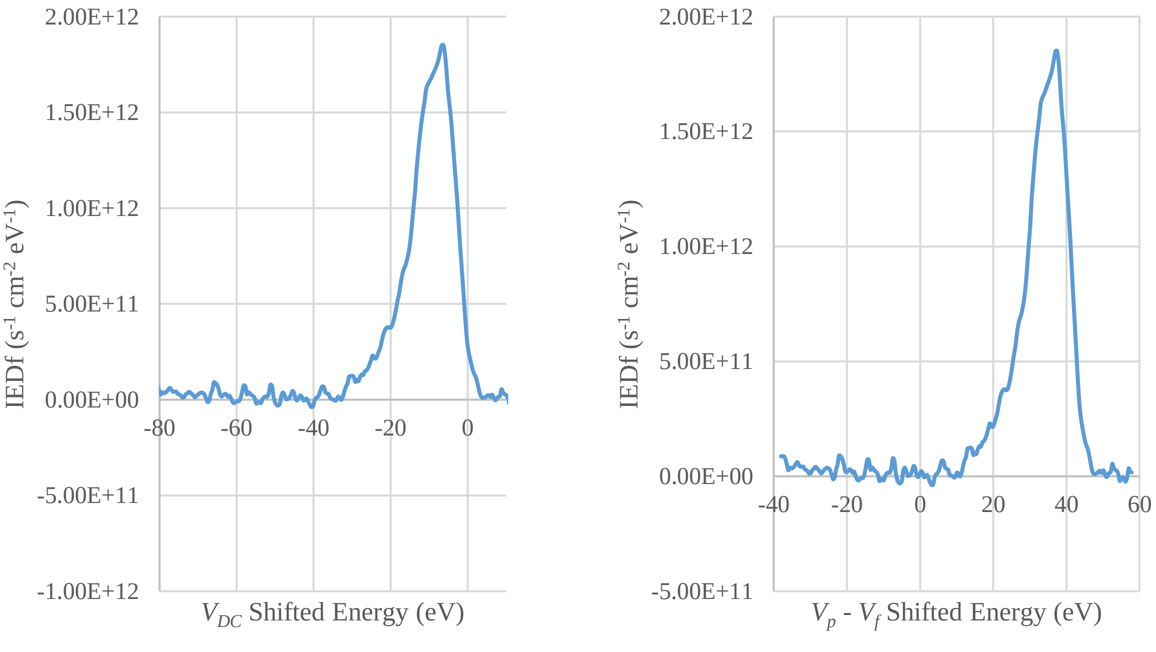

*(a)* *(b)*

*Fig. 112*: Plots of the shifted SM IEDf curves. (a) The original IEDf shifted by $V_{DC}$ (b) The new IEDf shifted by $V_p – V_f$. Shifting by $V_p – V_f$ now puts the SM IEDf in the positive region.

should push the real peak of the 80 mTorr SM IEDf in Fig. 109 to positive values. It would also shift the artificial 2nd grid peak to be in better agreement with the actual 2nd grid voltage applied (-65 V). In all the previous IEDfs, the energy gained from $V_p$ to 0 V was not accounted for in the shift though and the IEDfs were fine. This is probably due to the fact that, for the previously presented dual frequency IEDfs, the value for $V_{DC}$ was much larger than the value of $V_p$. Since $V_{DC}$ was so much larger, it still gave IEDf peaks close to the proper position. If the $V_p$ were to be accounted for, it would probably only shift these peaks by at most a couple of 10s of eV.

# CHAPTER 5: PROCESS CHEMISTRY RFEA MEASUREMENTS

## 5.1 Single Frequency Measurements

As chapter 4 looked at single frequency measurements in Ar, the next step in testing the RFEA is to take measurements with the RFEAs in gas compositions and power configurations more consistent with industrial processes. It is still desirable to increase the complexity of the measurement incrementally to elucidate mechanisms to ion energy distribution characteristics so, for the first set of measurements, like in chapter 4, the system was operated under a single frequency. As with the argon cases summarized in the previous chapter, the top electrode was again run at 60 MHz and the bottom electrode was grounded. The floating grid (1st) of the floating probe (F) was also externally grounded as in the measurements in section 4.1. The filter setup was exactly the same as in section 4.1 as well. Unlike chapter 4, this chapter focuses on the IEDf analysis and not on the IV characteristics from which they are derived. These measurements, although run under different conditions than those run in the previous chapter, did not show anything drastically different from the IV curves presented in section 4.1.2. The IV curves measured under these conditions had the same basic trends that were observed in the single frequency Ar plasma IV curves (See Appendix C). Since this is the case, one is referred to section 4.1.2 for an analysis of the IV curve characteristics that are also applicable here. Starting with this grounded setup, it makes easier to focus on the effects on the IEDfs caused by the addition of a process gas such as carbon tetrafluoride ($CF_4$).

### 5.1.1 Ar – $CF_4$ Comparison

Again, it was important to validate the IEDfs obtained from the RFEA measurements after the addition of $CF_4$. To do this, measurements were taken with the surface mount (SM), top mount (TM), and F probes and compared to results presented by Donko and Petrović [ 93 ]. For their simulations, particle-in-cell simulation with Monte-Carlo treatment of collisional phenomena (PIC/MCC) was used to model capacitively coupled plasmas (CCPs) composed of Ar, $CF_4$, and Ar – $CF_4$ for single and dual frequency RF sources. The particular results of interest were obtained by modeling a Ar – $CF_4$ plasma at 20 mTorr with a single frequency source at 100 MHz. The gas mixture contained 90% Ar and 10% $CF_4$. The 100 MHz source used a 60 V amplitude. A plot recreated from data they presented can be seen in Fig. 113.

Similar plasma conditions were created in the CCP chamber of this work. The pressure was set to 20 mTorr and a pressure ration of 90% Ar and 10% $CF_4$ was used as the gas mixture. As mentioned earlier, the bottom electrode was also grounded. There were two main differences between the simulated work and these measurements. The primary difference was that 60 MHz was used as the RF source frequency on the top electrode instead of 100MHz. Although this high of a frequency is not expected to have a significant impact on the IEDf shape at these density ranges, the partitioning of sheath voltage and electron heating will slightly favor the 100MHz case resulting in slightly higher plasma density at comparable electrode potentials. Voltage values on the top electrode were also unknown so the source power was varied, and multiple measurements were taken to capture IEDfs over the expected range of voltages and densities

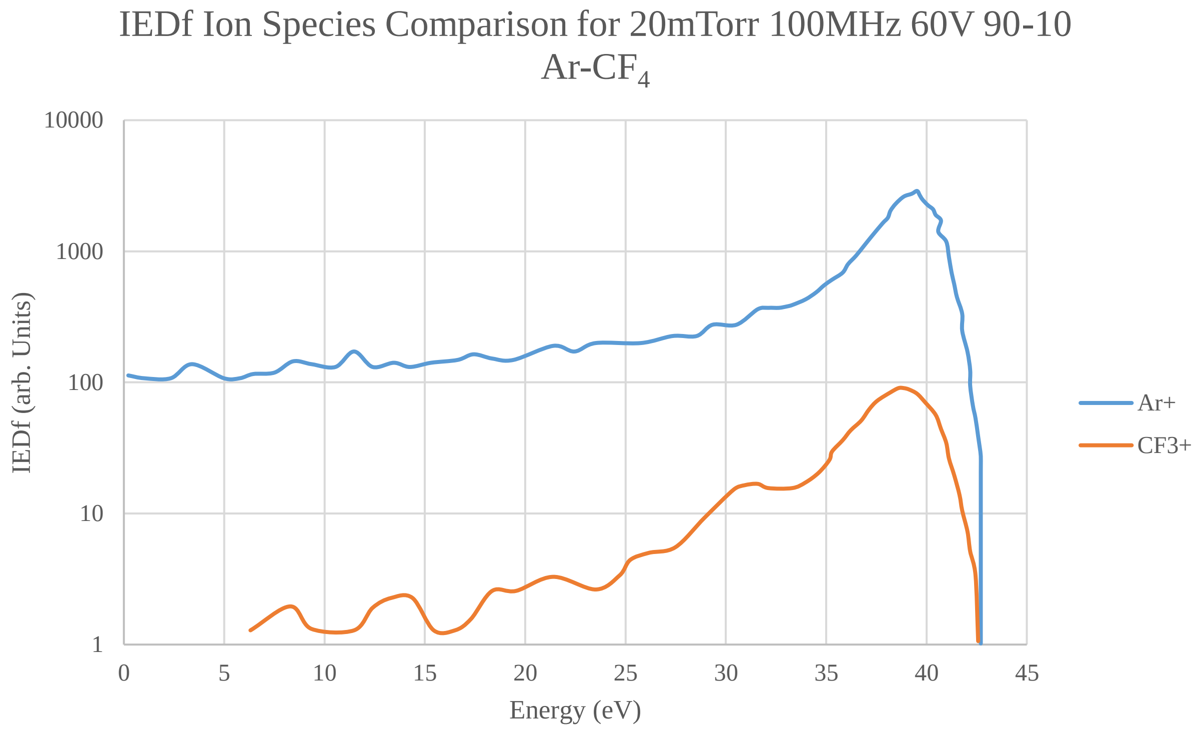

*Fig. 113*: IEDfs recreated from data presented by Donko and Petrović [ *93* ]. This plot shows the IEDf for $Ar^+$ and $CF_4^+$ ions for a simulated 20 mTorr CCP with a 100 MHz 60 V source and grounded secondary electrode.

from the simulation work. Third, since these measurements were made with an RFEA, and individual ion masses could not be discriminated, no distinction between the gas species was made. Lastly, to make the comparison between the simulated results and measured results easier, the IEDfs were normalized by their peak energies. This made it easier to focus on the peak location and shape of the IEDfs in comparison to one another.

Plots of the measured IEDfs compared to the simulation results can be seen in Fig. 114. Two separate plots were made due to the noisy nature of the TM IEDf. The cause of the noisy in the TM IEDf is unknown as no other IEDf measured with the TM probe at different 60 MHz powers produced the same kind of result (See Fig. 116). The 500 W case was chosen from the SM, TM, and F probe measurements since the 500 W case produced results most consistent with the 100 MHz 60 V simulation case presented. As can be seen in Fig. 114 (a), the IEDfs from the

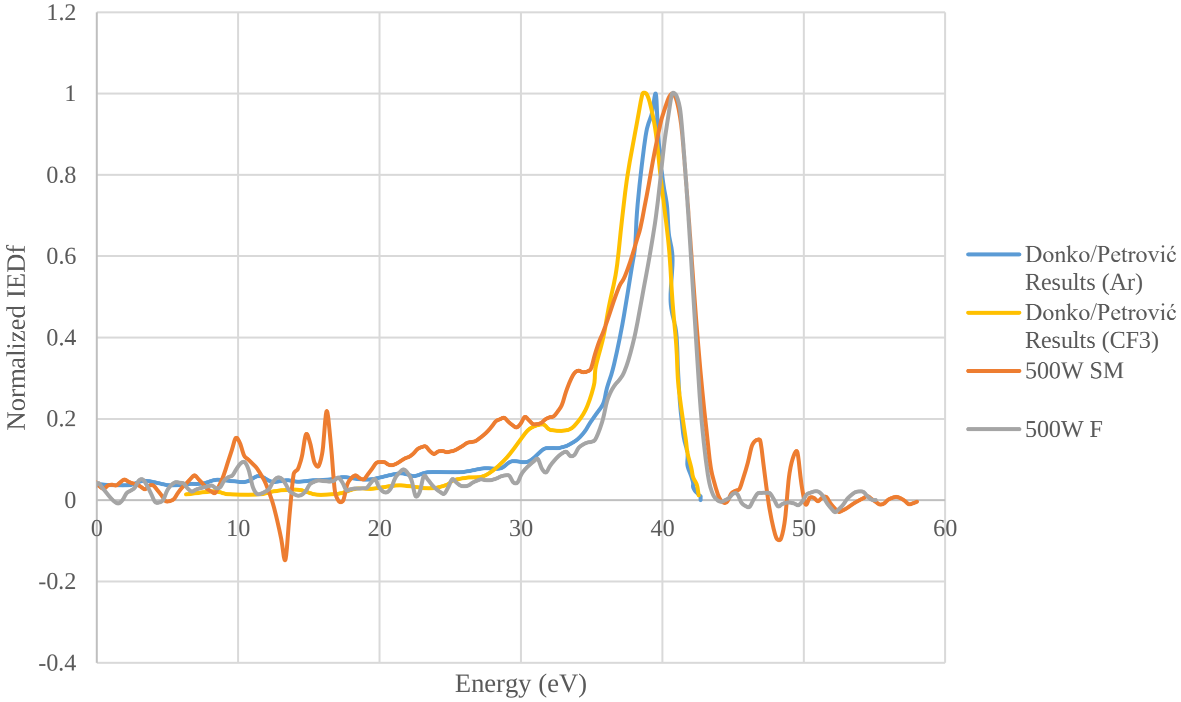

*(a)*

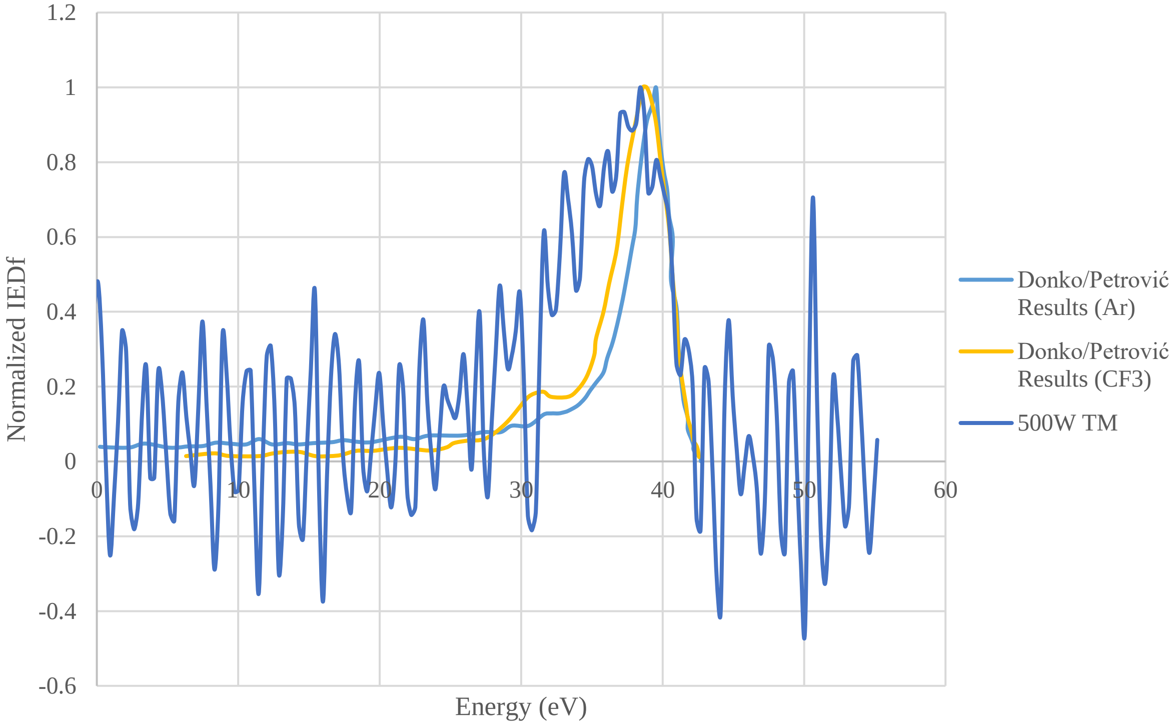

*(b)*

*Fig. 114*: Plots of the normalized measured IEDfs compared against the normalized simulations results presented by Donko and Petrović. [ *93* ] (a) IEDfs from the SM and F probes (b) IEDf from the TM probe. Two plots were made for clarity due to the noisy nature of the TM IEDf.

SM and F probes match the simulation results quite well. The peak locations are only off by couple of eV and the shape of the curves are very similar to one another. The IEDf from the TM probe also has a peak location very consistent with the simulation results (See Fig. 114 (b)). The shape of the TM IEDf seems to slightly off from the simulation results though. The slope of the low energy tail is more gradual in the TM IEDf. However, it is possible that this slope is due to the noisy nature of the IEDf. Overall though, the measured IEDfs from the SM, TM, and F probes are very consistent with simulation results from previous work and the RFEAs are providing reliable measurements in the more complex gas mixture.

### 5.1.2 Ar – $CF_4$ Probe Comparison

Having compared the Ar – $CF_4$ probe measurements against expected results, the IEDfs from the probes for this gas mixture can be further analyzed. For these measurements, the plasma measured was a 20 mTorr Ar – $CF_4$ plasma with a 90% to 10% pressure ratio between the gases. The 60 MHz source power was adjusted between 100 W and 600 W with 100 W increments. The resulting IEDfs from the wall probe (WP), SM, TM, and F probes can be seen in Fig. 115 and Fig. 116. The IEDfs obtained from all the probes are single peak IEDfs similar to what was observed in section 4.1.3. Again, even though a 60 MHz RF source is powering the plasma, a single peak is produced due to the chamber asymmetry and the sheath potential dependence on frequency. As mentioned in chapter 4, the combination of these two phenomena probably caused the RF potential across the sheath to be miniscule leaving the difference between the average plasma potential $\left(\overline{V_p}\right)$ and the grounded surface as the main source of ion acceleration. As expected, when the source power was increased, the peak energy and flux intensity also increased. The increased power will increase the $\overline{V_p}$ and plasma density causing the higher peak energy and flux intensity. The shape of the IEDfs are generally consistent as well. The only

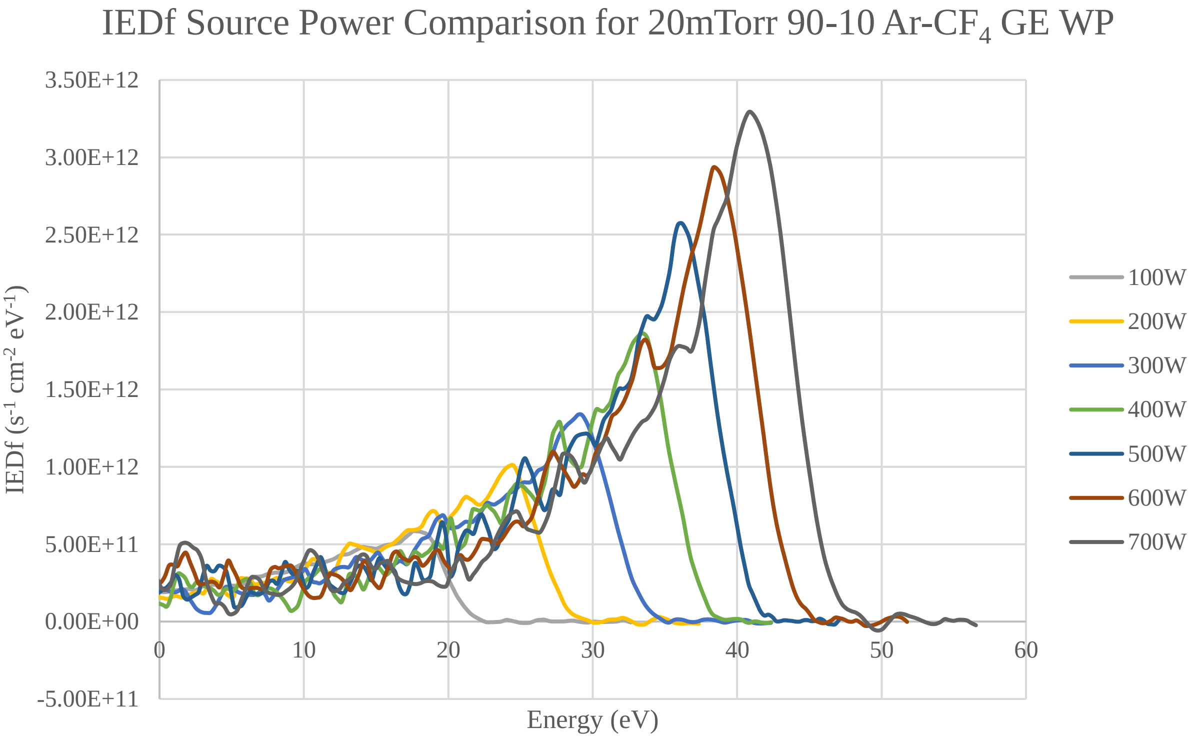

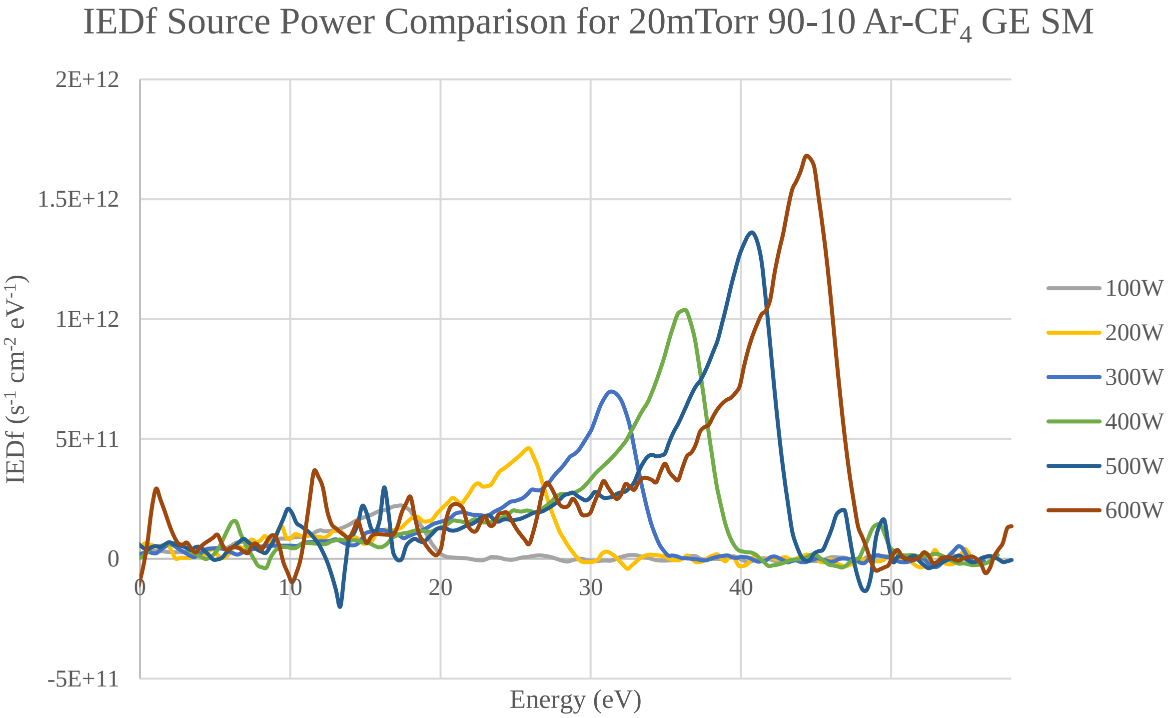

*Fig. 115*: Plots of IEDfs obtained from the WP and SM probes for a 20 mTorr 90-10 Ar-CF4 plasma at different 60 MHz source powers. The SM probe was housed in a grounded electrode (GE) during these measurements.

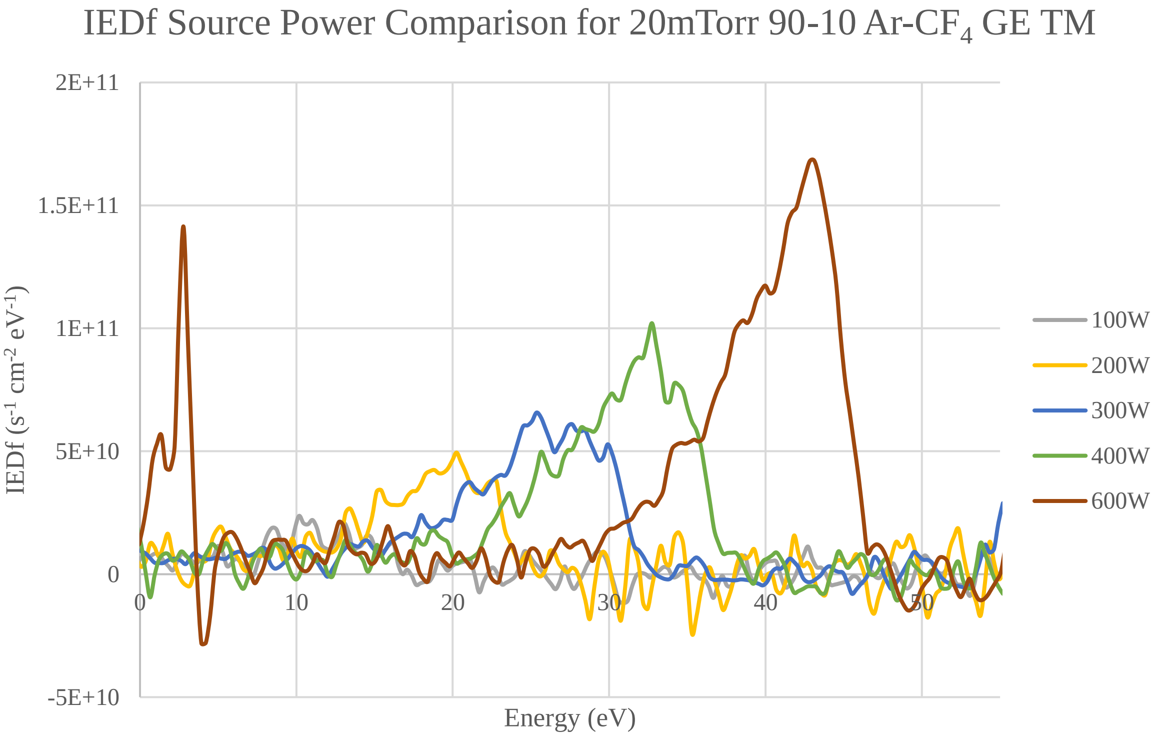

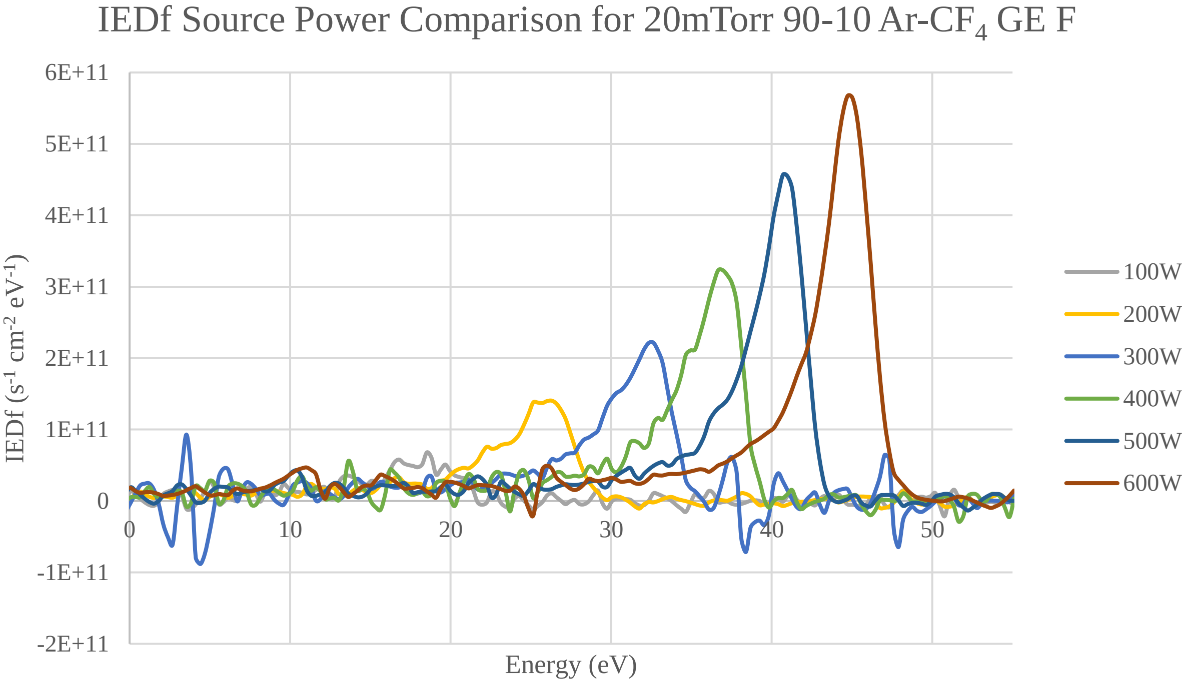

*Fig. 116*: Plots of IEDfs obtained from the TM and F probes for a 20 mTorr 90-10 Ar-CF4 plasma at different 60 MHz source powers. The TM and F probes were all housed in a grounded electrode (GE) during these measurements. The 500 W TM IEDf (See Fig. 114 (b)) was removed from the TM IEDf plot for clarity. For a clearer picture of the trends of the WP IEDf plot at lower powers, see Appendix B.

IEDfs that seems like they may have a larger low energy tail are TM IEDfs. This is reasonable though because the ions have to travel down the drift cone before reaching the RFEA, so they have a higher chance of experiencing a collision. The only thing that seems to contradict this idea is that the F IEDfs do not contain the same large low energy tail. The shape of the F IEDfs are more consistent with the WP and SM IEDfs even though the ions must traverse the drift cone to reach the F probe too. The only other possible cause would be plasma non-uniformity. The location of the TM and F probes are different. The TM probe is in the center of the chamber will the F probe is closer to the edge of the bottom electrode. The plasma density is likely higher in the center of the chamber which could cause more collisions, but it is possible that the density difference is enough to cause such a shape difference.

The locations of the peaks seem pretty consistent as well for each power setting. This is more clearly seen in Fig. 117 where the 400 W cases from each of the probes are compared with one another. A significant difference in intensity can also be seen depending on the probe used to obtain the IEDf. It is possible that some of intensity difference is due to plasma non-uniformity, but the WP is closest to the top electrode while being farthest radially from the center of the chamber. A more likely cause is differences in entrance geometries and the distance the ions must travel. The entrances to all the probes are through a grid with the same dimensions for hole diameter and aspect ratio (See Table 2 and Fig. 17). Where they differ is in the fill grid diameter. The entrance to the WP has a 0.069” (1.75 mm) fill diameter (See section 4.1.2) while the entrances to the SM, TM, and F probes has a 0.039” (1 mm) hole diameter in the Si wafer below the Si grids. This smaller entrance diameter could explain why the WP has the highest incoming flux. It is understandable that the WP and SM probes would have higher intensities than the TM and F probes because the ions do not have to travel through a 0.59” (15 mm) drift cone. Again,

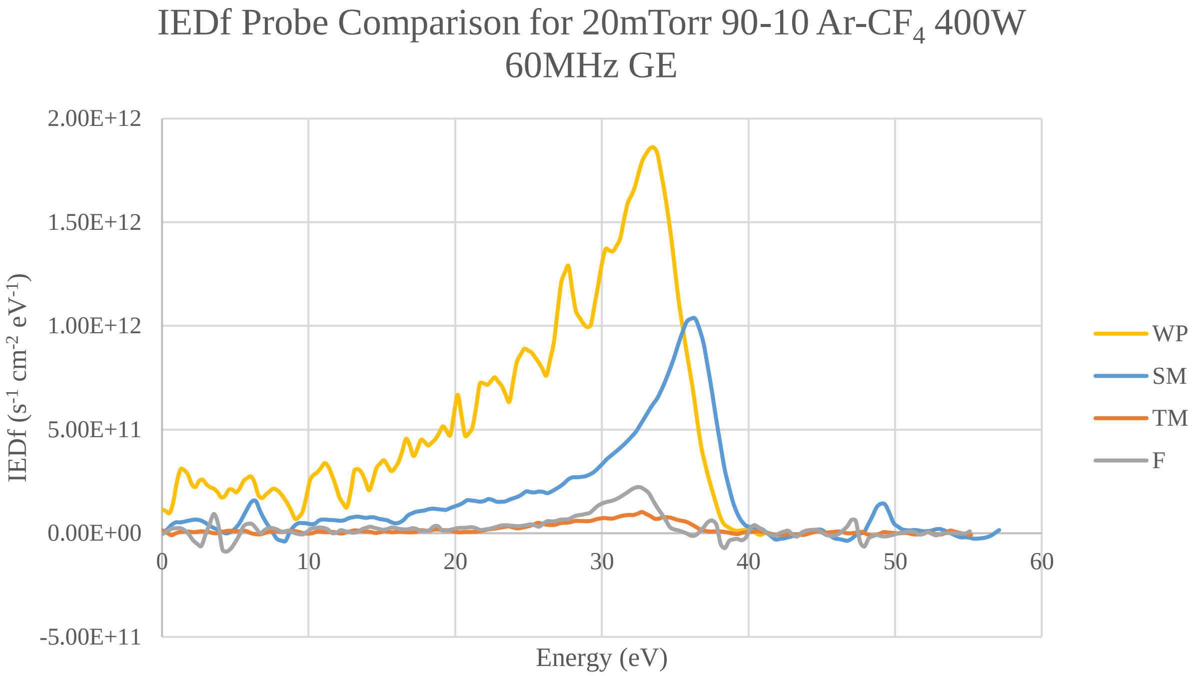

*Fig. 117*: Plot comparing the IEDfs from the WP, SM, TM, and F probes for a 20 mTorr 90-10 Ar-CF$_4$ plasma with a 400 W 60 MHz RF source. The peak energies line up quite well but a significant drop in intensity is seen depending on the probe used. The SM, TM, and F probes were all housed in a grounded electrode (GE) during these measurements.

the only case that seems a little counter intuitive is the TM and F IEDfs. In both cases, ions must travel down a drift cone and the only difference is their location in the chamber. As mentioned previously, it is possible it is due to density differences in the plasma. Whether that is enough to cause more collisions for the TM probe measurement though would require further investigation.

### 5.1.3 Ar – CF$_4$ Pressure Ratio Comparison

After looking at the effects of power on the IEDf for a Ar – CF$_4$ gas mixture, the next step is to analyze how changing the concentration of CF$_4$ affects the IEDf. For these measurements, the WP and SM probes were used for with a plasma pressure of 20 mTorr. The pressure ratio of the CF$_4$ was changed between 1% and 15%. For the measurements with the WP, the plasma was generated using a 400 W 60 MHz source. On the other hand, for the SM probe, the plasma was generated using a 200 W 60 MHz source. In both instances, the IEDf obtained for a pure Ar plasma was plotted along with the Ar – $CF_4$ IEDfs.

The resulting IEDfs can be seen in Fig. 118. For the WP measurements, a significant drop in intensity is observed by just adding in 1% $CF_4$ to the plasma. This is expected because of the loss of electrons with the addition of $CF_4$. For an Ar plasma, ionization typically happens by two methods. The first is a high energy electron, where the energy is above the ionization threshold of Ar (15.4 eV), collides with a ground state neutral Ar atom and causes an electron to be released. The second method, which can be comparable in frequency, is a two-step electron impact ionization process where a lower energy electron collides (11.6 eV) with an Ar atom raising the ion energy to a metastable state ($Ar^*$). Then, a second low energy electron collides with this $Ar^*$ and provides the last bit of energy necessary for ionization. Although this ionization process requires two steps, the necessary threshold energy for each step is sufficiently lower than the ionization threshold such that a much larger fraction of the electron population can contribute to the stepwise process.

However, when trace additives such as $CF_4$ are added to Ar, a process of dissociative electron attachment occurs [ 18 ]. In this process, a high energy electron collides with a $CF_4$ molecule and causes the molecule to split into a carbon trifluoride ($CF_3$) molecule and a fluorine atom (F). Both $CF_3$ and F are susceptible to electron attachment. What occurs most often is that the electron that caused the split of the $CF_4$ molecule afterwards combines with F to form $F^-$ ions. This results in a loss of low energy electrons. In addition to this electron loss, $CF_4$ quenches, or deexcites, the $Ar^*$ when added to the gas mixture. The slight addition of $CF_4$ has been shown to significantly decrease the $Ar^*$ density [ 94, 122 ]. With the decrease in electron and $Ar^*$ density, the number of $Ar^+$ ions formed through $Ar^*$ is drastically decreased. This decrease in electron

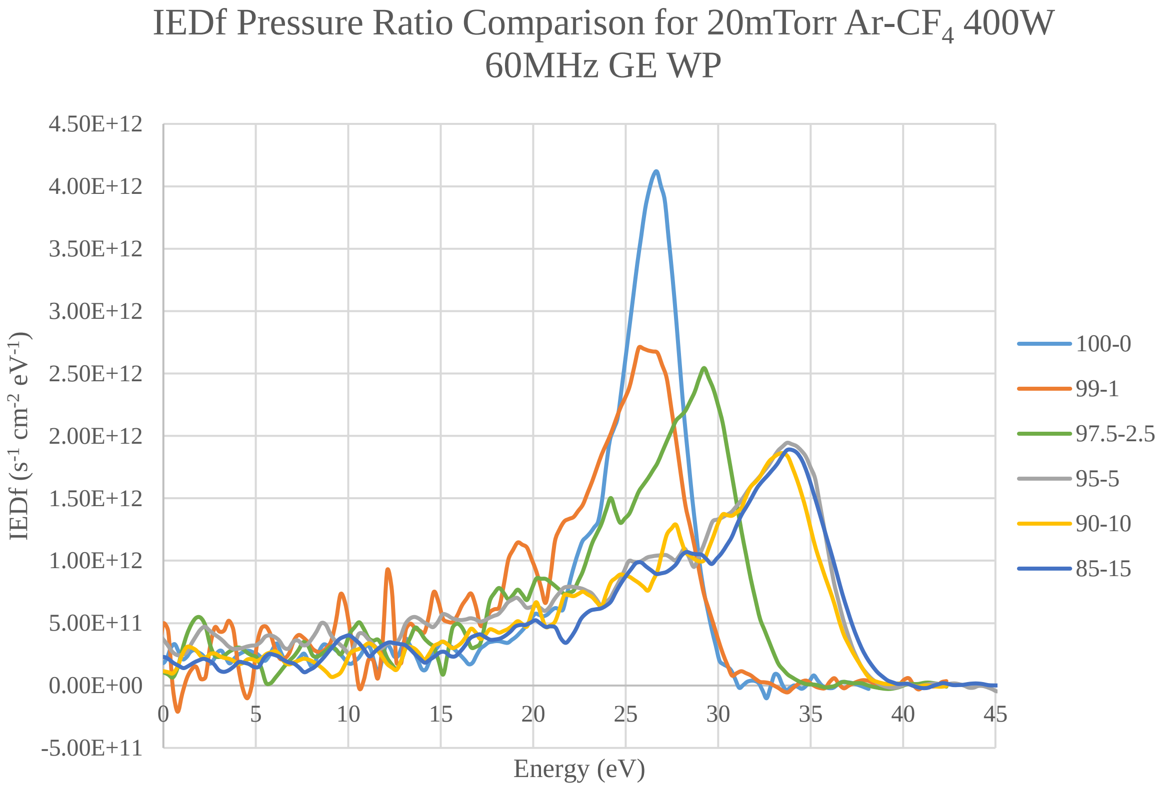

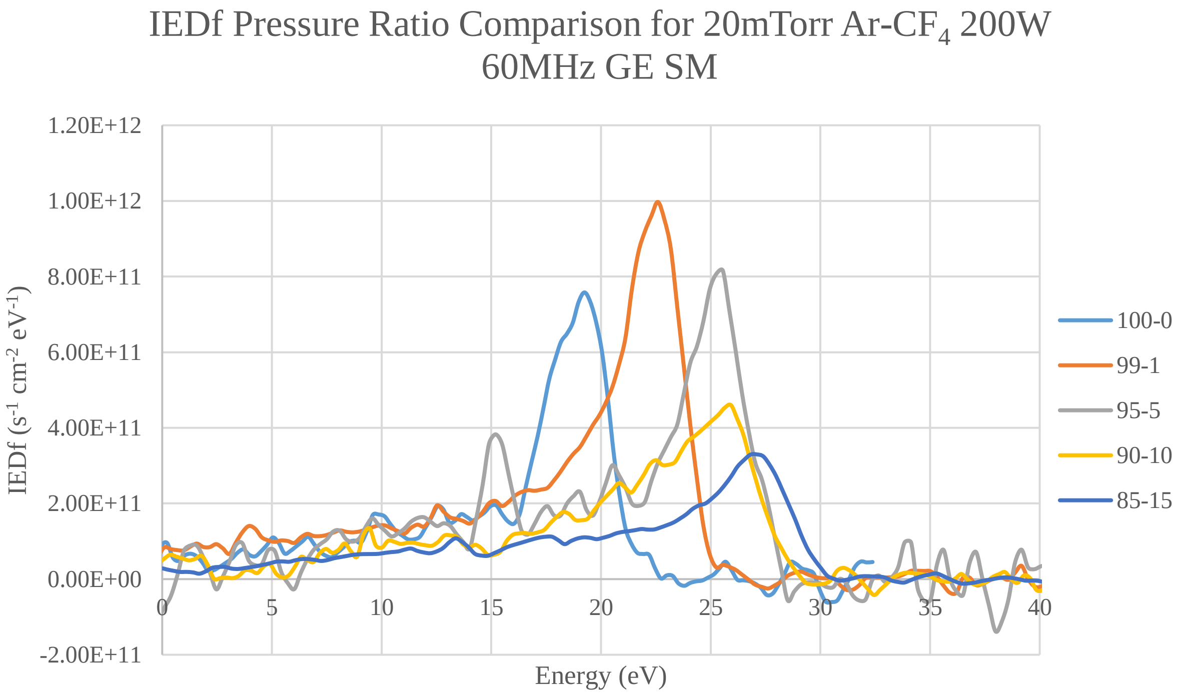

*Fig. 118*: Plots of the IEDf based on the pressure ratio of Ar-$CF_4$ from the WP and SM probes. The plasma was generated using either 400 W or 200 W from the 60 MHz source. The bottom electrode was grounded (GE).

and $Ar^*$ density continues with increasing $CF_4$ concentration resulting in lower WP IEDf intensities seen in Fig. 118.

This decrease in intensity is also seen in the SM IEDf measurements except between the pure Ar plasma and a 1% concentration of $CF_4$. A possible cause for this contradictory trend in the intensity is with the initial addition of $CF_4$, the plasma become less localized to the top 60 MHz electrode. As was mentioned in section 4.1.2, the data suggests for an Ar plasma that as the pressure increases, the plasma localizes towards the source electrode resulting in an intensity drop in the IEDfs measured by the probes. It is possible that the reduction in intensity caused by the density drop from the $CF_4$ addition may be offset by the decrease in localization in the plasma, so the intensity rises at 1% concentration $CF_4$. Then as the concentration increases, the density drop is more significant and is reflected in the IEDf intensity. The reason this was not observed in the WP measurements may be due to the fact that the impact of the localization is not as strong at the WP location.

For both the WP and SM IEDfs, an increase in peak energy is seen with increasing $CF_4$ concentration. Since the WP and SM IEDfs were obtained at grounded surfaces, the ion energy measured it created by the difference between the plasma potential $\left(V_p\right)$ and the ground potential (0 V). Since the ground potential remains unchanged with increasing $CF_4$ concentration, the $V_p$ must have increased to result in higher peak energies with increasing $CF_4$ concentration. The increase in peak energy comes with diminishing returns though. In the WP case, once the concentration reached 5%, the peak intensity and peak shift stopped. A similar trend is also observed with the SM IEDfs. For the SM case, the decrease in peak intensity and shift in peak energy does not stop but it shows a smaller decrease and shift as the $CF_4$ concentration continues to increase. These results show it takes only a small addition of $CF_4$ to drastically change the IEDf of the plasma.

Lastly, as pressure had an effect on the IEDfs for the Ar plasma measurements (See section 4.1.3), pressure was analyzed for the Ar – $CF_4$ measurements. In this case, the measurements were taken using the WP at 20 mTorr and 40 mTorr. The Ar – $CF_4$ pressure ratio was also varied. The concentration of $CF_4$ was varied the same way as the previous measurements. The plasma was generated using a 400 W 60 MHz RF source.

The IEDfs obtained from the WP measurements can be seen in Fig. 119. The 20 mTorr IEDfs was analyzed previously and the 40 mTorr IEDfs follow the same trends as the 20 mTorr

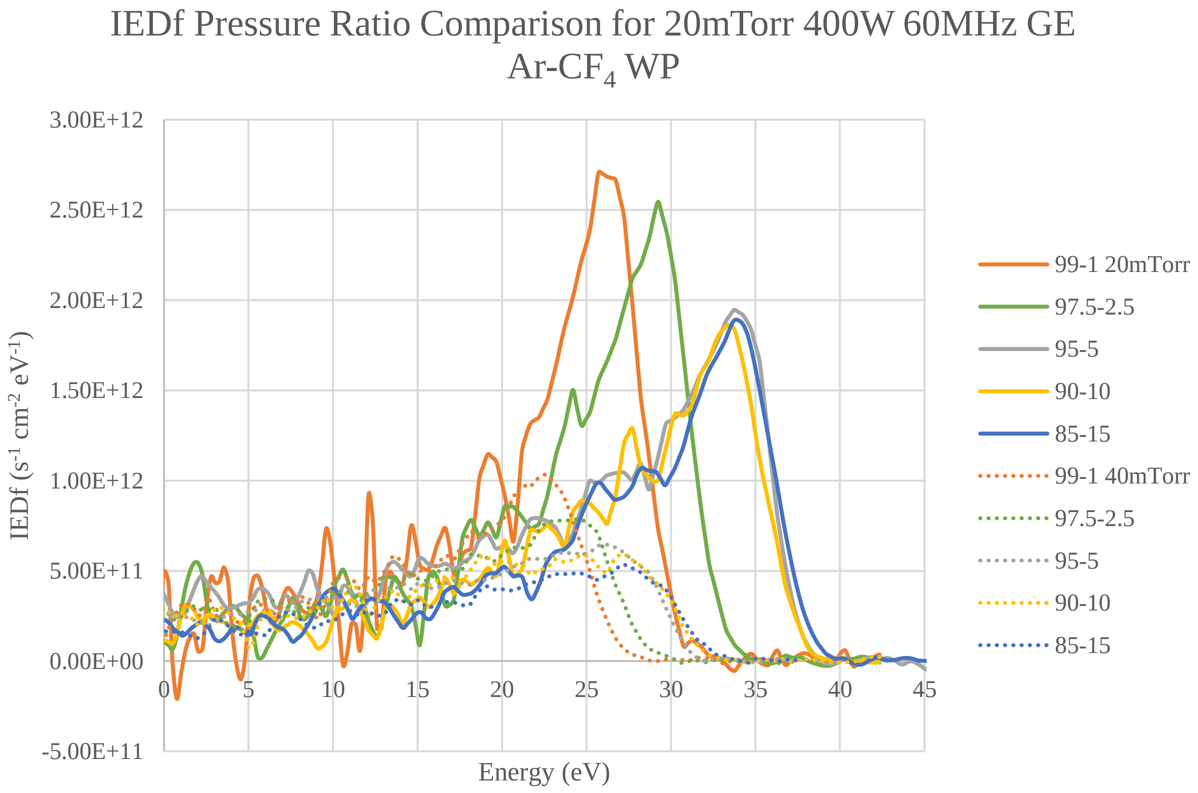

*Fig. 119*: Plot of the IEDfs obtain by the WP for a 20 mTorr and 40 mTorr Ar – $CF_4$ plasma generated by a 400 W 60 MHz RF source. The bottom electrode was grounded (GE) during these measurements.

measurements. The peak energies of the 40 mTorr IEDfs are a little lower than the 20 mTorr case. The likely reason for the peak energy drop is due to an increase in collisions from an increase in plasma density. The 40 mTorr data also shows the same diminishing return trend with increasing $CF_4$ concentration. The data shows that the ion energy increases and IEDf intensity decreases with increasing $CF_4$ until the $CF_4$ concentration reaches 5%. After this point, the peakenergy and peak intensity remains relatively constant. The cause for this trend is the same as explained previously. The energy increase is due to a $V_p$ increase and the intensity drop is due to a drop in plasma density.

The biggest difference between the 20 mTorr and 40 mTorr WP IEDfs is the peak intensity drop that occurred after increasing the pressure. This is similar to the peak intensity drop that occurred in the Ar plasma measurements (See section 4.1.3). The cause for this peak intensity drop is likely the same reason that caused the peak intensity drop in the Ar plasma measurements at higher pressures. As Ar plasma intensity changes and density measurements suggested, the peak intensity drop in from an increase in pressure is likely caused by localization of the plasma towards the 60 MHz source electrode effectively pulling the plasma away from the walls of the chamber.

To confirm this localization effect, hairpin resonator probe (or hairpin) measurements were also performed in an Ar – $CF_4$ plasma. For more detail on the hairpin resonator probe, one is referred to section 4.1.2. For these measurements, an Ar – $CF_4$ plasma was generated at 40 mTorr and 60 mTorr. The power of the 60 MHz RF source was varied between 100 W and 1200 W. The hairpin was located in the center of the chamber equidistant (approximately 1.57” or 4 cm) from the 60 MHz top electrode and the grounded bottom electrode. The plasma density measurements can be seen in Fig. 120. Except for a single power (100 W) the density plot shows a decrease in density when switching from 40 mTorr to 60 mTorr. This result is contradictory to what is generally expected for the center of the plasma. As such, this trend supports the idea that the plasma localizes towards the source electrode as the pressure increases.

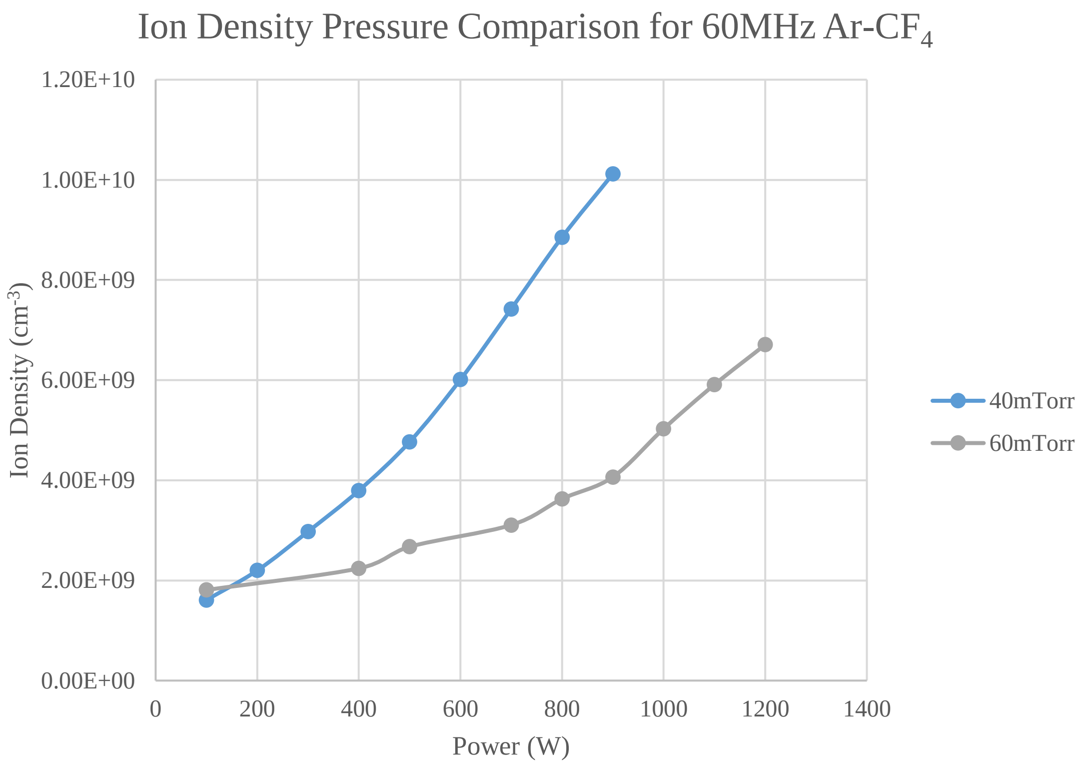

*Fig. 120*: Plot of the ion density taken using a hairpin resonator probe at two different pressures for a Ar-$CF_4$ plasma. In this case, only the 60 MHz source was used, and the bottom electrode was floating.

### 5.2 Dual Frequency Measurements

Having performed measurements with the grounded electrode, the next and last step to this set of measurements was to reconnect the 13.56 MHz generator back to the bottom electrode that houses the surface mount (SM), top mount (TM), and floating (F) probes. The chamber and filter setup for these measurements was exactly the same as the dual frequency Ar plasma measurements described in section 4.2. The Impedans Semion filter (See Fig. 95) and Allen

Avionics filters (See Fig. 96) were again used to filter out the RF noise on the signal lines running to the plasma electron rejection grid, discriminator grid, and collector. The Tektronix high voltage probe was also used again to measure the RF waveform on the 1st grid of the SM probe. The $V_{DC}$ for the measurement was obtained by taking the average of this waveform like described in section 4.2. Also, the floating (F) probe was not used in these measurements due to the results presented in section 4.2.2 that showed the F probe does not provide an accurate IEDf. The major difference between these measurements and those performed the previous chapter was that $CF_4$ was added to the Ar gas. Oxygen ($O_2$) was also added to the Ar – $CF_4$ mixture for some of the measurements. With the addition of these other gases, the plasma generated in this dual frequency capacitively coupled chamber are much more consistent with actual industrial processes used in the semiconductor industry.

With the addition of a second gas, and especially a molecular gas, the complexity of a dual frequency plasma increases. The number of ionic species found within the plasma drastically increases, especially with a molecular gas such as $CF_4$ or oxygen ($O_2$). The increase in ionic species includes both positive and negative ions. Since the RFEA was operated to measure positive ionic species, any negative ions that enter the detector are rejected similar to plasma electrons. Even if negative ion species are rejected, multiple positive ion species will be generated when using multiple gases or even just a molecular gas. This is a result of dissociation of the molecule by electron impact. The dissociated atoms or molecules are then capable of being ionized by more electron impact.

In general, RFEAs are not used, or even capable of distinguishing the IEDf peaks based on the species of ion unless they are with a mass spectrometer. Depending on the mass of the ion species created from the gas mixture though, it may be possible to assign ion species to specific peaks if they travel through an RF sheath. Edelberg *et al*. describe this process when looking at a gas mixture of Ar and neon (Ne) and the molecular gas $O_2$ [ 60 ]. The ion transit time in the sheath proportional to the ion mass [ 9, 10 ] (See Eq. 1), the multiple ion species will traverse the sheath at different rates. Based on this, it is possible that the different ion species will respond to the oscillating sheath differently. If the mass is sufficiently low, the ions will be able to travel across the sheath quickly and encounter little variation in the electric field of the sheath creating two peaks. On the other hand, if the mass is larger, it may experience a large amount of a single sheath oscillations or even multiple oscillations. In this case, the ions will respond to the time averaged electric field of the sheath generating two peaks with a smaller gap between the up to the extreme of a single peak. The results of Edelberg *et al*. showed that for an Ne (20 amu) and Ar (40 amu) plasma, four peaks are created in the IEDf. Based on the mass difference between the two ions, the out peaks are created by $Ne^+$ and the inner two peaks are created by $Ar^+$. When they moved to $O_2$, the IEDf showed four peaks as well. Since electron impact can dissociate $O_2$ into a single O and also ionize O so that it becomes $O^+$, the outer peaks were attributed to $O^+$ and the inner peaks to $O_2^+$ due to the mass difference. Since multiple gases, and molecular gases at that, are used to generate the results in this section, this multiple peak trend was observed in the IEDf.

Lastly, IV curves characteristics are not discussed like in section 5.1 since the IV curves obtained for these measurements did not show anything drastically different from the IV curves presented in section 4.2.1. The IV curves measured under these conditions had the same basic trends that were observed in the dual frequency Ar plasma IV curves (See Appendix C). Since this is the case, one is referred to section 4.2.1 for an analysis of the IV curve characteristics that are also applicable here.

### 5.2.1 Ar – $CF_4$ – $O_2$ Probe Comparison

As mentioned in section 4.2.2, with the addition of the 13.56 MHz generator, more control of the IEDf is obtained. The high frequency source (60 MHz) is mainly used to control the plasma density while the low frequency source (13.56 MHz) is used to control the ion energy impinging on the electrode [ 2, 3, 5, 10, 11, 13 - 23 ]. By adjusting the power output of these generators, the plasma density or $V_{DC}$ was held constant while the other property was varied similar to the measurements in section 4.2.2. Again, the IEDfs will come in two sets. The first set looks at the effects on the IEDf of changing the 13.56 MHz bias power with a constant plasma density (or constant 60 MHz source power). The other set looks at the effects on the IEDf when adjusting the 60 MHz source power and adjusting the 13.56 MHz bias power to keep a constant $V_{DC}$. These measurements were taken using a gas mixture composed of Ar, $CF_4$, and $O_2$. The gas was mixed according to a pressure ratio of 90% Ar, 5% $CF_4$, and 5% $O_2$.

The first set of IEDfs were taken from a 5 mTorr Ar – $CF_4$ – $O_2$ plasma generated from a constant 400 W 60 MHz RF signal. While keeping the 60 MHz source power constant, the 13.56 MHz RF power applied to the bottom electrode was varied between 25 W to 150 W. The IEDfs for these measurements can be seen in Fig. 121- Fig. 123. Again, like with the Ar measurements in section 4.2.2, the WP IEDfs from this set are composed of a single peak. The single peak formation is likely due to RF potential not coupling to the ground sheath resulting in a minimal variation in the electric field of the sheath. The ions are then only accelerated by the difference between the average plasma potential $(V_p)$ and the grounded chamber wall. There are some slight hints at dual peak formation in the 25 W, 100 W, 125 W, and 150 W cases. These peaks or humps may have been caused by a small RF potential across the sheath, but they could also have reasonably been caused by noise in the IV curve measurement. Like described in section 4.2.2

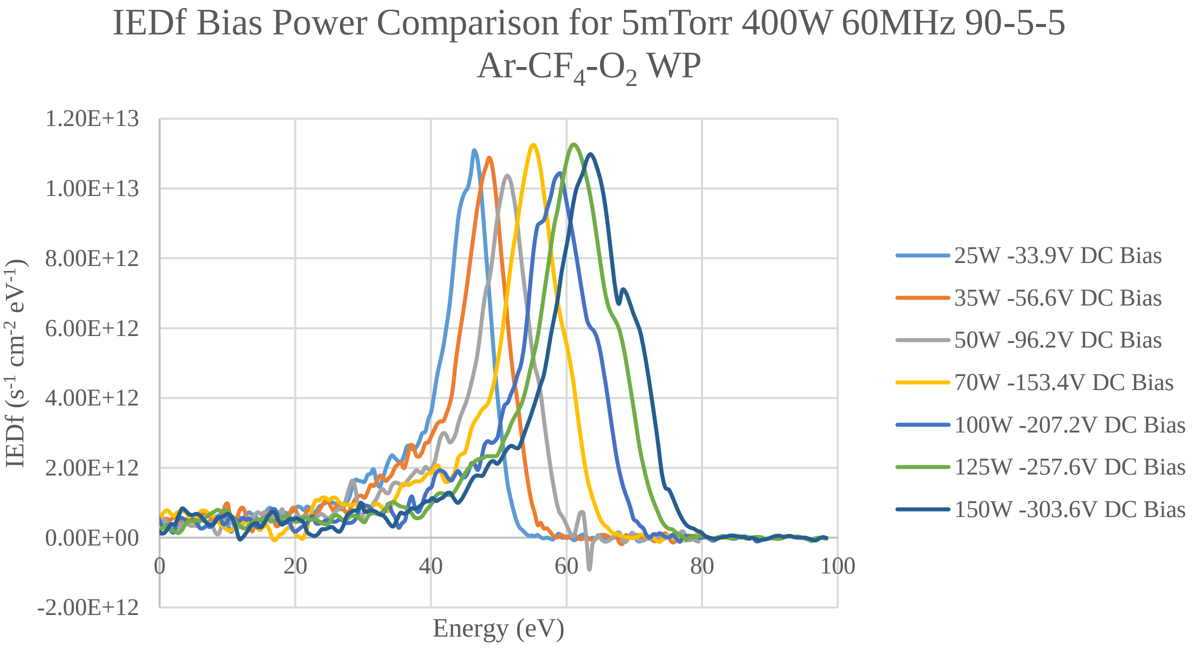

*Fig. 121*: Plots of the IEDfs obtained from the WP for a 5 mTorr 90-5-5 Ar – CF$_4$ – O$_2$ plasma generated by a 400 W 60 MHz RF source. The 13.56 MHz RF source power was varied between 25 W and 150 W.

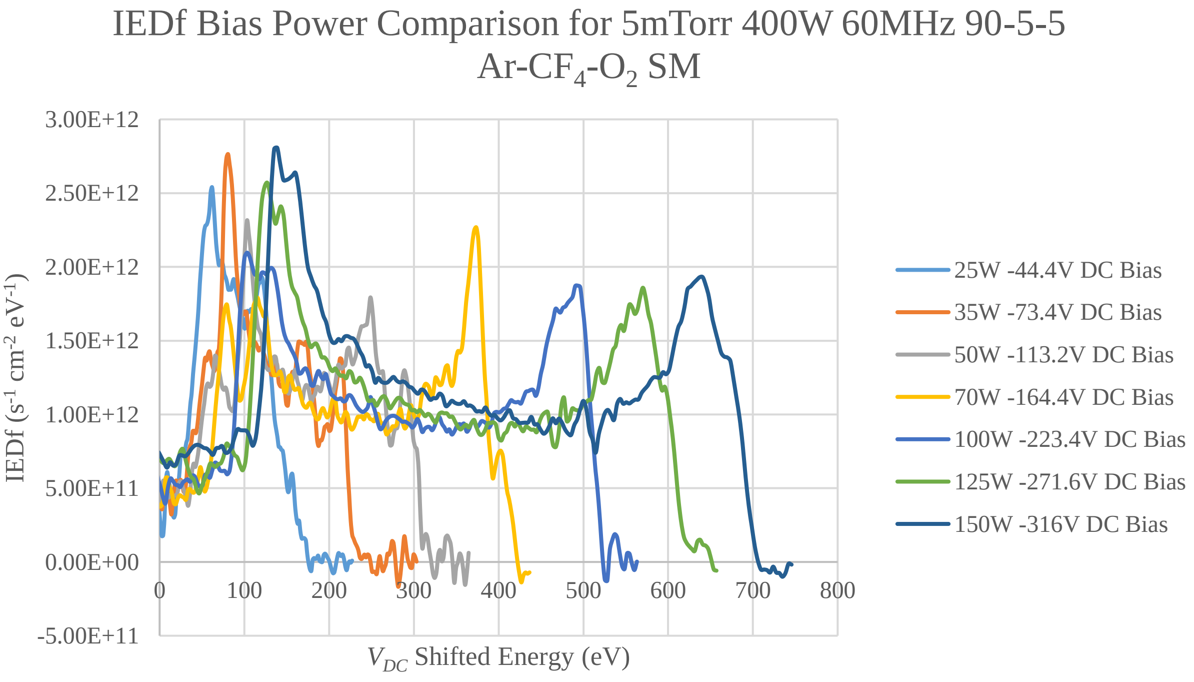

*Fig. 122*: Plots of the IEDfs obtained from the SM probe for a 5 mTorr 90-5-5 Ar – CF$_4$ – O$_2$ plasma generated by a 400 W 60 MHz RF source. The 13.56 MHz RF source power was varied between 25 W and 150 W. For a clearer picture of the trends of the SM IEDf plot at lower powers, see Appendix B.

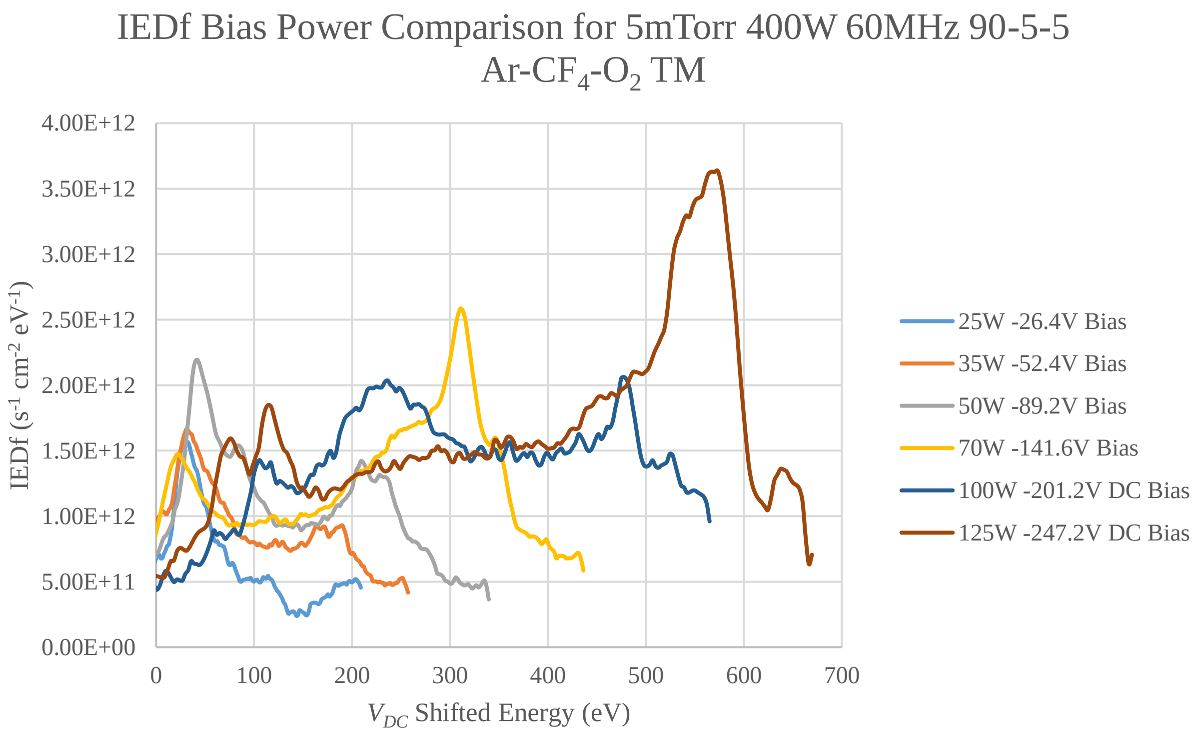

*Fig. 123*: Plots of the IEDfs obtained from the TM probe for a 5 mTorr 90-5-5 Ar – $CF_4$ – $O_2$ plasma generated by a 400 W 60 MHz RF source. The 13.56 MHz RF source power was varied between 25 W and 150 W.

though, a need for a more thorough sheath model at grounded surfaces is needed for RF plasmas to explain this phenomenon. The peak energy increases with an increase in bias power due to an increase in $V_p$. The increase in $V_p$ is likely caused by the need of the plasma to allow for appropriate sheath collapse on both electrodes of an asymmetric system. Since the grounded surface is constant, the potential differential across the sheath increases resulting in higher peak energy. The peak intensity is also quite consistent, which is expected since the plasma density remains roughly constant with the constant 400 W 60 MHz RF source. With the plasma density constant, the incoming flux will remain constant as well.

The SM and TM IEDfs are very consistent with dual frequency IEDfs obtained at the biased electrode. Again, the IEDfs show a saddle shape structure and the energies are reasonable. As with the dual frequency Ar measurements in section 4.2.2, as the bias power increases, the gap between the peaks also increases. Since the density is held constant and the $V_{DC}$ increases, this points to the sheath becoming smaller with increasing $V_{DC}$. The biggest difference between the SM and TM IEDfs is the shape and peak locations between them. The TM IEDfs typically have a lower peak energy and the saddle shape of the IEDf is somewhat distorted. This is consistent with the difference between the SM and TM Ar IEDfs in section 4.2.2 as well. As mentioned in that section, the shift in peak energies is likely due to collisions. The ions must travel significantly farther before reaching the RFEA because of the drift cone. This increase in travel distance increases the probability of collisions. Also, the distortion to the shape of the TM IEDfs is most likely caused by increasing electron current collection at higher collector potentials. Since electrons can travel around the probe in the electrode cavity, they can be collected by the screws that attach the signal lines to the collector plates (See Fig. 100).

The IEDfs obtained from the WP, SM, and TM probes for a constant -120 V $V_{DC}$ at varied 60 MHz RF source powers can be seen in Fig. 124 - Fig. 126. As with the constant 60 MHz source power case, the WP IEDfs are single peaks as expected. Again, there are slight humps or peaks that may be caused by a minimal RF potential across the sheath but may also be caused by noise in the IV curve. The peak energy increases with increasing source power due to an increase in $V_p$ likely caused for the same reason described in the previous case. The biggest difference between this case and the previous case is how the peak intensity changes. In the previous case, the peak intensity was constant as a result of a roughly constant plasma density. In this case though, with the 60 MHz source power changing, the peak intensity increases from an increase in plasma density and therefore incoming flux. This trend is consistent with the observed trend with dual frequency Ar measurements (See Fig. 102 - Fig. 107).

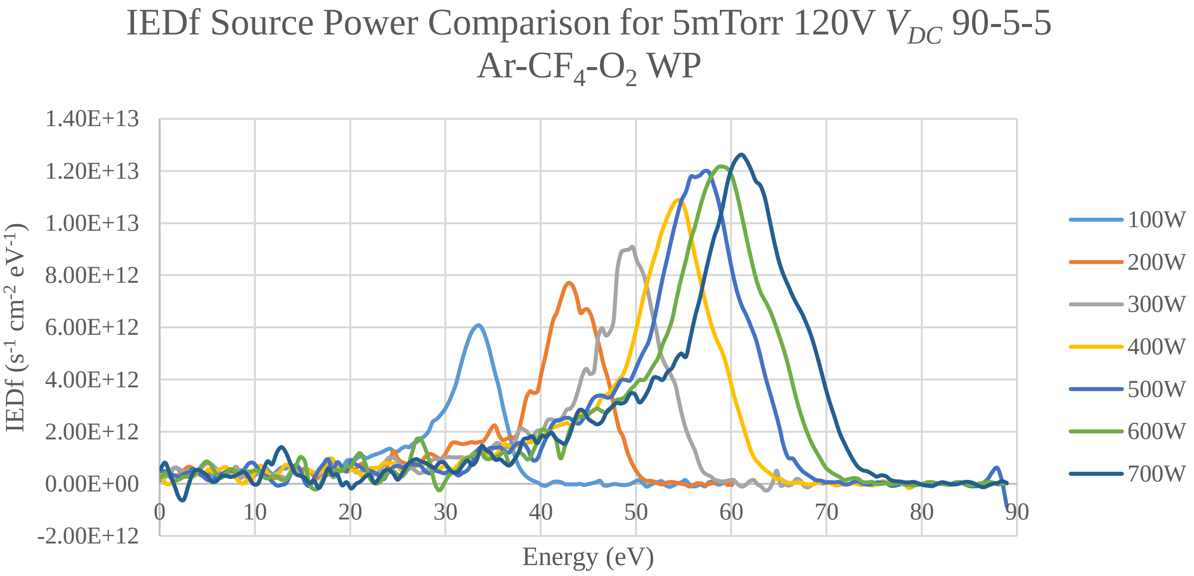

*Fig. 124*: IEDfs obtained from the WP for a 5 mTorr 90-5-5 Ar – $CF_4$ – $O_2$ for a constant -120V $V_{DC}$. The 60 MHz RF source power was varied between 100 W and 600 W.

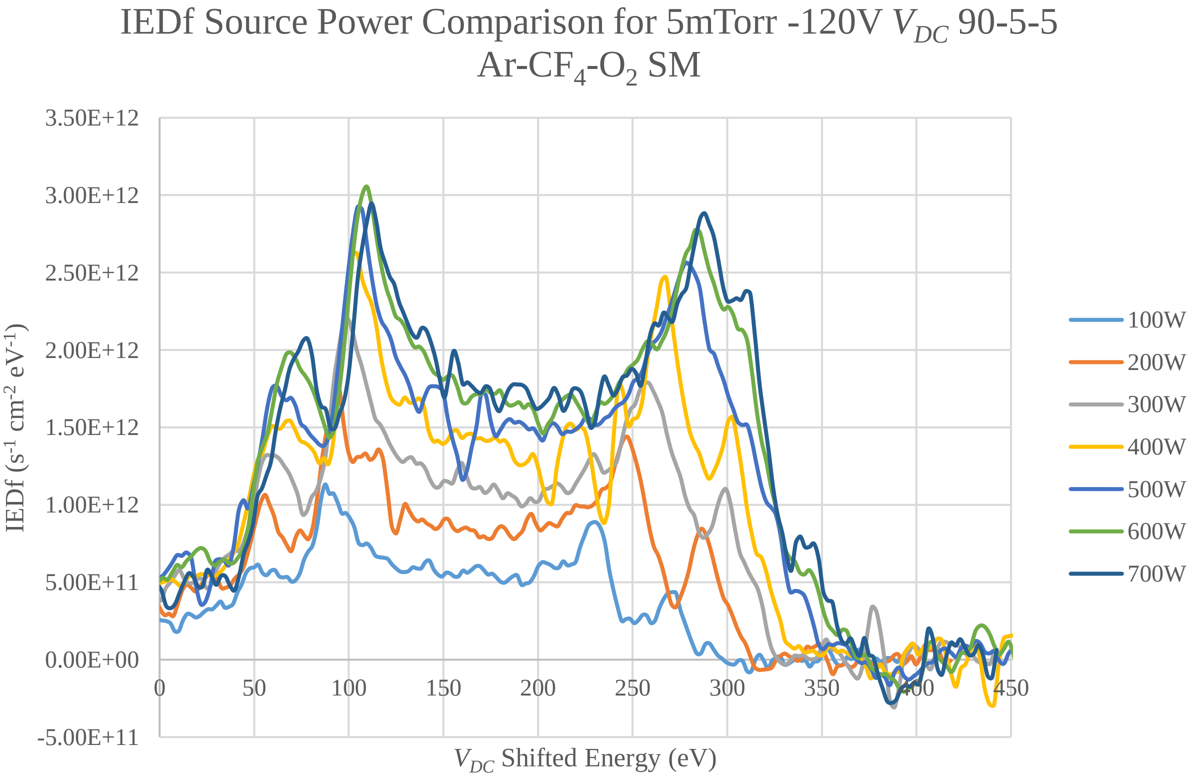

*Fig. 125*: IEDfs obtained from the SM probe for a 5 mTorr 90-5-5 Ar – $CF_4$ – $O_2$ for a constant -120V $V_{DC}$. The 60 MHz RF source power was varied between 100 W and 600 W.

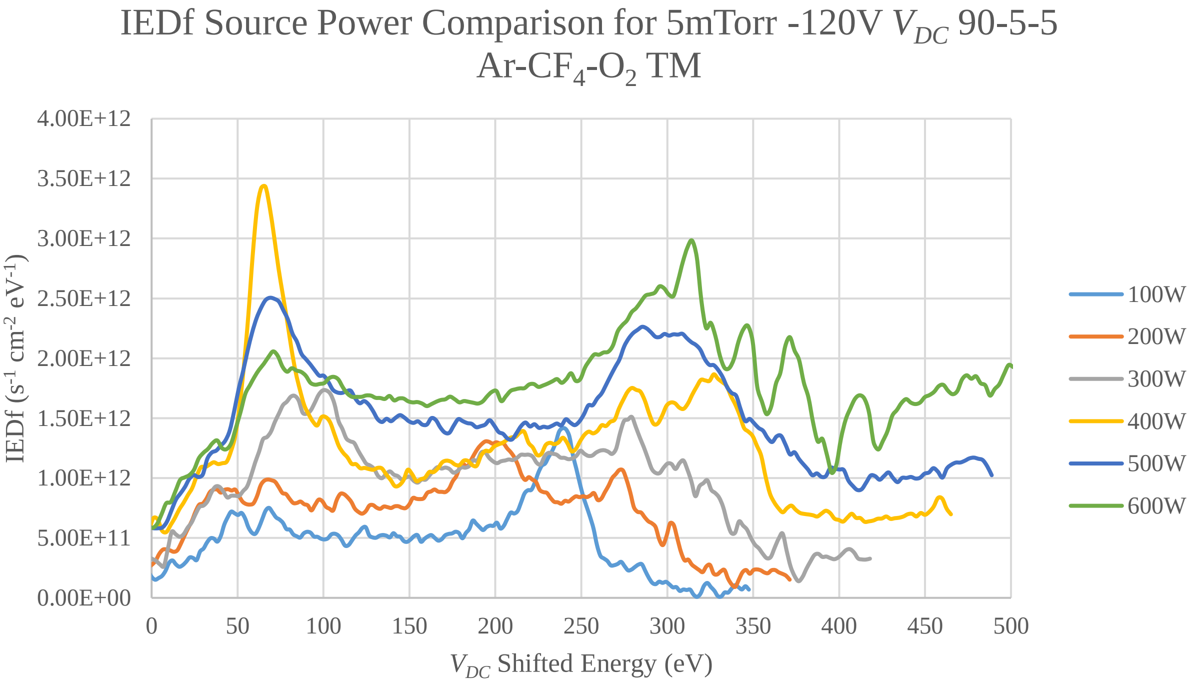

*Fig. 126*: IEDfs obtained from the TM probe for a 5 mTorr 90-5-5 Ar – $CF_4$ – $O_2$ for a constant -120V $V_{DC}$. The 60 MHz RF source power was varied between 100 W and 600 W.

Again, the SM and TM IEDfs are displaying similar trends to those already observed in the Ar dual frequency measurements (See section 4.2.2) and the constant 60 MHz source power. Both sets of IEDfs from the different probes have the expected saddle shape consistent with RFEA measurements at a biased electrode. As with the constant $V_{DC}$ dual frequency Ar measurements (See Fig. 105 - Fig. 107), as the source power increases, the peak intensities increase, and the high energy peak location shifts to higher energies. Like mentioned previously, the peak intensity increases due to an increase in plasma density and resulting higher incoming flux. The shift in peak energies is a result of changes in the sheath. Since the $V_{DC}$ is held constant, the sheath shrinks with an increase in plasma density. The shrinking sheath means ions traverse the sheath faster and are affected by the instantaneous electric field of the sheath as opposed to the average electric field in the sheath. Since the $V_{DC}$ is not changed through, the gap distance between the peaks remains relatively constant. This is best seen in the SM IEDfs since the TM IEDf shapes are less consistent. Again, the shape difference of the TM IEDfs is probably caused by electron current collection from outside the probe. The low energy peaks of the TM IEDfs are also located at lower energies than the SM IEDfs because of collisions occurring within the drift cone. Overall, the dual frequency Ar – $CF_4$ – $O_2$ measurements have been consistent with expectations and the dual frequency Ar measurements.

To more clearly see the effects of adding $CF_4$ and $O_2$ to an Ar plasma, a dual frequency Ar and Ar – $CF_4$ – $O_2$ measurement were plotted together (See Fig. 127 - Fig. 129). Measurements were taken with the WP, SM and TM probes at 5 mTorr with a 60 MHz RF source power of 400 W and a -120 V $V_{DC}$ on the bias electrode. The WP IEDfs are pretty similar in peak intensity and shape. The Ar – $CF_4$ – $O_2$ IEDf has a slightly larger low energy tail than the Ar IEDf. The major difference is the peak location though. The Ar – $CF_4$ – $O_2$ has a much lower peak energy than the Ar IEDf. The energy drop could be due to collisions but the collisional tail of the Ar – $CF_4$ – $O_2$ is only ever so slightly larger which probably would not result in such a drop in energy. The other possible cause of the lower peak energy is a reduction in the $V_p$. If this is the case, it is unexpected since the Ar – $CF_4$ IEDfs from the grounded electrode were at higher energy than the Ar IEDf under the same conditions.

The SM and TM Ar – $CF_4$ – $O_2$ IEDfs deviate more from the Ar IEDfs than seen with the WP. The first major difference is in the peak locations between the IEDfs. For the Ar – $CF_4$ – $O_2$ cases, the gap between the peaks is smaller than with the Ar case. This gap reduction is probably caused by an increase in the sheath distance compared to the Ar case. With an increased sheath distance, the ions take longer to traverse the sheath. Therefore, they are going to experience changes in the electric field from the RF oscillations unlike if they crossed it instantly in

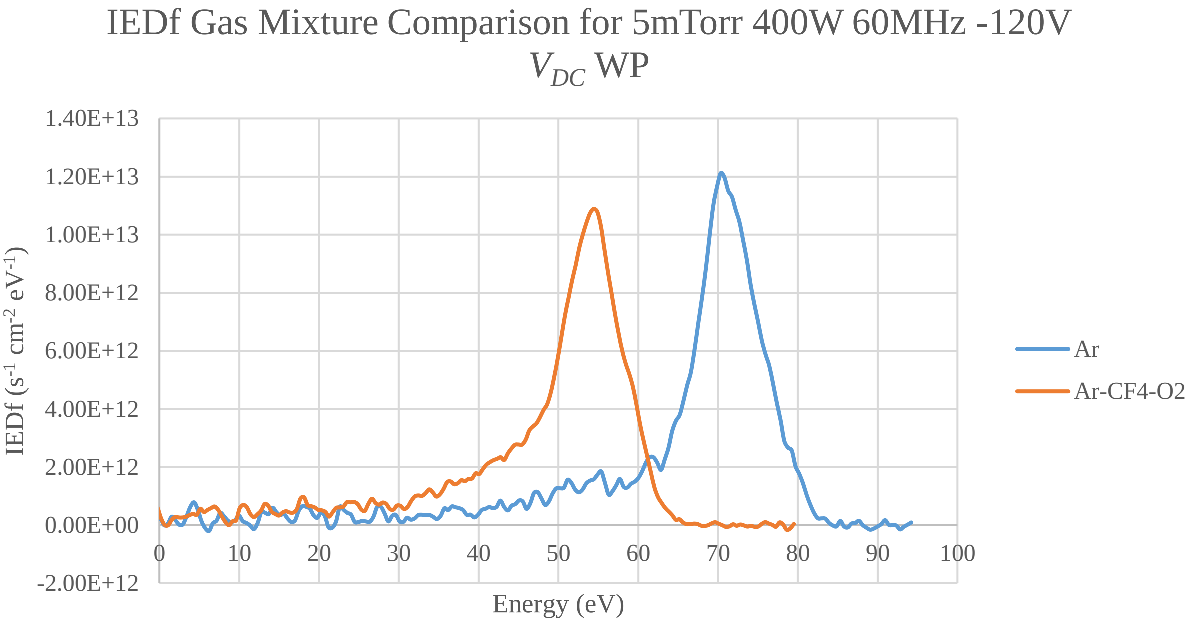

*Fig. 127*: IEDfs obtained with the WP for a 5 mTorr Ar and 5 mTorr Ar – $CF_4$ – $O_2$ at a 400 W 60 MHz RF source power and a -120 V $V_{DC}$ on the bias electrode.

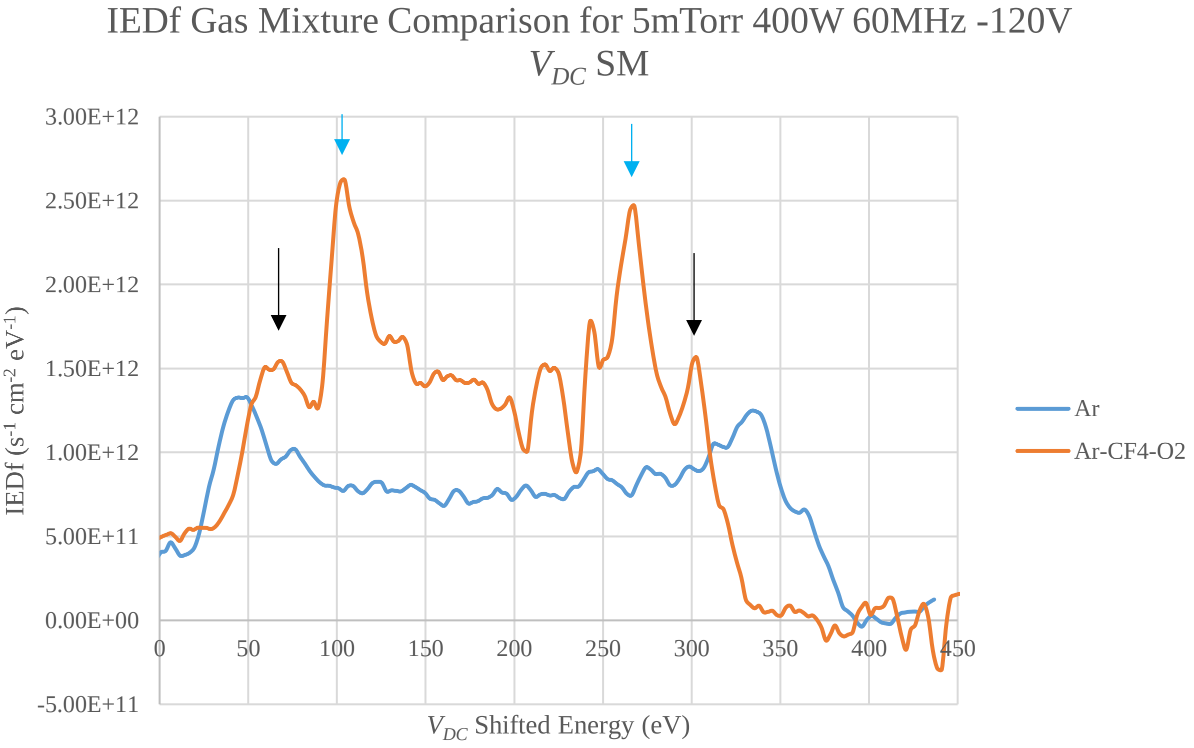

*Fig. 128*: IEDfs obtained with the SM probe for a 5 mTorr Ar and 5 mTorr Ar – $CF_4$ – $O_2$ at a 400 W 60 MHz RF source power and a -120 V $V_{DC}$ on the bias electrode. Arrows point out peaks from different ion species in the SM measurement.

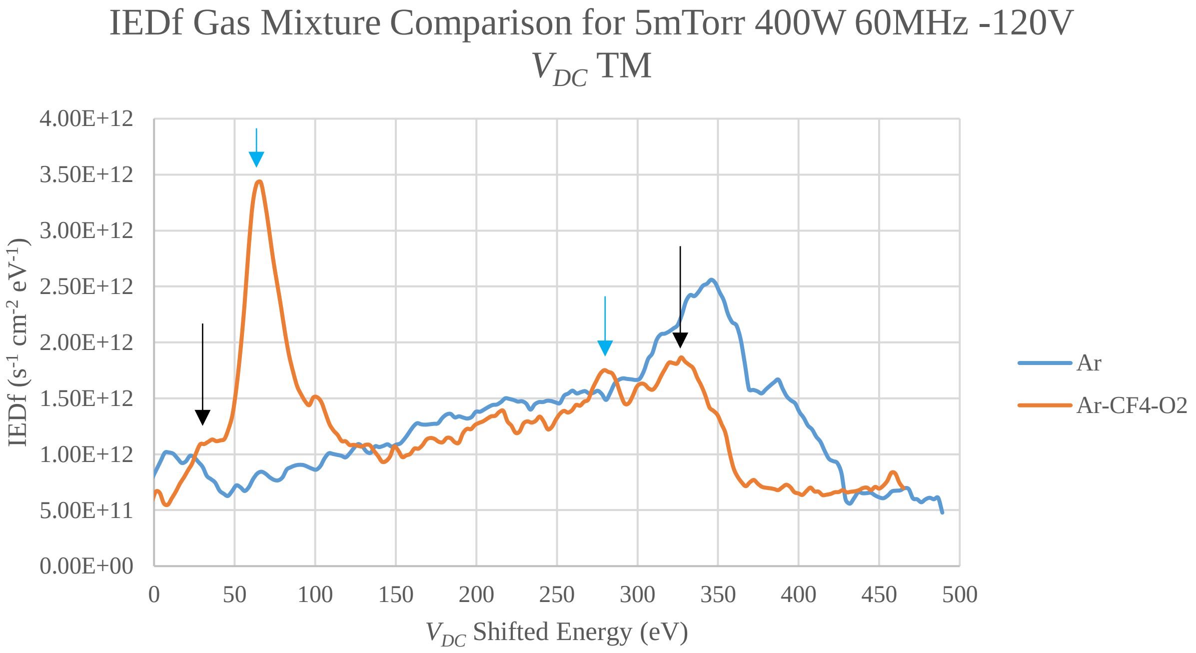

*Fig. 129*: IEDfs obtained with the TM probe for a 5 mTorr Ar and 5 mTorr Ar – $CF_4$ – $O_2$ at a 400 W 60 MHz RF source power and a -120 V $V_{DC}$ on the bias electrode. The arrows in the TM measurement points out possible peaks from different ion species but these are uncertain as they are not as distinct. The same color arrows point to peaks generated by the same ion species.

reference to the RF oscillation.

The next major difference is intensity of the IEDfs obtained. This is not so much of an issue with the TM IEDfs because it looks like the area under the larger peaks offset one another. However, with the SM probe, it seems that the Ar – $CF_4$ – $O_2$ IEDf has a larger intensity than the Ar IEDf. This is unexpected because the plasma density should be lower with the addition of $CF_4$ and $O_2$. A lower plasma density results in less incoming current or flux to the RFEA. Plasma non-uniformity could be a possible reason for this discrepancy. The plasma is likely to be more uniform in the center of the plasma where the TM probe is located while the gas composition could affect the uniformity of the plasma closer to the edge of the electrode where the SM probe is located. It is possible that this non-uniformity could be caused by localization since the plasma density is lower in the Ar – $CF_4$ – $O_2$. Density measurements for a 10 mTorr 90% Ar 10% $CF_4$

plasma do show a drop in the radial density profile (See Fig. 133) but more experiments would need to be run at 5 mTorr in Ar and Ar – $CF_4$ – $O_2$ to confirm the density drop radially is more significant for the Ar case.

The last major difference between the SM and TM IEDfs is the number of peaks that occur in the Ar – $CF_4$ – $O_2$ plasma measurements. In the Ar – $CF_4$ – $O_2$ IEDf, there are at least four peaks (See the arrows in Fig. 128 and Fig. 129) that are reliably consistent between different power measurements (See Fig. 121 - Fig. 126). The TM IEDf peaks are not as distinct as the SM IEDfs, so the certainty that these are actual peaks for different ion species is not as firm. The appearance of these additional peaks is not unexpected. As mentioned in the introduction to this section, with the addition of more gases, and especially molecular gases, the mass difference between the ion species can cause them to gain different amounts of energy as they travel through the RF sheath. If the sheath distance and ion mass is large enough, the ion may experience more of an RF cycle within the sheath than smaller mass ion species. As a result, the bimodal peaks associated with this ion will shift closer to one another since the ions respond more to an average change in the electric field. However, if the sheath distance remains small enough, all of the ions no matter their mass will respond to the instantaneous fields. This effect can be seen in Fig. 130. In this case, the 13.56 MHz bias power is changed from 50 W to 100 W. Since the plasma density is held constant by the 60 MHz source power and the $V_{DC}$ changes, the sheath thickness must decrease with increasing $V_{DC}$. As a result, the four peaks at 50 W merge into two separate peaks at 100 W creating the expected bimodal IEDf. Since only an RFEA was used to obtain the IEDf and more than two positive ion species ($Ar^+$, $CF_3^+$, $O_2^+$, $O^+$, etc.) are generated, it is not possible to determine which ion species generated which set of peaks.

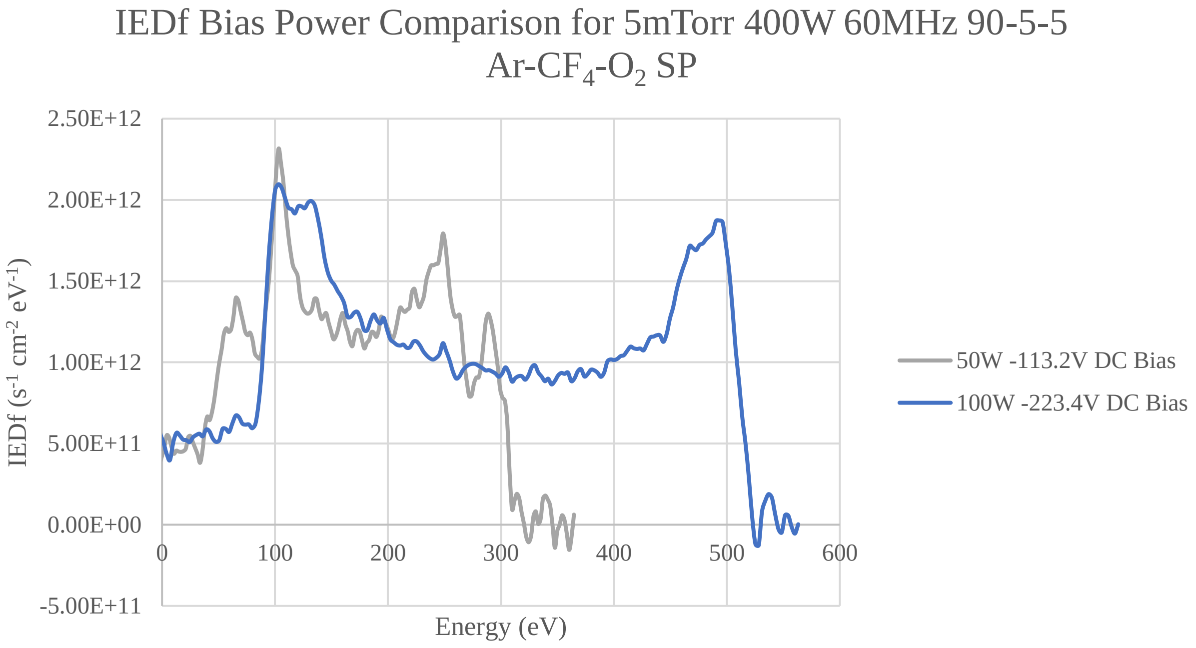

*Fig. 130*: Plot of the SM IEDfs at two different bias powers for a 5 mTorr Ar – $CF_4$ – $O_2$ plasma generated by a 400 W 60 MHz RF source. The plot shows a transition between a four peak IEDf to a dual peak IEDf. The transition is caused by a shrinking of the sheath.

The last comparison to analyze was how adjusting the pressure of the plasma affected the IEDf for an Ar – $CF_4$ – $O_2$ plasma. For this analysis, only the WP was used to take measurements. The plasma was generated with a 400 W 60 MHz RF source and the 13.56 MHz bias power was varied between 50 W and 70 W. Lastly, the pressure was also varied between 5 mTorr and 20 mTorr. A plot of the WP IEDfs obtained can be seen in Fig. 131. A couple of trends in these IEDfs are very consistent between the dual frequency Ar case (See section 4.2.2) and these IEDfs. The first similar trend is the reduction in peak intensity. As with the dual frequency Ar case, the loss in incoming flux is likely due to the localization of the plasma. The other similar trend is the reduction in peak energy at higher energies. This is due to the increased number of collisions the ions experience from an increase in plasma density. This last trend is also the one that is different than the dual frequency Ar case. The difference in peak energy between the 5 mTorr and 20 mTorr IEDfs in this case is drastically smaller than the difference in peak energy between the 5 mTorr and 20 mTorr IEDfs of the dual frequency Ar case. This difference is probably caused by the difference in plasma densities and the $V_p$. The difference in plasma for the Ar case is likely much larger than the difference in density between the Ar – $CF_4$ – $O_2$ case. The $V_p$ of the 5 mTorr Ar – $CF_4$ – $O_2$ is also much lower than the 5 mTorr Ar measurement based on the peak energies. Based on this, the $V_p$ does not seem to have as strong of a dependence on pressure when $CF_4$ and $O_2$ are added.

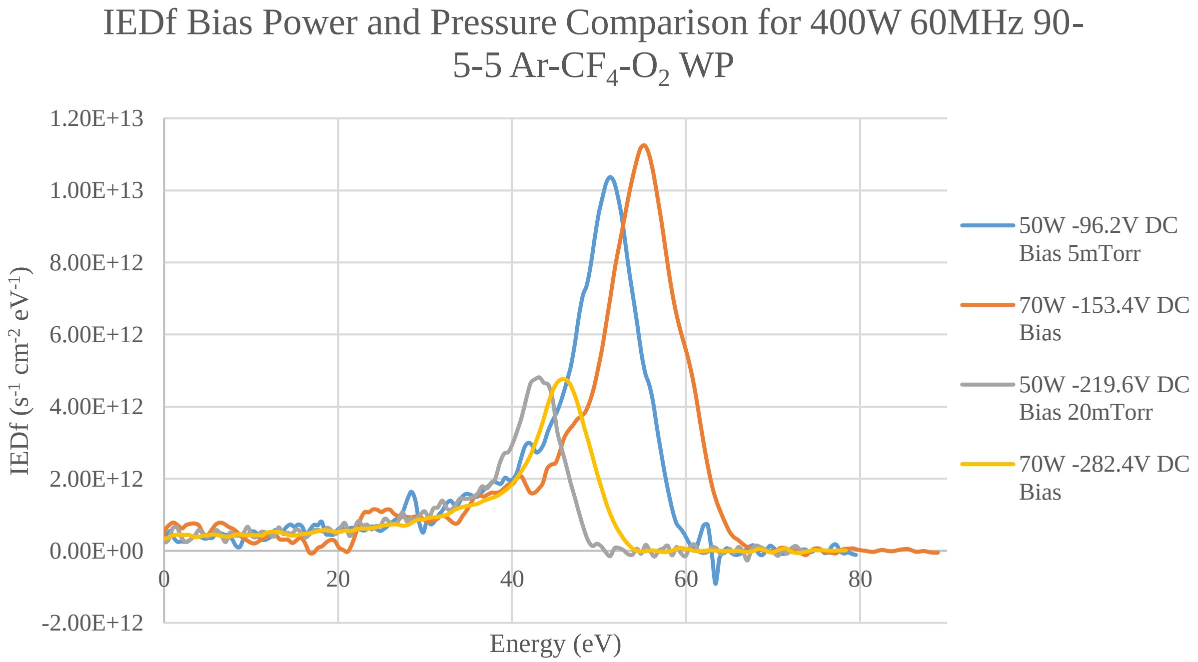

*Fig. 131*: IEDfs obtained from the wall probe for a 90-5-5 Ar – $CF_4$ – $O_2$ plasma generated by a 400 W 60 MHz RF source. The pressure was varied between 5 mTorr and 20 mTorr. The 13.56 MHz bias power was also varied between 50 W and 70 W.

### 5.2.2 Ar – $CF_4$ Pressure Ratio Comparison

After looking at power, pressure, and gas mixture effects on the IEDf, the last is too look at the effect of $CF_4$ concentration on the IEDf for a dual frequency Ar – $CF_4$ plasma. Only the

WP was used for these measurements. Again, measurements were taken for a constant 60 MHz RF source power when varying the 13.56 MHz bias power and for a constant -120V $V_{DC}$ when adjusting the 60 MHz source power. For the constant 60 MHz case, the source power was set at 400 W. Since the effects of power on the IEDfs in these measurements was the same as previously discussed (See section 5.1.3), only a single 13.56 MHz bias power and a 60 MHz source power was plotted for the respective case. For the constant 60 MHz power case, the 13.56 MHz RF bias power chosen was 70 W. For the constant -120 V $V_{DC}$ case, the 60 MHz RF source power chosen was 400 W. The concentration of $CF_4$ was adjusted between a 1% to 10% pressure ratio. The 15% concentration was not used because the IEDf stopped changing after 5% in the grounded electrode case (See section 5.1.3).

The WP IEDfs obtained for the constant 400 W 60 MHz RF source power and constant -120 V $V_{DC}$ cases can be seen in Fig. 132. The general trends observed in the IEDfs between the two cases is very similar. They also follow similar trends to what was seen for the grounded electrode case (See section 5.1.3). The peak energy increases with increasing $CF_4$ concentration, the peak intensity decreases with increasing $CF_4$ concentration, and the $CF_4$ concentration has significant effects on the IEDf for pressure ratios of 5% or less. The biggest difference between this case and the grounded electrode case is how the 100% Ar IEDfs compare to the Ar – $CF_4$ IEDfs. In the grounded electrode case, the 100% Ar IEDfs had a lower peak energy and higher peak intensity. In this case however, the 100% Ar IEDf has a peak energy that falls in the middle of the Ar – $CF_4$ IEDfs and a lower peak intensity than all the Ar – $CF_4$ IEDfs. It is possible the lower peak intensity is due to localization around the 60 MHz source electrode as mentioned in section 5.1.3. For the 100% Ar case, the plasma density will be higher and as previously mentioned, the higher density case (i.e. high pressure) the plasma seems to localize around the

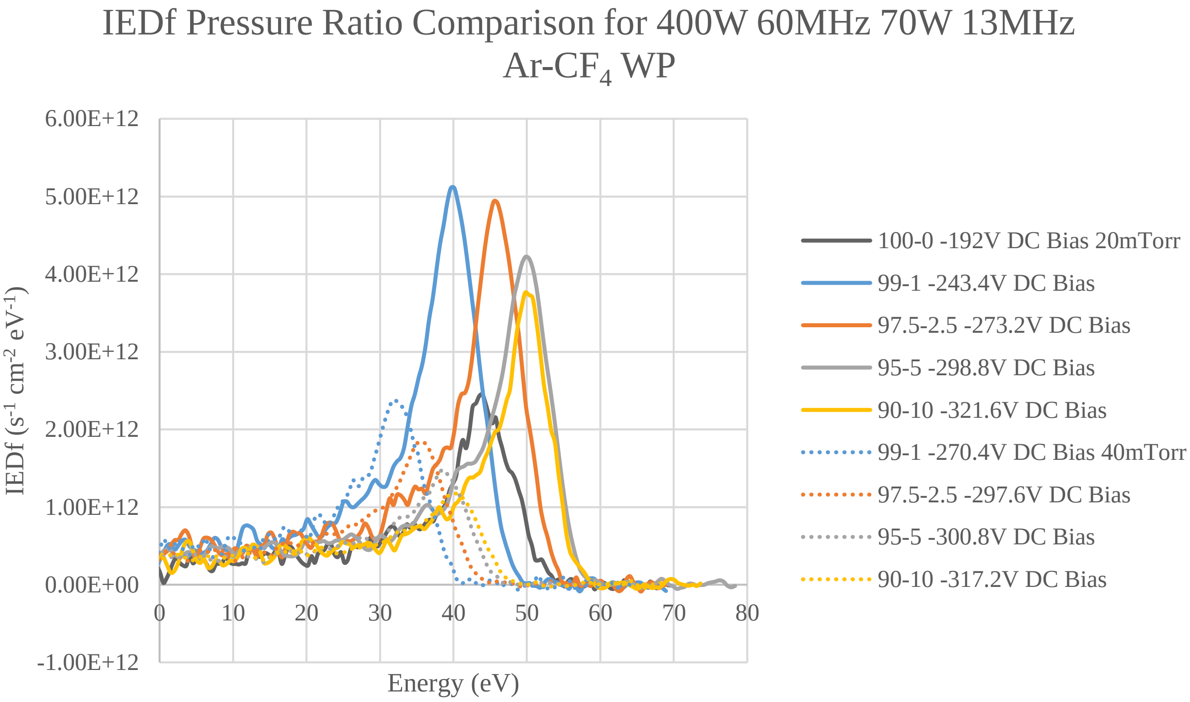

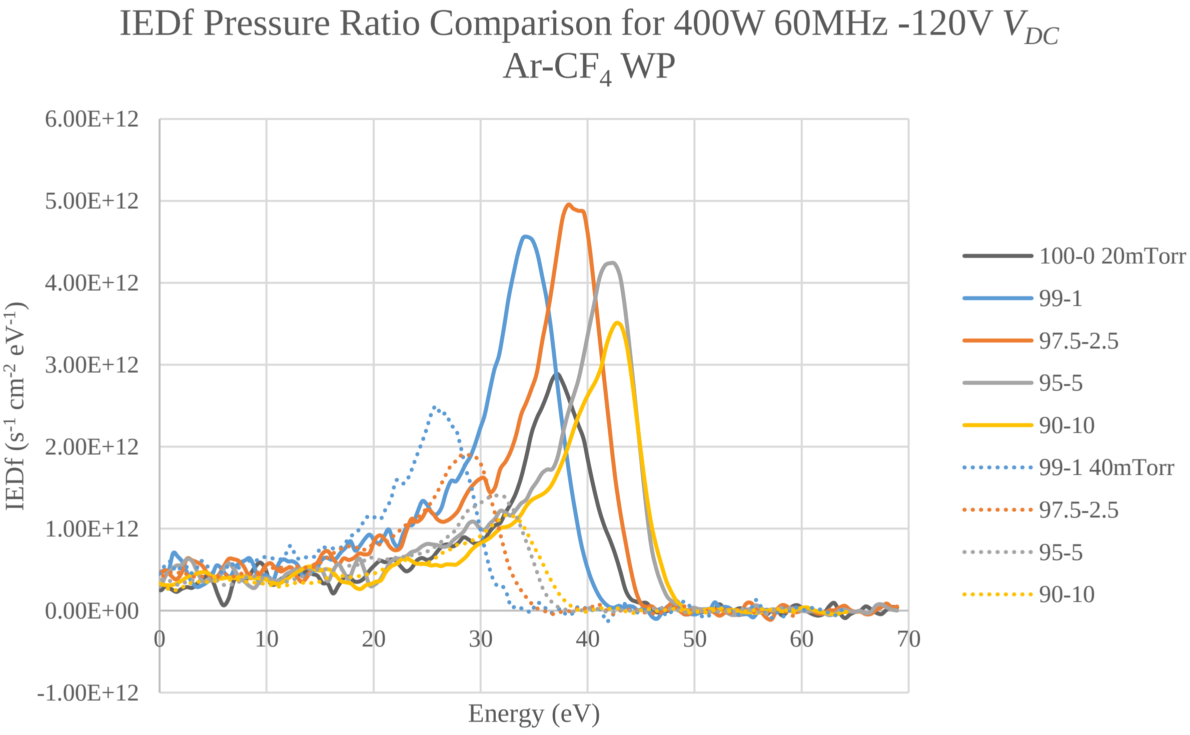

*Fig. 132*: Plots of the IEDfs obtained with the WP where the $CF_4$ concentration was adjusted for a Ar – $CF_4$ plasma when the 60 MHz RF source power was held constant and the $V_{DC}$ was held constant. A pressure of 20 mTorr and 40 mTorr were used. The 13.56 MHz RF bias power chosen in the constant 60 MHz case was 70 W. The 60 MHz RF source power chosen in the constant -120 V $V_{DC}$ case was 400 W.

source electrode. Once $CF_4$ is added to the Ar gas, the plasma density drops resulting in a reduction of localization. This would be why the peak intensity increases at the 1% $CF_4$ concentration. As the plasma density continues to drop with increasing $CF_4$ concentration, it has a greater impact on peak intensity than the reduction in localization. The reason for the increase in peak intensity of the -120 V $V_{DC}$ case is unknown as it didn't appear in the constant 60 MHz case. It is possible that it was a reduction in localization but could also just as reasonably be caused by measurement variation.

Like in the previous Ar, Ar – $CF_4$, and Ar – $CF_4$ – $O_2$ cases (See sections 4.1.3, 4.2.2, 5.1.3, and 5.2.1), the peak intensity drops with an increase in pressure. An increase in pressure typically means an increase in plasma density that should translate into an increase in incoming current or flux. As mentioned in the previous paragraph though, the reduction in peak intensity is likely due to plasma localization towards the 60 MHz source electrode. Just as with the grounded electrode Ar and Ar – $CF_4$ measurements (See sections 4.1.2 and 5.1.3), a hairpin resonator probe (or hairpin) was used to measure the plasma density at the center of the chamber to confirm a drop in density at high pressures. For more detail on the hairpin resonator probe, one is referred to section 4.1.2.

For this measurement, the plasma was generated using a 400 W 60 MHz RF source and a 70 W 13.56 MHz RF bias. The gas composition was 90% Ar and 10% $CF_4$. The pressure was varied from 10 mTorr to 40 mTorr. The hairpin was located equidistant (approximately 1.57" or 4 cm) from the top and bottom electrodes. The radial position of the hairpin was also varied at each of the pressures. The resulting density profile curves can be seen in Fig. 133. This data shows that as the pressure increases, the density across the whole chamber decreases. Again, this is counter intuitive because a higher pressure should result in higher plasma density.

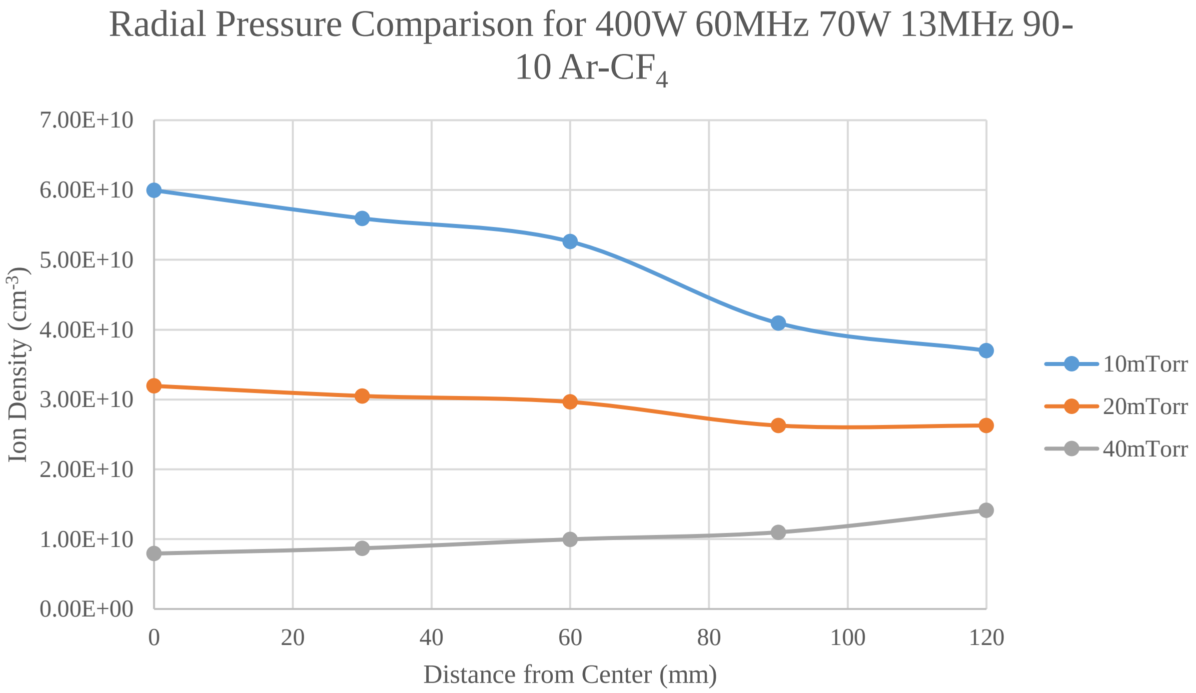

*Fig. 133*: Radial plasma density profiles obtained from a hairpin resonator probe for a 90-10 Ar – $CF_4$ plasma generated by a 400 W 60 MHz RF source and 70 W 13.56 MHz bias. The pressure was varied between 10 mTorr and 40 mTorr.

Nevertheless, these results suggestion that localization around the source electrode at high pressures is the cause.

In general, the density also drops when moving radially outward. This is expected because the highest density should be in the center of the plasma and away from the sheath and walls. The only measurement that seems to contradict this is the 40 mTorr case. This case shows the density increasing when moving radially outward. This result can be explained by the hairpin connection to the chamber wall. The hairpin was connected to the chamber through a 4” (10.16 cm) long 2 ¾” diameter pipe. A port cover was used to try and prevent plasma light-up in the tube (See Fig. 134). Due to the nature and design of the hairpin, a large hole was also created in the port cover to allow the hairpin to move in and out of the chamber radially. The port cover typically worked well except at higher pressures. Because of a high $V_p$, a large hole in the port cover, and a pipe used for the probe connection, the pipe formed a hallow cathode at these higher pressures generating a plasma behind the port cover. The plasma generated by this hallow cathode is the cause of the increase in density farther from the center of the chamber. That be said, the hairpin measurements generally confirm that plasma localization is likely the cause for a reduction in peak intensities in the IEDfs at higher pressures.

*Fig. 134*: Picture of the hairpin resonator probe (or hairpin) and corresponding port cover in the chamber wall. The port cover was designed to allow the hairpin to move in and out while trying to prevent light-up in the hairpin housing connected to the chamber wall

## CHAPTER 6: CONCLUSION

The previous chapters have discussed the need for, design considerations and optimization, and experimental measurements of a high voltage retarding field energy analyzer (RFEA) installed in the biased electrode of an industrial plasma system. IEDf measurements taken with an RFEAs from the surface of an RF biased electrode is not a novel diagnostic or technique. These measurements have been performed with RFEAs designed to sit on top of the RF biased electrode (traditional commercial system) as well as internally incorporated in the RF biased electrode at the surface level. These RFEAs were typically designed to be compact to avoid the need for differential pumping. As a result, these RFEAs were limited to low pressure (≤ 300 mTorr) regimes and operation voltages up to 2 kV [ 86 ]. The electrodes in which the RFEAs were installed were also heavily modified making them unsuitable for operation in current industrial plasma systems.

In this work, the previous RFEA designs were analyzed and a new design iteration of these RFEAs was created by Tokyo Electron America Inc. (TEL$^{TM}$) for operation in industrial process conditions. The grid gap distance was made larger to allow for increased operational voltages up to 5 kV. It was also designed to be differentially pumped (i.e. pumping ports in the grid plates) to compensate for the larger grid gap distance but also makes it viable to operate at higher pressures (> 300 mTorr) provided sufficient pumping is included. Due to the introduction of pumping ports and a larger grid gap distance, the electric fields between the grids and potentials across the grid surfaces were analyzed. This was done using electrostatic simulation software to model the electric fields between the grids and potentials within the grid holes. Based on this analysis, the geometric dimensions of the RFEA were optimized to provide a uniform electric field between the grids. Analyzing the potential across the grid surface made it possible to study the dependence of the grid hole potential on the same geometric parameters used in the electric field study. It was found that better energy resolution is obtained for a larger grid gap distance and smaller grid hole diameter.

Increasing the grid gap distance has advantages for operation potential and energy resolution but there is a disadvantage as well. The disadvantage stems from the fact that the line integrated number of ions between the grids increases. With a sufficient grid gap distance and incoming flux, the space charge build-up created by these ions could start rejecting ions that should be collected. The premature rejection of these ions causes a distortion in the IV curve which is carried through to the IEDf. The space charge build-up and distortion were investigated using the particle-in-cell (PIC) software package XPDP1 [ 62 ]. It was found that the space charge distortion alters the shape and peak height of the IEDf in the low ion energy regime ( < 100 eV). To account for space charge distortion, the post analysis process to obtain the IEDf. Theoretically, this is done by truncating the lower limit of the integral relationship between the IEDf and the measured current. In the regularized least-squares (RLS) solution method used to calculate the IEDf in this work, this truncation manifests as a truncation of the system matrix of the RLS method. Since the truncation is dependent on the shape of the IEDf, which is unknown, a first order linear approximation that uses information from the IV curves obtained from XPDP1 was used to truncate the system matrix. It was found that the first order model did correct for some of the distortion but not all of it. More complex models that followed the space charge potential (obtained from XPDP1) more closely provided better compensation and an exact truncation of the system matrix according to the space charge potential returns the undistorted IEDf exactly. This shows that with an accurate approximation of the space charge potential, space charge distortion can be corrected making it possible to operate RFEAs in a broader set of plasma conditions.

After a detailed analysis of the design of the RFEA had been performed, this work focused on the operation of the RFEA in an electrode that was compatible with an industrial system. The modification of the industrial system for the RFEA installation and differential pumping was kept to a minimum. Multiple probes were installed in the electrode. One probe (SM) was located only a millimeter below the top surface similar to previous work and another two (TM and F) were located below a 15 mm drift cone that lead to the surface of the electrode. These drift cone probes are how these RFEAs would be implemented in a commercial system as they used a smaller foot print then the probe at the surface of the electrode. This makes the probes less obtrusive to the other components (e.g. cooling lines, helium lines, electrostatic chuck, etc.) needed at the top of an industrial electrode. Measurements were taken with the three electrode probes and an additional wall probe for an argon (Ar) plasma under a variety of conditions. The chamber pressure ranged between 5 – 40 mTorr and a 60 MHz RF source on the top electrode. The bottom electrode containing the RFEAs was either grounded or connected to a 13.56 MHz RF generator.

In general, the resulting IEDfs contained the expected energy values and trends. For every measurement from the wall probe and the measurements from the electrode probes when grounded, the IEDfs were all single peaks that increased in energy with increased source power. When the bottom electrode was biased by the 13.56 MHz RF generator, the IEDfs from the SM and TM probes followed the expected saddle shape and there was only a slight deviation between the peak locations from these probes. The F probe did not produce a correct IEDf because the 1st grid of the RFEA was left floating instead of being connected to the electrode like the other two, so the potential that developed on this grid altered the IEDf. The major difference between the SM and TM probes was the IEDf peaks from the TM probe were typically wider and lower in intensity due to collisions in the drift cone and ion beam expansion. That being said, these measurements showed it is possible to get a reliable IEDf from a probe below a drift cone in an RF biased electrode of an industrial plasma system.

Lastly, the probes were also tested under a variety of pressures ( 5, 20, and 40 mTorr ) with gas mixtures (Ar and carbon tetrafluoride ($CF_4$) or Ar, $CF_4$, and oxygen ($O_2$)) at different concentration pressure ratios closer to those used in industrial processes. Again, the electrode probes were tested with a grounded and 13.56 MHz biased electrode. Just as with the Ar grounded electrode tests, the IEDfs from all the probes for a grounded electrode from an Ar – $CF_4$ plasma were single peaks. The trends observed between the different probes for Ar with a grounded electrode were the same for the Ar – $CF_4$ measurements at a grounded electrode. When comparing the Ar IEDfs to the Ar – $CF_4$ IEDfs under grounded conditions, the main difference observed is that the peak energy increased with the addition of $CF_4$. For the dual frequency measurements, an Ar – $CF_4$ – $O_2$ was used. Again, between the different probes, the IEDfs obtained were similar to the Ar dual frequency case. The WP IEDfs were single peaks again and had very similar shapes to the WP IEDfs for the Ar dual frequency measurements. The main difference this time was that the addition of $CF_4$ and $O_2$ caused a drop in peak energy. For the SM and TM IEDfs, bimodal peaks were obtained that showed the same trends observed for the Ar dual frequency SM and TM IEDfs. The biggest difference between the Ar and Ar – $CF_4$ – $O_2$ case is that at lower powers, there were multiple peaks in the IEDf. This is expected since the addition of $CF_4$ and $O_2$ introduces new ions with different masses compared to Ar. It was also seen that if the sheath width decreased, the multiple peaks would merge into a bimodal IEDf again. The general trend observes with increasing $CF_4$ concentration was the IEDf peak intensities dropped and the peak energy increased. As a result of these measurements, it has been shown that it is possible to obtain IEDfs from an imbedded RFEA in the electrode of an industrial plasma system with typical process gas mixtures.

Even with the capability to make IEDf measurements with an RFEA embedded in the electrode of an industrial plasma system, more work is needed to further the capability of taking RFEA measurements in an industrial system. Some of the issues that need to be resolved for this increased capability are small changes that could be made quickly while other issues will need more time and effort to be resolved. Some of the quick changes that could be made for the minor issues are the addition of a secondary electron rejection grid to the RFEA, new measurement electronics that allow for higher energy measurements, insulator coatings for the screws connecting the signal lines to the grids to prevent electron current collection, and larger grids for the RFEAs located below the drift cones to reduce the current reduction caused by beam expansion in the drift cones. To advance the capabilities in the long term, work investigating the beam expansion and collisional effects in the drift cone, development of a more robust and accurate model for space charge compensation and validation of the model, theoretical development of a sheath model and its dynamics at a grounded surface for a single or dual frequency RF plasma is needed. It may also be possible to develop the RFEA into a sensor that provides a current measurement for fast neutrals that are incident on the silicon (Si) wafer or electrode surface. Work performed in each of these areas would further the capabilities of RFEAs imbedded in the electrode of an industrial system providing more accurate and detailed results of the ion energy incident on the Si wafer. A more detailed discussion of the design changes and necessary future work is found in the following sections.

## 6.1 Design Recommendations

Through the measurement process, there were some unforeseen complications or observations to note that affected the measurements. Some of these observations (e.g. ion beam expansion, electron current collection, and plasma localization) have been mentioned in the previous chapters but there are a couple of others that have yet to be addressed. These are observations of issues that could be removed or changed in future measurements by making some design changes to the system. These changes would make the future measurements from the RFEAs easier to understand and more consistent across all the probes. These observations and the design recommendations to address them will be discussed in the following paragraphs.

The first observation that leads to some design changes is the expansion of the ions the drift cone. Due to this expansion, whether caused by Coulomb expansion, collisions, or the inherent radial velocity of the ions, the measured signal is smaller, and ions are able to travel around the outside of the probe. The ions traveling around the outside of the probe can be picked up by the collector when biased negative. A portion of this issue has previously been addressed (See section 4.1.2) by placing a cover over the collector so there is no longer a straight path to the collector for the ions. This does not, however, address the decrease in the measured signal as a result of lower incoming current.

There are two possible fixes for this issue. The first is to change the role of each of the 1st grid. If the 1st grid is not physically connected to the electrode, as is the case with the floating (F) probe, it could be biased with a more negative potential than the electrode. This would create an accelerating electric field for the ions between the walls of the drift cone and the 1st grid. By accelerating the ions, the possible reasons they expand (i.e. Coulomb expansion, collisions, or the inherent radial velocity) would become less influential as the ions will traverse the drift cone faster and are less likely to experience a collision at higher energies. This should not affect the resulting IEDf because the energy gained and lost while traversing the probe is represented by a state function. Any extra energy gained by the ions from the RFEA grids is accounted for as long as the potential applied to the grids is based off the DC bias ($V_{DC}$) of the electrode. This idea could be quickly tested using the F probe since the first grid is not directly attached to the electrode.

The second option is to increase the size of the grids of the RFEA. By increasing the size of the grids, the collection area increases so a larger portion of the expanded ion beam can enter the probe. This would take a little longer to implement as new probes would need to be constructed and installed. In the case where applying a negative bias to the 1st grid fails to increase the incoming current of the probe, this would be the only viable option. It could be done by increasing the diameter of the overall detector or by keeping it the same size and only increasing the grid size. Increasing the size of the detector makes it possible to collect a larger current without worrying about limitations caused by screw locations for other grids. On the other hand, this may decrease the amount of differential pumping that can occur in the drift cone effectively increasing the pressure in the drift cone. If only the grid size is adjusted, the differential pumping of the drift cone would be fine, but the grid size is limited by the bolt circle generated by the screws that hold the grids in the RFEA. Also, if the grid size increases, changes in the internal electric field would also occur which would affect the measured IEDf. Therefore, increasing the grid size is a tradeoff no matter which method is chosen to try and collect more current.

The next observation was the large negative currents measured by the top mount probe (TM) and F probe below the drift cone. This issue is likely caused by electrons traveling around the outside of the probes in the electrode like the ions since this negative current was not observed with the surface mount (SM) probe. In general, the electrons should not have been an issue once the insulator cover was placed over the collector because it should have made it extremely difficult for the electrons to reach the collector. Nevertheless, this cover did not account for the screws that hold the collector in place which are recessed in the polyimide base of the RFEA. The recess is sufficient to prevent any ions from being collected by these screws. The electrons on the other hand have much higher mobility and can be collected by these screws.

A couple of things might help in preventing the electron current collection. As mentioned with the ion beam expansion, biasing the 1st grid negative with respect to the $V_{DC}$ may help in preventing the electron current. If the bias of the 1st grid is large enough, it could force electrons traveling through the drift cone to be repelled back towards the plasma or towards the drift cone walls. This could prevent electrons from passing around the outside of the detector. Another option to prevent the electron collection in future experiments is to cover the screws in the base of the RFEA. The difficulty in covering the screws is also finding a material that can be removed if the probe needs to be dismantled or if a signal wire needs to be exchanged. A polymer adhesive (e.g. methacrylate) could be a viable option as a small coating could be used but would still provide access to the screws. By making some adjustments for the electrons that travel through the drift cone, the large negative currents measured by the TM and F probes could be fixed.

The localization of the plasma is an observation that may need to be corrected in future measurements. As was mentioned in the chapters 4 and 5, the peak intensity of the IEDfs decreased every time the pressure increased. Based on hairpin resonator probe measurements, the reduction in peak intensity is likely due to localization of the plasma towards the 60 MHz RF source electrode. The main reason the plasma kept localizing towards the top electrode at higher pressures is likely do to the gap distance between the electrodes. In typical industrial systems, the gap distance is smaller than the approximately 3.15” (8 cm) gap distance of this chamber. If the chamber height were reduced, it is possible that the localization would no longer occur or at least have a weaker dependence on the pressure of the system. This would make the RFEA IEDfs more consistent with the expected results at higher pressures.

Another common issue that was mentioned throughout the paper is secondary electron emission from the grids. Secondary electron emission was evident by the offset of the IV curves as well as negative energy peaks caused by light-up in the old WP design. There are two things that could be done to help reduce the secondary electron emission. The first option is to change the material used for the grids in the RFEA. Depending on the material, the ion-induced secondary electron emission coefficient of a different material may be lower than for aluminum. For example, stainless steel or copper both have lower emission coefficients than aluminum and could be used as the grids. The more consistent way to reduce the effects of secondary electron emission in the RFEA measurements is to switch to a four-grid operation mode. In this mode, a 4th grid is inserted between the discriminator and collector and used to repel electrons back to the collector. Making both modifications to the RFEAs would reduce the effects of the secondary electron emission on the measured IV curves.

Another benefit of changing the grid material could be an increase in the corrosion resistance of the RFEA, thus prolonging its life. In future measurements with the RFEAs, it may be desirable or necessary to use process gases that are more corrosive (e.g. chlorine, ammonia, etc.). Aluminum is corrosion resistant due to the oxide layer that develops on it but there are other materials, such as molybdenum, stainless steel, titanium, and tungsten, that are also corrosion resistant. Some of these are also less susceptible to sputtering (e.g. titanium and tungsten) [ 123, 124 ]. The difficulty in using some of these other materials results from the cost of the material or its manufacturability. In some instances, it may be more economical to use a material with a shorter life time but cheaper to purchase and manufacture.  In the end, depending on the future measurements needed, it may be necessary to switch to a different grid material.

The material choice of the overall chamber can also affect the measurements. As just mentioned, aluminum can be prone to sputtering. Laegreid and Wehner [ 123 ] studied the sputter yield of multiple metals for Ar ions. There results give a sputter yield of 0.2 for 100 eV Ar ions. This does not mean though that aluminum cannot be sputtered at Ar energies lower than

100 eV. Based on the WP measurements for Ar, the peak energy comes quite close (85 eV) to 100 eV. This shows that Ar ions incident on the walls and pumping baffle in the chamber are sputtering aluminum into the plasma possibly changing the plasma properties. In addition, the biggest issue with sputtering aluminum is that it can deposit on surfaces. It is even possible that it deposits on the polyimide insulators separating the grids. This could create a short circuit between the grids preventing the RFEA from operating correctly. The RFEA grids could do this too. The grids must be able to conduct a potential, but this is not necessary for the chamber wall or pumping baffle. Therefore, to reduce sputtering, these aluminum chamber parts could be anodized. This would reduce the sputtering of aluminum because the dielectric coating from the anodization would float to a higher potential reducing the ion energy incident on the wall.

The next design change for future measurements involves the measurement electronics. As mentioned in section 4.2.2, the ion energy in the measurements was limited by the potential at which the low voltage line of the PXI digital multimeter (DMM) could float above ground. The DMMs used in these measurements was limited to 500 V. This was mainly an issue for the DMM measuring the voltage drop across a resistor attached to the collector. Since the collector was tied to the discriminator grid, this meant that the maximum energy the discriminator could sweep was between approximately -500 V to 500 V. Based on the $V_{DC}$ on the bias electrode, the highest ion energy that could be measured in this work was up to about 700 eV. This is a high energy but the RFEA developed in this work should be able to operate up to 5 keV. This potential is substantially higher than most commercial RFEA systems. In order to operate at these higher potentials, there are two options. The first is to trade out the PXI DMM to one that allows the low voltage line to float higher above ground. This may be expensive. The other option is to change the configuration of the measurement electronics. To do this, the collector would no longer be tied to the discriminator grid. Were the RFEA modified to operate in four-grid mode to help reduce secondary electron emission, this adjustment would come inherently.

The last design change recommendation deals with the method used to obtain the $V_{DC}$. For this work, it was shown that the average of the RF waveform taken from the 1st grid of the SM probe provided an accurate $V_{DC}$ value. The RF waveform was measured on the 1st grid of the SM probe by using a HV Tektronix probe. This method was used mainly because the number of RF chokes was limited. All the available RF filters were used on the signal lines going to the other grids of the RFEA. In general, this method provided good $V_{DC}$ measurements but there was a strong dependence on the impedance of the RFEA signal lines in the electrode. It was found that if none of the electrode probes were used and only the 1st grid SM HV line remained, the measured $V_{DC}$ would be different than if external lines were attached to other RFEA probe signal lines. It was determined that adding open-ended 12” (30.48 cm) coax lines to the 2nd, 3rd, and collector lines of the SM or TM probes was sufficient to correct the $V_{DC}$. In future measurements, it would be better to obtain another RF filter and use the DC measurement method used to confirm the averaged waveform measurement. Using the DC measurement would provide a more reliable $V_{DC}$ value that should not be as dependent on the impedance of the probe signal lines.

## 6.2 Future Work

A RFEA has been installed in an industrial cathode and shown to provide a reliable IEDf as fulfilling the purpose of this research, but the completion of this work is just a stepping stone to future projects and studies. Some of these projects and studies were mentioned in the previous section but were mainly quick adjustments to make in the short term. A larger body of work can be built off the work presented here. The projects and studies mentioned here are bodies of work that would need to be investigated in the long term.

The first area that requires further investigation is the work that was done in analyzing the effects of space charge build-up in the RFEAs. The work presented here was done using a 1D particle-in-cell (PIC) code called XPDP1 [ 62 ]. Since these simulations focused on the 1D motion of the ions between planar grids, it was assumed that all radial fields were symmetric so no particle loss to the walls or any type of beam expansion was simulated. It also ignored any collisional effects that could occur in the drift cone. By removing some or all of these assumptions, the number of possibilities for detailed analysis are increased.

One possible area to explore is increasing the number of dimensions. The creators of XPDP1 have other codes (XPDC2 [ 125, 126 ], XOOPIC [ 127 ]) that look at particle motion in 2D. If the second dimension is assumed to be the radius or diameter of the grids, the space charge effects could be analyzed in 2D instead of the simple 1D cases presented here. In these simulations, the introduction of the second dimension would introduce beam expansion from Coulomb repulsion and radial velocity distributions. The effect of this beam expansion on space charge build up could be investigated because the beam expansion may cause particles to neutralize on the detector walls. Collisions could also be incorporated in the simulations which could not only cause more beam expansion but could also represent resonant charge exchange collisions resulting in changes of the IV curve measured in the simulation.

In addition to investigating higher order effects, experimental validation of the space charge simulations and compensation model could be performed. Some measurements have already been taken that show some signs of space charge distortion (See Fig. 135). These measurements were taken with the old wall probe (WP) design (See sections 2.1 and 4.1.2) for a

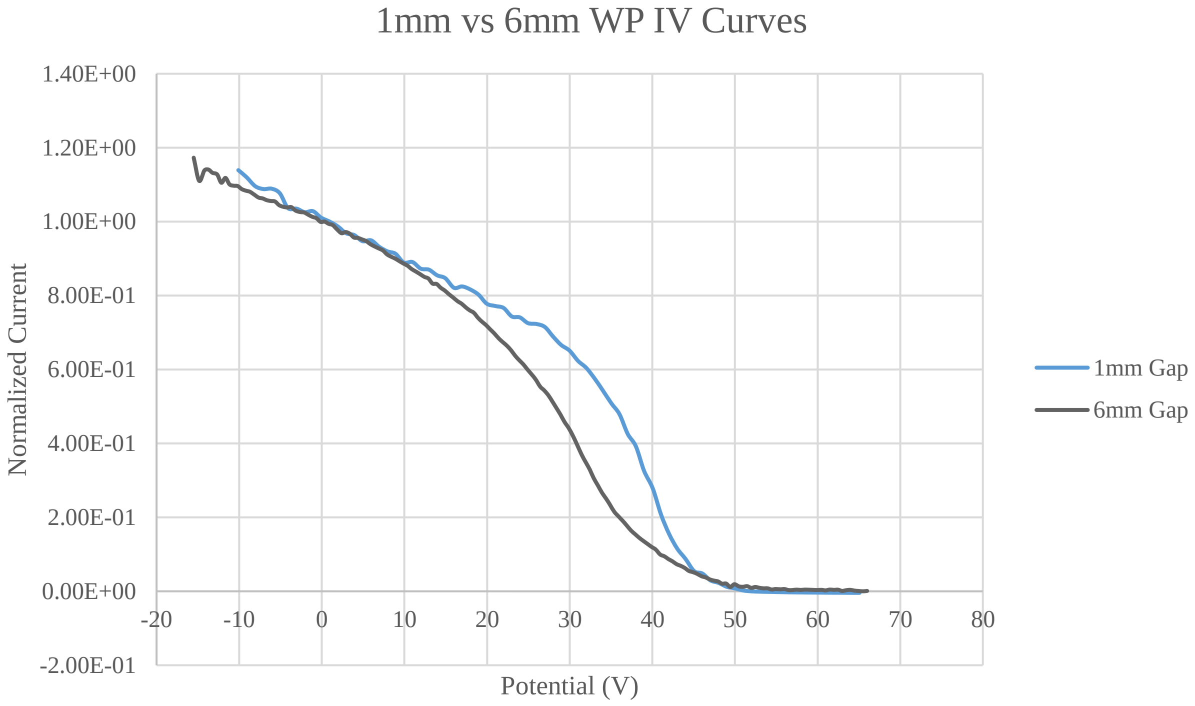

*Fig. 135*: Normalized IV curves that show signs of space charge distortion obtained from the old wall probe (WP) from a 5 mTorr Ar plasma created by a 500 W 60 MHz RF top electrode and a grounded bottom electrode. The gap distance between the plasma electron rejection grid and discriminator was increased from 1 mm to 6 mm.

5 mTorr Ar plasma with a 500 W 60 MHz RF top electrode and a grounded bottom electrode. The only difference between the measurements was the gap distance between the plasma electron rejection grid and the discriminator was increased from 1 mm to 6 mm. Each curve was normalized by the current measured at a discrimination potential of 0 V in order to focus on the shape of the curves. As can be seen in Fig. 135, the 6 mm IV curve drops off earlier than the 1 mm IV curve which is indicative of space charge. The curves also meet back up at higher energies like predicted in the XPDP1 simulations.

Even though the 6 mm IV curve shows signs of space charge distortion, the current compensation model was unable to provide good correction for the distortion like shown with the PIC simulations. The main reason for this was due to significant difference in measured current. As mentioned, the curves were normalized to focus on the shape of the IV curves. Nevertheless, the current measured by the RFEA with the 6 mm gap had a much lower overall current. This is likely due to collisions or losses at the side wall of the detector. Since the compensation model has a strong dependence on the saturation current, the fact that the space charge distorted curve had a much smaller incoming current than not only the PIC simulations but the 1 mm case also presented some problems when calculating the intercept potential and the convergence potential. These two potentials are the key to the linear truncation of the system matrix in the regularized least squares solution, so the resulting truncation did not provide the expected distortion compensation. More work could be done here by taking more measurements that are likely to be space charge distorted with smaller RFEA gaps so collisions and particle loss at the walls is less significant. The compensation model could also be updated by taking into account higher order effects in the derivation of the intercept potential and the convergence potential. More measurements and an updated model may make it possible to experimentally validate the simulation work while also confirming the ability to compensate for space charge distortion.

Another area in which the 2D PIC codes could be beneficial is in modeling the ion particle motion and their interactions within the drift cones of the electrode. As was mentioned in chapters 4 and 5, the drop in peak intensity of the top mount (TM) and floating (F) probes was due to beam expansion in the drift cone. This was also the cause of a linear current measurement in the ion saturation region mentioned in section 4.1.2 from ion collection outside the detector. The ion motion and their interactions within the drift cone was not studied before these observations were made. With the 2D PIC codes though, it would be possible to model the beam expansion and ion collisions that may occur in the drift cone as the ions traverse the distance to the RFEA. Some work in this area has already been performed by another student, Yao Du. He has used XOOPIC to model the ion trajectories down the drift cone for an Ar plasma (See Fig.

136). As can be seen in Fig. 136, the ion flux experiences significant expansions when traveling the length of the drift cone. Using this code, simulations could be run to see if it is possible to reduce the expansion by changing the potential of the grid at the bottom of the drift cone as mentioned in the previous section. It could also be used to analyze the effect that ion collisions have (Coulomb scattering or resonant charge exchange) on the measured current.

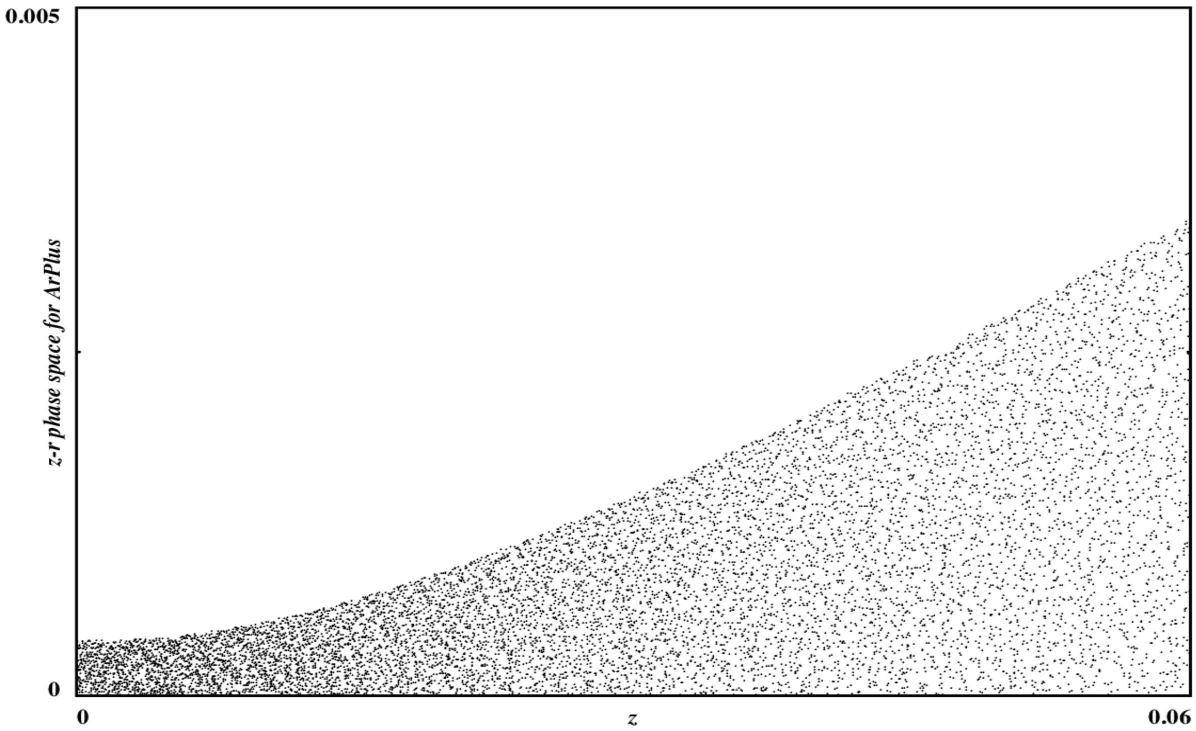

*Fig. 136*: Plot of the z-r phase space for Ar ions in the drift cone. This plot shows the expansion of the Ar ion flux as it travels the length of the drift cone.

With this ion beam expansion inside the drift cone, the effects of Coulomb collisions become more significant based on the entrance size of the detector. Using the dimensions of the silicon (Si) wafer grids, drift cone, and RFEA, it was determined that, for an ion to make it to the collector, the incident angle when entering the Si grid must be less than or equal to 5.5° from the vertical. Given that most Coulomb scattering collisions are small angle collisions introduces a problem for current collection if the ions must remain below that 5.5° threshold. Typically, work that has been done looking at the mean free path of ions for Coulomb scattering has focused on large angle collisions ($\geq 45°$) [ 12 ]. In order to gain a better understanding of the true mean free path of ions in the drift cone, the derivation of the Coulomb scattering cross-section would need to be revisited with a focus on smaller collision angles (e.g. $\geq 5°$ or $10°$).

The study of resonance charge exchange is another area that could be studied from this work. As mentioned in section 4.1.2 and 4.2.2, positive offsets of the IV curves were typically observed in the region where all ions should be repelled before reaching the collector. This positive current collection was attributed to fast neutrals created through resonant charge exchange that enter the detector. These fast neutrals can be quite important in plasma processing. Just as they pass through the RFEA without be diverted by the grid potentials, they can reach the bottom of small channels being etched into Si wafers without being diverted by charge build-up on the channel walls. When reaching the bottom of the channel, these fast neutrals retain enough energy to remove material at the site of impact. This is especially important in high aspect ratio etching processes where the channels are quite narrow and long. However, as they are neutral particles, it is hard to measure how many are incident on a surface. The 2D PIC simulations could help with this. Resonant charge exchange collisions could be added into the simulations to analyze the number of fast neutrals that are created when traveling down the drift cone. This would be beneficial as all the current loss in the measurements from the TM and F probes is not a result of beam expansion alone. Charge exchange collisions could also be a cause of current loss.

Another option that may be more relevant to the plasma processing community is the development of a measurement technique for fast neutrals. It seems possible that this could be done with two different RFEAs located close to one another and at the same distance from the plasma. The first RFEA would operate in four-grid mode where a secondary electron rejection grid forces all secondary electrons back to the collector. The second RFEA would operate in three-grid with no secondary electron rejection grid. Both RFEAs would take measurements at the point when all ions are rejected by the discriminator. If the four-grid RFEA is working properly, no current should be measured except any background noise from the measurement electronics. This probe would confirm there are no other sources of current measured in this regime. In the three-grid RFEA, no ion current should be measured but a small current caused by secondary electron emission from fast neutrals should be measured. By subtracting this small current by the baseline background noise and dividing by the secondary electron emission coefficient of the collector material, an estimate of the fast neutral current could be obtained. Of course, this calculation would be dependent on the accuracy of the secondary electron emission coefficient. Böhm and Perrin [ 80 ] provide results for secondary electron emission coefficients for different materials. There results give a global value and an ion induced value. However, the author is not aware if the fast neutral emission coefficient differs from the global or ion induced emission coefficients. Any difference between the coefficients introduces uncertainty and error in the approximation It would also be necessary to make sure the mean free path of the ions is large in the RFEAs. If the mean free path is too small, extra fast neutrals could be created within the probe itself artificially inflating the fast neutral current. If these two sources of error are taken into account though, this method would provide an estimation of the fast neutral current incident on a Si wafer surface.

One last area of study that could continue from this work is an analysis of the cause behind the single peak WP IEDfs. It has been well established that the plasma potential $(V_p)$ in an RF plasma oscillates [ 12, 14, 18, 32 ]. Since the $V_p$ oscillates but the grounded wall remains at 0 V, the boundary sheath at the chamber walls should oscillate as well. This should create a bimodal IEDf like observed by Soblolewski, Wang, and Goyette [ 15 ]. It is possible in the case were 60 MHz was the only power source that the oscillations of $V_p$ were too quick so the ions were unable to respond instantly to the changes. As a result, they responded to the average of the oscillation. Nonetheless, the WP IEDfs were single peaks even when the 13 MHz bias was added and the ions should be able to respond to the 13 MHz oscillations. The cause may lie in what happens at a ground interface of an RF plasma. Most sheaths have been studied at the electrode interface [ 1, 10, 12 ] where the plasma is at some positive potential, the plasma sheath interface is assigned 0 V, and then the electrode surface is a boundary condition given some potential below 0 V. A model of this setup can be seen in Fig. 137.

This sheath model works well for cases where the electrode sits at a negative $V_{DC}$ but would not work for a surface at ground. In the case of the grounded surface, the surface would be located at the sheath interface. Based on this model, the $V_p$ is found by

$$V_p = \frac{T_e}{2} \tag{39}$$

where $T_e$ is the electron temperature. In most industrial plasmas, the electron temperature is typically between 2 – 5 eV and possibly up to 10 eV. Based on Eq. 39, this means that the plasma potential would be around 1 – 5 V. However, a plasma with such a low potential is not very common. In the case of this work, the ion energy measured with the WP provides a measurement of $V_p$. The $V_p$ measured here ranged anywhere from 20 V to 80 V. This is drastically different than what Eq. 39 provides. Therefore, a new model developed for grounded sheaths is required to gain a better understanding of the sheath dynamics at grounded surfaces in RF plasmas.

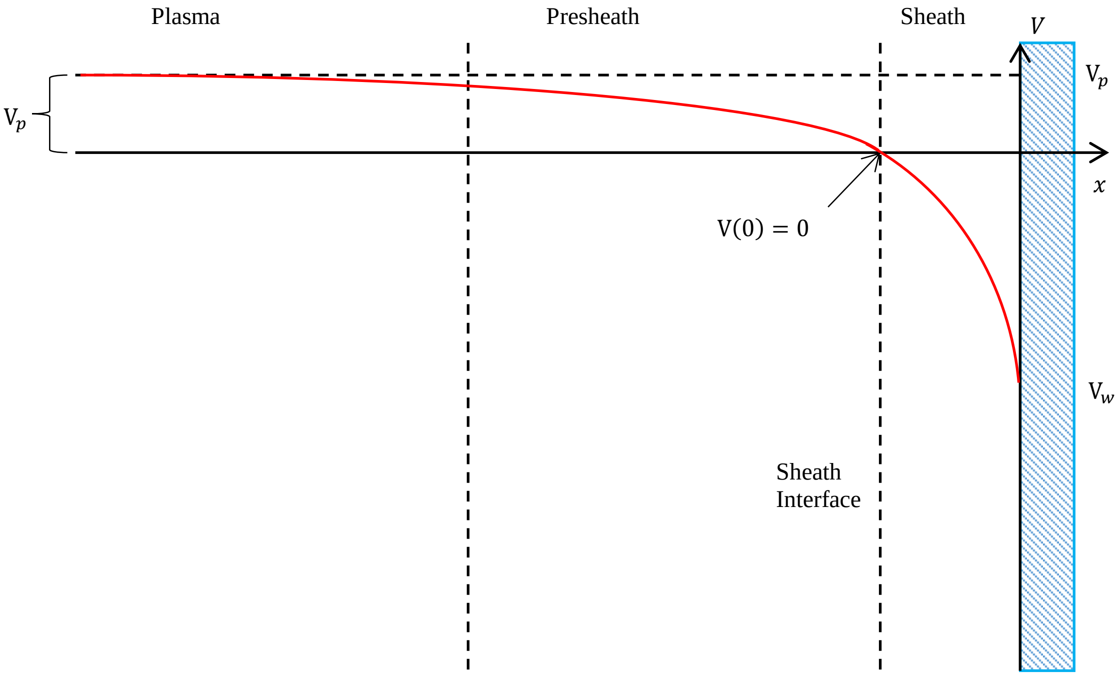

*Fig. 137*: Plot of the potential moving from the plasma, through the presheath, and then to the wall. This figure is modeled after the one presented by Lieberman and Lichtenberg [ 12 ]. In the plot, the plasma potential is $V_p$, the wall potential is $V_w$, and the potential at the sheath interface ($x = 0$) is $V(0)$.

# REFERENCES

1. Kortshagen, U. & Zethoff, M., Ion energy distribution functions in a planer inductively coupled RF discharge. *Plasma Sources Sci. Technol.* **4**, 541-550 (1995).
2. Coumou, D. J. *et al.*, Ion energy distribution skew control using phase-locked harmonic rf bias drive. *IEEE Transactions on Plasma Science* **42** (7), 1880 - 1892 (2014).
3. Edelberg, E. A., Perry, A., Benjamin, N. & Aydil, E. S., Compact floating ion energy analyzer for measuring energy distributions of ions bombarding radio-frequency biased electrode surfaces. *Review of Scientific Instruments* **70** (6), 2689 - 2698 (1999).
4. Enloe, C. L. & Shell, J. R., Optimizing the energy resolution of planar retarding potential analyzers. *Rev. Sci. Instrum.* **63** (2), 1788-1791 (1992).
5. Gahan, D., Dolinaj, B. & Hopkins, M. B., Retarding field analyzer for ion energy distribution measurements at a radio-frequency biased electrode. *Review of Scientific Instruments* **79**, 1 - 9 (2008).
6. Woodworth, J. R. *et al.*, Ion energy and angular distributions in inductively coupled radio frequency discharges in argon. *J. Appl. Phys.* **80** (3), 1304 - 1311 (1996).
7. Sowa, M. J., Blain, M. G., Jarecki, R. L. & Stevens, J. E., Spatially resolved electron temperature measurements with a micorfabricated retarding field analyzer. *Appl. Phys. Lett.* **80** (6), 932-934 (2002).
8. Ellmer, K., Wendt, R. & Wiesemann, K., Interpretation of ion distribution functions measured by a combined energy and mass analyzer. *International Journal of Mass Spectrometry* **223-224**, 679-693 (2003).
9. Chabert, P. & Braithwaite, N., in *Physics of Radio-Frequency Plasmas* (Cambridge University Press, Cambridge, 2011), pp. 96 - 130.
10. Panagopoulos, T. & Economou, D. J., Plasma sheath model and ion energy distribution for all radio frequencies. *J. Appl. Phys.* **85** (7), 3435-3443 (1999).
11. Rauf, S., Effect of bias voltage waveform on ion energy distribution. *J. Appl. Phys.* **87** (11), 7647-7651 (2000).
12. Lieberman, M. A. & Lichtenberg, A. J., *Principles of plasma discharges and materials processing*, 2nd ed. (John Wiley and Sons, Hoboken, 2005).
13. Mussenbrock, T., Modeling and simulation of ion energy distribution functions in technological plasmas. *Contrib. Plasma Phys.* **52** (7), 571-583 (2012).
14. Denpoh, K., Wakayama, G. & Nanbu, K., Sheath model for dual-frequency capacitively coupled plasmas. *Japanese Journal of Applied Physics* **43** (8A), 5533-5539 (2004).
15. Sobolewski, M. A., Wang, Y. & Goyette, A., Measurements and modeling of ion energy distributions in high-density, radio-frequency biased CF4 discharges. *J. Appl. Phys.* **91** (10), 6303-6314 (2002).
16. Lee, J. K., Manuilenko, O. V., Babaeva, N. Y., Kim, H. C. & Shon, J. W., Ion energy distribution control in single and dual frequency capacitive plasma sources. *Plasma Sources Sci. Technol.* **14**, 89-97 (2005).
17. Li, Z.-C. *et al.*, Experimental investigation of ion energy distributions in a dual frequency capacitively coupled Ar/CF4 plasma. *Physics of Plasmas* **17**, 033501 (2010).

18. Liu, J., Liu, Y.-X., Bi, Z.-H., Gao, F. & Wang, Y.-N., Experimental investigations of electron density and ion energy distribution in dual-frequency capacitively coupled plasmas for Ar/CF4 and Ar/O2/CF4 discharges. *J. Appl. Phys.* **115**, 013301 (2014).
19. Curley, G. A. *et al.*, Negative ions in single and dual frequency capacitively coupled fluorocarbon plasmas. *Plasma Sources Sci. Technol.* **16**, S87-S93 (2007).
20. Bi, Z.-H., Dai, Z.-L., Xu, X., Li, Z.-C. & Wang, Y.-N., Numerical results for the Ar and CF4 mixture gas in a dual frequency capacitively coupled plasma using a hybrid model. *Physics of Plasmas* **16**, 043510 (2009).
21. Georgieva, V. & Bogaerts, A., Numerical simulation of dual frequency etching reactors: influence of the external process parameters on the plasma characteristics. *J. Appl. Phys.* **98**, 023308 (2005).
22. Georgieva, V. & Bogaerts, A., Plasma characteristics of an Ar/CF4/N2 discharge in an asymmetric dual frequency reactor: numerical investigation by a PIC/MC model. *Plasma Sources Sci. Technol.* **15**, 368-377 (2006).
23. Rakhimova, T. V. *et al.*, Experimental and theoretical study of ion energy distribution function in single and dual frequency RF discharges. *IEEE Transactions on Plasma Science* **35** (5), 1229-1240 (2007).
24. Zhang, Y., Zafar, A., Coumou, D. J., Shannon, S. C. & Kushner, M. J., Control of ion energy distributions using phase shifting in multi-frequency capacitively coupled plasmas. *J. Appl. Phys.* **117** (23), 233302-1-233302-15 (2015).
25. Gupta, N. & Raju, G. R. G., Numerical and Analytic Techniques to Study. *IEEE Transactions on Dielectrics and Electrical Insulation* **7** (5), 705 - 720 (2000).
26. Flamm, D. L. & Donnely, V. M., The design of plasma etchants. *Plasma Chemistry and Plamsa Processing* **1** (4), 317-363 (1981).
27. Kanarov, V., Siegfried, D., Sferlazzo, P., Hayes, A. & Yevtukhov, R., High resolution energy analyzer for broad ion beam characterization. *Review of Scientific Instruments* **79**, 1-16 (2008).
28. Zabeida, O. & Martinu, L., Ion energy distributions in pulsed large area microwave plasma. *J. Appl. Phys.* **85** (9), 6366-6372 (1999).
29. Kuypers, A. D. & Hopman, H. J., Ion energy measurement at the powered electrode in an rf discharge. *J. Appl. Phys.* **63** (6), 1894 - 1898 (1988).
30. Kuypers, A. D. & Hopman, H. J., Measurement of ion energy distributions at the powered rf electrode in a variable magnetic field. *J. Appl. Phys.* **67** (3), 1229 - 1240 (1990).
31. Toups, M. F. & Ernie, D. W., Pressure and frequency dependence of ion bombardment energy distributions from rf discharges. *J. Appl. Phys.* **68** (12), 6125-6132 (1990).
32. Gahan, D. *et al.*, Ion energy distribution measurements in rf and pulsed dc plasma discharges. *Plasma Sources Sci. Technol.* **21**, 024004 (8pp) (2012).
33. Corbella, C. *et al.*, Ion energy distributions in bipolar pulsed-dc discharges of methane measured at the biased cathode. *Plasma Sources Sci. Technol.* **20**, 015006 (8pp) (2001).
34. Landheer, K. *et al.*, Note: Laser-cut molybdenum grids for a retarding field energy analyzer. *Review of Scientific Instruments* **88** (2017).
35. Kim, D., Hudson, E. A., Cooperberg, D., Edelberg, E. & Srinivasan, M., Profile simulation of high aspect ratio contact etch. *Thin Solid Films*, 4874-4878 (2007).

36. Nishikawa, K., Ootera, H., Tomohisa, S. & Oomori, T., Transport mechanisms of ions and neutrals in low-pressure, high-density plasma etching of high aspect ratio contact holes. *Thin Solid Films*, 190-207 (2000).
37. Kondyurin, A. & Bilek, M., Etching and structure changes in PMMA coating under argon plasma immersion ion implantation. *Nuclear Instruments and Methods in Physics Research B* **269**, 1361-1369 (2001).
38. Nikitenkov, N. N., Sutygina, A. N., Shulepov, I. A. & Kashkarov, E. B., Pulsed plasma-immersion ion implantation of aluminum into VT1-0 titanium. *Bulletin of the Russian Academy of Sciences. Physics* **80** (2), 117-119 (2016).
39. Edelberg, E. A. & Aydil, E. S., Modeling of the sheath and the energy distribution of ions bombarding rf-biased substrates in high density plasma reactors and comparison to experimental measurements. *J. Appl. Phys.* **86** (9), 4799 - 4812 (1999).
40. Jiang, N., Zhao, N., Hongfei, L. & Tongzhen, F., Mass-resolved retarding field energy analyzer and its measurement of ion energy distribution in helicon plasma. *Nuclear Instruments and Methods in Physics Research B* **229**, 508-518 (2005).
41. Ingram, S. G. & Braithwaite, N. S. J., Ion and electron energy analysis at surface in an RF discharge. *J. Phys. D: Appl. Phys.* **21**, 1496 - 1503 (1988).
42. Shannon, S., Hoffman, D., Yang, J. & Godyak, V., The need for three frequencies for truly independent plasma parameter control. *Proceedings of International Symposium on Dry Process* **5**, 345 (2005).
43. Yoshida, Y. *et al.*, *Selective etching by tailored RF ion energy control using frequency/phase locked RF power delivery*, presented at 70th Annual Gaseous Electronics Conference, Pittsburgh, 2017 (unpublished).
44. Marmet, P. & Kerwin, L., An improved electrostatic electron selector. *Can. J. Phys.* **38**, 787-796 (1960).
45. Janes, J. & Huth, C., Energy resolved angular distribution of argon ions at the substrate plane of a radio frequency plasma reactor. *J. Vac. Sci. Technol. A* **10** (6), 3522-3531 (1992).
46. Sar-el, H. Z., Cylindrical Capacitor as an Analyzer* I. N onrelativistic Part. *Rev. Sci. Instrum.* **38** (9), 1210-1216 (1967).
47. Olthoff, J. K., Van Brunt, R. J., Radovanov, S. B., Rees, J. A. & Surowiec, R., Kinetic-energy distributions of ions sampled from argon plasmas in a parallelplate, radio-frequency reference cell. *J. Appl. Phys.* **75**, 115-125 (1994).
48. Olthoff, J. K., Van Brunt, R. J. & Radovanov, S. B., Studies of ion kinetic-energy distributions in the gaseous electronics conference RF reference cell. *Journal of Research of the National Institute of Standards and Technology* **100** (4), 383-400 (1995).
49. Rao, M. V. V. S., Van Brunt, R. J. & Olthoff, J. K., Resonant charge exchange and transport of ions at high electric-field to gas-density ratios (E/N) in argon, neon, and helium. *Phy. Rev. E* **54** (5), 5641-5656 (1996).
50. Mizutani, N., Nagata, Y., Kubo, A. & Hayashi, T., Ion energy and mass analyzer at radio frequency electrode in a plasma chamber. *Rev. Sci. Instrum.* **69** (4), 1918-1919 (1998).

51. Wang, Y. & Olthoff, J. K., Ion energy distrubutions in inductively coupled radio-frequency discharge in argon, nitrogen, oxygen, chlorine, and their mixtures. *J. Appl. Phys.* **85** (9), 6358-6365 (1999).
52. Coburn, J. W. & Kay, E., Positive-ion bombardment of substrates in rf diode glow discharge sputtering. *J. Appl. Phys.* **43** (12), 4965-4971 (1972).
53. Seeböck, R. J., Köhler, W. E. & Römheld, M., Pressure dependence of the mean electron energy in the bulk plasma of an rf discharge in argon. *Contrib. Plamsa Phys.* **32** (6), 613-622 (1992).
54. Dillon, J. A., Sheridan, W. F., Edwards, H. D. & Ghosh, S. N., Charge transfer reactions in monatomic and diatomic gases. *The Journal of Chemical Physics* **23** (5), 776-779 (1955).
55. Ghosh, S. N. & Sheridan, W. F., Experimental determinations of charge transfer cross sections and secondary electron emission by ion bombardment. *The Journal of Chemical Physics* **26** (3), 480-485 (1957).
56. Ushakov, A. *et al.*, Study of fluorocarbon plasma in 60 and 100 MHz capacitively coupled discharges using mass spectrometry. *J. Vac. Sci. Technol. A* **26** (5), 1198-1207 (2008).
57. Gulbrandsen, N., Miloch, W. J. & Fredriksen, Å., Interpretation of ion velocity distributions measured with a grounded retarding field energy analyzer in an inductively coupled helicon plasma. *Contrib. Plamsa Phys.* **53** (1), 27-32 (2013).
58. Denpoh, K., Simulation of ion energy and angular distribution functions using Monte Carlo method coupled with multidimensional radio frequency sheath model developed utilizing COMSOL Multiphysics. *Japanese Journal of Applied Physics* **53**, 080304 (4pp) (2016).
59. Charles, C., Degeling, A. W., Sheridan, T. E., Harris, J. H. & Lieberman, M. A., Absolute measurements and modeling of radio frequency electric fields using a retarding field energy analyzer. *Phys. Plasmas* **7** (12), 5232-5241 (2000).
60. Edelberg, E. A., Perry, A., Benjamin, N. & Aydil, E. S., Energy distributions of ions bombarding biased electrodes in high density plasma reactors. *J. Vac. Sci. Technol. A* **17** (2), 506-516 (1999).
61. Lee, C. & Lieberman, M. A., Global model of Ar, O2, Cl2, and Ar/O2 highdensity plasma discharges. *J. Vac. Sci. Technol.* **13** (2), 368-380 (1995).
62. Verboncoeur, J. P., Alves, M. V., Vahedi, V. & Birdsall, C. K., Simultaneous potential and circuit solution for 1D bounded plasma particle simulation codes. *Journal of Computational Physics* **104** (2), 321-328 (1993).
63. Yang, M. & Gong, Y., *An improved analytic collisionles sheath model*, presented at ISTC, 2001 (unpublished).
64. Hanson, W. B. & McKibbin, D. D., An ion-trap measurement of the ion concentration profile above the F2 peak. *Journal of Geophysical Research* **66** (6), 1667-1671 (1961).
65. Tochikubo, F., Suemasa, K. & Watanabe, T., Application of image reconstruction technique for the measurement of two-dimensional ion energy distributions using a retarding field energy analyzer. *Jpn. J. App. Phys.* **35**, L 1219-L 1221 (1996).
66. Simpson, J. A., Design of retarding field energy analyzers. *Review of Scientific Instruments* **32** (12), 1283-1293 (1961).

67. DeNeef, C. P. & Theiss, A. J., Effect of finite analyzer size on the distribution functions measured in field-free plasmas. *Rev. Sci. Instrum.* **50** (3), 378-381 (1979).
68. Goldan, P. D., Yadlowsky, E. J. & Whipple, Jr., E. C., Errors in ion and electron temperature measurements due to grid plane potential nonuniformities in retarding potential analyzers. *Jounal of Geophysical Research* **78** (16), 2907-2916 (1973).
69. Hanson, W. B., Frame, D. R. & Midgley, J. E., Errors in retarding potential analyzers caused by nonuniformity of the grid-plane potential. *Journal of Geophysical Research* **77** (10), 1914-1922 (1972).
70. Mizutani, N. & Hayashi, T., Ion energy analysis through rf-electrode. *Jpn. J. Appl. Phys.* **36**, L 1470-L1473 (1997).
71. Rafalskyi, D., Dudin, S. & Aanesland, A., Magnetized retarding field energy analyzer measuring the particle flux and ion energy distribution of both positive and negative ions. *Rev. Sci. Instrum.* **86** (5), 053302 (2015).
72. Bardakov, V. M., Ivanov, S. D., Kazantsev, A. V. & Strokin, N. A., Peculiarities of measuring ion energy distribution in plasma with a retarding field analyzer. *Rev. Sci Instrum.* **86** (5), 053501 (2015).
73. Chao, C. K. & Su, S.-Y., Charged particle motion inside the retarding potential analyzer. *Physics of Plasmas* **7** (1), 101-107 (2000).
74. Knudsen, W. C., Evaluation and demonstration of the use of retarding potential analyzers for measuring several ionospheric quantities. *Journal of Geophysical Research* **71** (19), 4669-4678 (1966).
75. Donoso, G., Martin, P. & Puerta, J., Experimental verification of the grid effects in a velocity analyzer with varible geometry. *Rev. Sci. Instrum.* **57** (8), 1507-1511 (1986).
76. Donoso, G. & Martin, P., Grid effects on velocity analyzers of variable geometry. *Rev. Sci. Instrum.* **57** (8), 1501-1506 (1986).
77. Blain, M. G., Stevens, J. E. & Woodworth, J. R., High-resolution submicron retarding field energy analyzer for low-temperature plasma analysis. *Appl. Phys. Lett.* **75** (25), 3923-3925 (1999).
78. Fisher, L. E. *et al.,* Including sheath effects in the interpretation of planar retarding potential analyzer's low-energy ion data. *Rev. Sci. Instrum.* **87**, 043504 (2016).
79. Sharma, S., Gahan, D., Scullin, P., Daniels, S. & Hopkins, M. B., Ion angle distribution measurement with a planar retarding field analyzer. *Rev. Sci. Instrum.* **86** (11), 113501 (2015).
80. Böhm, C. & Perrin, J., Retarding-field analyzer for measurements of ion energy distributions and secondary electron emission coefficients in low-pressure radio frequency discharges. *Review of Scientific Instruments* **64** (1), 31 - 44 (1993).
81. Brunner, D., LaBombard, B., Ochoukov, R. & Whyte, D., Scanning retarding field analyzer for plasma profile measurements in the boundary of the Alcator C-Mod tokamak. *Rev. Sci. Instrum.* **84** (3), 033502 (2013).
82. Green, T. S., Space charge effects in plasma particle analyzers. *Plasma Phys.* **12**, 877-883 (1970).
83. Donoso, G. & Martin, P., Space-charge effects in a velocity analyzer of variable geometry. *Rev. Sci. Instrum.* **61** (11), 3381-3383 (1990).

84. Pitts, R. A. *et al.*, Retarding field energy analyzer for the JET plasma boundary. *Rev. Sci. Instrum.* **74** (11), 4644-4657 (2003).
85. Jones, R., Optimization and performance of electrostatic particle analyzers. *Review of Scientific Instruments* **49** (21), 21-23 (1978).
86. Semion Single Sensor, Available at https://www.impedans.com/semion-single-sensor (2017).
87. Brown, S. C., *Basic Data of Plasma Physics* (Technology Press of the Massachusetts Institue of Technology, Cambridge, 1959).
88. Martin, P. & Donoso, G., A new Langmuir-Child equation including temperature effects. *Phys. Fluids B* **1** (1), 247-251 (1989).
89. Kaufman, H. R. & Robinson, R. S., Ion Source Design for Industrial Applications. *AIAA Journal* **20** (6), 745-760 (1982).
90. Rovang, D. C. & Wilbur, P. J., MS Thesis, 1984.
91. Spangenberg, K. R., *Vacuum tubes* (McGraw-Hill, New York, 1948).
92. Henneberg, W., Das Potential von Schlitzblende und Lochblende. *Zeitschrift für Physik* **94**, 22-27 (1935).
93. Donko, Z. & Petrovic, Z. L., Ion behavior in capacitively-coupled dual frequency discharges. *Journal of Physics: Conference Series* **86**, 012011 (2007).
94. Rauf, S. & Kushner, M. J., Argon metastable densities in radio frequency Ar, Ar/O2 and Ar/CF4 electrical discharges. *J. Appl. Phys.* **82** (6), 2805-2813 (1997).
95. Kono, A., Konishi, M. & Kato, K., Behaviours of electron and negative-ion densities in low-pressure high-density inductively coupled plasmas of SF6, NF3, CF4, and C4F8 gases diluted with Ar. *Thin Solid Films* **407**, 198-203 (2002).
96. Booth, J.-P. *et al.*, Fluorine negative ion density measurement in a dual frequency capactive plasma etch reactor by cavity ring-down spectroscopy. *Appl. Phys. Lett.* **88** (15), 151502 (2006).
97. Georgieva, V., Bogaerts, A. & Gijbels, R., Particle-in-cell/Monte Carlo simulation of capacitively coupled radio frequency Ar/CF4 discharge: effect of gas composition. *J. Appl. Phys.* **93** (5), 2369-2379 (2003).
98. Zhang, Z., Tang, H., Zhang, Z., Wang, J. & Cao, S., A retarding potential analyzer design for keV-level ion thruster beams. *Rev. Sci. Instrum.* **87** (12), 123510 (2016).
99. Baloniak, T., Reuter, R., Flötgen, C. & von Keudell, A., Calibration of a miniaturized retarding field analyzer for low-temperature plasmas: geometrical transparency and collisional effects. *J. Phys. D: Appl. Phys.* **43**, 055203 (2010).
100. SolidWorks [Computer Software], Available at https://www.solidworks.com (2016, 2017).
101. The Magnetic and Electric Field and Force Software for Electromagnetic Applications, Available at https://www.emworks.com/products/EMS (2016).
102. High Frequency Simulation: Antenna and Electromagnetic Simulation Software [Computer Software], Available at https://www.emworks.com/product/hfworks (2016).
103. Zheng, S., Conductance calculation - molecular flow, long tube of circular cross section, Available at lss.fnal.gov/archive/other/ssc/ssc-gem-tn-93-382.pdf (1993).

104. Hansen, P. C., in *Rank-deficient and discrete ill-posed problems* (Society for Industrial and Applied Mathematics, Philadelphia, 1998), pp. 99-133.
105. Samarskii, A. A. & Vabishchevich, P. N., in *Numerical methods for solving inverse problems of mathematical physics* (Walter de Gruyter GmbH & Co., Berlin, 2007), pp. 127-137.
106. Shannon, S., Holloway, J. P. & Brake, M. L., Spatially resolved fluorine actinometry. *J. Vac. Sci. Technol. A* **17** (5), 2703-2708 (1999).
107. Holloway, J. P., Shannon, S., Sepke, S. M. & Brake, M. L., A reconstruction algorithm for a spatially resolved plasma optical emission spectroscopy sensor. *Journal of Quantitative Spectroscopy & Radiative Transfer* **68** (1), 101-115 (2001).
108. Saghir, A. E., Kennedy, C. & Shannon, S., Electron energy distribution function extraction using integrated step function response and regularization methods. *IEEE Transactions on Plasma Science* **38** (2), 156-162 (2010).
109. Saghir, A. E. & Shannon, S., Reduction of EEDF measurement distortion in regularized solutions of the Druyvesteyn relation. *IEEE Transactions on Plasma Science* **39** (1), 596-602 (2011).
110. Nanbu, K. & Kitatani, Y., An ion-neutral species collision model for particle simulation of glow discharge. *J. Phys. D: Appl. Phys.* **28**, 324-330 (1995).
111. Rapp, D. & Francis, W. E., Charge exchange between gaseous ions and atoms. *The Journal of Chemical Physics* **37** (11), 2631-2645 (1962).
112. Cramer, W. H., Elastic and inelastic scattering of low-velocity ions: Ne+ in A, A+ in Ne, and A+ in A. *The Journal of Chemical Physics* **30** (3), 641-642 (1959).
113. McDaniel, E. W., Mitchell, B. A. & Rudd, M. E., *Atomic collisions: heavy particle projectiles* (Wiley, New York, 1993).
114. Piejak, R. B., Al-Kuzee, J. & Braithwaite, N. S. J., Hairpin resonator probe measurements in RF plasmas. *Plasma Sources Sci. Technol.* **14**, 734-743 (2005).
115. Piejak, R. B., Godyak, V. A., Garner, R., Alexandrovich, B. M. & Sternberg, N., The hairpin resonator: a plasma density measuring technique revisited. *J. Appl. Phys.* **95**, 3785 (2004).
116. Peterson, D. J., Kraus, P., Chua, T. C., Larson, L. & Shannon, S. C., Electron neutral collision frequency measurement with the hairpin resonator probe. *Plasma Sources Sci. Technol.* **26**, 095002 (2017).
117. Karkari, S. K., Gaman, C., Ellingboe, A. R., Swindells, I. & Bradley, J. W., A floating hairpin resonance probe technique for measuring time-resolved electron density in pulse discharge. *Measurement Science and Technology* **18**, 2649-2656 (2007).
118. Sands, B. L., Siefert, N. S. & Ganguly, B. N., Design and measurement considerations of hairpin resonator probes for determining electron number density in collisional plasmas. *Plasma Sources Sci. Technol.* **16**, 716-725 (2007).
119. Haas, F. A., Al-Kuzee, J. & Braithwaite, N. S. J., Electron and ion sheath effects on a microwave "hairpin" probe. *Appl. Phys. Lett.* **87**, 201503 (2005).
120. Dankov, P., Stefanov, P., Gueorguiev, V. & Ivanov, T., Hairpin-resonator probe design and measurement considerations. *Journal of Physics: Conference Series* **207**, 012015 (2010).

121. Conway, J., Sirse, N., Karkari, S. K. & Turner, M. M., Using the resonance hairpin probe and pulsed photodetachment technique as a diagnostic for negative ions in oxygen plasma. *Plamsa Sources Sci. Technol.* **19**, 065002 (2010).
122. McMillin, B. K. & Zachariah, M. R., Two-dimensional laser-induced fluorescence imaging of metastable density in low-pressure radio frequency argon plasmas with added O2, Cl2, and CF4. *J. Appl. Phys.* **79** (1), 77-85 (1996).
123. Laegreid, N. & Wehner, G. K., Sputtering yields of metals for Ar+ and Ne+ ions with energies from 50 to 600 eV. *J. Appl. Phys.* **32** (3), 365-369 (1961).
124. Somogyvári, Z., Langer, G. A., Erdélyi, G. & Balázs, L., Sputtering yeilds for low-energy Ar+- and Ne+-ion bombardment. *Vacuumj* **86**, 1979-1982 (2012).
125. Vahedi, V., Birdsall, C. K., Lieberman, M. A., DiPeso, G. & Rognlien, T. D., Verification of frequency scaling laws for capacitive radio-frequency discharges using two-dimensional simulations. *Phys. Fluids B* **5** (7), 2719-2729 (1993).
126. Vahedi, V. & DiPeso, G., Simultaneous potential and circuit solution for two-dimensional bounded plasma simulation codes. *J. Comp. Phys.* **131**, 149-163 (1997).
127. Verboncoeur, J. P., Langdon, A. B. & Gladd, N. T., An object-oriented electromagnetic PIC code. *Comp. Phys. Comm.* **87**, 199-211 (1995).

# APPENDICES

# Appendix A: Electron Temperature and Sheath Density Code

Plasma Impedance Model
ClearAll

Clear[$x$]
Input Parameters
$P_{abs}$= Quantity[75.0,"Watts"]

ω = {2.0*π*UnitConvert[Quantity[2.26*$10^{6}$,"Hertz"]],2.0*π*UnitConvert[Quantity[13.56*$10^{6}$,"Hertz"]],2.0*π*UnitConvert[Quantity[27.12*$10^{6}$,"Hertz"]],2.0*π*UnitConvert[Quantity[67.8*$10^{6}$,"Hertz"]]}

p = UnitConvert[Quantity[0.01,"Torr"],"SI"]

$R_{R}$=Quantity[0.15, "Meters"]

$L_{R}$=Quantity[0.3, "Meters"]

$T_{g}$=Quantity[300.0,"Kelvins"]

$M_{u}$ = Quantity[39.996238312372, "AtomicMassUnit"] (*Argon Specific*)

$M_{Ar}$ = UnitConvert[$M_{u}$]

q = Quantity[1.6022*$10^{-19}$,"Coulombs"]

$m_{e}$=Quantity[9.1095*$10^{-31}$,"Kilograms"]

$k_{B}$=Quantity[1.3807*$10^{-23}$,"Joules"/"Kelvins"]

$\alpha_{R}$=11.08 (*Argon Specific, Pg.60 Lieberman*)

$\chi_{01}$=2.4048 (*First root of the zero order Bessel function*)

$E_{iz}$=Quantity[15.76,"Electronvolts"] (*Argon Specific Pg. 81 *)

$E_{ex}$=Quantity[12.14,"Electronvolts"] (*Argon Specific Pg. 81 *)

$V_{RF}$={Quantity[100.0,"Volts"],Quantity[1000.0,"Volts"]} (*Estimate based on power for a capacitive discharge*)

ϵ0=Quantity[8.8542*$10^{-12}$,"Farads"/"Meters"]

$\mu_{0}$=Quantity[4.0*π*$10^{-7}$,"Henries"/"Meters"]

$b_c$ = Quantity[0.2,"Meters"] (*Radius of the inductive antenna coil*)

$N_c$= 4.0 (*Number of turns of the inductive antenna coil*)

### Gas Density and Mean Free Path

The gas density is found using the ideal gas law with the Boltzmann constant.

$n_g$=UnitConvert[p/($k_B$*$T_g$)]

The mean free path is based on argon where the ion-atom collision cross-section ($\sigma_i$) for Argon is approximately $10^{-14}$ cm$^2$.

$\sigma_i$=Quantity[1.0*$10^{-14}$,("Centimeters")$^2$]

$\lambda_i$=1.0/($n_g$*$\sigma_i$) (*Eq. 3.1.6 *)

### Particle Flux Loss Coefficients (Heuristic Result)

#### Bohm Velocity

Here, it is necessary to start creating functions because the best fit model for both the axial and radial geometry is dependent on the electron temperature. First it is necessary to define the Bohm velocity ($u_B$) and Ambipolar diffusion coefficient ($D_a$).

$u_B$[T_]:=\[Sqrt]UnitConvert[(Abs[T]*q*Quantity[1.0,"Joules"/"Coulombs"])/$M_{Ar}$]

Note: In the above equation, “T” is in units of electron volts. The absolute value is there to tell Mathmatica that "$u_B$" will not have imaginary values.

#### Ambipolar Diffusion Coefficient

For the Ambipolar diffusion coefficient, it is necessary to define the macroscopic mobility and diffusion constants for each species (electrons and ions) when no assumptions are made about the magnitude of temperature and mobility between the species. It will be assumed that the ion temperature is equal to the gas temperature. For the mobility of each species, the collision frequency is calculated using the Langevin rate constants (Pg. 62 Lieberman).

$T_i$=$T_g$

$K_{Le}$=Quantity[3.85*$10^{-8}$*Subscript[α, R]$^{1/2}$,("Centimeters")$^3$/"Seconds"] (*Eq. 3.3.16 *)

$K_{Li}$=Quantity[8.99*$10^{-10}$*(Subscript[α, R]/(Subscript[M, u]/Quantity[1.0,"AtomicMassUnit"]))$^{1/2}$,("Centimeters")$^3$/"Seconds"] (*Eq. 3.3.17 *)

$\nu_e$=$n_g$*$K_{Le}$ (*Eq. 3.3.14 *)

$\nu_i$=$n_g$*$K_{Li}$ (*Eq. 3.3.14 *)

$\mu_e$=UnitConvert[q/($m_e$*$\nu_e$) ,"SI"](*Eq. 5.1.4 *)

$\mu_i$=UnitConvert[q/($M_{Ar}$*$\nu_i$),"SI"] (*Eq. 5.1.4 *)

$D_e$[T_]:=UnitConvert[(T*q*Quantity[1.0,"Joules"/"Coulombs"])/($m_e$*$\nu_e$)] (*Eq. 5.1.5 *)

Note: In the above equation, “T” is in units of electron volts (Hence we dropped the "$k_B$").

$D_i$=UnitConvert[($k_B$*$T_i$)/($M_{Ar}$*$\nu_i$)] (*Eq. 5.1.5 *)

$D_a$[T_]:=($\mu_i$*$D_e$[T]+$\mu_e$*$D_i$)/($\mu_i$+$\mu_e$) (*Eq. 5.1.12 *)

## Particle Flux Loss Coefficients

Now that the ambipolar diffusion coefficient and the Bohm velocity have been defined, it is possible to define the particle flux loss coefficients.

$h_L$[T_]:=0.86/(3.0+Subscript[L, R]/(2.0*Subscript[λ, i])+(0.86*Subscript[L, R]*Subscript[u, B][T]/(π*Subscript[D, a][T]))^2)$^{1/2}$ (*Eq. 5.3.16 *)

$h_R$[T_]:=0.8/(4.0+Subscript[R, R]/Subscript[λ, i]+(0.8*Subscript[R, R]*Subscript[u, B][T]/(Subscript[χ, 01]*BesselJ[1,Subscript[χ, 01]]*Subscript[D, a][T]))^2)$^{1/2}$ (*Eq. 5.3.17 *)

Note: In the above equations, “T” is in units of electron volts.

## Effective Plasma Size for Particle Loss and Ionization Reaction Rate

### Effective Plasma Size for Particle Loss

Now that the particle flux loss coefficients have been defined, it is possible to define the effective plasma size for particle loss. This will be used along with the gas density ($n_g$), Bohm velocity ($u_B$), and the ionization reaction rate ($K_{iz}$) to numerically solve for the electron temperature. The first step is to calculate the effective area for particle loss.

$A_{eff}$[T_]:=2.0*π*Subscript[R, R]$^2$*$h_L$[T]+2.0*π*$R_R$*$L_R$*$h_R$[T] (*Eq. 10.2.11 *)

Note: In the above equation, “T” is in units of electron volts.
Note: For “T = 0”, the ambipolar diffusion coefficient equals 0 and therefore *Mathematica* does not like the 0 in the denominator.

The effective particle loss coefficient is defined as follows:

$d_{eff}$[T_]:=π*Subscript[R, R]$^2$*$L_R$/$A_{eff}$[T] (*Eq. 10.2.13 *)

Note: In the above equation, “T” is in units of electron volts.
Note: For “T = 0”, the ambipolar diffusion coefficient equals 0 and therefore *Mathematica* does not like the 0 in the denominator.

### Ionization Reaction Rate

The last part needed is the ionization reaction rate dependence on the electron temperature. This comes from the interaction table in Lieberman on Pg. 81.

$K_{iz}$[T_] :=Quantity[2.34*$10^{-14}$,("Meters")$^{3}$/"Seconds"]*$T^{0.59}$*$E^{(-17.44/T)}$ (*Table 3.3 *)

Note: For “T = 0”, the exponential disappears, but *Mathematica* does not like the 0 in the denominator.

### Electron Temperature

To find the electron temperature, it is necessary to numerically solve using the effective plasma size ($d_{eff}$), gas density ($n_g$), Bohm velocity ($u_B$), and the ionization reaction rate ($K_{iz}$).

$T_e$=(T*Quantity[1.0,"Electronvolts"])/.FindRoot[$K_{iz}$[T]/$u_B$[T]==1.0/($n_g$*$d_{eff}$[T]),{T,10.0}]

### Total Energy Loss per Electron-Ion Pair Lost

The next step is to calculate the energy loss per electron-ion pair lost ($E_T$) . This is based on the collisional energy loss per electron-ion pair formed ($E_c$), the mean kinetic energy lost per electron lost ($E_e$), and the mean kinetic energy lost per ion lost ($E_i$).

### Collisional Energy Loss per Electron-Ion Pair Formed

This is dependent on the electron temperature as well as the elastic collisions ($K_{el}$), ionization ($K_{iz}$), and excitation ($K_{ex}$) rate constants.

$K_{ex}$ = Quantity[2.48*$10^{-14}$,("Meters")$^{3}$/"Seconds"]*(Subscript[T, e]/Quantity[1.0,"Electronvolts"])$^{0.33}$*Exp[Quantity[-12.78,"Electronvolts"]/$T_e$] (*Table 3.3 *)

$K_{el}$=Quantity[2.336*$10^{-14}$,("Meters")$^{3}$/"Seconds"]*(Subscript[T, e]/Quantity[1.0,"Electronvolts"])$^{1.609}$*Exp[0.0618*(Log[Subscript[T, e]/Quantity[1.0,"Electronvolts"]])$^{2}$-0.1171*(Log[Subscript[T, e]/Quantity[1.0,"Electronvolts"]])$^{3}$] (*Table 3.3 *)

$E_c$=$E_{iz}$+($K_{ex}$/$K_{iz}$[$T_e$/Quantity[1.0,"Electronvolts"]])*$E_{ex}$+($K_{el}$/$K_{iz}$[$T_e$/Quantity[1.0,"Electronvolts"]])*((3.0*$m_e$)/$M_{Ar}$)*$T_e$ (*Eq. 3.5.8 *)

### Mean Kinetic Energy Lost per Electron Lost

For a Maxwellian electron, the mean kinetic energy lost per electron lost was shown to be:

$E_e$=2.0*$T_e$ (*Eq. 2.4.11 *)

### Mean Kinetic Energy Lost per Ion Lost

For mean kinetic energy lost per ion lost, it is necessary to take into account the energy gained as an ion moves across the sheath. For no significant voltages applied across the sheath (Inductive discharge), the sheath voltage ($V_{s,i}$) is:

$V_{s,i}$=$T_e$*(Log[Subscript[M, Ar]/(2.0*π*Subscript[m, e])])$^{1/2}$ (*Eq. 10.2.4 *)

For a $V_{RF}$>>$T_e$ (Capacitive discharge), then the sheath voltage ($V_{s,c}$) of an asymmetrically driven discharge can be estimated as:

$V_{s,c}$=Quantity[0.8,"Electronvolts"/"Volts"]*$V_{RF}$ (*Eq. 10.2.7 *)

The mean kinetic energy lost per ion lost is then found as for a capacitive discharge:

$E_{i,c}$=$V_{s,c}$+(1/2)*$T_e$ (*Eq. 10.2.8 *)

### Total Energy Lost per Electron-Ion Pair Lost

With the above energy losses, the total energy lost per electron-ion pair lost can be found for a capacitive discharge it is:

$E_{T,c}$=$E_c$+$E_e$+$E_{i,c}$ (*Eq. 10.2.9 *)

### Core and Sheath Plasma Density

Once the total energy lost per electron-ion pair lost is found, the core plasma density can be found for a capacitive ($n_{0,c}$) discharge. Here, the plasma density is specified. This just means that you would have a range of powers (which may not be feasible) that would generate this density for the given geometry and pressure.

```
linearmesh2[a_, b_, n_Integer /; n > 0] := Range[a, b, (b - a)/n]
linearmesh[a_,b_,n_Integer/;n>1]:=Range[a,b,(b-a)/n]
```

$n_{0,c}$=UnitConvert[{Quantity[1.0*$10^{12}$,("Centimeters")$^{-3}$],Quantity[2.0*$10^{12}$,("Centimeters")$^{-3}$]}]

The sheath plasma density is calculated using the particle flux loss coefficients calculated earlier.

$n_{s,c}$=$n_{0,c}$*$h_R$[$T_e$/Quantity[1.0,"Electronvolts"]]

# Appendix B: IEDfs Plots with Fewer Curves for Clarity

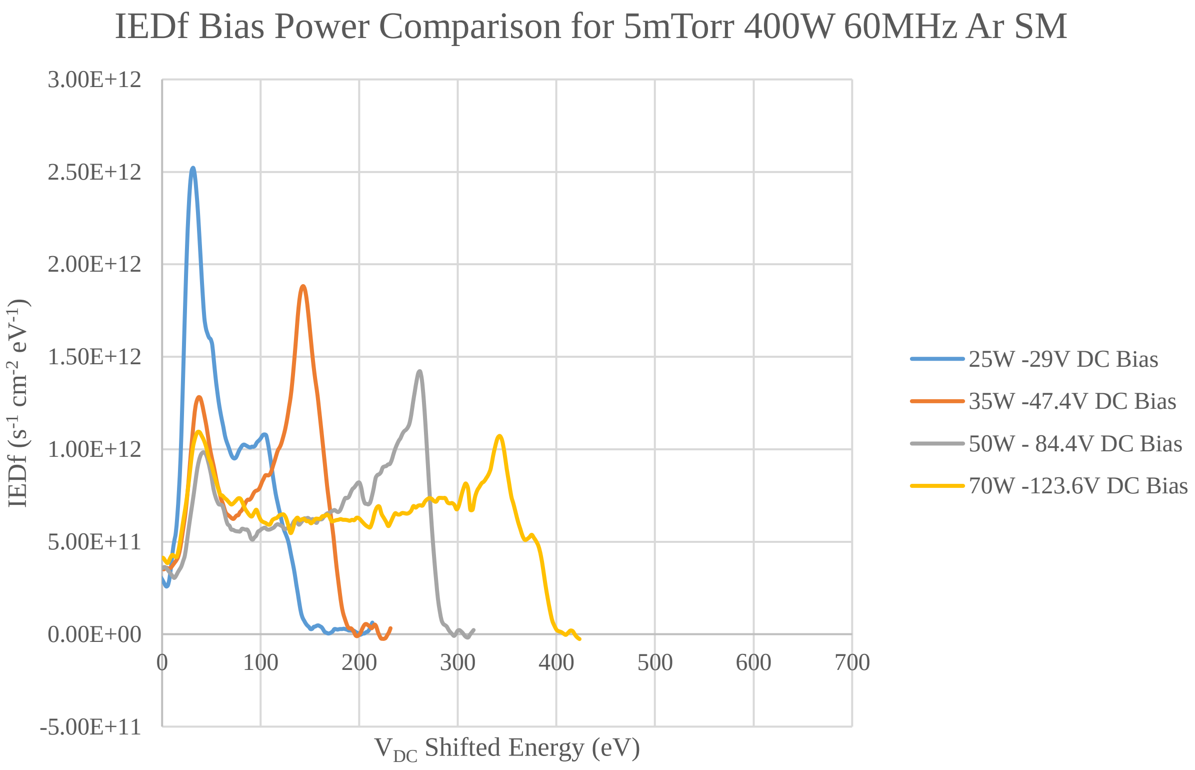

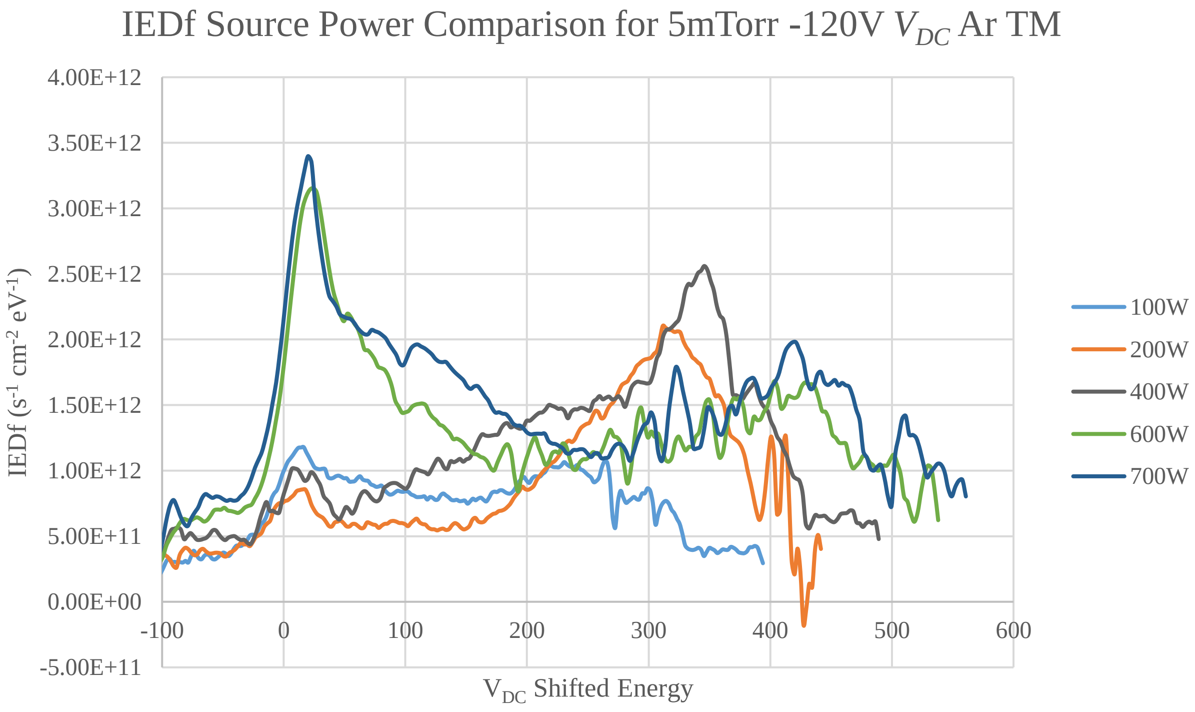

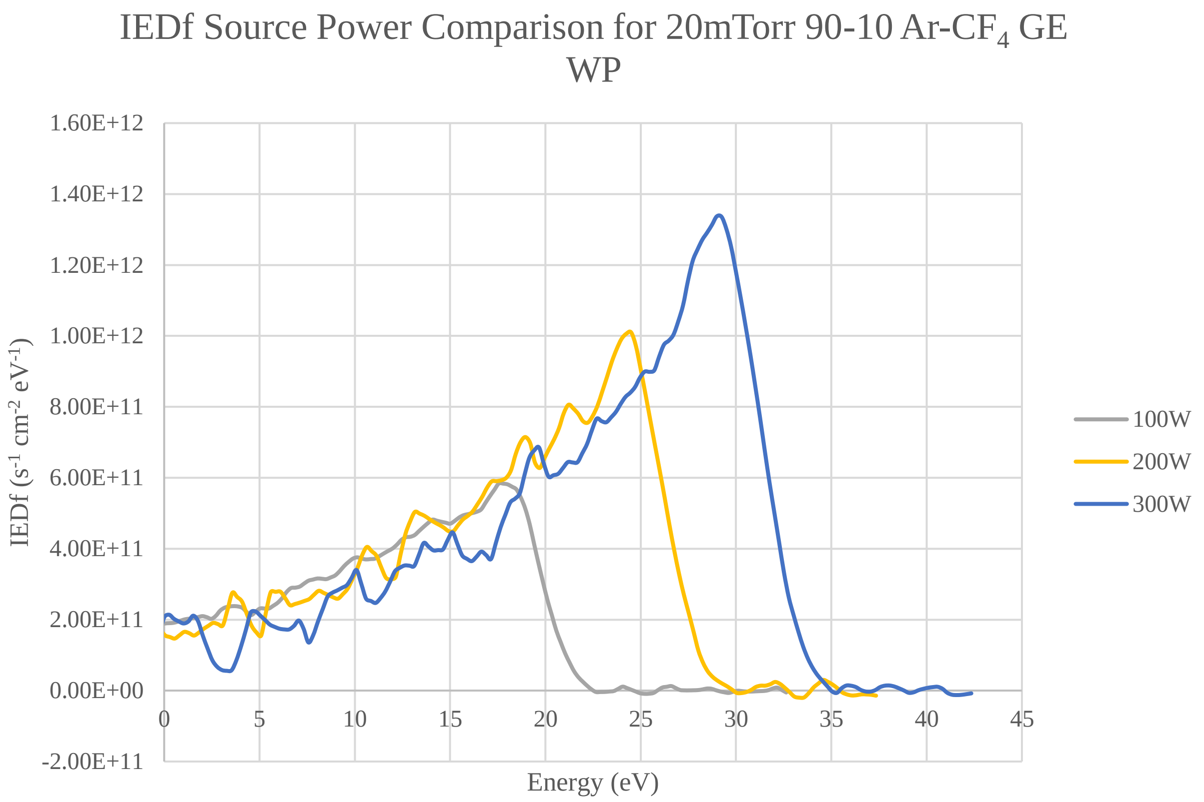
IEDf Source Power Comparison for 20mTorr 90-10 Ar-CF$_4$ GE WP
IEDf (s$^{-1}$ cm$^{-2}$ eV$^{-1}$)
1.60E+12
1.40E+12
1.20E+12
1.00E+12
8.00E+11
6.00E+11
4.00E+11
2.00E+11
0.00E+00
-2.00E+11
0
5
10
15
20
25
30
35
40
45
Energy (eV)
100W
200W
300W

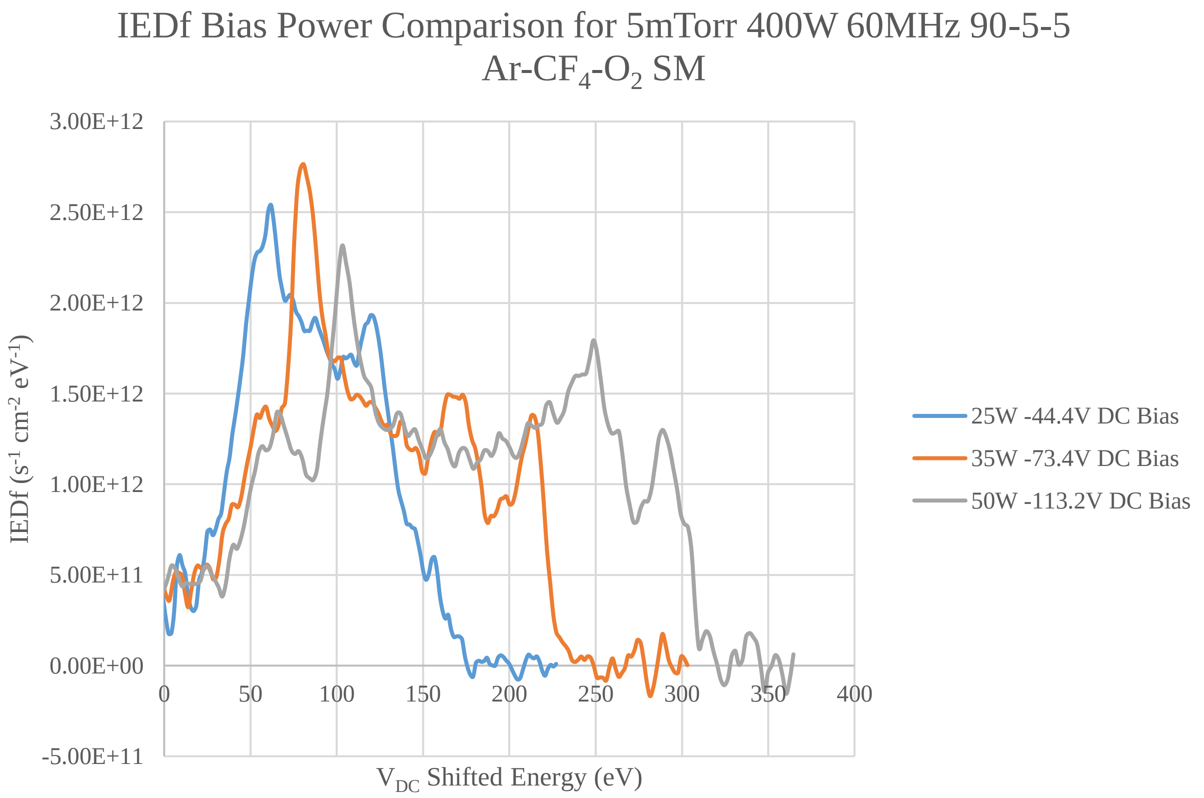
IEDf Bias Power Comparison for 5mTorr 400W 60MHz 90-5-5 Ar-CF$_4$-O$_2$ SM
IEDf (s$^{-1}$ cm$^{-2}$ eV$^{-1}$)
3.00E+12
2.50E+12
2.00E+12
1.50E+12
1.00E+12
5.00E+11
0.00E+00
-5.00E+11
0
50
100
150
200
250
300
350
400
V$_{DC}$ Shifted Energy (eV)
25W -44.4V DC Bias
35W -73.4V DC Bias
50W -113.2V DC Bias

# Appendix C: Ar – $CF_4$ and Ar – $CF_4$ – $O_2$ IV Curves

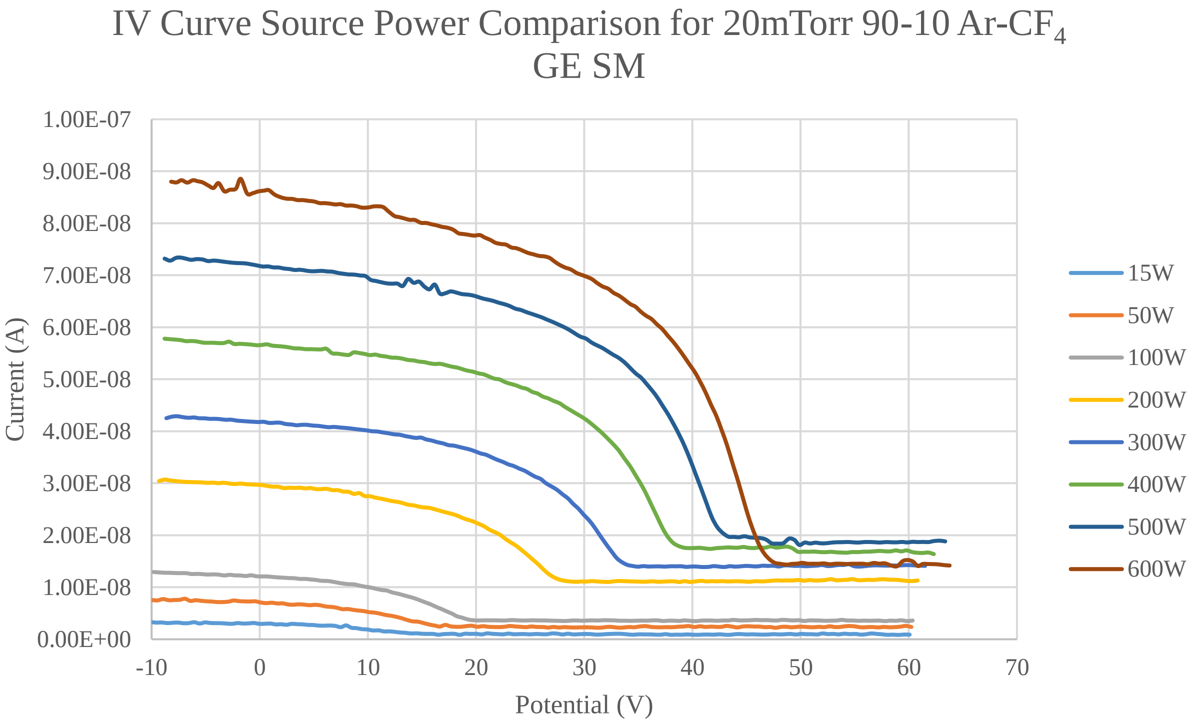

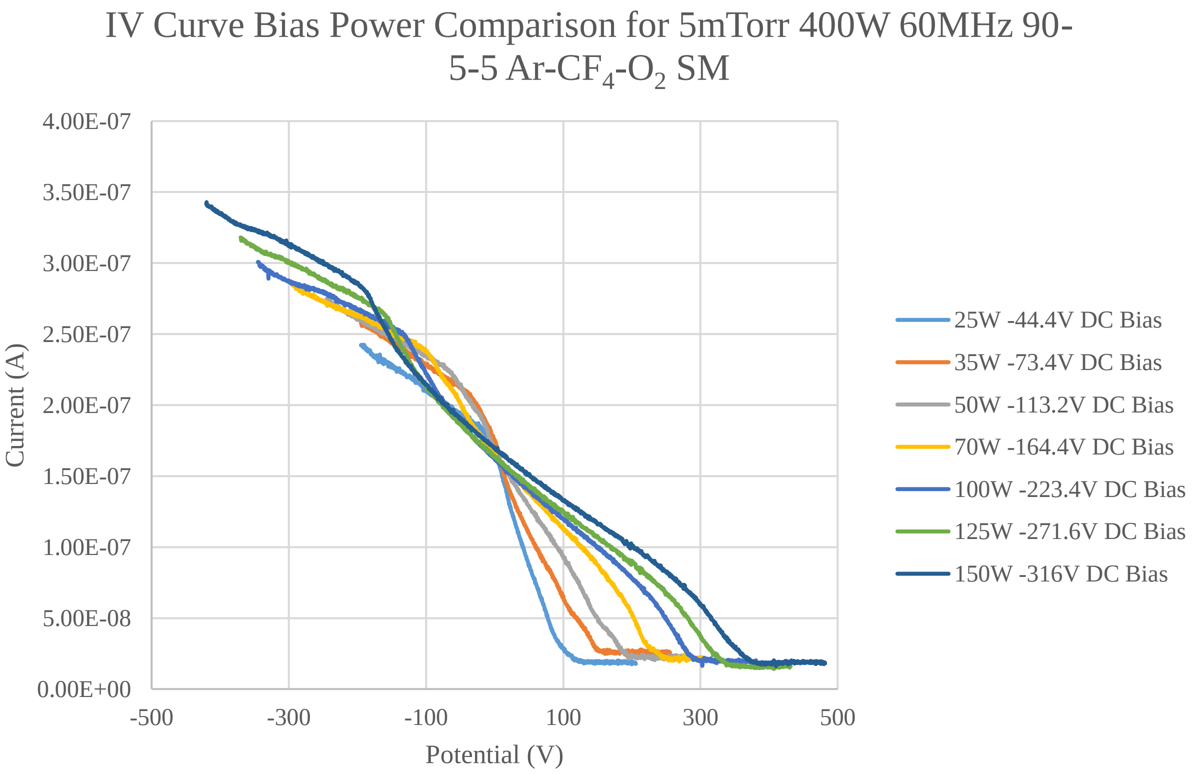

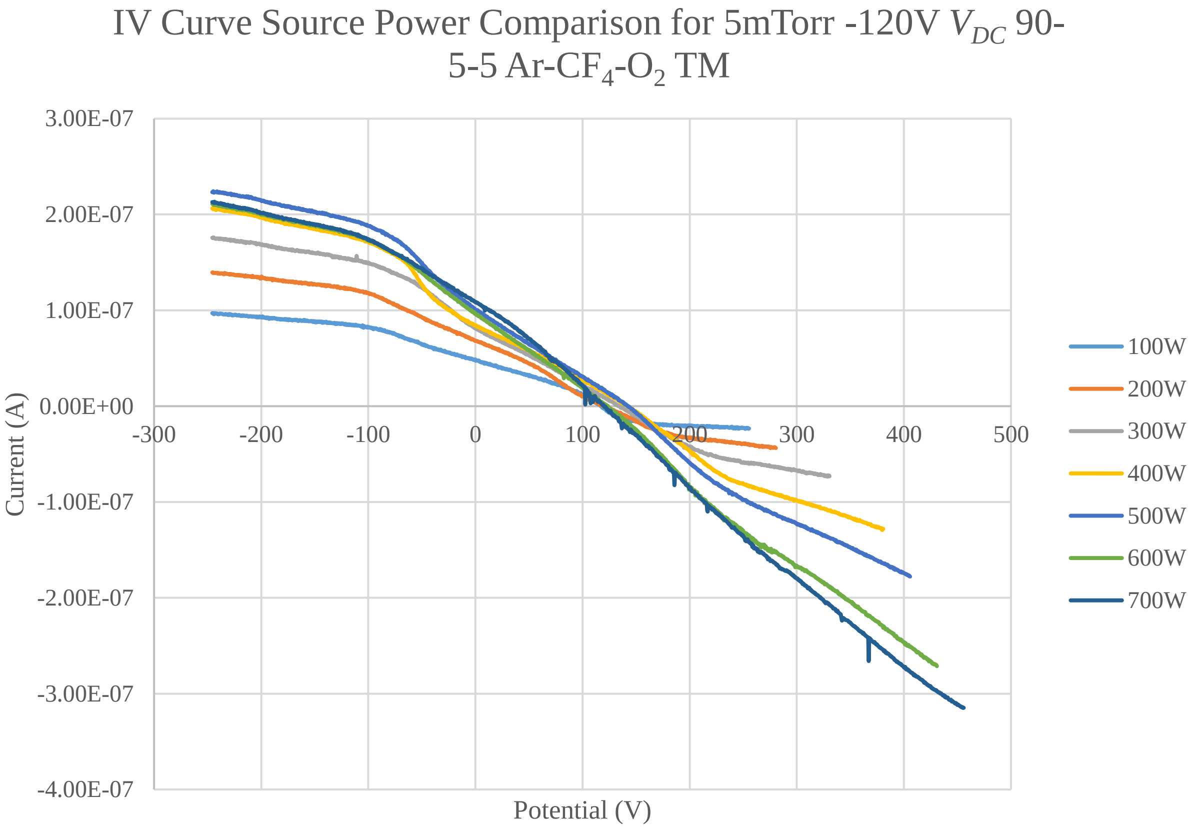
IV Curve Source Power Comparison for 5mTorr -120V $V_{DC}$ 90-5-5 Ar-$CF_4$-$O_2$ TM
3.00E-07
2.00E-07
1.00E-07
0.00E+00
-1.00E-07
-2.00E-07
-3.00E-07
-4.00E-07
Current (A)
-300
-200
-100
0
100
200
300
400
500
Potential (V)
100W
200W
300W
400W
500W
600W
700W